Technical Physics, Vol. 45, No. 6, 2000, pp. 667–671. Translated from Zhurnal Tekhnicheskoĭ Fiziki, Vol. 70, No. 6, 2000, pp. 1–5.

The Cross-Correlation Integral: Its Features and Application to Nonstationarity Detection in Time Series

I. V. Fel'dshteĭn

Keldysh Institute of Applied Mathematics, Russian Academy of Sciences, Miusskaya pl. 4, Moscow, 125047 Russia

Received June 16, 1998; in final form, December 7, 1999

Abstract—A generalization of the correlation integral, called the cross-correlation integral, is suggested. Features of the cross-correlation integral are studied, and a new attribute of a time series is defined. It is viewed as some kind of dimension and is associated with the fill rate of the attractor. It is demonstrated that the cross-correlation integral is calculated in much the same way as the wavelet transform of the density of points in the attractor. The cross-correlation integral is applied to detection of nonstationarity in time series. A comparison with statistical methods is made. © *2000 MAIK "Nauka/Interperiodica".*

INTRODUCTION

The correlation integral is among the basic tools for the analysis of time series [1]. It has received broad application in the last 10–15 years. For example, it was used as the basis for evaluating the dimension of an embedding for a system under study, defining the concept of correlation dimension, and differentiating random noise from deterministic chaos, to name but a few. The correlation integral has been applied to various types of data pertaining to technology, medicine, hydrodynamics, astrophysics, finance, etc. On the other hand, the approach can be extended to a wealth of problems beyond the scope of the analysis of individual systems and their related time series. This new direction consists in comparing the modes of behavior of two different systems or those of the same system observed at different instants. The latter problem can be regarded as nonstationarity detection.

This paper suggests a generalization of the correlation integral, studies certain features of the new mathematical object, and defines a new attribute of a time series. The last-named quantity is viewed as some kind of dimension and is associated with the fill rate of the attractor. In this work, the generalized correlation integral is applied to nonstationarity detection in time series and is compared with statistical methods.

DEFINITION OF CROSS-CORRELATION INTEGRAL

The analysis of time series in nonlinear dynamics widely employs the correlation integral $C(r)$ [1]. Let $\rho(y_i, y_j)$ be the distance between phase vectors y_i and y_j. Then the correlation integral $C(r)$ of an N-point vector time series $\{y_i\}_N$ is defined as

$$C(r) = \frac{1}{N^2}\sum_{i,j=1}^{N}\Theta(r-\rho(y_i, y_j)),$$

where Θ is the Heaviside function.

If the available time series $\{x_i\}$ is a scalar one, it can be associated with a vector time series $\{y_i\}$ by the Takens method [2] (see also [3]):

$$y_j = (x_j, x_M, \ldots, x_{j+(d-1)M})^T,$$

where d is the dimension and M is the delay.

We generalize this concept as follows. Let vector time series $\{y_i\}_n$ and $\{z_i\}_m$, comprising, respectively, n and m points, be available. Let $\rho(y_i, z_j)$ denote the distance. Then the cross-correlation integral $C^+(r)$ is defined as

$$C^+_{y,z}(r) = \frac{1}{mn}\sum_{i,j=1}^{n,m}\Theta(r-\rho(y_i, z_j)). \qquad (1)$$

Obviously, $C^+_{y,y}(r) = C(r)$.

This study deals with the case where the cross-correlation integral is taken over segments from the same time series $\{x_i\}$. The segments differ only in location. Let them be numbered and $C^+_{i,j}$ denote the cross-correlation integral for segments i and j. For the sake of convenience, define the quantities

$$\Delta_{ij}(r) = \left|\ln C^+_{i,j}(r) - \ln C^+_{j,j}(r)\right| \qquad (2)$$

and

$$\delta_{ij} = \int_{r_{\min}}^{r_{\max}}\Delta_{ij}(r)dr. \qquad (3)$$

1063-7842/00/4506-0667$20.00 © 2000 MAIK "Nauka/Interperiodica"

They reflect both the local (with regard for scale) and aggregate variations in the density of attractor points for segments i and j. Here, r_{max} is the saturation scale of the cross-correlation integral (r_{max} is of the order of the maximum attractor size) and r_{min} is the scale corresponding to the minimum distance between attractor points (for the sample at hand) or to the noise amplitude for noisy data. We restrict ourselves to the case $j = 1$, denoting $\Delta_{i,1}$ as Δ_i and $\delta_{i,1}$ as δ_i. In other words, the variations are considered with reference to segment 1.

CROSS-CORRELATION INTEGRAL AND WAVELET TRANSFORM

Let us calculate the cross-correlation integral of two one-dimensional random variables ξ_1 and ξ_2, their probability distribution functions (PDFs) being F_1 and F_2, respectively. If the probability density function of ξ_1 is p_1, then an interval dx around x contains $p_1(x)dx$ values of ξ_1. The number of ξ_2 values whose distance from x is less than or equal to r is $F_2(x + r) - F_2(x - r)$. Thus, the cross-correlation integral $C^+_{\xi_1\xi_2}$ has the form

$$C^+_{\xi_1\xi_2}(r) = \int_{-\infty}^{+\infty} p_1(x)(F_2(x+r) - F_2(x-r))dx.$$

Let the width of F_2 be changed by a factor a. (In a Gaussian case, the width is the variance.) Then the cross-correlation integral becomes

$$C^+_{\xi_1\xi_2}(r, a) = \int_{-\infty}^{+\infty} p_1(x)\left(F_2\left(\frac{x+r}{a}\right) - F_2\left(\frac{x-r}{a}\right)\right)dx. \quad (4)$$

Expression (4) is similar to the wavelet transform

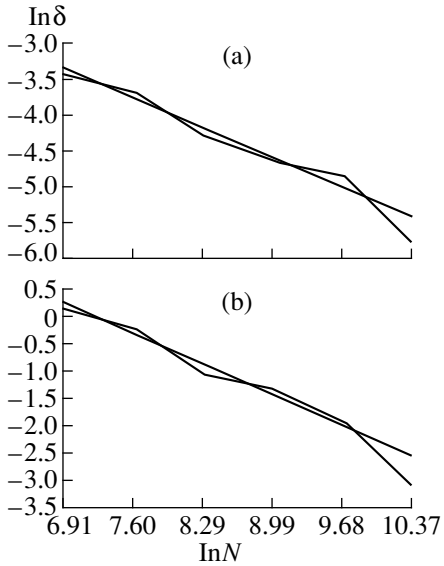

Fig. 1. δ vs. sample size for the (a) Lorentz system and (b) Rössler system. Straight line, linear approximation.

of p_1 [4]:

$$S(r, a) = \frac{1}{\sqrt{a}}\int_{-\infty}^{+\infty} p_1(x)F\left(\frac{r-b}{a}\right)dx. \quad (5)$$

Transforms (4) and (5) differ from each other in two respects. First, (4) is "symmetric" in r (except for sign). Second, recall that the kernel F is usually assumed to meet the condition

$$\int_{-\infty}^{+\infty} F(x)dx = 0,$$

and sometimes also the higher order moment condition

$$\int_{-\infty}^{+\infty} x^k F(x)dx = 0.$$

With transform (4), for any r and a, this requirement is satisfied by the PDF difference (in brackets):

$$\int_{-\infty}^{+\infty} x^k\left(F_2\left(\frac{x+r}{a}\right) - F_2\left(\frac{x-r}{a}\right)\right)dx = 0.$$

Note that formula (4) can be modified to meet the normalization condition [see the factor $1/\sqrt{a}$ in (5)].

In (4), integrating by parts demonstrates the symmetry of the cross-correlation integral: $C^+_{\xi_1\xi_2} = C^+_{\xi_2\xi_1}$. The multidimensional case can obviously be treated similarly.

The linkage with the wavelet transform applied to the PDFs seems to be helpful when time series of the system are unavailable or more difficult to obtain than the PDFs.

ATTRACTOR FILL RATE

For a stationary time series, δ is nonzero [see (3)], since any time series is a finite and discrete entity. Let us trace how δ depends on the length N of the segment used to estimate C^+. Figure 1 shows the behavior of δ for the Lorentz and Rössler systems. It is seen that the curves approximately obey the power law $\delta \sim N^{-d_{fr}}$. Here, d_{fr} refers to the fill rate of the system attractor for a given accuracy (of computation or measurement). It can be viewed as a dimension (by construction). Notice that the curves deviate downward at large N. The value of N^* at which the deviation from the power law becomes considerable could be regarded as the maximum length suitable for analyzing the density of attractor points: increasing N any further refines the picture insignificantly.

NONSTATIONARITY DETECTION IN TIME SERIES

It may be very important to know whether a time series of interest is stationary. (By stationarity, one may mean that the parameters of the generating system are independent of time.) Stationarity is a necessary condition for many algorithms of nonlinear dynamics, such as those evaluating dimensions, the Lyapunov exponents, etc.

Let us apply the cross-correlation integral to nonstationarity detection in time series and compare the results with those of traditional statistical methods.

Statistical Methods

Nonstationarity is commonly detected with the help of mathematical statistics. It enables one to estimate the probability that two samples are the realizations of random processes with differing PDFs (the $\mathbf{H}_1$ hypothesis). The most efficient tool to solve this problem is the Kolmogorov–Smirnov method [5], which is stated as follows. Let samples $\{x_i^1\}_m$ and $\{x_i^2\}_n$ be available, comprising, respectively, m and n points. Furthermore, assume that

$$F_1(a) = \frac{\nu_1(a)}{m}, \quad F_2(a) = \frac{\nu_2(a)}{n},$$

where $\nu_1(a)$ and $\nu_2(a)$ the numbers of points from $\{x_i^j\}$ such that $x_i^j < a$ ($j = 1$ or 2), and denote

$$D_{m,n} = \max_a |F_1(a) - F_2(a)|.$$

Then the PDF of the random variable $\sqrt{mn/(m+n)}\,D_{m,n}$ tends to

$$K(q) = 1 - 2\sum_{k=1}^{\infty} e^{-2q^2k^2}. \qquad (6)$$

The graph of $K(q)$ is shown in Fig. 2. Given $\sqrt{mn/(m+n)}\,D_{m,n} = K^*$, the probability q^* for the $\mathbf{H}_1$ hypothesis to be true is determined from (6) subject to $K(q^*) = K^*$. The Kolmogorov–Smirnov method was applied to attractor identification (see, e.g., [6]). It has proven to be highly efficient for many model systems. However, there are cases where the method is inappropriate or suffers from limitations. To exemplify the difficulties, consider the Lorentz and Rössler systems with the following dependences of the system parameter r on time:

$$r = f_1(t) = r_{\min} + (r_{\max} - r_{\min})t/T_{\max},$$

$$r = f_2(t) = \begin{cases} r_{\min} & 0.45T_{\max} \le t \le 0.55T_{\max} \\ r_{\max} & t < 0.45T_{\max}, \quad t > 0.55T_{\max}. \end{cases}$$

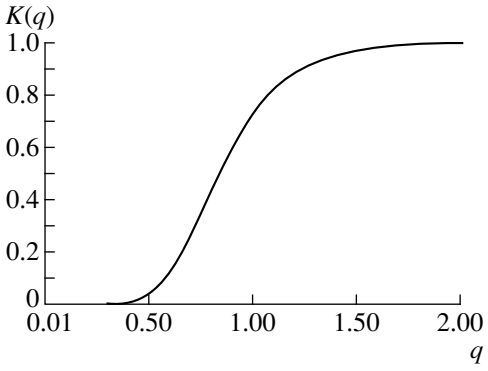

Fig. 2. The Kolmogorov–Smirnov distribution $K(q)$.

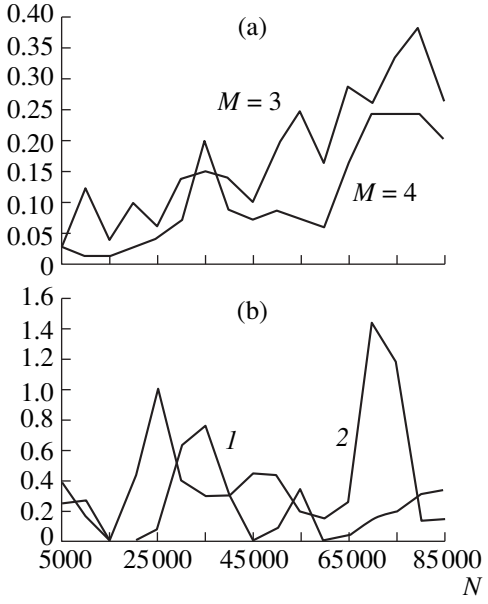

Fig. 3. Estimated values of $\sqrt{mn/(m+n)}\,D_{m,n}$ vs. sequence number of the first point in a segment of interest. Panel (a) refers to the system R_1; Panel (b), to the systems (*1*) L_1 and (*2*) L_2. The parameter M indicates the degree of thinning.

The Lorentz system L_1 is

$$\dot{x} = \sigma(y - x), \quad \dot{y} = rx - y - xz, \quad \dot{z} = xy - bz.$$

Here, we set $b = 8/3$, $\sigma = 10$, $r = f_1(t)$, $T_{\max} = 5000$ (the sample comprises 100000 points with the time step 0.05), $r_{\max} = 29$, and $r_{\min} = 28$. In the Lorentz version L_2, we set $r = f_2(t)$, the other parameters being as in L_1. The Rössler system R_1 is

$$\dot{x} = -(y + z), \quad \dot{y} = x + 0.2y, \quad \dot{z} = 0.2 + z(x - r).$$

Here, we set $r = f_2(t)$, $T_{\max} = 50000$ (the sample comprises 100000 points with the time step 0.5), $r_{\max} = 4.30$, and $r_{\min} = 4.23$. In the Rössler version R_2, we set $r = f_2(t)$, the other parameters being as in R_1.

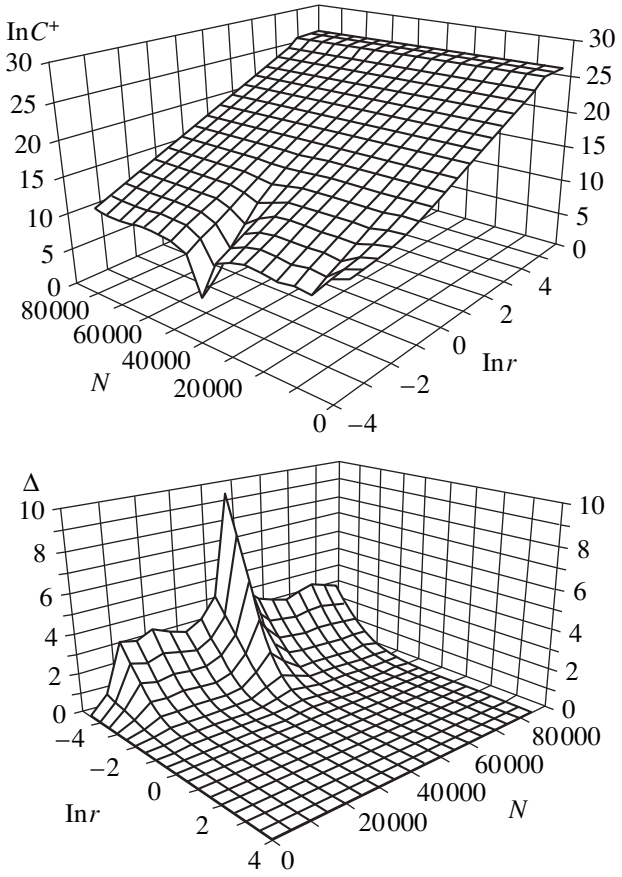

Fig. 4. $C_{i,1}^{+}$ and Δ_i for L_2.

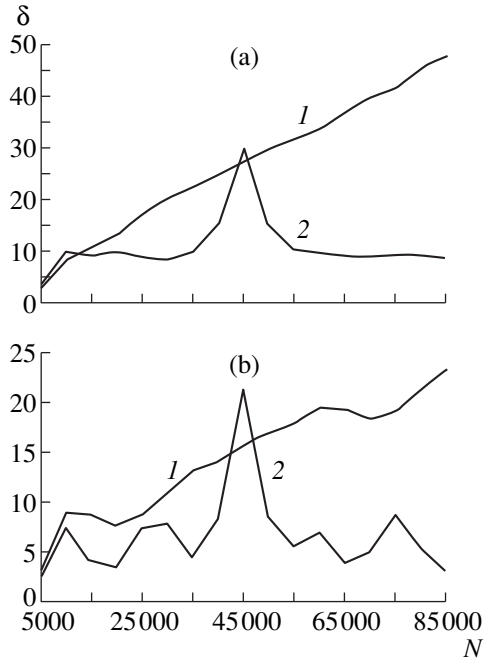

Fig. 5. δ for (a) L_1 and L_2 and (b) R_1 and R_2. The meaning of N is as in Fig. 3.

The check for stationarity is based on the Kolmogorov–Smirnov method applied to samples comprising 10000 successive points. Beginning with the second sample, each sample is shifted by 5000 against its immediate predecessor so that sample 1 covers points 1–10000; sample 2, points 5001–15000; sample 3, points 10001–20000; and so on.

To avoid internal correlations, the original time series $\{x_i\}$ is "thinned": we take only the points x_1, x_{M+1}, x_{2M+1}, etc. The necessity of thinning and its realization are comprehensively discussed in [6].

Figure 3a refers to R_1. It shows estimated values of $\sqrt{mn/(m+n)}\,D_{m,n}$ against the sequence number of the first point in a segment of interest. The thinning parameter M is set at 3 or 4 so that the autocorrelation integral is zero: for the Rössler systems, examined at the time step $\tau = 0.5$, the integral is positive at 3τ and negative at 4τ. It is seen that the estimates vary considerably and the curves give no idea of how the system parameters behave. Indeed, one could estimate the correlation length more accurately if the system were defined formally (e.g., in terms of ordinary differential equations). However, such a definition is impossible in practice. For the Lorentz systems, the correlation length T_{corr} estimated from x is very large, so that thinning at the corresponding value of M leaves too little data for estimating the PDFs. By convention, M may be set equal to the quarter-quasi-period (mean distance between successive peaks). This gives $M \sim 5$ for the time series at hand. For L_1 and L_2, estimated values of $\sqrt{mn/(m+n)}\,D_{m,n}$ are plotted in Fig. 3b. It is seen that the estimates do not reflect the behavior of the system parameter. In fact, they may indicate that the parameter has different values for the two samples when its actual values are the same.

Thus, approaches based on the Kolmogorov–Smirnov method may be sensitive, e.g., to M. For the Lorentz system, similar techniques of attractor identification may be sensitive to initial conditions as well [6]. This paper suggests an alternative approach, which is built around the cross-correlation integral.

Using the Cross-Correlation Integral for Nonstationarity Detection

Let us apply the cross-correlation integral to nonstationarity detection in L_1, L_2, R_1, and R_2.

Figure 4 depicts $C_{i,1}^{+}$ and Δ_i for L_2. Notice that the maximum deviation relates to the segment where the deviation of the parameter is maximum in terms of time. The values of δ_i are displayed in Fig. 5a for L_1 and L_2 and in Fig. 5b for R_1 and R_2. It is seen that the behavior of δ_i faithfully reflects the variations in the system parameter.

Consider the sensitivity of the method to M (for d = 5). Figure 6a shows estimated values of δ_i for L_2 at M =

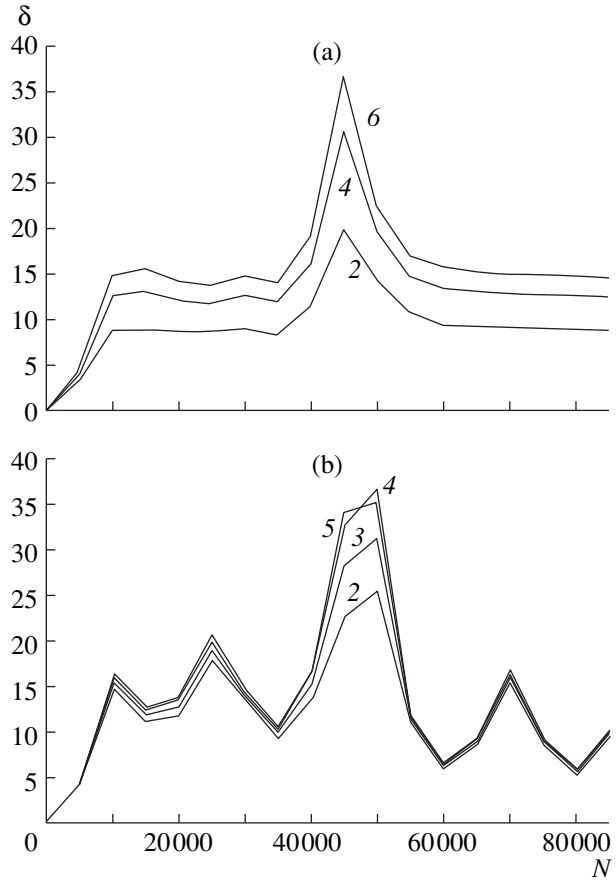

Fig. 6. δ for (a) L_2 and M = 2, 4, and 6 and (b) R_2 and M = 2, 3, 4, and 5. The meaning of N is as in Fig. 3.

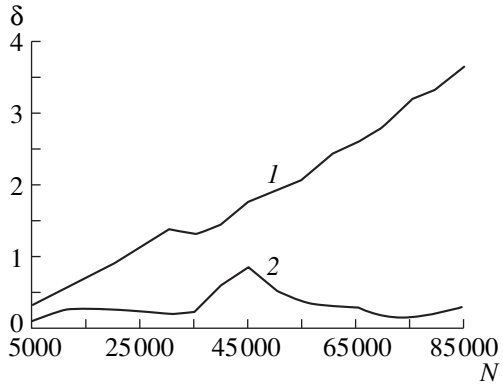

Fig. 7. δ for (*1*) L_1 and (*2*) L_2 under the action of additive noise. *1*, $f_1(t)$; *2*, f_2(t).

2, 4, and 6. Figure 6b displays those for R_2 at M = 2, 3, 4, and 5. The results are qualitatively the same and correspond to the variations in the system parameter.

Figure 7 shows the graphs of δ_i for L_1 and L_2 in the presence of additive noise. The noise is uniformly distributed over the interval (–a, a), where a is equal to 10% of the standard deviation of the time series. Qualitatively, the result is immune to the noise.

If a time series is the realization of a nonstationary random process, the outcome of the cross-correlation-integral approach is similar.

CONCLUSION

We suggested a generalization of the correlation integral. The new mathematical tool was called the cross-correlation integral. Its similarity to the wavelet transform of the PDF was demonstrated. The effect of sample size was studied. We defined the quantity characterizing the aggregate discrepancy between the correlation and cross-correlation integrals. It was found that this quantity is a power function of sample size. The exponent governs the fill rate of the attractor. The sample size for which the deviation from the power law becomes considerable can be regarded as the maximum size suitable for estimating the density of attractor points (with regard for the accuracy of a time series). The cross-correlation integral was applied to nonstationarity detection in time series. A comparison with statistical methods was made. It demonstrated that the method of the cross-correlation integral is advantageous in some cases. The effect of additive noise was considered.

ACKNOWLEDGMENTS

I am grateful to A.B. Potapov and G.G. Malinetskiĭ for valuable discussion and comments.

This work was supported in part by the Russian Foundation for Basic Research, grant nos. 96-02-18689 and 97-01-00396.

REFERENCES

1. P. Grassberger and I. Procaccia, Physica D **9**, 189 (1983).
2. F. Takens, *Lect. Notes Math.* (Springer, Berlin, 1981), Vol. 898, pp. 336–381.
3. G. G. Malinetskiĭ, A. B. Potapov, and A. I. Rakhmanov, Preprint No. 10, IPM RAN (Keldysh Inst. of Applied Mathematics, Russian Academy of Sciences, Moscow, 1993).
4. A. Grossmann, R. Kronland-Martinet, and J. Morlet, in *Wavelet* (Springer-Verlag, Berlin, 1991), pp. 2–21.
5. P. Hennequin and A. Tortrat, *Théorie des probabilités et quelques applications* (Masson, Paris, 1965; Nauka, Moscow, 1974).
6. A. S. Dmitriev and O. L. Krupskiĭ, Zh. Tekh. Fiz. **63** (10), 1 (1993) [Tech. Phys. **38**, 835 (1993)].

Translated by A. A. Sharshakov

Technical Physics, Vol. 45, No. 6, 2000, pp. 672–676. Translated from Zhurnal Tekhnicheskoĭ Fiziki, Vol. 70, No. 6, 2000, pp. 6–9.

Phenomenological Equations of the Glass Transition in Liquids

A. I. Olemskoĭ and A. V. Khomenko

Sumy State University, Sumy, 244007 Ukraine

Received January 28, 1999

Abstract—The paper presents a theoretical analysis of the glass transition. It is demonstrated that the kinetics of glass transition is described by the following equations: the Maxwell equation of a viscoelastic medium; the equation of elastic relaxation, which, in addition to the usual Debye term, involves a nonlinear term due to the positive feedback between the strain field and temperature; and the equation of specific heat continuity, in which the entropy term includes the contribution of elastic fields and the heat flux contains a term related to external cooling. These equations are analogous to the Lorenz synergetic system, in which the strain plays the role of an order parameter, the conjugate field reduces to elastic stresses, and the temperature is a controlling parameter.

Despite great scientific and practical interest, the nature of the glass transition in liquids is not yet clearly understood [1–4]. This is primarily associated with an ambiguous interpretation of the amorphous state. At present, there are three main concepts of the amorphous state [5–9]. The first concept has a thermodynamic character and assumes the occurrence of a structural glass phase, which, in essence, is described in the same fashion as spin glasses: the frozen disorder in the parameters of interatomic interaction brings about frustrations and, hence, the loss of ergodicity of the glass phase [5–7]. Within the second approach, the glass transition is treated as a kinetic transition to a nonergodic stationary state [3]; however, according to Das and Mazenko [8], this transition cannot be realized. As regards the third approach, Stein and Palmer [9] proposed a scheme according to which the glass transition leads neither to the formation of a thermodynamic phase nor to the realization of a stationary kinetic state but is accompanied by the complete loss of stability of metastable states of the liquid whose configurations become trapped in the regions of the phase space bounded by barriers of finite height.

The loss of ergodicity upon glass transition is a common feature of the above approaches. The first approach assumes the absolute loss of ergodicity in the configuration space of states, whereas the second approach implies absolute ergodicity loss in the space of fluxes. In the framework of the latter approach, it is supposed that, owing to a finite barrier height, the regions of the phase space are governed by the distribution of barriers and their configuration changes in a fluctuational way. It is evident that such a slow evolution corresponds to the structural relaxation of the glass. Consequently, although the glass is not associated with a particular state, it is assumed that the glass is a set of stationary nonergodic states which has evolved in accordance with the structural relaxation.

From the foregoing, it is seen that a rather paradoxical situation arises today in the theory of the glass transition. Actually, all the above concepts are based on the microscopic approach, whereas the phenomenological scheme of the glass transition (similar to the Landau theory of phase transitions) is currently absent. The reason is that the violation of ergodicity upon glass transition is a more complex phenomenon than the phase transition [10]. Indeed, in order to obtain the thermodynamic description of the phase transition, it is sufficient to represent the behavior of the sole hydrodynamic mode whose amplitude reduces to the order parameter. At the same time, the representation of the overall pattern of the loss of ergodicity requires the description of specific features in the distribution of microstates over the phase space of the system as a whole, which, quite apparently, cannot be achieved with a single parameter [10]. In the theory of spin glasses, this is embodied in the fact that, in addition to the memory parameter introduced by Edwards and Anderson [11], there arises the necessity of applying the nonergodicity parameter accounting for the de Almeida–Thouless instability [12].

However, it should be remembered that the aforementioned simple scheme of the phase transition makes it possible to represent only the thermodynamic behavior of the hydrodynamic mode in a thermostat whose state does not depend on the order parameter. When describing the kinetics of phase transition, this condition is violated, and it is necessary to consider the self-consistent behavior of the hydrodynamic mode and the thermostat. In our earlier work [13], we showed that this can be accomplished with the use of the Lorenz synergetic scheme. Within this scheme, the state of a thermostat is represented as a field which is conjugate to the order parameter and a controlling parameter of the temperature type. Such a three-parameter model enables one to construct a nontrivial kinetic scheme of phase transition, which, at a certain ratio between

1063-7842/00/4506-0672$20.00

relaxation times, reduces to the Landau–Khalatnikov dissipative dynamics. Since the glass transition in a liquid is a kinetic transition, the aforesaid brings up the reasonable question as to whether the phenomenological theory of the glass transition in liquids can be constructed using the Lorenz scheme, which provides the simplest description of a self-organizing system [14]. The purpose of the present work was to derive the basic equations of this theory.

Although the glass transition is attended by the loss of ergodicity, in our derivation, we will deliberately ignore this circumstance and proceed from the concept of a viscoelastic medium, which goes back to rheological models. To put it differently, instead of primary glass transition parameters, such as the parameters of memory and nonergodicity, we will use the secondary parameters—the strain of the medium, the elastic stress, and the temperature, which, within the synergetic approach, fulfill the role of an order parameter, its conjugate field, and a controlling parameter, respectively. This parametrization is justified by the fact that, in the phenomenological representation, the fundamental difference between a liquid and a glass resides in the relaxation character of the shear component of elastic stresses: in a perfect glass, they persist infinitely long, whereas, in liquid, relaxation proceeds over a finite period of time [15]

$$\tau = \eta/G, \tag{1}$$

where η is the dynamic shear viscosity and G is the shear modulus.

In the simplest case, it is suggested that the glass transition is due to the purely kinetic effect of freezing the liquid when the viscosity η becomes infinite at a finite shear modulus G [16]. At the same time, the opposite situation is observed upon the usual second-order phase transition when τ also infinitely increases at the critical point. Actually, in going from the viscoelastic liquid to the general case, formula (1) takes the form $\tau = \chi/\gamma$, where χ is the generalized susceptibility and γ is the kinetic coefficient (in relationship (1), these quantities are G^{-1} and η^{-1}, respectively) [17]. Upon the phase transition, the susceptibility χ infinitely increases and the kinetic coefficient γ has no singularity. In formula (1), this is equivalent to the fact that the shear modulus G tends to zero at a finite viscosity η. Such a situation corresponds to the viscoelastic transition [18].

As a rule, the glass transition is attended by the emergence of thermodynamic features such as an increase in the heat capacity [1, 2]. It is believed that, in actual fact, the glass transition in a liquid does not always reduce to a purely mechanical process of supercooling during which the shear viscosity becomes infinite. Moreover, it is known that liquids of the metal melt type undergo a glass transition only at cooling rates exceeding a critical value [1, 2]. This follows from the simplest qualitative considerations [19]; the basic equations of the quantitative theory will be determined below. Essentially, the proposed approach is as follows: the glass transition is provided by the self-organization of the elastic fields of the shear components of stresses σ and strains ε, on the one hand, and of the temperature T, on the other.[1] If the relationship between the first two components is well known and, in the simplest case, is described by the Maxwell model [15], the effect of temperature is ensured by the critical increase in the shear modulus $G(T)$ with a decrease in the temperature: $G = 0$ in the liquid state, and $G \neq 0$ in the glass.

The main finding that underlies the following derivation of the synergetic equations resides in the fact that the total strength of the gauge field is the sum of the pure force and material components (the former component is determined by the field equations, and the latter component reduces to the order parameter characterizing the self-organization of the medium) [20]. Specifically, for a magnet, we have [21]

$$\mathbf{H} + 4\pi\mathbf{M} = \mathrm{curl}\mathbf{A}, \tag{2}$$

where the strength $\mathbf{H}$ represents the force contribution, and the magnetization $\mathbf{M}$ is the material component.

It is characteristic that the total strength, namely, the magnetic induction $\mathbf{B} = \mathrm{curl}\mathbf{A}$, reduces to the derivative of the vector potential $\mathbf{A}$. A similar situation takes place for a ferroelectric [21]:

$$\mathbf{D} - 4\pi\mathbf{P} = -\nabla\varphi, \tag{3}$$

where the electric induction $\mathbf{D}$, the polarization $\mathbf{P}$, and the potential φ determine the force, material, and total components of the electric field, respectively.

In the case of the viscoelastic liquid under consideration, the tensor of total strain $\hat{\varepsilon}_t$ fulfills the role of a gauge field strength and the potential is the displacement vector $\mathbf{u}$. Taking into account the symmetry of $\hat{\varepsilon}_t$, these quantities are related by the relationship [15]

$$\hat{\varepsilon}_t = \frac{1}{2}(\nabla\mathbf{u} + \mathbf{u}\nabla). \tag{4}$$

Similar to the quantities defined by formulas (2) and (3), the total strain $\hat{\varepsilon}_t$ involves the field (purely elastic) component $\hat{\varepsilon}$ and the material component $\hat{\varepsilon}^0$. For thermoelastic stresses, this component is determined by a change in the temperature and reduces to the dilatation [15]

$$\hat{\varepsilon}^0 = \varepsilon^0\hat{I}, \quad \varepsilon^0 = \alpha(T - T_0), \tag{5}$$

[1] In relation to the synergetic concept as applied to the description of the glass transition in a liquid, it should be noted that a scheme of this type was proposed earlier in [19]. However, instead of the temperature, we used the site occupation density, which is inversely proportional to the atomic volume. This model is essentially a lattice model rather than a continual one and gives the critical value for the free volume rather than for the cooling rate [3].

where α is the thermal expansion coefficient, T_0 is the equilibrium temperature, and $\hat{I}$ is the unit tensor.

For the glass-forming liquid under consideration, the material component is due to nonzero shear moduli $G(T)$ arising with a decrease in the temperature. This is conveniently expressed by the shear component of the strain tensor $\varepsilon^0 \equiv G^{-1}(G - G(T))$ in the linear approximation with respect to temperature

$$\varepsilon^0 = G^{-1}\left|\frac{dG(T)}{dT}\right|_{T=0} T, \tag{6}$$

where G is the characteristic value of the shear modulus.

Now, we turn to the direct derivation of the synergetic equations for a viscoelastic medium. The basic equation reduces to the Maxwell equation [15]

$$\dot{\varepsilon} = -\varepsilon/\tau + \sigma/\eta. \tag{7}$$

Here, the point signifies differentiation with respect to time, the first term in the right-hand side describes the Debye relaxation with time (1), and the second term represents the flow of viscous liquid under the shear component of elastic stresses. It is important to keep in mind that equation (7) involves only the force (rather than material) components of strain ε and stresses σ. In the stationary case $\dot{\varepsilon} = 0$, kinetic equation (7) transforms into the equation describing the Hooke law

$$\sigma = G\varepsilon. \tag{8}$$

The equation for determining the time dependence of elastic stresses $\sigma(t)$ is given by

$$\dot{\sigma} = -\sigma/\tau_\sigma + g_\sigma \varepsilon T, \tag{9}$$

where τ_σ and g_σ are positive constants.

As in the Maxwell equation (7), the first term on the right-hand side of relationship (9) describes the dissipative process of stress relaxation toward the equilibrium value $\sigma = 0$. However, the process is accomplished in a microscopic time τ_σ rather than in a macroscopic time τ. The former time reduces to a Debye time of $\sim 10^{-12}$ s, so that the condition $\tau_\sigma \ll \tau$ (important for the subsequent consideration) is met. As regards the second term in relationship (9), it accounts for the positive feedback between the elastic strain ε and temperature T, which results in an increase in the elastic stresses σ and, thus, governs the self-organization process. The physical meaning of this term can be easily understood for the stationary case when $\dot{\sigma} = 0$. Then, equation (9) takes the form

$$\sigma = (a_\sigma/v)T_\varepsilon, \tag{10}$$

where we introduced the dimensionless positive constant

$$a_\sigma \equiv g_\sigma \tau_\sigma v \tag{11}$$

and v is the atomic volume.

Comparison of equation (10) with the relationship following from expression (6) for the material component $\sigma^0 = G\varepsilon^0$ demonstrates that they coincide at $\varepsilon = 1$. Hence, it follows that the nonlinear term in equation (9) accounts for the relation between the material and elastic components of the strain, and parameter (11) of this relation has the form

$$a_\sigma = v\left|\frac{dG}{dT}\right|, \quad \left|\frac{dG}{dT}\right| \equiv \left|\frac{dG(T)}{dT}\right|_{T=0}. \tag{12}$$

The kinetic equation for the temperature can be deduced by analogy with the derivation of the heat conductivity equation (see [15, §31]). In this case, it is necessary to proceed from the heat equation of continuity $\delta Q = T\delta S$:

$$T\dot{S} = -\nabla \mathbf{q}. \tag{13}$$

Here, the heat flux is described by the Onsager relationship

$$\mathbf{q} = -k\nabla T, \tag{14}$$

where $\mathbf{k}$ is the heat conductivity.

In the simplest case of thermoelastic stresses, the entropy

$$S = S_0(T) + K\alpha\varepsilon^0 \tag{15}$$

is the sum of the purely thermodynamic component S_0 and the field contribution (5), where K is the bulk modulus [15, §6]. It is easy to see that, in the glass-forming liquid, we should go from the dilatation component $K\alpha\varepsilon^0$ to the elastic energy of the shear component divided by the temperature $\sigma\varepsilon/T$ [here, the minus sign allows for the relation (at $S_0 = \text{const}$) $T\delta S = p\delta V \Rightarrow -\sigma\delta\varepsilon$, which is due to the opposite signs of the pressure p and stresses σ]. As a result, equation (13) becomes

$$T\dot{S}_a(T) - \sigma\dot{\varepsilon} = k\nabla^2 T. \tag{16}$$

Let us now take into account the definition of the heat capacity $c_p = TdS_0/dT$ and, within the one-mode approximation, replace ∇^2 by $-l^{-2}$, where l is the heat conductivity scale. Then, from relationship (16), we obtain

$$c_p\dot{T} = -kl^{-2}T + \sigma\dot{\varepsilon}. \tag{17}$$

Substitute the relationship for $\dot{\varepsilon}$ from equation (7) into formula (17). The term σ^2/η appearing in this case describes a trivial effect of dissipative heating of a viscous liquid flowing under the stresses σ. The specific feature of the glass transition in liquids consists in providing oppositely directed heat removal of the intensity $\mathbf{q}_0$, whose magnitude does not reduce to the Onsager component but is determined by external conditions. With allowance made for the above circumstances, the kinetic equation for temperature takes the final form

$$\dot{T} = -T/\tau_T - g_T\varepsilon\sigma + Q. \tag{18}$$

Here, $\tau_T = c_p l^2/k$ is the time of relaxation due to the thermal diffusivity $\chi \equiv k/c_p$, $g_T \equiv (\tau c_p)^{-1}$ is the constant of the negative feedback, and the last term

$$Q = Q_0 + \sigma^2/\eta c_p, \quad Q_0 \equiv \nabla \mathbf{q}_0/c_p \tag{19}$$

is the sum of the external component Q_0 and a quadratic contribution of elastic stresses. An explicit form of the latter contribution considerably complicates the subsequent analysis, even though it leads only to a trivial renormalization of the quantities. Hence, hereafter, the term Q in equation (18) is assumed to be constant. Note that equation (18) was derived under the assumption that the equilibrium temperature T_{00} is equal to 0. It is evident that, otherwise, when the liquid is cooled to the temperature $T_{00} \neq 0$, the term T_{00}/τ_T should enter into relationship (19).

The Maxwell equation (7) assumes the use of the idealized Hencky model, in which the strain dependence of the stress $\sigma(\varepsilon)$ is represented by the Hooke law $\sigma = G\varepsilon$ at $\varepsilon < \varepsilon_m$ and by the constant $\sigma_m = G\varepsilon_m$ at $\varepsilon \geq \varepsilon_m$ (the stresses $\sigma > \sigma_m$ give rise to viscous flow with the strain rate $\dot{\varepsilon} = (\sigma - \sigma_m)/\eta$. Actually, the simplest curve $\sigma(\varepsilon)$ exhibits not one but two portions: the first (Hookean) portion is characterized by a large slope specified by the shear modulus G; and the second, substantially flatter portion of plastic strain has a slope determined by the strain hardening coefficient $\Theta < G$. Obviously, this pattern implies that the shear modulus entering [through the relaxation time (1)] into equation (7), in actuality, depends on the strain. Let us use the simplest approximation

$$G(\varepsilon) = \Theta + \frac{G - \Theta}{1 + \varepsilon/\varepsilon_p}, \tag{20}$$

which describes the above transition from elastic to plastic strain. This transition occurs at the characteristic strain ε_p, which should not exceed the maximum value ε_m (otherwise, plastic strain is not observed). As a consequence, the relaxation time (1) becomes dependent on the strain:

$$\frac{1}{\tau(\varepsilon)} = \frac{1}{\tau_p}\left(1 + \frac{\theta^{-1} - 1}{1 + \varepsilon/\varepsilon_p}\right). \tag{21}$$

In this relationship, we introduced the relaxation time for the plastic flow (cf. formula (1))

$$\tau_p = \eta/\Theta \tag{22}$$

and the parameter

$$\theta = \Theta/G < 1, \tag{23}$$

which characterizes the ratio between the slopes of the plastic and Hookean portions in the strain curve. It should be noted that a relationship of type (21) was first proposed by Haken [22] for the description of a hard mode of laser radiation and then was used in our earlier work [13] in order to describe the kinetics of the first-order phase transition. However, in this case, relationship (21) included the ratio $\varepsilon/\varepsilon_p$ squared, and the resulting dependence of the synergetic potential $V(\varepsilon)$ on the order parameter ε was even. The description of structural phase transitions in liquids is characterized by the presence of third invariants, which violate this parity [23]. Hence, in approximation (21), we used the linear term $\varepsilon/\varepsilon_p$ rather than the quadratic term $(\varepsilon/\varepsilon_p)^2$. As can be seen, the corresponding dependence of the synergetic potential on the order parameter is not even.

It is easily seen that kinetic equations (7), (9), and (18) coincide in their form with the known Lorenz system, which was first applied to the description of turbulent streams in the atmosphere [24]. Allowance made for the strain dependence of the modulus in going from the Hookean portion in the dependence $\sigma(\varepsilon)$ to the flat portion of plastic flow, which is characterized by the hardening $\Theta < G$, permits one to adequately describe the glass transition in liquids. The investigation of the appropriate synergetic scheme calls for special consideration.

ACKNOWLEDGMENTS

This work was supported in part by the Ukrainian State Committee of Science and Engineering, project no. 2.4/4.

REFERENCES

1. *Metallic Glasses: Papers Presented at a Seminar of the Materials Science Division of the American Society for Metals, 1976*, Ed. by J. J. Gilman and H. J. Leamy (American Society for Metals, Metal Park, Ohio, 1978; Metallurgiya, Moscow, 1984).
2. *Amorphous Metal Alloys*, Ed. by F. E. Lyuborskiĭ (Metallurgiya, Moscow, 1987).
3. W. Götze, *Liquid–Glass Transition* (Univ. of Munich, Munich, 1987; Nauka, Moscow, 1991).
4. J. Jäckle, Rep. Prog. Phys. **49**, 171 (1986).
5. M. Mezard, G. Parisi, N. Sourlas, *et al.*, J. Phys. (Paris) **45**, 843 (1984).
6. K. Binder and A. P. Young, Rev. Mod. Phys. **58**, 801 (1986).
7. S. L. Ginzburg, *Irreversible Processes in Spin Glasses* (Nauka, Moscow, 1989).
8. S. P. Das and G. F. Mazenko, Phys. Rev. A **34**, 2265 (1986).
9. D. L. Stein and R. G. Palmer, Phys. Rev. B **38**, 12035 (1988).
10. R. G. Palmer, Adv. Phys. **31** (6), 669 (1982).
11. S. F. Edwards and P. W. Anderson, J. Phys. F **5**, 965 (1975).
12. J. R. L. de Almeida and D. J. Thouless, J. Phys. A **11**, 983 (1978).
13. A. I. Olemskoĭ and A. V. Khomenko, Zh. Éksp. Teor. Fiz. **110**, 2144 (1996) [JETP **83**, 1180 (1996)].
14. A. I. Olemskoĭ and V. A. Petrunin, Izv. Vyssh. Uchebn. Zaved., Fiz., No. 1, 82 (1987).

15. L. D. Landau and E. M. Lifshitz, *Theory of Elasticity* (Nauka, Moscow, 1987, Pergamon, Oxford, 1986, 3rd ed.).

16. A. Havranek and M. Marvan, Ferroelectrics **176**, 25 (1996).

17. A. A. Katsnel'son and A. I. Olemskoĭ, *The Microscopic Theory of Inhomogeneous Structures* (Mosk. Gos. Univ., Moscow, 1987).

18. V. G. Bar'yakhtar and A. I. Olemskoĭ, Fiz. Tverd. Tela (Leningrad) **33**, 2705 (1991).

19. A. I. Olemskoĭ and E. A. Toropov, Fiz. Met. Metalloved., No. 9, 5 (1991).

20. A. I. Olemskoĭ and I. A. Sklyar, Usp. Fiz. Nauk **162** (6), 29 (1992) [Sov. Phys. Usp. **34**, 375 (1992)].

21. L. D. Landau and E. M. Lifshitz, *Course of Theoretical Physics: Vol. 8. Electrodynamics of Continuous Media* (Nauka, Moscow, 1982; Pergamon, New York, 1984).

22. H. Haken, *Synergetics: An Introduction* (Springer-Verlag, Berlin, 1977; Mir, Moscow, 1980).

23. L. D. Landau and E. M. Lifshitz, *Statistical Physics* (Nauka, Moscow, 1976; Pergamon, Oxford, 1980), Part 1.

24. E. N. Lorenz, J. Atmos. Sci. **20**, 130 (1963).

Translated by O. Borovik-Romanova

Technical Physics, Vol. 45, No. 6, 2000, pp. 677–682. Translated from Zhurnal Tekhnicheskoĭ Fiziki, Vol. 70, No. 6, 2000, pp. 10–15.

The Synergetic Theory of the Glass Transition in Liquids

A. I. Olemskoĭ and A. V. Khomenko

Sumy State University, Sumy, 244007 Ukraine

Received January 28, 1999

Abstract—The glass transition is treated as a spontaneous emergence of the shear components of strain and stress elastic fields upon cooling a liquid at a rate exceeding the critical value. The stationary elastic strains and stresses and the effective relaxation time are determined within the adiabatic approximation. It is shown that the glass transition process occurs through the mechanism of a first-order kinetic transition with allowance made for the strain dependence of the shear modulus. The critical cooling rate turns out to be proportional to the thermal diffusivity and unrelaxed shear modulus and inversely proportional to the temperature derivative of the relaxed shear modulus and the square of the heat conductivity length of the sample. © *2000 MAIK "Nauka/Interperiodica".*

In our previous work [1], starting from the rheological concept of a viscoelastic medium possessing heat conductivity, we derived a set of kinetic equations (7), (9), and (18), which describe the self-consistent variation in the shear components of strains and stresses and the temperature of the medium. The present work is dedicated to analysis of these equations within the synergetic approach. This approach is based on the adiabatic approximation for the characteristic times of changes in the strain ε, the stresses σ, and the temperature T:

$$\tau_\sigma \ll \tau, \quad \tau_T \ll \tau. \tag{1}$$

According to (1), during the evolution of the medium, the elastic stresses $\sigma(t)$ and temperature $T(t)$ follow the change in the strain $\varepsilon(t)$. The first condition in (1) relates the microscopic time $\tau_\sigma \sim 10^{-12}$ s and the macroscopic time τ and always holds. By using the definitions of the thermal diffusivity $\chi = \kappa/c_p$, the kinematic viscosity $\nu = \eta/\rho$, the relaxation time $\tau = \eta/G$, and the sound velocity $c = (G/\rho)^{1/2}$ (where κ is the heat conductivity coefficient, c_p is the heat capacity, η is the shear viscosity, ρ is the density, and G is the shear modulus), it is convenient to rearrange the second condition in (1) as follows:

$$l^2 \ll L^2, \tag{2}$$

from which it follows that the characteristic length of heat conductivity $l = (\chi\tau_T)^{1/2}$ should not exceed the quantity

$$L = \frac{(\chi\nu)^{1/2}}{c}. \tag{3}$$

The physical meaning of this condition can be illustrated by the hydrodynamic inequality

$$\tau_T\tau_\varepsilon\omega_{\mathbf{k}}^2 \ll 1, \tag{4}$$

which implies that the geometric mean of the heat conductivity time τ_T and the convection time τ_ε is considerably less than the reciprocal of the sound frequency $\omega_{\mathbf{k}}$ (here, we took into consideration the relationships $kl \sim 1$, $\tau_\varepsilon^{-1} \equiv \nu k^2$, $\omega_{\mathbf{k}} ck$, and $\tau\tau_\varepsilon\omega_{\mathbf{k}}^2 = 1$, where $\mathbf{k}$ is the wavevector). In systems susceptible to the glass transition, this conditions is universally fulfilled. Let us rewrite equations (7), (9), and (18), taken from [1], in the following form:

$$\tau\dot{\varepsilon} = -\varepsilon + \sigma/G, \tag{5}$$

$$\tau_T\dot{T} = (\tau_T Q - T) - (a_T\nu)\varepsilon\sigma, \tag{6}$$

$$\tau_\sigma\dot{\sigma} = -\sigma + (a_\sigma/\nu)\varepsilon T, \tag{7}$$

where the constant

$$Q = Q_0 + \sigma^2/\eta c_p \tag{8}$$

is determined by the external heat removal Q_0 and the contribution from elastic stresses, which accounts for the dissipative heating of the viscous liquid. In equations (5)–(7), we introduced the dimensionless constants [1]

$$a_\sigma \equiv \tau_\sigma g_\sigma \nu = \nu\left|\frac{dG}{dT}\right|, \quad a_T \equiv \frac{\tau_T g_T}{\nu} = \frac{\tau_T\tau_\varepsilon\omega_{\mathbf{k}}^2}{c_p\nu}. \tag{9}$$

According to (4), the condition $a_T \ll 1$ is met.

Taking into account conditions (1), the left-hand sides of equations (6) and (7), which contain the short relaxation times τ_σ and τ_T, can be set equal to zero. As a result, these equations are rearranged to give the following expressions for temperature and elastic stresses in terms of the strain:

$$T = \frac{\tau_T Q}{1 + \varepsilon^2/\varepsilon_m^2}, \tag{10}$$

$$\sigma = \frac{a_\sigma}{\nu}(\tau_T Q)\varepsilon\left(1 + \frac{\varepsilon^2}{\varepsilon_m^2}\right)^{-1}, \quad (11)$$

where we introduced the designation

$$\varepsilon_m^{-2} \equiv a_T a_\sigma = \frac{1}{c_p}\left|\frac{dG}{dT}\right|\tau_T\tau_\varepsilon\omega_{\mathbf{k}}^2 \quad (12)$$

[the second equality is obtained with the use of relationships (9)].[1] According to equation (10), as the strain ε increases from $\varepsilon = 0$ to $\varepsilon = \varepsilon_m$, the temperature T monotonically decreases from $T^0 \equiv \tau_T Q$ to $T^0/2$. It is obvious that this decrease is caused by the negative feedback in equation (6), which is a manifestation of Le Chatelier's principle for the problem under consideration. Indeed, the self-organization of the liquid that results in the glass transition is accounted for by the positive feedback between the strain and temperature in equation (7). Therefore, an increase in the temperature should enhances the self-organization effect. However, as follows from relationship (10), the system is constructed so that the result of the self-organization—an increase in the elastic strain—leads to a decrease in its cause, namely, the temperature. With regard to dependence (11) relating the elastic stress to the strain, at $\varepsilon \ll \varepsilon_m$, it exhibits a linear behavior corresponding to the Hooke law with the effective shear modulus

$$G_{\text{eff}} \equiv (a_\sigma/\nu)\tau_T Q = \left|\frac{dG}{dT}\right|\tau_T Q, \quad (13)$$

where the second equality follows from relationship (9).

The function $\sigma(\varepsilon)$ reaches a maximum at $\varepsilon = \varepsilon_m$ and decreases at $\varepsilon > \varepsilon_m$, which has no physical meaning. Hence, it follows that the constant ε_m defined by equality (12) is the maximum attainable strain. As is seen from relationships (12) and (13), an increase in the temperature derivative of the modulus $|dG/dT|$ leads to a decrease in the maximum strain ε_m and an increase in the effective modulus G_{eff}, which is proportional to the characteristic temperature $T^0 = \tau_T Q$. On the other hand, the ratio between the characteristic values of the thermal energy $E_T = c_p\tau_T Q$ and the elastic energy $E_\varepsilon = G_{\text{eff}}\varepsilon_m^2$, that is,

$$\frac{E_T}{E_\varepsilon} = \tau_T\tau_\varepsilon\omega_k^2, \quad (14)$$

has, according to (4), small values. Substitution of equation (11) into formula (5) gives the equation for the evolution of the system in the course of the glass transition

$$\eta\dot{\varepsilon} = -\frac{\partial V}{\partial\varepsilon}. \quad (15)$$

Its form is determined by the strain dependence of the synergetic potential $V(\varepsilon)$

$$V = \frac{G\varepsilon_m^2}{2}\left[\frac{\varepsilon^2}{\varepsilon_m^2} - \frac{T^0}{T_c}\ln\left(1 + \frac{\varepsilon^2}{\varepsilon_m^2}\right)\right], \quad (16)$$

where the characteristic temperatures are defined as

$$T^0 \equiv \tau_T Q, \quad (17)$$

$$T_c \equiv \frac{\nu G}{a_\sigma} = G\left|\frac{dG}{dT}\right|^{-1} \quad (18)$$

and relationship (9) is used in the second equality (18). It is of interest that the ratio between these temperatures

$$\frac{T^0}{T_c} = \frac{G_{\text{eff}}}{G} \quad (19)$$

reduces to the ratio between the effective shear modulus (13) and its characteristic value G. At $T^0 \le T_c$, dependence (16) exhibits a monotonically increasing behavior with a minimum at the point $\varepsilon = 0$. This implies that, in the stationary state ($\dot{\varepsilon} = 0$), the elastic strain is absent; i.e., the liquid state is realized when the strain caused by external stresses relaxes for a time

$$\tau_{\text{eff}} = \tau(1 - T^0/T_c)^{-1}. \quad (20)$$

This relationship follows from equation of motion (15), which is written in the linear approximation. As the effective temperature T^0 increases up to the critical temperature T_c, the relaxation time infinitely increases; and, at $T^0 > T_c$, the system transforms into the vitreous state. In this case, a multiplier of 1/2 appears in dependence (20) and the minimum of synergetic potential (16) corresponds to the elastic strain

$$\varepsilon_0 = \varepsilon_m(T^0/T_c - 1)^{1/2}, \quad (21)$$

which increases as the root with an increase in the difference $T^0 - T_c$. According to equation (10), the temperature of the system becomes critical [relationship (18)] and the elastic stresses reach the stationary value

$$\sigma_0 = G\varepsilon_0 = \sigma_m(T^0/T_c - 1)^{1/2}, \quad (22)$$

where $\sigma_m \equiv G\varepsilon_m$.

Physically, the glass transition is due to the fact that, at $T^0 > T_c$, in accordance with (19), the effective shear G_{eff} exceeds the characteristic value G. As follows from definitions (17) and (18), the original reason for the glass transition is an increase in the cooling rate (8) up

[1] Note that, if the term quadratic in σ is retained in (8), the dependences (10) and (11) should be expressed in terms of roots of the quadratic equation, which substantially complicates analysis and furnishes no radically new result.

to the Q values exceeding the critical rate

$$Q_c \equiv \frac{G}{\tau_T}\left|\frac{dG}{dT}\right|^{-1} = \frac{\kappa}{c_p l^2} G\left|\frac{dG}{dT}\right|^{-1}. \quad (23)$$

Among the parameters affecting the critical rate Q_c are the kinetic parameters, which determine the heat conductivity time τ_T, and the synergetic parameters characterizing the self-organization of elastic and temperature fields. According to relationship (23), the first group of parameters involves the thermal diffusivity κ/c_p and the heat conductivity length l. An increase in the former parameter results in an increase in Q_c, whereas an increase in l causes an opposite, stronger (quadratic) effect. The influence of the synergetic factors is governed by the ratio between the shear modulus G and its temperature derivative $|dG/dT|$: the smaller this ratio, the lower the critical rate of quenching. In other words, systems with relatively small shear moduli that strongly depend on temperature are susceptible to the glass transition. It is this situation that is realized in polymers [2]. Among metallic glasses, eutectics possess this property [3, 4].

In the above treatment, we assumed that the cooling rate Q is a model parameter independent of ε, σ, and T. However, it is seen from expression (8) that the quantity Q is the sum of the component Q_0, which is associated with the external heat removal, and the dissipative contribution $\Delta Q = \sigma^2/\eta c_p$ specified by elastic stresses (22). By assuming that Q is independent of σ, we actually ignored the term ΔQ. Therefore, in the above cases, the quantity Q should be taken to mean the external component Q_0. Let us correct this approximation by using the stationary value of the dissipative contribution, that is,

$$\Delta Q_0 \equiv \frac{\sigma_0^2}{\eta c_p} = \frac{G\varepsilon_m^2}{\tau c_p Q_c}(Q_0 - Q_c) = Q_0 - Q_c. \quad (24)$$

Then, from equation (8), it follows that

$$Q = 2Q_0 - Q_c, \quad (25)$$

and relationships (20)–(22) take the form

$$\tau_{\text{ef}} = (\tau/2)|1 - Q_0/Q_c|^{-1}, \quad (26)$$

$$\varepsilon_0 = 2^{1/2}\varepsilon_m(Q_0/Q_c - 1)^{1/2}, \quad (27)$$

$$\sigma_0 = 2^{1/2}\sigma_m(Q_0/Q_c - 1)^{1/2}. \quad (28)$$

Here, the last two relationships correspond to the supercritical region $Q_0 > Q_c$ and the first relationship, to the subcritical region [in passing through Q_c, according to the law of duality, an additional multiplier of 1/2 appears in formula (26)]. A comparison of equalities (20)–(22) and (26)–(28) demonstrates that allowance made for the dissipative heating of the medium at the rate defined by (24) leads to a trivial twofold decrease in the relaxation time τ_{eff} and an increase in the stationary elastic fields of strain ε_0 and stresses σ_0 by a factor of $\sqrt{2}$.

Now let us replace τ in the set of Lorenz equations (5)–(7) by the dependence $\tau(\varepsilon)$ [1]:

$$\frac{1}{\tau(\varepsilon)} = \frac{1}{\tau_p}\left(1 + \frac{\Theta^{-1} - 1}{1 + \varepsilon/\varepsilon_p}\right), \quad (29)$$

where we introduced the relaxation time for plastic flow $\tau_p = \eta/\Theta$ (Θ is the strain hardening coefficient), the parameter $\Theta = \Theta/G < 1$, and the characteristic strain $\varepsilon_p < \varepsilon_m$.

It is easy to see that, within the adiabatic approximation (1), this set, as before, reduces to the Landau–Khalatnikov equation (15). However, in this case, the coefficient G in synergetic potential (16) is replaced by Θ and there appears the odd term proportional to $G - Q$,

$$V = \Theta\frac{\varepsilon_m^2}{2}\left[\frac{\varepsilon^2}{\varepsilon_m^2} - \frac{T^0}{T_{c0}}\ln\left(1 + \frac{\varepsilon^2}{\varepsilon_m^2}\right)\right] + (G - \Theta)\varepsilon_p^2\left(\frac{\varepsilon}{\varepsilon_p} - \ln\left|1 + \frac{\varepsilon}{\varepsilon_p}\right|\right). \quad (30)$$

Here, we introduced the critical temperature [cf. formula (18)]

$$T_{c0} \equiv \frac{\nu\Theta}{a_\sigma}. \quad (31)$$

At low effective temperatures T^0 [formula (17)], potential (30) exhibits a monotonically increasing behavior with a minimum at the point $\varepsilon = 0$, which corresponds to the stationary liquid state. As can be seen from Fig. 1, at the values

$$T_c^0 = T_{c0}\left\{(D^{1/2} - q/2)^{1/3} - (D^{1/2} + q/2)^{1/3} - \frac{\alpha^2}{12}[(\Theta^{-1} + 9)^2 - 2^2 3^3] + 1\right\};$$

$$\alpha \equiv \varepsilon_p/\varepsilon_m, \quad D \equiv (p/3)^3 + (q/2)^2,$$

$$p \equiv -\frac{1}{3}\{(\alpha/2)^2[(\Theta^{-1} + 9)^2 - 2^2 3^3] - 3\}^2 + (\alpha^2/\Theta)[(\alpha/\Theta)^2 - 5/\Theta + 3^2] + 3,$$

$$q \equiv \frac{2}{3^3}\{(\alpha/2)^2[(\Theta^{-1} + 9)^2 - 2^2 3^3] - 3\}^3 - \frac{1}{3}\{(\alpha/2)^2[(\Theta^{-1} + 9)^2 - 2^2 3^3] - 3\} \times \{(\alpha^2/\Theta)[(\alpha/\Theta)^2 - 5/\Theta + 3^2] + 3\} - [(\alpha/\Theta)^2 + 1]^2 \quad (32)$$

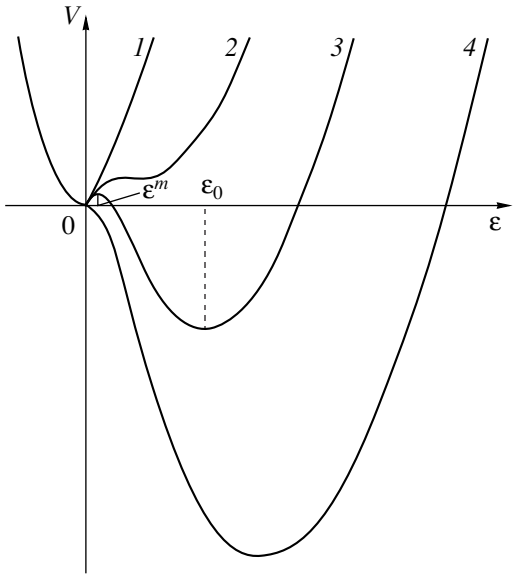

Fig. 1. Dependences of the synergetic potential on the elastic strain at different temperatures: (*1*) $T^0 < T_c^0$, (*2*) $T^0 = T_c^0$, (*3*) $T_c^0 < T^0 < T^c$, and (*4*) $T^0 \geq T^c$.

there appears a plateau, which, at $T^0 > T_c^0$, transforms into a minimum (corresponding to the strain $\varepsilon_0 \neq 0$) and a maximum ε^m, which separates the minima at $\varepsilon = 0$ and ε_0. With a further increase in the effective temperature T^0, the minimum of an ordered phase, which corresponds to the vitreous state $\varepsilon = \varepsilon_0$, becomes deeper and the height of the interface barrier decreases and becomes zero at the critical value

$$T^c \equiv T_{c0}/\Theta = (G/\Theta)T_{c0}, \tag{33}$$

which exceeds the critical temperature T_{c0} [formula (31)]. The above stationary strains for the vitreous state (Figs. 1, 2) are given by

$$\left.\begin{matrix}\varepsilon_0\\ \varepsilon^m\end{matrix}\right\} = \varepsilon_m\left[2\epsilon\cos\left(\frac{\varphi}{3} \pm \frac{2\pi}{3}\right) - \frac{\alpha}{3\Theta}\right];$$

$$\epsilon \equiv \operatorname{sgn}\omega(\psi/3)^{1/2}, \quad \cos\varphi \equiv \omega/2\epsilon^3,$$
$$\psi \equiv \left(\frac{T^0}{T_{c0}} - 1\right) + \frac{(\alpha/\Theta)^2}{3}, \tag{34}$$
$$\omega \equiv \frac{2\alpha}{3\Theta}\left[\left(\frac{\alpha}{3\Theta}\right)^2 + 1\right] + \alpha\frac{T^0}{T_{c0}}\left(\frac{\Theta^{-1}}{3} - 1\right).$$

The stationary elastic stress σ_0 is determined by the substitution of ε_0 into relationship (11). At $T^0 \geq T^c$, the character of the dependence $V(\varepsilon)$ is identical to that observed in the absence of the strain dependence of the modulus (Fig. 1, curve *4*).

The aforementioned features correspond to the positive strains ε. In the negative semiaxis, as $|\varepsilon|$ increases, the potential $V(\varepsilon)$ passes through a very weak minimum and then infinitely increases at $\varepsilon = -\varepsilon_p$. Thus, the negative elastic fields ε and σ turn out to be virtually unrealizable.

The characteristic feature of our scheme resides in the fact that the energy barrier inherent in the first-order synergetic transition manifests itself only in the presence of the strain dependence of the modulus. Since this dependence always occurs in reality, it can be concluded that the glass transition in liquids is a first-order, rather than a second-order, synergetic transition. Note that the situation under consideration is substantially more complex than that observed upon conventional phase transitions. Indeed, in the latter case, the stationary temperature of the system T_0 reduces to the temperature T_{00} for a thermostat (above, it was assumed that $T_{00} = 0$). In our case, for the second-order synergetic transition occurring in the absence of the strain dependence of the modulus, T_0 reduces to the critical temperature T_c. The inclusion of the strain dependence of the modulus leads to the temperature

$$T_0 = \frac{T^0}{1 + (\varepsilon_0/\varepsilon_m)^2}, \tag{35}$$

which is determined by the location of the minimum in dependence (30). According to equalities (34) and (35), the temperature T_0 gradually decreases from

$$T_m = T_c^0\left\{1 + \left[3^{-1/2}\left(\frac{T_c^0}{T_{c0}} + \frac{(\alpha/\Theta)^2}{3} - 1\right)^{1/2} - \frac{\alpha}{3\Theta}\right]^2\right\}^{-1} \tag{36}$$

at $T^0 = T_c^0$ to T_{c0} at $T^0 \longrightarrow \infty$. It is seen from Fig. 3 that a quasi-static increase in the parameter T^0 from 0 to T^c brings about a linear increase in the stationary temperature of the system in the same range. The temperature T^0 abruptly diminishes at $T^0 = T^c$ and then smoothly decreases. As the temperature T^0 decreases, the T_0 quantity at T_{c0} [see relationships (32)] abruptly increases from T_m (36) to T_{c0} (32). Since, in the actual range of the parameters α and Θ, which is limited by the maximum value

$$\Theta^m = (\alpha^2/2)(\sqrt{1 + \alpha^2} - 1)^{-1}, \tag{37}$$

the temperature of the medium T_m (36) is lower than the minimum thermostat temperature (32), it can be seen from Fig. 3 that the temperature of the medium T_0 is always less than its value T^0 provided by cooling of the system at the rate $Q = T^0/\tau_T$.

The above picture is based on the assumption that the glass transition is caused by the self-organization of the shear components of the stress and strain elastic fields, on the one hand, and of the sample temperature,

on the other. Note that the strain ε plays the role of an order parameter, the conjugate field reduces to the elastic stresses σ, and the temperature T is a controlling parameter. The original reason for the self-organization is the positive feedback between the temperature T and strain ε [see relationship (7)]. According to (9), this feedback results from the temperature dependence of the characteristic shear modulus. Since the strain dependence of the modulus was not taken into account in the above relationships, they involved the shear modulus G. However, it is easily seen that, in actuality, it is necessary to employ not the initial shear modulus G, which is virtually temperature-independent, but the relaxed quantity Θ determining the slope of the σ(ε) dependence in the portion of the plastic strain. Hence, G should be replaced by Θ in formulas (5), (9), (12), (13), (16), (18), (19), and (22)–(24). Then, with due regard for renormalization (33), expression (23) for the critical cooling rate Q^c takes the form

$$Q^c = \frac{\kappa}{c_p l^2} G \left| \frac{d\Theta}{dT} \right|^{-1}. \tag{38}$$

It is characteristic that this quantity is determined by both the unrelaxed shear modulus G and the relaxed shear modulus Θ.

The kinetics of the glass transition is defined by the Landau–Khalatnikov equation (15), in which the synergetic potential has the form (30) typical of a first-order transition. In the supercooled liquid state ($\eta = \infty$), the system can be frozen ($\dot{\varepsilon} \longrightarrow 0$) even in the nonstationary state ($\partial V/\partial \varepsilon \neq 0$).

The picture under discussion has a phenomenological character, and it is expedient to compare the obtained data with the microscopic theory [5, 6]. Within this theory, the role of the state parameters is played by the quenching temperature T_{00} and the intensity of quenched disorder

$$h^2 \equiv N^{-1} \sum_i (\sigma_i - \bar{\sigma})^2 - N^{-1} \sum_i (\sigma_i(t) - \sigma(t))^2,$$
$$\bar{\sigma} \equiv N^{-1} \sum_i \sigma_i, \quad \sigma(t) \equiv N^{-1} \sum_i \sigma_i(t). \tag{39}$$

This intensity is equal to the difference between the variance of the microstresses σ_i produced by quenching and the variance of the microscopic quantities $\sigma_i(t)$, which, on the time scale $\sim\tau_\sigma$, vary in a fluctuational manner near the macroscopic quantity $\sigma(t)$ [in relationships (39), N is the number of atoms over which the summation is carried out].[2] According to [5, 6], in the field $h \neq 0$, the term $-(h^2/2)\varepsilon^2$ arises in the effective Hamiltonian, whose function, in our case, is fulfilled by

[2] Owing to the adiabatic approximation, we went from the microstresses $\sigma_i(t)$ to the macroscopic quantities $\sigma(t)$.

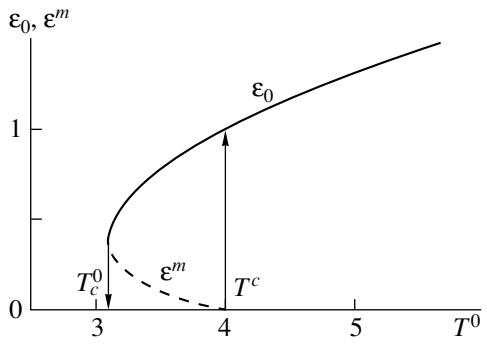

Fig. 2. Dependences of the stationary strains on the thermostat temperature at $\varepsilon_m = 1$, $T_{c0} = 1$, $\Theta = 0.25$, and $\alpha = 0.5$. The solid line corresponds to the stable state ε_0, and the dashed line represents the unstable state ε^m.

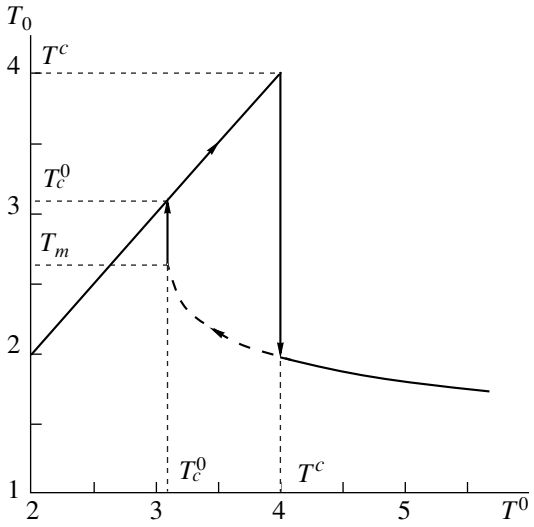

Fig. 3. Dependence of the stationary temperature of the system T_0 on the thermostat temperature at $T_{c0} = 1$, $\Theta = 0.25$, and $\alpha = 0.5$.

synergetic potential (30). By expanding the logarithms in the potential, we obtain the term

$$-\left(\Theta \frac{T^0}{T_{c0}} - (G - \Theta)\right)\frac{\varepsilon^2}{2},$$

which corresponds to the above contribution of the quenched disorder. Taking into consideration dependences (17) and (31), the disorder intensity can be written as

$$h^2 \equiv \Theta(T^0/T_{c0}) - (G - \Theta)$$
$$= \tau_T |d\Theta/dT| Q - (G - \Theta). \tag{40}$$

With allowance made for renormalization (25) and dependence (38), we obtain an expression in terms of the initial cooling rate Q_0:

$$h^2 = \Theta + 2G(Q_0/Q^c - 1). \tag{41}$$

Hence, it follows that the quenched disorder

$$h^2 = 2G(Q_0 - Q_{c0})/Q^c \quad (42)$$

appears only at the quenching rates exceeding the quantity

$$Q_{c0} = Q^c(1 - Q/2G). \quad (43)$$

The dependences obtained make it possible to express the results of the microscopic theory in terms of the experimentally observed quantity—the quenching rate Q_0. Indeed, for the Edwards–Anderson parameter q and the nonergodicity parameter Δ, we have $q \propto h^{2/3}$ and $\Delta \propto h^{2/3} - h_c^{2/3}$, where the critical field h_c corresponds to the quenching rate (38) at which the glass transition leads to the loss of ergodicity. According to [7, 8], for a viscoelastic medium, the nonergodicity parameter $\Delta \propto \eta_g - \eta$ is determined by the difference between the viscosities in the vitreous (nonergodic) and liquid (ergodic) states. Then, taking into account formula (42), one obtains the relationships

$$q \propto [(Q_0 - Q_{c0})/Q^c]^{1/3}, \quad (44)$$

$$\Delta \propto [(Q_0 - Q_{c0})/Q^c]^{1/3} - h_c^{2/3}, \quad (45)$$

in which it is assumed that $Q_0 > Q_{c0}$. Therefore, with an increase in the quenching rate, the liquid in the vicinity of the glass transition point Q^c (at $Q_{c0} \leq Q^c$) acquires memory, whose parameter begins to increase very rapidly at the point $Q_0 = Q_{c0}$. As follows from relationship (45), at the glass transition point, the difference in shear viscosities $\eta_g - \eta \propto \Delta$ increases equally sharply.

It is clear that the above features should be observed experimentally. In particular, a singular increase in the relaxation time $\tau_g \propto \eta_g$ should be expected upon the glass transition. In this case, the memory effects manifest themselves in a nontrivial fashion [5, 6]. Specifically, in low-frequency measurements of elastic stress relaxation times (for example, with the use of the internal friction technique [9]), the τ_g value obtained upon quenching of the sample, which was initially subjected to constant shear stresses, should be larger than the τ time obtained upon quenching in the absence of stresses. A similar difference that is proportional to the irreversible response (45) should also be observed for the material component of the strain $\varepsilon^0 = G^{-1}|dG(T)/dT|_{T=0}T$ [1]. As for spin glasses [6], it should be expected that, in the course of structural relaxation, the above difference will very slowly decrease with time. However, the time dependence can be described not only by a logarithmic function, but also by the power and Kohlrausch (stretched exponent) laws; moreover, even a double logarithmic dependence (virtually the termination of structural relaxation) can occur [10].

ACKNOWLEDGMENTS

We would like to thank V.G. Bar'yakhtar and the participants at the Workshop guided by him for their participation in discussions of the results and M. Marvan for helpful discussions and the kind hospitality extended during our residence at Karlov University (Prague).

This work was supported in part by the Ukrainian State Committee of Science and Engineering, project no. 2.4/4.

REFERENCES

1. A. I. Olemskoĭ and A. V. Khomenko, Zh. Tekh. Fiz. **70** (6), 6 (2000) [Tech. Phys. **45** (6), 672 (2000)].
2. M. Doi and S. F. Edwards, *The Theory of Polymer Dynamics* (Clarendon, Oxford, 1986).
3. *Metallic Glasses: Papers Presented at a Seminar of the Materials Science Division of the American Society for Metals, 1976*, Ed. by J. J. Gilman and H. J. Leamy (American Society for Metals, Metal Park, Ohio, 1978; Metallurgiya, Moscow, 1984).
4. *Amorphous Metal Alloys*, Ed. by F. E. Lyuborskiĭ (Metallurgiya, Moscow, 1987).
5. K. Binder and A. P. Young, Rev. Mod. Phys. **58** (4), 801 (1986).
6. S. L. Ginzburg, *Irreversible Processes in Spin Glasses* (Nauka, Moscow, 1989).
7. A. I. Olemskoĭ and I. A. Sklyar, Usp. Fiz. Nauk **162** (6), 29 (1992) [Sov. Phys. Usp. **35**, 455 (1992)].
8. A. I. Olemskoĭ and I. V. Koplyk, Usp. Fiz. Nauk **165** (10), 1105 (1995) [Phys. Usp. **38**, 1061 (1995)].
9. V. S. Postnikov, *Internal Friction in Metals* (Metallurgiya, Moscow, 1974).
10. A. I. Olemskoĭ, in *Physics Reviews*, Ed. by I. M. Khalatnikov (Gordon and Breach, London, 1996), Vol. 18, Part 1, pp. 1–173.

Translated by O. Borovik-Romanova

Technical Physics, Vol. 45, No. 6, 2000, pp. 683–686. Translated from Zhurnal Tekhnicheskoĭ Fiziki, Vol. 70, No. 6, 2000, pp. 16–19.

Evolution of a Randomly Modulated Breather in a Nonlinear Medium

F. Kh. Abdullaev and A. A. Abdumalikov

Physicotechnical Institute, Academy of Sciences of Uzbekistan, Tashkent, 700084 Uzbekistan

Received April 13, 1999

Abstract—The evolution of a randomly modulated sine-Gordon breather in a nonlinear medium is studied theoretically. The initial wave field is affected by multiplicative noise. For breather amplitude and velocity, the probability distribution function is determined by means of the inverse scattering transform and the method of cumulants. The distributions are shown to be non-Gaussian. The mean and the most probable values of the breather amplitude and velocity are calculated. © *2000 MAIK "Nauka/Interperiodica".*

INTRODUCTION

Investigating the evolution of random fields in nonlinear dispersive media is among the basic challenges in the theory of nonlinear waves [1–3]. Of particular interest is the propagation of randomly modulated solitons and soliton systems in media described by integrable or nearly integrable nonlinear wave equations. Problems of this type are raised in areas such as optical-soliton propagation in fibers with amplifiers [4], optical-pulse propagation in resonant media [5], soliton generation in nematic liquid crystals [6], and the effects of quantum noise on fluxon dynamics in long Josephson junctions. The inverse scattering transform [7] has been instrumental in attacking them. This approach was applied to the propagation of a nonlinear-Schrödinger [4, 8–10], Korteweg–de Vries [8], or dark soliton [11] under random modulation. All of the soliton distribution functions (DFs) obtained in those studies have a Gaussian shape. On the other hand, for nonlinear-Schrödinger and sine-Gordon (SG) solitons, it has recently been demonstrated that second-order noise effects result in a non-Gaussian DF for parameters of single solitons generated [7, 12]. It is therefore interesting to consider the problem in the context of a system of randomly modulated solitons. One could give many examples of coupled soliton systems, including soliton pairs that form breathers. Of special importance is a randomly modulated SG-equation breather. Being a bound state of a kink–antikink pair, it has a finite binding energy, in contrast to nonlinear-Schrödinger or other breathers with a zero binding energy. Due to the energy and the internal-oscillation parameter, a breather may interact with noise in a variety of ways and even undergo decay. Breathers are a key issue in the statistical mechanics of soliton systems and nonequilibrium processes related to solitons. Taking them into account helps one understand the nature of noise in distributed systems. For example, breathers contribute to noise in long Josephson junctions [13]. To understand fluctuations in these structures, one should consider the effect of quantum fluctuations on kinks and breathers.

This paper studies the evolution of an SG breather with a randomly modulated initial condition.

FORMALISM OF THE INVERSE SCATTERING TRANSFORM FOR CHANGES IN THE BREATHER PARAMETERS

Consider the SG equation

$$u_{tt} - u_{xx} + \sin(u) = 0 \tag{1}$$

with the randomly modulated initial breather condition

$$\begin{aligned} u(x, t = 0) &= u_b(x), \\ u_t(x, t = 0) &= u_b(x)(1 + \varepsilon(x)), \end{aligned} \tag{2}$$

where $\varepsilon(x)$ is a Gaussian random function for which

$$\langle \varepsilon(x) \rangle = 0, \quad \langle \varepsilon(x)\varepsilon(y) \rangle = B(x - y; l). \tag{3}$$

Here, $B(x)$ is the noise correlation function and l is the correlation length; the angled brackets denote the averaging over all realizations of $\varepsilon(x)$. The noise intensity is assumed to be small, so that $B \ll 1$. This model applies to soliton excitation in liquid crystals [6] and to quantum effects in long Josephson junctions [13].

Now, we give some relevant formulas of the inverse scattering transform, the notation being borrowed from [14]. Recall that this technique associates a nonlinear evolution equation with a linear spectral problem:

$$L\psi = \lambda\psi. \tag{4}$$

In the case of the SG equation, L is a 2×2 matrix and $\psi = (\psi_1, \psi_2)$. The complex number λ is called the spectral parameter. Let $a(\lambda)$ and $b(\lambda)$ denote the Jost coefficients. A breather relates to a symmetric pair of zeros of $a(\lambda)$ in the λ-plane, denoted as $\lambda_1 = \mu + i\nu$ and

$\lambda_2 = -\mu + i\nu$. A breather solution has the form

$$u_b = 4\arctan\left\{(\tan(\gamma))\sin\left(\frac{\psi(t) - xv}{\sqrt{1-v^2}}\cos(\gamma)\right)\right.$$
$$\left.\times \operatorname{sech}\left(\frac{x-\xi(t)}{\sqrt{1-v^2}}\sin(\gamma)\right)\right\}. \quad (5)$$

Here, $\xi(t) = \xi_0 + vt$ and the phase of the breather is

$$\psi(t) = t - \psi_0\frac{\sqrt{1-v^2}}{\cos(\gamma)}.$$

The amplitude of the breather is $\gamma = \arctan(\nu/\mu)$. Furthermore,

$$\mu = \frac{1}{2}\sqrt{\frac{1+v}{1-v}}\cos(\gamma), \quad \nu = \frac{1}{2}\sqrt{\frac{1+v}{1-v}}\sin(\gamma). \quad (6)$$

The Jost coefficients are expressed as

$$a(\lambda) = \frac{(\lambda-\lambda_1)(\lambda-\lambda_2)}{(\lambda-\lambda_1^*)(\lambda-\lambda_2^*)},$$
$$a'(\lambda_1) = \frac{\mu}{2i\nu\lambda_1}, \quad a'(\lambda_2) = \frac{\mu}{2i\nu\lambda_2}. \quad (7)$$

It is very difficult to solve the problem in a general case. We therefore concentrate on the limit of a small-amplitude breather: $\nu \ll \mu$ and $\nu \ll |\lambda_1|$. Under this condition, the analysis can be carried out completely. The corresponding solution is

$$u \approx 4\gamma\sin\left(\left(1-\frac{\gamma^2}{2}\right)\frac{t-xv}{\sqrt{1-v^2}} - \psi_0\right)$$
$$\times \operatorname{sech}\left(\gamma\frac{(x-\xi(t))}{\sqrt{1-v^2}}\right). \quad (8)$$

The Jost functions of a small-amplitude breather are

$$\psi_1 = \frac{(\lambda^2 - |\lambda_1|^2 + i\lambda\nu)\cosh(z) + 2i\lambda\nu\sinh(z)}{(\lambda-\lambda_1^*)(\lambda+\lambda_1)\cosh(z)}$$
$$\times \exp(ikr),$$
$$\psi_2 = \frac{2\nu(\lambda\cos(\varphi) - i\eta\sin(\varphi))}{(\lambda-\lambda_1^*)(\lambda+\lambda_1)\cosh(z)}\exp(ikr), \quad (9)$$

where

$$k(\lambda) = \frac{1}{2}\left(\lambda - \frac{1}{4\lambda}\right), \quad z = \nu\left(1 + \frac{1}{4|\lambda_1|^2}\right)x - \frac{\ln|c|}{2\nu},$$
$$\varphi = \mu\left(1 - \frac{1}{4|\lambda_1|^2}\right)x + \arg c,$$
$$c_1 = c, \quad c_2 = c_1^* = c^*, \quad c_n = \frac{b_n}{a'(\lambda_n)}.$$

The statistical characteristics of breather parameters are computed from variational derivatives of the scattering data. The derivatives give corrections to the scattering data:

$$\Delta\lambda = \int_{-\infty}^{\infty}\frac{\delta\lambda}{\delta u_t}\Delta u_t dx. \quad (10)$$

The first variational derivative of the spectral parameter λ_1 is

$$\frac{\delta\lambda_1}{\delta u_t} = -\frac{i\nu\eta}{4\lambda_1\cosh^2(z)}\cosh(z + i\varphi).$$

The second variational derivative is

$$\frac{\delta^2\lambda_1}{\delta u_t(x)\delta u_t(y)} = -\frac{\nu\eta}{32\lambda_1}\operatorname{sech}^2 z(x)\operatorname{sech}^2 z(y)$$
$$\times[(\exp(z(x)-z(y)) - \exp(-i\varphi(x) + i\varphi(y)))$$
$$\times \exp(ik_1(x-y))\vartheta(x-y)$$
$$-i[\cos((z+i\varphi)(x))\cos((z-i\varphi)(x))$$
$$+ \cos((z+i\varphi)(y))\cos((z-i\varphi)(y))]. \quad (11)$$

A correction to $a(\lambda)$ comes from

$$\frac{\delta a(\lambda)}{\delta u_t(x)} = \frac{i}{4}(\psi^{(1)}\phi^{(2)} - \psi^{(2)}\phi^{(1)}), \quad (12)$$

and

$$\frac{\delta^2 a}{\delta u_t(x)\delta u_t(y)} = -i\left(\frac{\eta}{8\lambda_1\cosh(z)}\right)^2$$
$$\times(\exp(z(x)-z(y)) - \exp(-i\varphi(x) + i\varphi(y)))$$
$$\times \exp(ik_1(x-y))\vartheta(x-y). \quad (13)$$

This gives corrections to the breather amplitude:

$$\delta_1\gamma = \frac{\delta\gamma}{\delta u_t(x)}\delta u_t(x),$$
$$\delta_2\gamma = \frac{\delta^2\gamma}{\delta u_t(x)\delta u_t(y)}\delta u_t(x)\delta u_t(y). \quad (14)$$

The first- and second-order corrections to the breather velocity are calculated similarly:

$$\delta_1 v = -8\frac{\lambda_1\delta_x\lambda_1^* + \lambda_1^*\delta_x\lambda_1}{(1+4|\lambda_1|^2)^2}\delta u_t(x),$$

$$\delta_2 \nu = -8\left(\frac{\lambda_1\delta_{xy}\lambda_1^* + \lambda_1^*\delta_{xy}\lambda_1}{(1+4|\lambda_1|^2)^2} + \nu\frac{\delta_y\lambda_1\delta_x\lambda_1^* + \delta_y\lambda_1^*\delta_x\lambda_1}{(1+4|\lambda_1|^2)^2} + 8\frac{\lambda_1^2\delta_x\lambda_1^*\delta_y\lambda_1^* + \lambda_1^{*2}\delta_x\lambda_1\delta_y\lambda_1}{(1+4|\lambda_1|^2)^3}\right)\delta u_t(x)\delta u_t(y). \quad (15)$$

BREATHER-PARAMETER DISTRIBUTION

Let us calculate the DF of the breather parameters. We employ the method of cumulants [15]. According to (13) and (14), the corrections to λ are nonlinear functionals of the random process $\varepsilon(x)$. Therefore, the DF of the corrections is non-Gaussian. Cumulants are more convenient than moments as far as a non-Gaussian DF is concerned. First, a few cumulants suffice for describing the shape of a non-Gaussian DF: the first and the second cumulants refer to the Gaussian approximation of the DF shape, whereas the higher cumulants describe the deviation of the DF from the Gaussian DF.

Recall that the DF of a random variable Δ is the Fourier transform of the characteristic function χ:

$$\chi(u) = \langle \exp(i\Delta u)\rangle = \int_{-\infty}^{\infty} d\Delta P(\Delta)\exp(i\Delta u). \quad (16)$$

The cumulants K_n are determined from the coefficients of the expansion

$$\ln\chi(u) = \sum_{i=1}^{\infty}\frac{i^n u^n}{n!}K_n. \quad (17)$$

To calculate K_n, let us express them in terms of the moments M_n:

$$\begin{aligned} K_1 &= M_1 \approx \langle\Delta_2\lambda\rangle + \langle\Delta_4\lambda\rangle + O(\varepsilon^6),\\ K_2 &= M_2 - M_1^2 \approx \langle(\Delta_1\lambda)^2\rangle + \langle(\Delta_2\lambda)^2\rangle - \langle\Delta_2\lambda\rangle^2\\ &\quad + 2\langle\Delta_1\lambda\Delta_3\lambda\rangle + O(\varepsilon^6), \quad (18)\\ K_3 &= M_3 - 3M_1M_2 + 2M_1^3 \approx 3\langle(\Delta_1\lambda)^2\Delta_2\lambda\rangle\\ &\quad - 3\langle\Delta_2\lambda\rangle\langle(\Delta_1\lambda)^2\rangle + O(\varepsilon^6). \end{aligned}$$

Formulas (16)–(18) yield an expression for the DF:

$$P(\Delta) \approx \frac{1}{\sqrt{2\pi K_2}}\left[1 - \frac{\alpha_3}{2}y\left(1 - \frac{y^2}{3}\right)\right]\exp\left(-\frac{y^2}{2}\right), \quad (19)$$

where $y = (\Delta - K_1)/\sqrt{K_2}$ and $\alpha_3 = K_3/(K_2)^{3/2}$.

In (18), all of the cumulants are developed in ε up to fourth-order terms, since $K_3 \sim \varepsilon^4$. Looking at (19), notice that K_3 appears only in the term K_3^2/K_2^3. The joint contribution of K_2 and K_3 is of the order of ε^2. It is therefore sufficient to develop K_3 up to ε^4 and K_1 and K_2 up to ε^2.

In the following, we use the correlation function

$$B(x-y) = B_0\exp\left(-\frac{|x-y|}{l}\right), \quad (20)$$

where l is the correlation length.

STATISTICAL CHARACTERISTICS OF BREATHER-PARAMETER FLUCTUATIONS

Amplitude Fluctuations

Using (14), we arrive at formulas for amplitude-correction cumulants:

$$K_1^\gamma = -\frac{8}{15}\sigma^2\nu^2\left(1 + \frac{1}{4\eta^2}\right)^2\left(1 + \frac{21}{8}\gamma^2\right), \quad (21)$$

$$K_2^\gamma = \frac{1}{4}\sigma^2\nu^2\gamma\left(1 + \frac{1}{4\eta^2}\right)^2(1 - 6\gamma^2), \quad (22)$$

and

$$K_3^\gamma = \frac{3}{32}\sigma^4\nu^4\gamma\left(1 + \frac{1}{4\eta^2}\right)^4. \quad (23)$$

Here, $\sigma^2 = B_0 l$ with $B_0 = \varepsilon^2$. The DF peak of $P(\Delta\gamma)$ is at K_1^γ. The mean amplitude is found from the equation $\langle\Delta\gamma\rangle = K_1^\gamma$. We have

$$\begin{aligned} \langle\gamma\rangle &= \gamma + \langle\Delta\gamma\rangle\\ &= \gamma\left(1 - \frac{8\sigma^2\nu^2}{15\gamma}\left(1 + \frac{1}{4\eta^2}\right)^2\left(1 + \frac{21\gamma^2}{8}\right)\right). \end{aligned} \quad (24)$$

This indicates that breather amplitude falls as σ^2 rises. The dependence of the correction is not monotonic at larger γ. The most probable breather amplitude is

$$\begin{aligned} \gamma_{mp} &= \gamma + (\Delta\gamma)_{mp} = \gamma + K_1^\gamma - \frac{K_3^\gamma}{2K_2^\gamma}\\ &= \gamma - \frac{\sigma^2\nu^2}{40}\left(1 + \frac{1}{4\eta^2}\right)^2\left(\frac{173}{6} + 101\gamma^2\right). \end{aligned} \quad (25)$$

Thus, the most probable amplitude is less than the mean amplitude.

The deviation of the DF from the Gaussian law is characterized by the coefficient of skewness

$$\alpha_3^\gamma = \frac{K_3^\gamma}{(K_2^\gamma)^{3/2}} = \sigma\nu\gamma^{-1/2}\left(1+\frac{1}{4\eta^2}\right)^2(1-6\gamma^2)^{-3/2}. \quad (26)$$

For example, if $\sigma = 0.1$, $\eta = 1$, $\gamma = 0.1$, and $\nu = 0.5$, then α_3^γ is as large as 0.17, which is an appreciable deviation from a Gaussian distribution.

Breather Velocity Fluctuations

Velocity-correction cumulants are

$$K_1^v = \frac{8}{15}\sigma^2\sqrt{1-v^2}\frac{\nu^3}{\mu^3}, \quad (27)$$

$$K_2^v = \frac{16}{15}\sigma^2\sqrt{1-v^2}\frac{\nu^3}{\mu}\frac{1}{(1+4|\lambda_1|^2)^2}, \quad (28)$$

and

$$K_3^v = \frac{4}{75}\sigma^4(1-v^2)\frac{\nu^6}{\mu^4}\frac{1}{(1+4|\lambda_1|^2)^2} \times(1+8\mu^2+32\mu^4). \quad (29)$$

The peak of the velocity DF is at $\langle\Delta v\rangle = K_1^v$, so that the mean breather velocity is

$$\langle v\rangle = v + \langle\Delta v\rangle = v\left(1+\frac{8\sigma^2\nu^3}{15\mu^3 v}\sqrt{1-v^2}\right). \quad (30)$$

The correction is positive and decreases with increasing v. Furthermore, $\Delta v \longrightarrow 0$ with $v \longrightarrow 1$. The correction is maximum when the initial velocity is zero.

The most probable breather velocity is

$$(v)_{mp} = v - \frac{\sigma^2\nu^3}{\mu^3}\sqrt{1-v^2}\left(\frac{7}{15}+8\mu^2+32\mu^4\right). \quad (31)$$

Thus, the most probable velocity is less than the mean velocity. The velocity skewness coefficient is

$$\alpha_3^v = \sqrt{\frac{3}{5}}\frac{\sigma\nu^3 2(1-v^2)^{1/4}(1+8\mu^2+32\mu^4)}{16\mu^{5/2}} \times(1+4|\lambda_1|^2). \quad (32)$$

Thus, the velocity DF of the breather becomes less asymmetric as $v \longrightarrow 1$ (relativistic limit). On the other hand, the asymmetry grows with decreasing amplitude.

CONCLUSIONS

We studied the effect of a noisy initial condition on the evolution of an SG-equation breather. Since the SG equation is a completely integrable equation, the evolution of the initial wave field results in the formation of a breather with random parameters together with a radiation field. The former and the latter separate in a fairly short time, allowing one to examine their statistical properties individually. Using the inverse scattering transform and the method of cumulants, we found the DFs for the amplitude and velocity of an asymptotic breather generated by the noisy initial condition. Both of the DFs are non-Gaussian. Finally, we calculated the coefficients of skewness and the most probable and mean values for the breather amplitude and velocity.

ACKNOWLEDGMENTS

This study was funded in part by the US Civilian Research Development Foundation (Award ZM1-342).

REFERENCES

1. S. Gredeskul and Yu. S. Kivshar, Phys. Rep. **122**, 1 (1992).
2. F. Kh. Abdullaev, *Theory of Solitons in Inhomogeneous Media* (Wiley, Chichester, 1994).
3. A. Gurbatov, S. Malakhov, and A. Saichev, *Stochastic Waves in Nonlinear Media without Dispersion* (Nauka, Moscow, 1988).
4. J. N. Elgin, Phys. Lett. A **110**, 441 (1985).
5. H. Haus and J. P. Gordon, Opt. Lett. **11**, 665 (1986).
6. V. G. Kamenskiĭ, Zh. Éksp. Teor. Fiz. **87**, 1262 (1984) [Sov. Phys. JETP **60**, 723 (1984)].
7. F. Kh. Abdullaev and A. A. Abdumalikov, Physica D **113**, 115 (1998).
8. F. Kh. Abdullaev and S. A. Darmanyan, Zh. Tekh. Fiz. **58**, 265 (1988) [Sov. Phys. Tech. Phys. **33**, 162 (1988)].
9. F. Kh. Abdullaev and M. R. Dzhumaev, Zh. Tekh. Fiz. **65** (8), 221 (1995) [Tech. Phys. **40**, 749 (1995)].
10. V. V. Konotop and V. E. Vekslerchik, J. Phys. A **24**, 767 (1991).
11. S. A. Gredeskul and L. A. Pastur, in *Nonlinearity with Disorder*, Ed. by F. Kh. Abdullaev, A. R. Bishop, and S. Pnevmatikos (Springer, Heidelberg, 1991), pp. 126–133.
12. F. Kh. Abdullaev, S. A. Darmanyan, and F. Lederer, Opt. Commun. **126**, 89 (1996).
13. D. W. McLaughlin and A. C. Scott, Phys. Rev. A **18**, 1652 (1978).
14. S. P. Novikov, S. V. Manakov, L. P. Pitaevskii, and V. E. Zakharov, *Theory of Solitons: The Inverse Scattering Method* (Nauka, Moscow, 1980; Consultants Bureau, New York, 1984).
15. A. N. Malakhov, *Cumulant Analysis of Stochastic Non-Gaussian Processes and Their Transforms* (Sov. Radio, Moscow, 1978).

Translated by A. A. Sharshakov

Technical Physics, Vol. 45, No. 6, 2000, pp. 687–693. Translated from Zhurnal Tekhnicheskoĭ Fiziki, Vol. 70, No. 6, 2000, pp. 20–26.

GASES AND LIQUIDS

Some Laws of Polarization and Dispersion of a Drop in an Electrostatic Field

S. O. Shiryaeva

Yaroslavl State University, Sovietskaya ul. 14, Yaroslavl, 150000 Russia

Received February 16, 1999

Abstract—The laws of distribution among contributions in various interactions to the total polarization energy of a conductor in a uniform electrostatic field was analyzed. It is shown that in a closed system, spontaneous shape variations of a liquid conductor with a free surface in an external magnetic field are possible only if they are accompanied by an increase in the conductor dipole moment. Variations of the intrinsic energy of a conductor are studied by the example of a conductive liquid drop in the case where a drop affected by a polarization charge becomes unstable. Analytical expressions defining the sizes and charges of the droplets ejected out of the initial drop under the conditions of instability are derived. *© 2000 MAIK "Nauka/Interperiodica".*

INTRODUCTION

In spite of numerous theoretical and experimental investigations of the laws of polarization of a conductor in an external electrostatic field, some problems concerning this phenomenon are still poorly understood so far. This is related to a certain complexity in solving electrostatic problems, on the one hand, and to the fact that physical models used for the theoretical description of electrostatic phenomena are not realistic, on the other hand [1–5]. Suffice it to recollect a well-known problem concerning the relation between the surface density of the electric charge of a conductor and the curvature of its surface, shortcomings resulting from the "point" charge idealization, and the problem in obtaining the linear and surface distributions of charges when their own sizes are ignored [4, 6, 7]. In particular, temporal variation in the shape of a conducting liquid drop in the electrostatic field $\mathbf{E}_0$, the theoretical study of which is based on the conductor polarization phenomenon [8], is poorly understood.

1. The expression for the polarization energy of an uncharged conductor in a uniform electrostatic field of strength $\mathbf{E}_0$ is easily derived [1, 2] and has the form

$$U = -\frac{1}{2}\mathbf{p}\mathbf{E}_0, \tag{1}$$

where $\mathbf{p}$ is the dipole moment of the conductor in the field $\mathbf{E}_0$.

On the other hand, it is known [1–5] that the energy U_d of an arbitrary rigid dipole $\mathbf{p}$ in the field $\mathbf{E}_0$ is defined by the expression

$$U_d = -\mathbf{p}\mathbf{E}_0. \tag{2}$$

The distinction between (1) and (2) is caused by the fact that (2) is derived neglecting the energy U_* of interaction between the dipole charges, which is constant for the model of a "rigid" dipole, and neglecting the intrinsic energy $2U_0$ of both charges, which is also constant both for dipoles consisting of point charges and for those consisting of charges distributed over small finite volumes (let us recollect here that the intrinsic energy of point charges is assumed to be infinite).

Neglect of constant terms of the energy when deriving (2) is based on the fact that, in practice, we observe only energy variations, but not constant energy values [5]. However, if we deal with a polarized conductor, neither the energy U_* of the interaction of the charges of the polarization dipole with each other nor the intrinsic energy $2U_0$ of both charges should be assumed constant, because these energies depend on external field strength $\mathbf{E}_0$ and, for finite volumes of conducting liquid bounded by a free equilibrium surface, they also depend on the surface shape.

It is easy to see from (1) and (2) that the intrinsic energy $U_{gd} \equiv U_* + 2U_0$ of a conductor polarized in the field $\mathbf{E}_0$ is defined by the expression

$$U_{gd} \equiv U_* + 2U_0 = U - U_d = \frac{1}{2}\mathbf{p}\mathbf{E}_0. \tag{3}$$

The energy U_* of interaction of the dipole charges with each other is negative, because the dipole charges are of opposite sign. The intrinsic energy $2U_0$ of the dipole charges is always positive, and its absolute magnitude satisfies the condition [5]

$$2U_0 \geq |U_*|. \tag{4}$$

It is clear that the equality sign in (4) is impossible for the system of polarization charges under consideration, because it would contradict relation (3).

1063-7842/00/4506-0687$20.00

2. If the conductor dipole moment is known, one can easily derive expressions for the conductor polarization energy U and the intrinsic energy U_{gd} on the basis of (1) and (3). Let us do this for a conductor of spherical shape. Surface density $\kappa = \kappa(\Theta)$ of a polarization charge at a sphere is known and is given by the expression [1]

$$\kappa(\Theta) = \frac{3}{4\pi}E_0\cos\Theta, \tag{5}$$

where the angle Θ is reckoned from the direction of field $\mathbf{E}_0$.

Therefore, it is possible to determine the polarization dipole characteristics, namely, the value q of the charges involved and the distance l between their "centers of gravity." To derive an expression for q, it is sufficient to integrate (5) over a half of the sphere, with the angle Θ varying in a range of $0 \le \Theta \le \pi/2$. As a result, we obtain

$$q = \frac{3}{4}E_0R^2. \tag{6}$$

Multiplying (5) by $2z \equiv 2R\cos\Theta$ and integrating Θ over the angle again, we obtain the dipole moment of the polarized sphere [1]

$$\mathbf{p} = R^3\mathbf{E}_0. \tag{7}$$

It is easy to the find dipole length l by dividing (7) by (6); i.e.,

$$l = \frac{4R}{3}. \tag{8}$$

Consequently, the energy U of the conducting sphere polarized in the field $\mathbf{E}_0$ and the intrinsic energy of the charges of the polarization dipole U_{gd} are defined by the expression

$$U = -U_{gd} = -\frac{1}{2}R^3E_0^2.$$

3. Let us explore the influence of deformation of the conductor shape on the energy U of its polarization and on intrinsic energy U_{gd} of a polarization dipole in the field $\mathbf{E}_0$. While on the subject of conductor deformation, we will imply deformations caused by the action of field $\mathbf{E}_0$ itself bearing in mind applications of the problem under consideration to the problem of stability of the free surface of a conducting liquid with respect to the polarization and intrinsic charges (see, for example, [8–12] and the references therein). In particular, it is known that the equilibrium shape of a conducting liquid drop in the field $\mathbf{E}_0$ is close to a prolate spheroid [1] (it coincides to the approximation linear with respect to the square of the eccentricity e^2 [8, 13]). Therefore, in the further consideration, we will assume that an initially spherical drop of a conducting liquid subjected to a constant uniform electrical field $\mathbf{E}_0$ will suffer transformation into a prolate spheroid with the eccentricity governed by the strength of the external uniform electrostatic field $\mathbf{E}_0$, the surface tension σ of the liquid and the initial radius of the drop. To the approximation linear with respect to e^2, the relation between the square of the eccentricity of the equilibrium spheroid and the aforementioned parameters is defined by the expression [7, 13]

$$e^2 \cong \frac{9}{16\pi}\frac{RE_0^2}{\sigma}. \tag{9}$$

This expression for the dipole moment of the spheroid is valid only to the approximation linear in e^2. For arbitrary values of e^2, the polarization dipole moment of a conducting spheroidal drop in the field $\mathbf{E}_0$ is defined by the expression [1]

$$\mathbf{p} = 3R^3\frac{e^3}{(1-e^2)(\operatorname{arctanh} e - e)}\mathbf{E}_0.$$

The equation describing a spheroid surface in a spherical coordinate system with the origin at the spheroid center is

$$\begin{aligned} r(\Theta) &= R(1-e^2)^{1/6}(1-e^2\cos^2\Theta)^{-1/2} \\ &\cong R\left[1-\frac{e^2}{6}(1-3\cos^2\Theta)\right]. \end{aligned} \tag{10}$$

To the approximation linear with respect to the square of the eccentricity, the surface density of the polarization charge of the prolate spheroid is defined by the expression [1, 13]

$$\kappa(\Theta) = \frac{3E_0}{4\pi}\cos\Theta[1-e^2(0.6-\cos^2\Theta)]. \tag{11}$$

Let us integrate (11) over half of the spheroid (i.e., over $0 \le \Theta \le \pi/2$) using equation (10), which defines the free surface of the spheroid, and determine the polarization charge value

$$q = \frac{3}{4}E_0R^2\left(1+\frac{e^2}{15}\right). \tag{12}$$

To determine the dipole moment of the polarized spheroid, we multiply (11) by $2r(\Theta)\cos\Theta$ and integrate the resulting expression with respect to the angle Θ over the interval $0 \le \Theta \le \pi/2$. As a result, we have

$$\mathbf{p} = R^3\mathbf{E}_0\left(1+\frac{2e^2}{5}\right). \tag{13}$$

Dividing (12) by (13), we obtain an expression for the dipole length l:

$$l = \frac{4R}{3}\left(1+\frac{e^2}{3}\right). \tag{14}$$

If the above is referred to the equilibrium spheroidal shape of the conducting drop in the field $\mathbf{E}_0$, it should be remembered that, in expressions (12)–(14), the

square of the eccentricity and the external field strength are related by expression (9).

Comparing relations (6)–(8) and (12)–(14), we can see that the transformation of an initially spherical drop in the field $\mathbf{E}_0$ into a prolate spheroid leads to an increase in all characteristics of the polarization dipole, namely, the charge, length, and moment. Transition from the initial spherical shape of the drop to the equilibrium spheroidal shape starts at an infinitely low strength of the field $\mathbf{E}_0$. This transition is accompanied by a decrease in the total potential energy of the closed system involving the drop, uniform external field $\mathbf{E}_0$, and infinitely distant charges inducing this field.

The fact that we are dealing with spontaneous deformations of a drop in a closed system imposes certain restrictions on the form of admissible deformations. Indeed, only deformations accompanied by a decrease in the total potential energy may spontaneously occur in a closed system. In the considered case of a conducting drop in an external electrostatic field, the only admissible deformations are those for which the dipole moment of the drop increases and the electrical part of the total potential energy (described by relation (1)) decreases, because the energy of the surface tension forces at any deformations may only increase proportionally to an increase in the drop surface. The intrinsic energy U_{gd} of the polarization dipole at such deformations will increase according to (3); and the energy of interaction of polarization charges U_* decreases, because, according to (12) and (14), if the drop elongates, the charge q increases much more slowly than the length l of the dipole does. An increase in U_{gd} with a simultaneous decrease in U_* may occur only due to a considerable increase in the electrostatic intrinsic energy $2U_0$ of the polarization charges (see (3), (4)).

In particular, it follows from the above that spontaneous deformations of the drop in the field $\mathbf{E}_0$ transforming the drop into an prolate spheroid lead to a decrease in the potential energy of the system and deformations resulting in an oblate spheroid cause an increase in it. We note that the polarization dipole characteristics of an oblate spheroid with its axis parallel to the field $\mathbf{E}_0$ differ from (11)–(14) only in the sign of the term e^2. In the calculation of a bubble shape in a liquid in an external electrostatic field, an inverse dependence will be encountered: deformation of the bubble in the field $\mathbf{E}_0$ resulting in an oblate spheroid is accompanied by a decrease in the polarization energy, because the main contribution to the polarization energy is made by the polarization of the liquid surrounding the bubble. However, in the bubble problem, depending on the surface mobility of the charges at the bubble walls and the permitivity of the surrounding liquid (depending on the ratio between the contributions to the total potential-energy variation caused by polarization of the surrounding liquid and the bubble itself due to redistribution of the free charge at its walls), various deformation types may occur: an oblate spheroid, sphere, and prolate spheroid as was mentioned previously [14, 15].

We now demonstrate that the further evolution of the instability of a conducting drop in an external uniform electrostatic field leads to a decrease in the potential energy of the system as well.

4. A drop of radius R of an ideally conducting incompressible liquid with surface tension σ is subjected to an external uniform electrostatic field of strength E_0; as a result, the drop takes a spheroidal shape specified by the eccentricity defined by relation (9). As the field strength increases, the drop eccentricity, as well as the surface density of the charge induced at the drop apices, increases too. At a certain critical strength E_0 (when $E_0 \geq (2.6\sigma/R)^{1/2}$ [7, 16]), the drop becomes unstable with respect to a virtual increase in the eccentricity and then starts to elongate rapidly (faster than according to the exponential law [17]). When the pressure of the electric field of the charges induced at the drop apices (this field strengthens with increasing e^2, see Section 3 of this paper) exceeds the pressure of the capillary forces, the drop charge starts to decrease owing to an emission of highly dispersed, strongly charged droplets from both of the drop apices and the drop eccentricity growth ceases. The square of the eccentricity e^2 of the parent drop at this instant is unknown, because expression (9) is valid only for equilibrium forms.

We note that the emission of the daughter droplets occurs from the emitting bulges being formed at the apices of the unstable drop owing to superposition of the high-order modes of the capillary oscillations of the drop, which lose stability when the surface density of the induced charge increases. The emission of the daughter droplets involves the detachment of the tips of the emission bulges by the field together with the polarization charges accumulated at them. Formation of the emission bulges, according to the aforesaid, leads to an increase in the drop dipole moment and to a decrease in the total potential energy of the system.

Assuming that there is axial symmetry, as well as symmetry about the equatorial plane of the drop, we will consider the droplets simultaneously detaching from the opposite apices of the parent drop as being alike in size, with their charges being equal in magnitude but opposite in sign. It is possible to assume that two simultaneously emitted daughter droplets form dipole $\mathbf{p}$ with a loose coupling and the dipole extent grows as the droplets fly apart. Thus, the process of the emission of the daughter droplets again leads to an increase in the dipole moment and to a decrease in the potential energy of the entire system. The intrinsic electrostatic energy of the system in this process steadily increases.

We now find the variation of the potential energy of the system resulting from simultaneous emission of two identical but opposite-charged daughter droplets from the opposite apices of the parent drop specified by

eccentricity e and major semiaxis a. We neglect the influence of evaporation and condensation, and we assume the temperature of the system to be constant. A specific mechanism for the emission of droplets will not be considered (typical models can be found, for example, in [11, 18]), and instead we assume that the daughter droplets are virtually formed at a distance on the order of the characteristic linear size of the daughter droplet (the radius of a spherical drop r of equal volume) from an apex of the parent drop. Thus, the distance l between the centers of simultaneously emitted daughter droplets is defined by the expression $l \approx 2(a + r)$. Let q denote the daughter droplet charge; then the dipole formed by two opposite-charged droplets has the magnitude of $p = ql$.

An expression for the potential energy of the parent drop just before shedding the surface charge can be easily written as

$$U_1 = 4\pi\sigma R^2 A(e) - \frac{1}{2}R^3 C(e)E_0^2,$$

where

$$A(e) = \frac{1}{2}(1-e^2)^{-1/6}\left[(1-e^3)^{1/2} + \frac{1}{2}\arcsin e\right],$$

$$C(e) = \frac{3e^3}{(1-e^2)(\operatorname{arctanh} e - e)}.$$

The first term in the expression for U_1 defines the energy of the surface tension forces, and the second term accounts for the polarization energy of the drop in the field $\mathbf{E}_0$.

The potential energy of the parent drop and a pair of the emitted daughter droplets forming the dipole $\mathbf{p}$ is given by

$$\begin{aligned} U_2 = {} & 4\pi\sigma R^2 A(e)\left[1 - 2 - \frac{r^3}{R^3}\right]^{2/3} + 8\pi\sigma r^2 A(e_0) \\ & - \frac{1}{2}(R^3 - 2r^3)C(e)E_0^2 - \mathbf{p}(\mathbf{E}_0 + \mathbf{E}_*) \\ & + \frac{2q^2}{2r}B(e_0) - 2\frac{1}{2}r^3 C(e_0)(E_0 + E_*)^2. \end{aligned} \quad (15)$$

$$B(e_0) = \frac{1}{e_0}(1-e_0^2)^{1/3}\operatorname{arctanh} e_0.$$

Here, E_* is the field strength of the induced charge of the parent drop and e_0 is the eccentricity of the daughter droplet. The first term in (15) defines the energy of the surface-tension forces of the parent drop with regard to a decrease in its surface area; the second term is the energy of the surface tension forces of the two daughter droplets; the third term is the polarization energy of the remainder of the parent drop in the field $\mathbf{E}_0$; the fourth term is the energy of the dipole consisting of the daughter droplets in the resultant electric field near the parent drop apices (this field is assumed to be quasi-uniform throughout the daughter-droplet volumes); the fifth term is the intrinsic electrostatic energy of the daughter droplets; and the sixth term defines the polarization energy of the daughter droplets in the resultant electric field in the vicinity of the parent drop apices.

When writing expression (15), we disregarded small energetic contributions of the interaction of intrinsic polarization charges of the daughter droplets with each other and of the interaction between the charges of the emitted droplets and their images in the parent drop. In this sense, expression (15) is approximate. To make our concepts of the ratio between the magnitudes of various terms in (15) consistent with the results of experimental and theoretical investigations (see, for example, [8, 11, 19] and references therein), we will consider the charge q of the daughter droplet and its characteristic linear dimension (that is, the radius r of a spherical droplet of the same volume) as small quantities of the first order. Further calculations will be performed in the context of a quadratic approximation with respect to small parameters, which will allow us to simplify expression (15) somewhat by omitting the sixth summand and to discard the terms of the third order of smallness in the first and third summands.

The potential-energy variation ΔU resulting from the emission of a pair of daughter droplets takes the form

$$\Delta U = -\mathbf{p}(\mathbf{E}_0 + \mathbf{E}_*) + \frac{q^2}{r}B(e_0) + 8\pi r^2\sigma A(e_0).$$

The daughter-droplet eccentricity e_0 is related to its characteristic linear dimension r and the strength of field $(E_0 + E_*)$ by an expression of type (9) [13]:

$$e_0^2 \approx 9w^2 X(1 + W^2)T^2(e, \nu),$$

$$T(e, \nu) \equiv \left\{1 - \left[\operatorname{arctanh}\frac{e}{\nu} - \frac{e\nu}{\nu^2 - e^2}\right](\operatorname{arctanh} e - e)^{-1}\right\}, \quad (9a)$$

$$W^2 \equiv \frac{q^2}{16\pi\sigma r^3}, \quad w^2 \equiv \frac{E_0^2 R}{16\pi\sigma}, \quad X \equiv \frac{r}{R}, \quad \nu = \left(1 + \frac{\xi}{a^2}\right)^{1/2}.$$

Here, W^2 is the Rayleigh parameter characterizing the stability of a charged drop of a conducting liquid with respect to its intrinsic charge: the drop is stable for $W^2 < 1$ and is unstable for $W \geq 1$ [8,11,18]; the parameter w^2 characterizes the stability of the parent drop with respect to the polarization charge: the drop is unstable for $w^2 > 2.6/16\pi$ [16, 18]; ξ is the spheroidal coordinate of the daughter droplet's center of gravity; and ν is the distance between the centers of the daughter and parent drops rendered dimensionless by dividing by the major semiaxis $a = R(1 - e^2)^{-1/3}$ of the sphe-

roidal parent drop. The dipole length l is related to the dimensionless coordinate ν by the simple expression

$$l = 2\nu a \equiv 2\nu R(1-e^2)^{-1/3}.$$

When deriving (9a), it was taken into account that the field strength near the parent drop apices at the symmetry axis of the system, where the daughter droplets are virtually formed (we ignore the specific mechanism for the emission of the daughter droplets), is defined by the well-known expression [1, 18]

$$\mathbf{E}_0 + \mathbf{E}_* = \mathbf{E}_0 T(e, \nu).$$

Figure 1 displays the system energy variation ΔU (rendered dimensionless by dividing by $8\pi R^2\sigma$) in relation to dimensionless radius X and dimensionless charge $Y \equiv q/E_0R^2$ of the droplets for W = const, w = const, and ν = const. It can easily be seen that the function $\Delta U = \Delta U(X, Y)$ has a minimum. Physically, the minimum of function $\Delta U = \Delta U(r, q)$ means that, according to the principle of minimality of the energy dissipation in nonequilibrium processes (the Onsager principle), the system's energy variation in the course of losing excess charge by an unstable drop is extremal [20]. In a small neighborhood of the minimum of the function $\Delta U = \Delta U(r, q)$, relations

$$\frac{\partial(\Delta U)}{\partial r} = 0, \quad \frac{\partial(\Delta U)}{\partial q} = 0$$

should be fulfilled.

These conditions will result in a set of homogeneous algebraic equations for the determination of the charge q and radius r of the daughter droplets at the instant of their separation from the parent drop, namely,

$$-\frac{q^2}{r^2}B(e_0) + 16\pi\sigma r A(e_0) = 0, \qquad (16)$$

$$-l(E_0 + E_*) + \frac{2q}{r}B(e_0) = 0. \qquad (17)$$

Analyzing the set of equations (16) and (17), we should bear in mind that the characteristic linear dimension r and the daughter-droplet charge q, as well as the field strength $(E_0 + E_*)$ in the vicinity of the separated droplets, are functions of distance ν (or, which is just the same, of dipole length l). For this reason, to close the set of equations, it is necessary to complement (16) and (17) with another equation relating e, q, and ν. For such an equation, we take the condition for balancing the forces inside the neck linking the separating daughter droplets with the parent drop at the instant of neck disruption [19],

$$2\pi r_*\sigma = q(E_0 + E_*), \qquad (18)$$

where r_* is the radius of the neck at the instant of disruption.

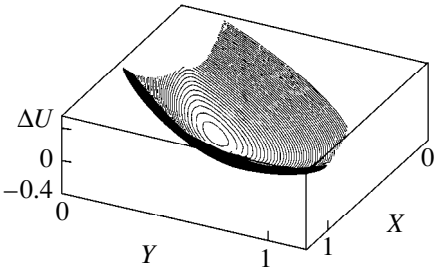

Fig. 1. Variation of the dimensionless system energy caused by emission of two daughter droplets in relation to their nondimensional radius X and charge Y for e = 0.85, w^2 = 0.05, and ν = 1.32.

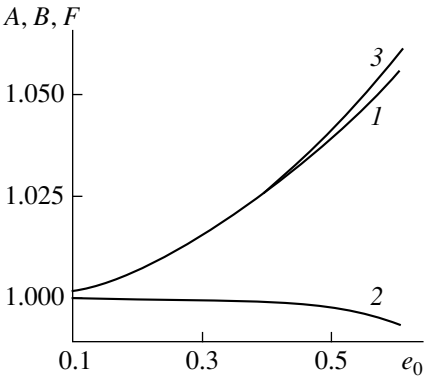

Fig. 2. The dependences of coefficients A, B, and F on the daughter-droplet eccentricity e_0.

5. The set of equations (16)–(18) is rather clumsy and should be solved numerically. However, one can acquire helpful information on the process of losing excess charge by the unstable drop, even without solving system (16)–(18), on the basis of a general analysis of it. Dividing the first term by the second term in (16), we obtain

$$W^2 \equiv \frac{q^2}{16\pi\sigma r^3} = \frac{A(e_0)}{B(e_0)}. \qquad (16a)$$

In Fig. 2, the functions $A = A(e_0)$, $B = B(e_0)$, and $F = F(e_0) \equiv A(e_0)/B(e_0)$ are represented by curves *1–3*. It can be seen that $W^2 > 1$ for all daughter droplets (note that calculated value $e_0 \approx 0.4$). Thus, the daughter droplets emitted by the parent drop, being unstable with respect to the polarization charge, in their turn, are unstable with respect to their intrinsic charges and will disintegrate. The disintegration of drops unstable with respect to their intrinsic charges may occur, depending on their size and the liquid viscosity, in two ways: either by fission into two parts of comparable size or in the form of the emission of a large number of highly charged droplets whose sizes are smaller by a factor of roughly 0.01 [8, 11, 18, 21].

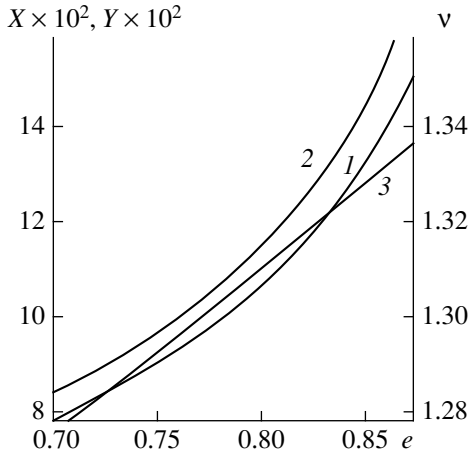

Fig. 3. Dimensionless (*1*) radius X and (*2*) charge Y of the daughter droplets and (*3*) the distance ν between the centers of the parent and daughter drops at the instant of rupture of the neck linking them in relation to the parent drop eccentricity e for $w^2 = 0.05$ and $\beta = 0.9$.

Relation (16a) also indicates that orders of smallness of charge q and size r of the daughter droplets are different. From (16a), it follows that, if r varies, charge q changes according to the law $q \sim r^{3/2}$. This, in particular, means that, when carrying out a rigorous numerical analysis of the expression for the system's energy change ΔU caused by the emission of the daughter droplets, it is necessary to take into account terms of the second order of smallness in q and the third order of smallness in $r \sim r^3$.

We now multiply (17) by $q/32\pi\sigma r^2 A(e_0)$ and then, taking into account (16a), obtain

$$lq(E_0 + E_*)/32\pi\sigma r^2 A(e_0) = 1.$$

This means that the ratio of the energy of the dipole formed by simultaneously detaching opposite-charged droplets in the field $(E_0 + E_*)$ at the instant of their separation to the energy of their surface tension forces is constant; that is, it is independent of the ordinal number of the emission event.

6. From set (16) and (17), it is easy to find analytical expressions for the sizes and charges of the daughter droplets as functions of eccentricity e of the parent drop and distance ν. We have

$$X(e, \nu) = \frac{T^2(e, \nu)w^2}{4A(e_0)B(e_0)(1-e^2)^{2/3}};$$
$$Y(e, \nu) = \frac{T^3(e, \nu)w^2}{8A(e_0)B^2(e_0)(1-e^2)}. \quad (19)$$

The relation between the parent-drop eccentricity e and the distance ν is defined by expression

$$\beta(1-e_0^2)^{1/6}(1-e^2)^{1/3}B(e_0) = 4w^2T^2(e, \nu);$$
$$\beta \equiv r_*/r(1-e_0^2)^{1/6}, \quad (20)$$

derived from (16)–(18). The value of parameter β related to the uncontrolled neck radius r_* (β is considered to be constant during loss of the excess charge by the parent drop) is chosen on the basis of semiphenomenological reasons [11, 18] to be equal $\beta = 0.9$.

From (19) and Fig. 2, one can see that for fixed parameter w^2 and distance ν, the dimensionless sizes and charges of the daughter droplets essentially depend only on the parent-drop eccentricity. In Fig. 3, the dependences $X = X(e)$ and $Y = Y(e)$ calculated using (9a), (16a), (19), and (20) are shown (curves *1*, *2*); it can be seen that sizes X and charges Y of the daughter droplets decrease with decreasing parent-drop eccentricity (as the parent drop volume decreases in the course of losing the polarization charge [8, 18, 19]).

If we use the current radius of the parent drop corresponding to the instant of separation of the next pair of droplets (rather than the initial radius of the parent drop) as a characteristic linear scale to render the radii and charges of the daughter droplets dimensionless, then the radii and charges of the daughter droplets rendered dimensionless in such a way will increase with decreasing parent-drop eccentricity or, which is the same, with increasing ordinal number of a pair of the emitted droplets, which was observed in calculations [18]. Curve *3* In Fig. 3 shows the dependence of the distance ν between the centers of the parent and daughter drops depends on the parent-drop eccentricity at the instant of neck rupture. The dependence was calculated using (9a), (16a), (19), and (20). It can be seen that the dimensionless distance ν between the drops decreases as the parent-drop eccentricity e decreases.

7. An accurate estimate of contributions of various interactions to the total polarization energy of a liquid conductor bounded by a free surface in an external electrostatic field $\mathbf{E}_0$ allows one to obtain additional information about the laws of equilibrium deformation of the conductor in the field. It is found that, in a closed system, spontaneous variations of the shape of a liquid conductor in field $\mathbf{E}_0$ are possible only if they are accompanied by an increase in the polarization dipole moment of the conductor. This means, in particular, that an initially spherical drop in uniform field $\mathbf{E}_0$ will elongate, transforming into a body close to a spheroid. A bubble in a liquid dielectric in the field $\mathbf{E}_0$ may transform into an oblate or prolate spheroid, or retain its spherical shape depending on the extent of the surface mobility of free charges at its surface, and conductivity and permitivity of the liquid (for various laws of polarization dipole moment evolution). A correct consideration of the polarization energy of a drop of a conducting liquid suffering instability with respect to the polar-

ization charge allows one to derive analytical expressions for calculating the sizes and charges of the daughter droplets and is indicative of their initial instability with respect to the intrinsic charge.

REFERENCES

1. L. D. Landau and E. M. Lifshitz, *Course of Theoretical Physics. Vol. 8. Electrodynamics of Continuous Media* (Nauka, Moscow, 1982; Pergamon, New York, 1984).
2. J. A. Stratton, *Electromagnetic Theory* (McGraw-Hill, New York, 1941; Gostekhizdat, Moscow, 1948).
3. W. Smythe, *Static and Dynamic Electricity* (McGraw-Hill, New York, 1950; Innostrannaya Literatura, Moscow, 1954).
4. W. K. H. Panofsky and M. Phillips, *Classical Electricity and Magnetism* (Addison–Wesley, Reading, 1962; Fizmatgiz, Moscow, 1963).
5. I. E. Tamm, *The Foundations of the Theory of Electricity* (Nauka, Moscow, 1976).
6. A. I. Grigor'ev and S. O. Shiryaeva, Élektrokhim. Obrab. Met., No. 4, 44 (1991).
7. L. Enze, J. Phys. D **19** (1), 1 (1986).
8. A. I. Grigor'ev and S. O. Shiryaeva, Izv. Ross. Akad. Nauk, Mekh. Zhidk. Gaza, No. 3, 3 (1994).
9. A. I. Grigor'ev, Zh. Tekh. Fiz. **55**, 1272 (1985) [Sov. Phys. Tech. Phys. **30**, 736 (1985)].
10. A. I. Grigor'ev and O. A. Sinkevich, Izv. Akad. Nauk SSSR, Mekh. Zhidk. Gaza, No. 6, 10 (1985).
11. A. I. Grigor'ev and S. O. Shiryaeva, Zh. Tekh. Fiz. **61** (3), 19 (1991) [Sov. Phys. Tech. Phys. **36**, 258 (1991)].
12. A. I. Grigor'ev, O. A. Grigor'ev, and S. O. Shiryaeva, Zh. Tekh. Fiz. **62** (9), 12 (1992) [Sov. Phys. Tech. Phys. **37**, 904 (1992)].
13. A. I. Grigor'ev, S. O. Shiryaeva, and E. I. Belavina, Zh. Tekh. Fiz. **59** (1), 27 (1989) [Sov. Phys. Tech. Phys. **34**, 602 (1989)].
14. Ch. T. O'Konski and F. E. Harris, J. Phys. Chem. **61**, 1172 (1957).
15. S. Torza, R. G. Cox, and S. G. Mason, in *Rheology of Suspensions* (Mir, Moscow, 1975), p. 285; Philos. Trans. R. Soc. London, Ser. A **69** (1198), 295 (1971).
16. G. Taylor, Proc. R. Soc. London, Ser. A **280**, 383 (1964).
17. A. I. Grigor'ev, Pis'ma Zh. Tekh. Fiz. **24** (24), 36 (1998) [Tech. Phys. Lett. **24**, 962 (1998)].
18. S. O. Shiryaeva and A. I. Grigor'ev, Pis'ma Zh. Tekh. Fiz. **19** (18), 87 (1993) [Tech. Phys. Lett. **19**, 600 (1993)].
19. A. I. Grigor'ev and S. O. Shiryaeva, J. Phys. D **23**, 1361 (1990).
20. S. O. Shiryaeva and A. I. Grigor'ev, Zh. Tekh. Fiz. **65** (2), 11 (1995) [Tech. Phys. **40**, 122 (1995)].
21. V. A. Koromyslov, A. I. Grigor'ev, and S. O. Shiryaeva, Zh. Tekh. Fiz. **68** (8), 31 (1998) [Tech. Phys. **43**, 904 (1998)].

Translated by N. Mende

Technical Physics, Vol. 45, No. 6, 2000, pp. 694–697. Translated from Zhurnal Tekhnicheskoĭ Fiziki, Vol. 70, No. 6, 2000, pp. 27–30.

Breakup of an Uncharged Droplet in an Electrostatic Field

S. I. Shchukin and A. I. Grigor'ev

Yaroslavl State University, Sovietskaya ul. 14, Yaroslavl, 150000 Russia

Received March 10, 1999

Abstract—The breakup of an uncharged electrically conducting liquid dropet placed in a uniform electrostatic field into two daughter droplets caused by strong nonspheroidal deformation is qualitatively analyzed by applying the principle of minimum potential energy under spontaneous virtual variations of the droplet's state. It is shown that the breakup mechanism involves asymmetric mass distribution among the daughter droplets, which are found to be stable with respect to their respective intrinsic charges. © *2000 MAIK "Nauka/Interperiodica".*

INTRODUCTION

Characterization of the instability of uncharged droplets and clusters in intense electric fields is of interest for numerous applications in geophysics, electrospray mass spectrometry, metal liquid-phase epitaxy, and lithography [1–3]. The instability may develop by different scenarios, depending on the amplitude and geometry of the initial droplet deformation; the droplet's size, viscosity, and electrical conductivity; and the intensity and degree of nonuniformity of the external electric field [1–9].

The breakup of a highly charged droplet of a low-viscosity liquid characterized by high conductivity has been analyzed in most detail [1–4, 6, 9]. In this case, a droplet whose charge exceeds the threshold of instability with respect to polarization breaks up into a host of highly charged secondary droplets, which are smaller by two orders of magnitude. A charged or uncharged droplet of a high-viscosity or low-conductivity liquid placed in an intense electrostatic field can break up into a few fragments of comparable size [1, 5, 10]. The latter breakup scenario, which is characteristic of very small droplets of various liquids [3, 11–13], has so far been analyzed incompletely, even though it is of interest for numerous applications. The breakup of a droplet nonspheroidally deformed by an external electric field has not been analyzed at all, despite the fact that some experimental studies of this scenario have been conducted [14]. In this paper, we present a qualitative analysis of the breakup of an uncharged parent droplet into two daughter droplets caused by its nonspheroidal deformation in an external electric field. Our analysis is analogous to that carried out in [10] for a charged droplet that spontaneously breaks up into two fragments through a strong nonspheroidal deformation.

1. Suppose that a spherical droplet of a perfectly conducting liquid of radius R, characterized by a surface tension α breaks up into two daughter droplets as shown in Fig. 1. Assuming that the daughter droplets that form after the liquid bridge of length L is disrupted are close to spheres of radii R_1 and R_2 and their respective charges are $-q$ and q, we express the potential energy U_p of the highly distorted parent droplet shown in Fig. 1b just before the breakup as follows:

$$U_p = \frac{4\pi\alpha R^2(1+x^2)}{(1+x^3)^{2/3}} - \frac{qRE_0(1+x+z\sqrt[3]{1+x^3})}{\sqrt[3]{1+x^3}}$$
$$- \frac{q^2\sqrt[3]{1+x^3}}{(1+x+z\sqrt[3]{1+x^3})R} + \frac{q^2\sqrt[3]{1+x^3}}{2R}\left(1+\frac{1}{x}\right) \qquad (1)$$
$$- \frac{1}{2}E_0^2R^3 - \frac{R^3E_0^2x^3}{(1+x^3)(1+x+z\sqrt[3]{1+x^3})},$$

where $x = R_2/R_1$ and $z = L/R$.

The first term in (1) represents the energy of surface tension; the second term, the energy of a dipole that consists of two daughter droplets and has the moment $q(R_1 + R_2 + L)$ in a field of intensity $\mathbf{E}_0$; the third one, the energy of interaction between two point charges separated by the distance $(R_1 + R_2 + L)$ in the absence of an external electric field; the fourth one, the intrinsic electrostatic energy of droplets of radii R_1 and R_2 whose charges are q and $-q$, respectively; the fifth one, the energy of the dipoles induced by the field $\mathbf{E}_0$ in each

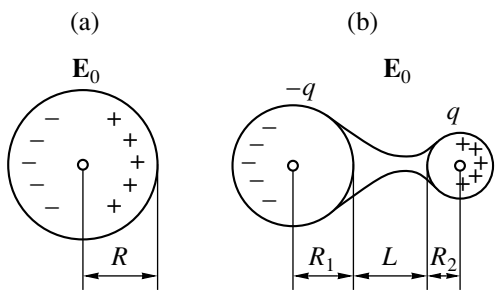

Fig. 1. Deformation of a droplet that breaks up into two fragments of comparable size.

1063-7842/00/4506-0694$20.00 © 2000 MAIK "Nauka/Interperiodica"

daughter droplet; and the sixth one, the energy of interaction between dipoles separated by the distance ($R_1 + R_2 + L$), with dipole moments equal to those induced by the field $\mathbf{E}_0$ in the spherical daughter droplets.

Normalizing U_p to the total potential energy of the spherical parent droplet placed in a field of intensity $\mathbf{E}_0$,

$$U_s = 4\pi\alpha R^2 - \frac{1}{2}R^3E_0^2,$$

we rewrite (1) as

$$U = \left\{\frac{1+x^2}{(1+x^3)^{2/3}} - \frac{(1+x+z\sqrt[3]{1+x^3})y}{\sqrt[3]{1+x^3}}\sqrt{\frac{w}{\pi}}\right.$$

$$-\sqrt[3]{1+x^3}\left(\frac{1}{2}+\frac{1}{2x}-\frac{1}{(1+x+z\sqrt[3]{1+x^3})}\right)y^2 - \frac{w}{8\pi} \quad (2)$$

$$\left.-\frac{x^3w}{4(1+x^3)(1+x+z\sqrt[3]{1+x^3})^3\pi}\right\}\left(1-\frac{w}{8\pi}\right)^{-1},$$

where $w = E_0^2 R\alpha^{-1}$ is the Taylor parameter of the parent droplet, which characterizes its instability with respect to polarization (developing when $w \geq 2.62$ [2] and resulting in the loss of polarized charge through ejection of a host of highly charged minuscule droplets), and $y = q(4\pi\alpha R^3)^{-1/2}$ is the normalized charge of a daughter droplet.

Figure 2 illustrates the general form of $U = U(x, y)$ for w = const and z = const and demonstrates that there exist combinations of w, x, y, and z for which the potential energy of a droplet distorted as in Fig. 1 is lower than that of the parent droplet ($U < 1$) and, therefore, spontaneous virtual transitions from its initial state to the final state can occur.

Equating the normalized energy given by (2) to unity and solving the equation $U = 1$ with constant z and w, one can determine the locus of $\{y, x\}$ at which the total potential energy of the resulting two-droplet system is lower than that of the parent droplet (i.e., the breakup of a droplet into two is unlikely to occur as illustrated by Fig. 1 for energy reasons). Figure 3 shows the graphs of $y = y(x)$ obtained for $w = 0.8$, 1.6, and 2.4 (curves *1*) with *a*, *b*, and *c* corresponding to the dimensionless liquid-bridge lengths $z = 0.1$, 0.2, and 0.4. The domains encompassed by the curves are the ranges of admissible daughter-droplet size and charge. One trend exposed by Fig. 3 is that the breakup of a droplet into two through the deformation depicted in Fig. 1 can occur when the Taylor parameter w is well below the threshold value for its instability with respect to polarization in the case of a purely spheroidal deformation (2.62, according to [2]). This is explained by the fact that the deformation illustrated by Fig. 1 can occur at arbitrarily small q and E_0.

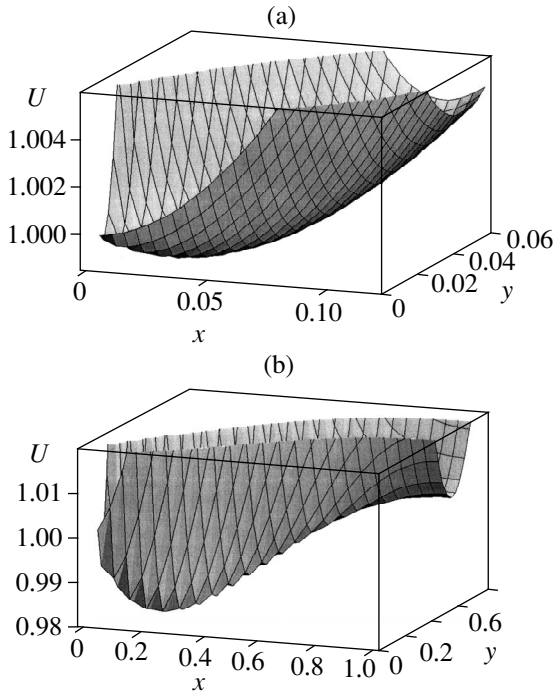

Fig. 2. Total potential energy U of a disintegrating droplet as a function of the diameter ratio x and normalized charge y of the daughter droplets: (a) $w = 0.8$, $z = 0.1$ and (b) $w = 2.4$, $z = 0.4$.

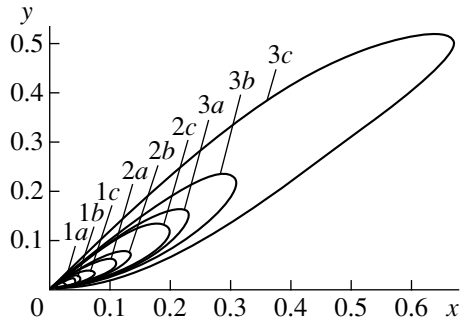

Fig. 3. Ranges of admissible values of the diameter ratio x and normalized charge y of the daughter droplets.

2. As noted above, a spontaneous droplet breakup induced by $\mathbf{E}_0$ proceeds in such a manner that the energy of the resulting system in Fig. 1b (treated as closed) is minimal with respect to x and y while w and z are held constant. The necessary conditions for an extremum have the form

$$\frac{\partial U}{\partial x} = 0, \quad \frac{\partial U}{\partial y} = 0.$$

They lead to the following set of equations for x and y corresponding to an extremal state:

$$\frac{\partial U}{\partial x} = \left\{\frac{3wx^2}{4\pi gh^3}\left(\frac{x^3}{g}+\frac{xr}{h}-1\right)+\frac{2x}{g^{2/3}}\left[1-\frac{(1+x^2)x}{g}\right]\right.$$

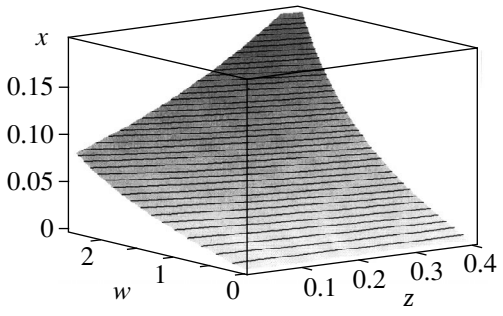

Fig. 4. Most probable diameter ratio x for daughter droplets as a function of the parent-droplet Taylor parameter w and liquid-bridge length z.

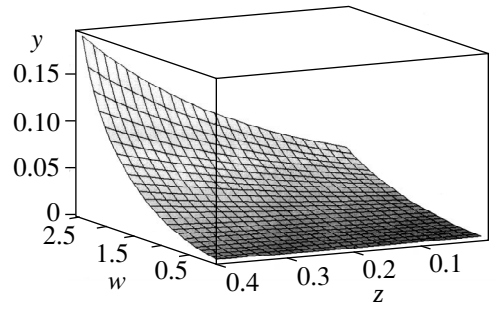

Fig. 5. The most probable daughter-droplet charge y as a function of the parent-droplet Taylor parameter w and liquid-bridge length z.

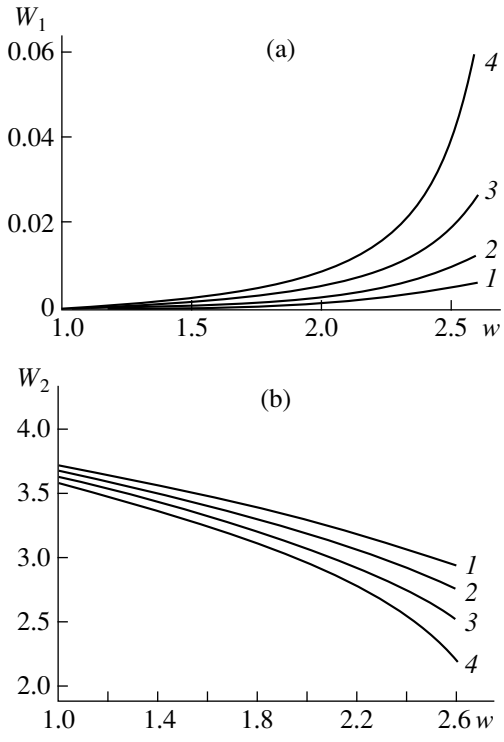

Fig. 6. The Rayleigh parameters of the daughter droplets as functions of the Taylor parameter w of the parent droplet: (a) larger droplet; (b) smaller droplet.

$$-\frac{y}{2g^{1/3}}\sqrt{\frac{w}{\pi}}\left(r-\frac{hx^2}{g}\right)+\frac{x^2y^2}{g^{2/3}}\left(\frac{1}{2}+\frac{1}{2x}-\frac{1}{h}\right) \qquad (3)$$

$$+g^{1/3}\left(\frac{r}{h^2}-\frac{1}{2x^2}\right)y^2\Bigg\}\left(1-\frac{w}{8\pi}\right)^{-1}=0;$$

$$\frac{\partial U}{\partial y}=\left\{2g^{1/3}\left(\frac{1}{2}+\frac{1}{2x}-\frac{1}{h}\right)y-\frac{h}{2g^{1/3}}\sqrt{\frac{w}{\pi}}\right\}$$

$$\times\left(1-\frac{w}{8\pi}\right)^{-1}=0, \qquad (4)$$

$$g\equiv 1+x^3;\quad h\equiv 1+x+zg^{1/3};\quad r\equiv 1+\frac{zx^2}{g^{2/3}}.$$

Solutions to the set of equations (3) and (4) are plotted in Figs. 4 and 5 as graphs of $x = x(w, z)$ and $y = y(w, z)$. It quite clear (see also Fig. 3) that the breakup is asymmetric in the general case, which agrees with experimental results [14]. The functions $x = x(w, z)$ and $y = y(w, z)$ are obviously monotonic with respect to z and w. With increasing Taylor parameter w, both x and y increase. Moreover, the breakup tends to become symmetric: the parent droplet splits in two daughter droplets of nearly equal size (see Fig. 3).

Figures 6a and 6b show the Rayleigh parameters ($W_1 \equiv q^2/4\pi\alpha R_1^3$) and ($W_2 \equiv q^2/4\pi\alpha R_2^3$) of the larger and smaller droplets, respectively, as functions of w obtained by solving (3) and (4) numerically. Here, curves *1–4* correspond to $z = 0.1$, 0.2, 0.3, and 0.4, respectively. The Rayleigh parameter characterizes the stability of a droplet with respect to its intrinsic charge: a droplet is unstable when $W \geq 4$ [3, 15]. According to Fig. 6, each charged droplet resulting from the breakup of an uncharged droplet in an intense electrostatic field $\mathbf{E}_0$ is stable with respect to polarization of its intrinsic charge, but the smaller one is very close to the instability threshold, and its breakup through the Rayleigh mechanism can be caused by a sufficiently large spheroidal deformation as observed in [3, 16, 17].

It should be noted that the relative size x and charge y calculated for daughter droplets resulting from a deformation illustrated by Fig. 1 are consistent with the system's extremal energy only. They are not related to the self-consistent evolution of a droplet distorted by a field $\mathbf{E}_0$, in contrast to the case of droplet breakup through the Taylor mechanism [11]. We leave the mechanism of droplet deformation illustrated by Fig. 1b outside the scope of the present analysis, assuming that the daughter droplets acquire their charges through polarization. If the deformation is supposed to be induced by external forces of nonelectrical nature, then the analysis presented above makes sense. However, the analysis becomes incorrect if the deformation discussed here is attributed to the field $\mathbf{E}_0$,

because the daughter-droplet charge q must tend to zero with the external field intensity $\mathbf{E}_0$. Unlike the present qualitative treatment, an analysis of the breakup of a droplet severely distorted by a weak electric field $\mathbf{E}_0$ as shown in Fig. 1, when one resultant droplet is much smaller than the other, should take into account the interaction between polarization-induced charges in order to yield the correct asymptotic limit $q \longrightarrow 0$ as $E_0 \longrightarrow 0$.

CONCLUSIONS

The analysis presented here shows that the strength of a uniform electrostatic field $\mathbf{E}_0$ required to break a droplet through a severe nonspheroidal deformation can be much weaker as compared to the Taylor threshold value for a spheroidally distorted droplet and depends on the initial nonspheroidal deformation. The parent-droplet mass is asymmetrically distributed among the daughter droplets, which agrees with experimental results [14]. However, the breakup tends to become symmetric as the Taylor parameter w of the parent droplet and the distance z between the centers of the daughter droplets at the moment of breakup increase. The intrinsic charges of the daughter droplets do not exceed the Rayleigh threshold values.

REFERENCES

1. W. A. Macky, Proc. R. Soc. London, Ser. A **133** (A822), 565 (1931).
2. G. Taylor, Proc. R. Soc. London, Ser. A **280**, 565 (1964).
3. A. I. Grigor'ev and O. A. Sinkevich, Izv. Akad. Nauk SSSR, Mekh. Zhidk. Gaza, No. 6, 10 (1985).
4. J. N. Elgin, Phys. Lett. A **110**, 441 (1985).
5. J. D. Sherwood, J. Fluid Mech. **188**, 133 (1988).
6. A. I. Grigor'ev and S. O. Shiryaeva, J. Phys. D **23**, 1361 (1990).
7. S. O. Shiryaeva and A. I. Grigor'ev, Zh. Tekh. Fiz. **62** (3), 35 (1992) [Sov. Phys. Tech. Phys. **37**, 254 (1992)].
8. S. O. Shiryaeva and A. I. Grigor'ev, Zh. Tekh. Fiz. **62** (11), 49 (1992) [Sov. Phys. Tech. Phys. **37**, 1071 (1992)].
9. S. O. Shiryaeva and A. I. Grigor'ev, Pis'ma Zh. Tekh. Fiz. **29** (18), 87 (1992).
10. V. A. Koromyslov, A. I. Grigor'ev, and S. O. Shiryaeva, Zh. Tekh. Fiz. **68** (8), 31 (1998) [Tech. Phys. **43**, 904 (1998)].
11. S. O. Shiryaeva and A. I. Grigor'ev, Pis'ma Zh. Tekh. Fiz. **21** (9), 67 (1995) [Tech. Phys. Lett. **21**, 346 (1995)].
12. S. O. Shiryaeva, O. A. Grigor'ev, M. I. Munichev, and A. I. Grigor'ev, Zh. Tekh. Fiz. **66** (10), 47 (1996) [Tech. Phys. **41**, 997 (1996)].
13. S. O. Shiryaeva, A. I. Grigor'ev, and D. F. Belonozhko, Pis'ma Zh. Tekh. Fiz. **23** (16), 32 (1997) [Tech. Phys. Lett. **23**, 330 (1997)].
14. J. R. Adam, N. R. Lindblad, and C. D. Hendrics, J. Appl. Phys. **39**, 5173 (1968).
15. Rayleigh (Lord Strett), Philos. Mag. **14**, 182 (1882).
16. S. I. Shchukin and A. I. Grigor'ev, Pis'ma Zh. Tekh. Fiz. **24** (7), 73 (1998) [Tech. Phys. Lett. **24**, 277 (1998)].
17. S. I. Shchukin and A. I. Grigor'ev, Zh. Tekh. Fiz. **68** (11), 48 (1998) [Tech. Phys. **43**, 1314 (1998)].

Translated by A. S. Betev

Technical Physics, Vol. 45, No. 6, 2000, pp. 698–703. Translated from Zhurnal Tekhnicheskoĭ Fiziki, Vol. 70, No. 6, 2000, pp. 31–36.

GASES AND LIQUIDS

Effect of Surface-Tension Relaxation on the Spectrum of Motions of a Liquid with Charged Free Surface

S. O. Shiryaeva and O. A. Grigor'ev

Yaroslavl State University, Sovietskaya ul. 14, Yaroslavl, 150000 Russia

Received March 23, 1999

Abstract—The spectrum of capillary–relaxational motions of a charged free liquid surface is analyzed. The analysis takes into account the effect of surface-tension relaxation and the existence of two relaxation times due to different physical mechanisms. Each relaxation mechanism is associated with certain liquid wave motions. Motions due to different relaxation processes interact with each other and with capillary–gravity waves through nonlinear mechanisms. *© 2000 MAIK "Nauka/Interperiodica".*

Relaxation of surface tension, also known as dynamic surface tension, manifests itself by the dependence of surface tension on the time scale of surface deformation at frequencies $10^{-9} \le \omega \le 10^{9}$ Hz. Being an essentially dispersive phenomenon, it is of interest for a variety of applications [1–5]. For example, this effect plays an important role in electrically driven liquid atomization, which is characterized by time scales shorter than 0.01 s [6, 7]. However, current research is mainly focused on measurements of the characteristics of dynamic surface tension for specific liquids under various external conditions, whereas studies of its physical nature remain scarce and are restricted to qualitative characterization. In particular, the physical mechanism of interactions between capillary motions and dispersive motions (due to the dependence of surface tension on the perturbation time scale) is poorly understood even though some work is in progress (see [4–10] and references cited therein).

The effect of relaxation of surface tension on the spectrum of liquid motions can be described by introducing a complex surface tension σ as given by Maxwell's formula [1, 5]

$$\sigma = \sigma_\infty - \sigma_*(1 - i\omega\tau)^{-1} = \sigma_0 - i\omega\tau\sigma_*(1 - i\omega\tau)^{-1};$$

$$\sigma_* = \sigma_\infty - \sigma_0,$$

which is the Fourier transform of the simplest time-dependence of the surface tension of a perturbed free liquid surface,

$$\sigma(t) = \sigma_0 + \sigma_* \exp(-t/\tau).$$

Here, σ_0 is the surface tension at zero frequency (i.e., when the liquid is in equilibrium), σ_∞ is the surface tension at high frequencies (for $\omega\tau \gg 1$), τ is the surface-tension relaxation time (i.e., the characteristic time of formation of a double electric layer at the liquid surface), ω is the complex frequency in the exponential time dependence of capillary-motion amplitudes of the form $\zeta(t) \sim \exp(i\omega t)$, and i is the imaginary unit.

In this paper, we analyze the dynamic surface tension of a liquid characterized by several surface-tension relaxation times, keeping in mind the fact that the physicochemical nature of this phenomenon is explained by the existence of a double electric layer at the liquid surface, which can develop through physically different mechanisms. (These mechanisms include the effect of a free surface on the orientation of molecular dipoles, electrostatic interactions between bound and free charged liquid particles near the surface, diffusive chaotization of the ordered liquid structure near the surface, and effects due to the presence of surfactants and their concentration).

1. Suppose that the surface tension $\sigma(t)$ is characterized by two relaxation times τ_1 and τ_2:

$$\sigma(t) = \sigma_0 + \sigma_1 \exp(-t/\tau_1) + \sigma_2 \exp(-t/\tau_2),$$

where σ_0 is the equilibrium surface tension and σ_1 and σ_2 are additional contributions to the surface tension due to different relaxation mechanisms that manifest themselves when the surface is perturbed.

Variations of surface pressure and curvature are related by the equation

$$\Delta p = \int_{-\infty}^{t} \sigma(t - \tau)\frac{dU(\tau)}{d\tau}d\tau.$$

where $U(\tau)$ is the surface curvature [1, 11], which entails a relation between their Fourier transforms:

$$\Delta p(\omega) = \left(\sigma_0 + \sigma_1\frac{-i\omega\tau_1}{1 - i\omega\tau_1} + \sigma_2\frac{-i\omega\tau_2}{1 - i\omega\tau_2}\right)U(\omega).$$

Hence, one obtains the required expression for a complex surface tension involving two relaxation

times:

$$\sigma(\omega) = \sigma_0 + \sigma_1\frac{-i\omega\tau_1}{1-i\omega\tau_1} + \sigma_2\frac{-i\omega\tau_2}{1-i\omega\tau_2}. \quad (1)$$

2. Consider an infinite plane surface of a viscous, incompressible, perfectly conducting liquid carrying a charge of surface density $\varkappa$. The liquid occupies the half-space $z < 0$ in a gravitational field characterized by acceleration $\mathbf{g} \| -\mathbf{n}_z$ ($\mathbf{n}_z$ is the unit vector in the z-direction). In the Cartesian coordinate system, the unperturbed free liquid surface is described by the equation $z = 0$. We denote the surface tension, kinematic viscosity, and density of the liquid by σ, ν, and ρ, respectively.

The capillary motions of a liquid with a charged free surface are described by the linearized Navier–Stokes equations and the continuity equation for an incompressible fluid,

$$\frac{\partial U}{\partial t} = -\frac{1}{\rho}\nabla P + \nu\Delta\mathbf{U} + \mathbf{g}, \quad \nabla\cdot\mathbf{U} = 0, \quad (2)$$

supplemented with the boundary conditions

$$\frac{dF}{dt} = \frac{\partial F}{\partial t} + \mathbf{U}\cdot\nabla F = 0, \quad (3)$$

$$\boldsymbol{\tau}(\mathbf{n}\cdot\nabla)\mathbf{U} + \mathbf{n}(\boldsymbol{\tau}\cdot\nabla)\mathbf{U} = 0, \quad (4)$$

$$P - 2\rho\nu\mathbf{n}(\mathbf{n}\cdot\nabla)\mathbf{U} + \sigma\frac{\partial^2\zeta}{\partial x^2} + 4\pi\varkappa^2 k\zeta = 0, \quad (5)$$

which are set on the free surface described by the equation

$$F(\mathbf{r}, t) \equiv z - \zeta(x, t) = 0.$$

In these equations, $\mathbf{U}(\mathbf{r}, t)$ is the liquid velocity field associated with capillary motions of the free surface, $P(\mathbf{r}, t)$ is the pressure induced in the liquid by the velocity field $\mathbf{U}(\mathbf{r}, t)$, k is the wavenumber, and $\boldsymbol{\tau}$ and $\mathbf{n}$ are the unit vectors tangential and normal to the free surface, the third term in (5) is the pressure induced by surface-tension forces below an initially plane surface distorted by a capillary wave motion, and the last term in (5) represents the electrical pressure on the charged free liquid surface written in the linear approximation with respect to the surface-perturbation amplitude $\zeta(x, t) = A\exp(ikx - i\omega t)$ [12]. The fields of liquid velocity $\mathbf{U}(\mathbf{r}, t)$ and pressure $P(\mathbf{r}, t)$ are small quantities on the order of ζ.

The set of equations (2) supplemented with boundary conditions (3)–(5) and expression (1) is the mathematical formulation of the problem to be solved.

By the Helmholtz theorem, the velocity field in problem (1)–(5) should be sought as the sum of potential and solenoidal components (see [13]),

$$U_x(x, z, t) = (ikB\exp(kz) - lC\exp(lz))\exp(ikx - i\omega t),$$
$$U_z(x, z, t) = (kB\exp(kz) + ikC\exp(lz))\exp(ikx - i\omega t), \quad (6)$$
$$l^2 = k^2 - i\omega\nu^{-1},$$

where A, B, and C are constant coefficients and l^{-1} is the length scale of the spatial variation of the solenoidal velocity component.

Substituting (6) into (2)–(5), repeating the analysis performed in [13] to derive the dispersion equation for capillary–gravity waves in a viscous fluid, and assuming that σ is given by (1), one readily obtains a dispersion equation for capillary–gravity waves and the relaxational waves induced by dynamic surface tension. In terms of the dimensionless quantities

$$y = \frac{\omega}{\nu k^2};\ \alpha = \frac{\omega_0}{\nu k^2},\ \beta_1 = \sigma_1/\rho\nu^2 k,\ \beta_2 = \sigma_2/\rho\nu^2 k,$$
$$\gamma_1 = \nu k^2\tau_1,\ \gamma_2 = \nu k^2\tau_2,$$
$$\omega_0^2 = \frac{k}{\rho}(g\rho + \sigma_0 k^2 - 4\pi k\varkappa^2),$$

the dispersion equation is written as

$$(1 - i\gamma_1 y)(1 - i\gamma_2 y)([2 - iy]^2 + \alpha^2 - 4\sqrt{1 - iy}) - iy(\beta_1\gamma_1 + \beta_2\gamma_2) + y^2\gamma_1\gamma_2(\beta_1 + \beta_2) = 0. \quad (7)$$

3. Note that the dispersion equation to be analyzed is a transcendental one. We can eliminate the radical by isolating it and squaring the resulting equation (7). Then, we have an algebraic equation of the eighth degree for the complex variable y. It is clear that not all of its eight roots are physically meaningful, because equation (7) contains a radical and is therefore defined on a two-sheeted Riemann surface. Physical branches of the dispersion equation should be sought on the upper sheet of the Riemann surface, which corresponds to the positive value of the radical in (7).

The solutions to the dispersion equation corresponding to the negative value of the radical in (7) are physically meaningless, because, according to (6), the radical is the dimensionless ratio l/k (the ratio of the wavelength k^{-1} to the length scale l^{-1} of the solenoidal velocity field), which cannot be negative.

Figures 1–7 show the imaginary and real parts of the dimensionless complex frequency, $\mathrm{Im}y(\alpha^2)$ and $\mathrm{Re}y(\alpha^2)$, which were calculated numerically by solving (7) for constant values of the parameters γ_1, γ_2, β_1, and β_2. In these figures, branches *1–3* correspond to capillary–gravity wave motions of the liquid and branches *4* and *5* represent the relaxational waves associated with the time dependence of surface tension and character-

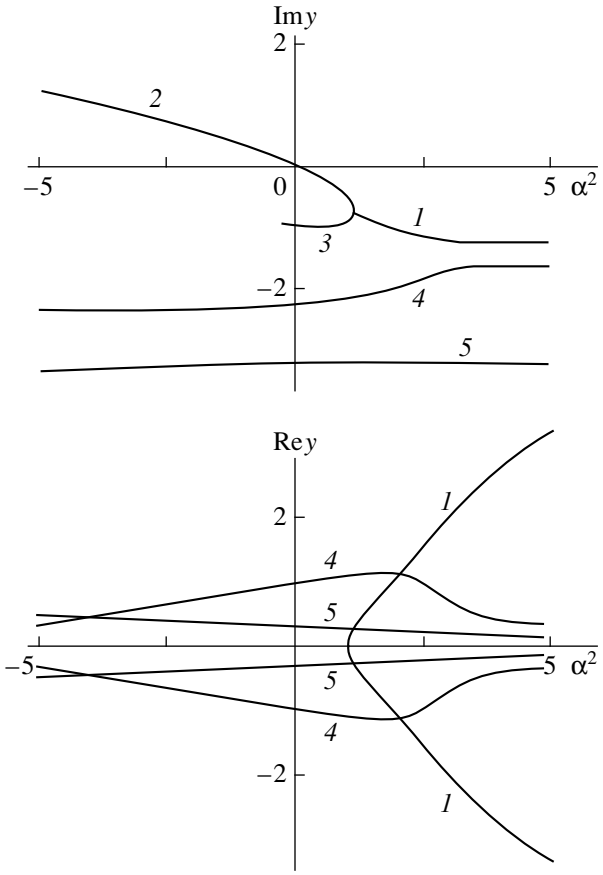

Fig. 1. Imaginary and real parts of the dimensionless frequency y as a function of the parameter α^2 characterizing pressure balance on a free liquid surface at $\beta_1 = 1$, $\gamma_1 = 0.5$, $\beta_2 = 0.5$, and $\gamma_2 = 0.3$.

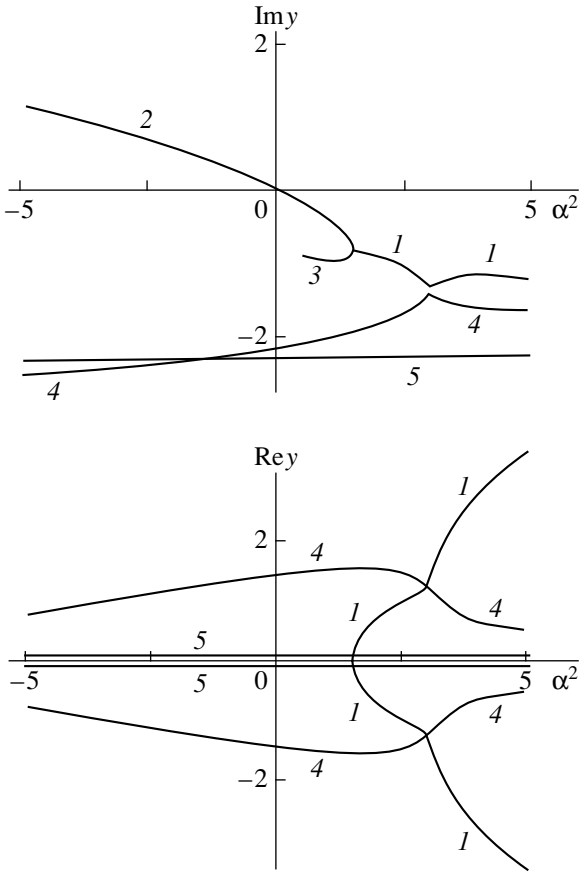

Fig. 2. Same as Fig. 1, with $\gamma_2 = 0.43$.

ized by the time scales τ_2 and τ_1, respectively. Branches *6–9* correspond to the mixed capillary–relaxational waves generated as a result of interaction between capillary–gravity and relaxational waves. The portion of branch *2* lying in the left half-plane (at $\alpha^2 < 0$) determines the Tonks–Frenkel instability increment.

Our calculations show that each of the two relaxation processes described by (1) is associated with a corresponding spectrum of capillary liquid motions qualitatively similar to capillary motions of a free surface. The liquid motions associated with different relaxation mechanisms interact with each other and with the capillary–gravity motions of the free liquid surface. These interactions manifest themselves in the mixed motions corresponding to certain combinations of the parameters γ_i and β_j (branches *6–9* in Figs. 3–7). Figures 1–7 are designed to illustrate numerical results by exposing the interactions of relaxational motions with capillary waves and with each other.

Figures 1–4 correspond to $\gamma_1 = 0.5$, $\beta_1 = 1$, $\beta_2 = 0.5$, and $0.3 \le \gamma_2 \le 0.65$ and illustrate the interaction between the liquid motion associated with the relaxation process denoted by subscript 2 (branch *4*) and the capillary–gravity motions of the free surface (branches *1–3*). When $0.43 \le \gamma_2 \le 0.44$, the interaction between branches *1* and *4* gives rise to the mixed motions represented by branches *6* and *7*. It is interesting to note that the frequencies and decrements of the motion denoted by subscript 1 and represented by branch *5* are also modified by this interaction.

With further increase in γ_2 (see Figs. 5–7), branches *5–7* are distorted. The mixed capillary–relaxational branch *7* and the "first" relaxational branch *5* join together at $0.93 \le \gamma_2 \le 0.94$, transforming into new capillary–relaxational branches *8* and *9*. Note that both purely relaxational and capillary–relaxational wave motions exist at both positive and negative values of α^2, whereas capillary–gravity waves exist only at $\alpha^2 > 0$.

Figures 1–7 demonstrate that the decrements of both relaxational motions decrease with increasing γ_2. Over a greater part of the α^2 domain, the decrements of both purely relaxational and mixed capillary–relaxational waves are close to—or even higher than—the corresponding frequencies (particularly at $\alpha^2 < 0$). Therefore, one should be cautious in interpreting the relax-

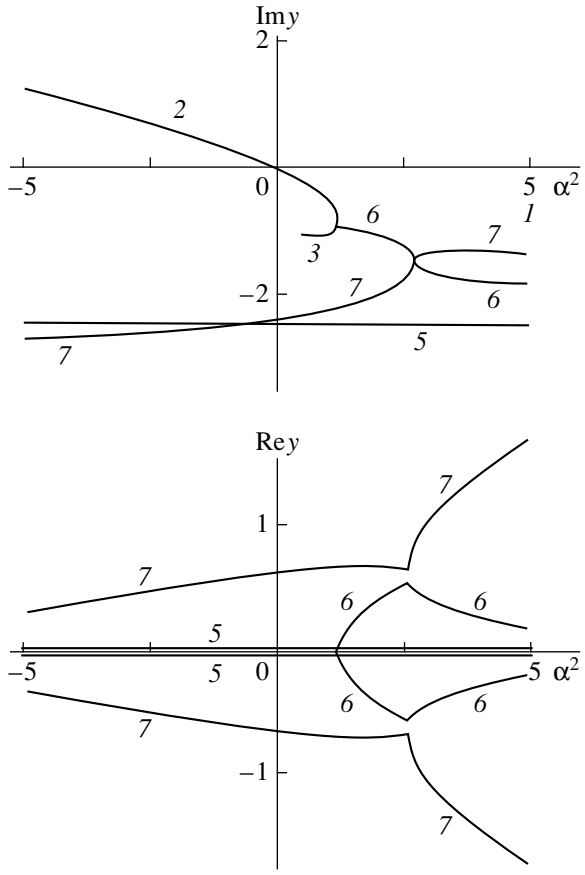

Fig. 3. $\gamma_2 = 0.44$.

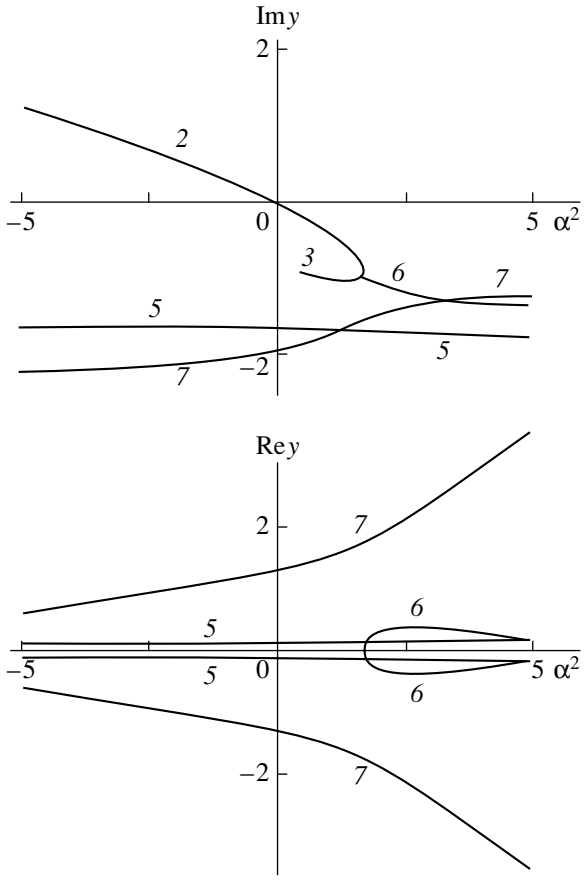

Fig. 4. $\gamma_2 = 0.65$.

ational modes as "wave" motions in view of their substantial decay over a single period. The *1–2–3* bifurcation point of the capillary–gravity motions moves rightwards as γ_2 is increased (and wave frequencies decrease). According to [14], this means that the spectrum of physically observable waves contracts at its short-wavelength boundary.

The quantitative change in the frequencies of relaxational wave motions and mixed capillary–relaxational waves associated with increasing γ_2 is insignificant, whereas their qualitative dependence on α^2 may vary in quite a complicated manner.

Our numerical analysis shows that the interactions of the two relaxational motions with each other and with capillary motions cannot be reduced to simple superpositions of the corresponding branches of the dispersion equation; rather, they involve distortions, mergers, and reconnections and result in new branches. These changes could be expected to occur, since equation (7) combines different relaxation processes in a multiplicative, rather than additive, manner. Note that the interactions involve only waves (as described by branches of the dispersion equation), whereas aperiodic motions do not interact with waves. In any event, an interaction takes place when the frequencies and decrements of certain waves are equal (i.e., when branches representing different waves intersect). After the interacting branches have reconnected and transformed into those corresponding to mixed motions, the newly formed branches diverge with a further increase in γ_2. As they diverge, the frequency of one mixed motion increases while its decrement decreases, and the frequency of the other decreases while its decrement increases, so that the latter can be only formally interpreted as a wave motion.

A numerical analysis shows that the diagrams of capillary and dispersive waves characterized by equal relaxation times are qualitatively similar in structure: each contains a single branch describing a decaying wave that exists on a semi-infinite interval of α^2 and two branches representing decaying motions, one of which disappears as it goes to the other sheet of the Riemann surface at certain values of (α^2, γ, and β). There exists another aperiodic branch on a semi-infinite interval of α^2. Analyzing numerically the effect of surface-tension relaxation on the Tonks–Frenkel instability, we found that its increment decreases by one-tenth of its value as the relaxation time τ decreases by an order of magnitude. The increment strongly depends only on the

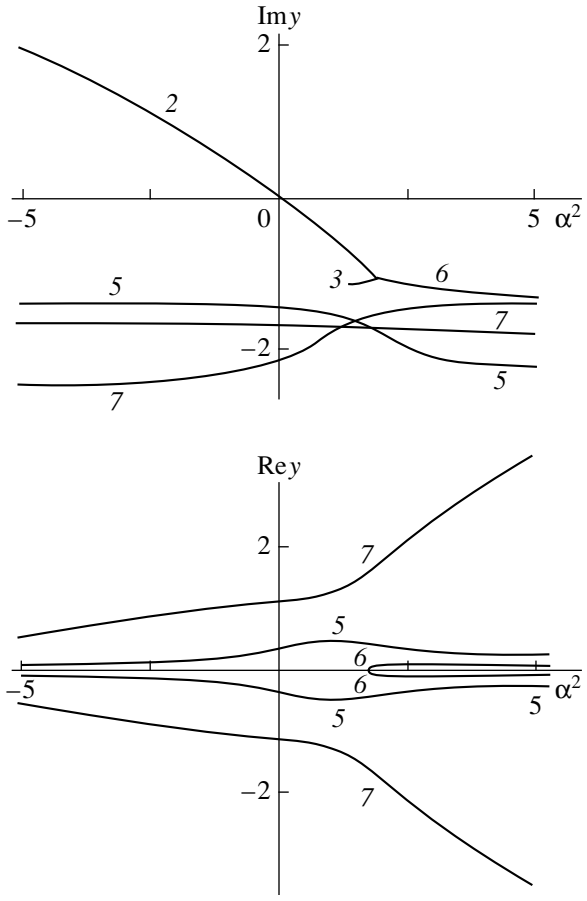

Fig. 5. $\gamma_2 = 0.8$.

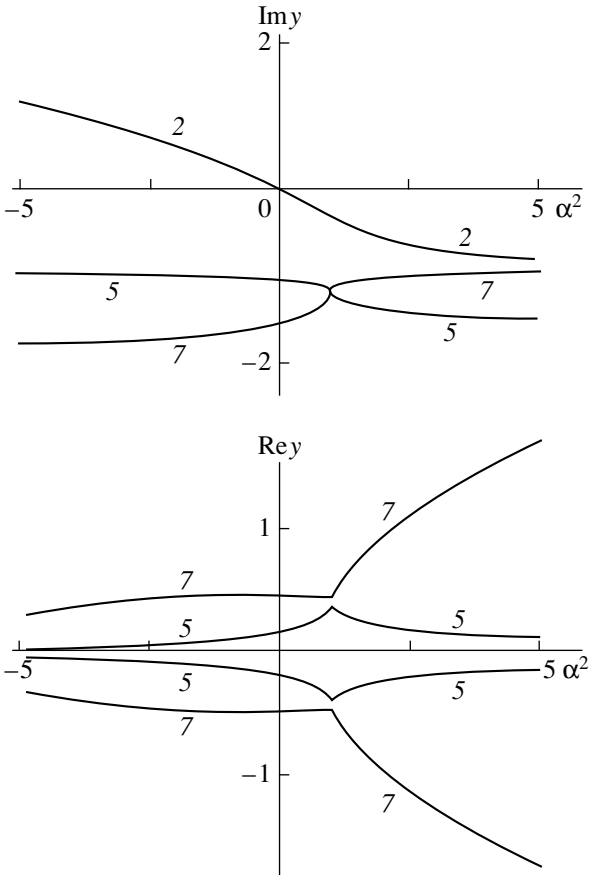

Fig. 6. $\gamma_2 = 0.93$.

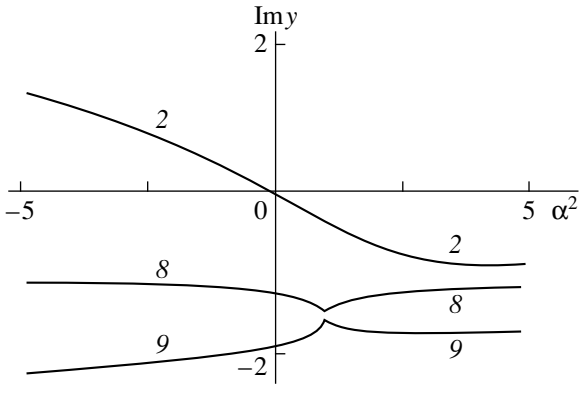

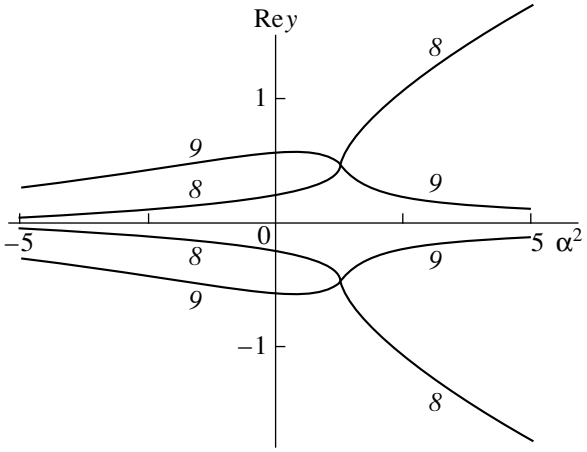

Fig. 7. $\gamma_2 = 0.94$.

extent of the surface-charge supercriticality, rapidly increasing with it.

In summary, we note that the spectrum of capillary–relaxational motions of a liquid with a charged free surface characterized by two physically different surface-tension relaxation times is strongly affected by interactions between capillary–gravity and relaxational wave motions. Motions due to different relaxation processes interact with each other and with capillary–gravity waves through nonlinear mechanisms. An increase in the relaxation time of a charged free surface results in an insignificant decrease in the Tonks–Frenkel instability increment.

In experimental studies of surface-tension relaxation, it should be kept in mind that the relaxation may involve several time scales and the detected waves may

be attributed to mixed wave processes resulting from interactions between capillary–gravity waves and at least one relaxational wave motion, rather than to purely relaxational waves. Therefore, measurements should span several ranges of physical parameters of the system, and special attention should be given to rapidly decaying wave motions, which may be associated with relaxation phenomena. To identify different relaxation processes in surface-tension dynamics, one may analyze their temperature-dependent behavior: for example, surfactants are characterized by quite a substantial temperature dependence of solubility and concentration, whereas the diffusive contribution to the formation of a double electric layer depends on temperature only through the weakly temperature-dependent transport coefficients [15].

REFERENCES

1. Yu. A. Bykovskiĭ, É. A. Manykin, P. P. Poluéktov, *et al.*, Zh. Tekh. Fiz. **46**, 2211 (1976) [Sov. Phys. Tech. Phys. **21**, 1302 (1976)].
2. B. A. Pastukhov, S. B. Pasynkov, V. V. Khlynov, *et al.*, Rasplavy **1** (3), 63.
3. A. Bonfillon, J. Colloid Interface Sci. **164** (2), 497 (1994).
4. O. A. Grigor'ev and S. O. Shiryaeva, Izv. Ross. Akad. Nauk, Mekh. Zhidk. Gaza, No. 1, 98 (1996).
5. G. A. Levacheva, É. A. Manykin, and P. P. Poluéktov, Izv. Akad. Nauk. SSSR, Mekh. Zhidk. Gaza, No. 2, 17 (1985).
6. S. O. Shiryaeva and A. I. Grigor'ev, J. Electrost. **34**, 51 (1995).
7. S. O. Shiryaeva and A. I. Grigor'ev, Zh. Tekh. Fiz. **64** (3), 13 (1994) [Tech. Phys. **39**, 229 (1994)].
8. *Monodispersion of Substances: Principles and Applications*, Ed. by V. A. Grigor'ev (Énergoatomizdat, Moscow, 1991).
9. O. A. Grigor'ev, Pis'ma Zh. Tekh. Fiz. **20** (1), 15 (1994) [Tech. Phys. Lett. **20**, 974 (1994)].
10. S. O. Shiryaeva, O. A. Grigor'ev, and A. I. Grigor'ev, Zh. Tekh. Fiz. **66** (10), 31 (1996) [Tech. Phys. **41**, 989 (1996)].
11. R. Christensen, *Theory of Viscoelasticity* (Academic, New York, 1971; Mir, Moscow, 1974).
12. L. D. Landau and E. M. Lifshitz, *Course of Theoretical Physics. Vol. 8. Electrodynamics of Continuous Media* (Nauka, Moscow, 1982; Pergamon, New York, 1984).
13. V. G. Levich, *Physicochemical Hydrodynamics* (Fizmatgiz, Moscow, 1959).
14. P. N. Antonyuk, Dokl. Akad. Nauk SSSR **286** (6), 1324 (1986) [Sov. Phys. Dokl. **31**, 102 (1986)].
15. R. C. Reid and T. K. Sherwood, *The Properties of Glasses and Liquids* (McGraw-Hill, New York, 1966; Khimiya, Leningrad, 1971).

Translated by A. S. Betev

Technical Physics, Vol. 45, No. 6, 2000, pp. 704–709. Translated from Zhurnal Tekhnicheskoĭ Fiziki, Vol. 70, No. 6, 2000, pp. 37–42.

Dispersion of a Charged Gas Bubble in a Liquid Dielectric in an Electric Field

A. N. Zharov, S. O. Shiryaeva, and A. I. Grigor'ev

Yaroslavl State University, Sovietskaya ul. 14, Yaroslavl, 150000 Russia

Received April 24, 1999

Abstract—Onsager's principle of minimum energy dissipation in nonequilibrium processes is applied to calculate the characteristics of a surface-conducting charged bubble breakup in a liquid dielectric in a uniform electrostatic field. The domains of physical parameters are determined in which daughter bubbles are ejected from both apexes and are not ejected from only one apex. © *2000 MAIK "Nauka/Interperiodica".*

INTRODUCTION

Fluid dispersion in external electrostatic fields, as well as equilibrium geometry and stability of charged drops and bubbles in dielectric liquids, are of interest for applications in technical physics, geophysics, and engineering [1–3]. Nevertheless, many problems concerning the stability of bubbles in dielectric liquids with respect to their intrinsic charge or polarization have been studied very superficially, although some experimental [3, 4] and theoretical [3, 5–8] research has been conducted in this line. However, the most interesting problem raised in the experimental work reported in [4], namely, bubble dispersion in a liquid dielectric by external electrostatic fields, has remained almost unstudied theoretically, although this effect, which leads to a rapid increase in both dispersion of bubbles and the area of their contact with the ambient liquid, is of certain interest. The goal of this paper is to fill this gap.

1. Suppose that, in a liquid dielectric characterized by a dielectric constant ε, density ρ, and surface tension σ, there is a speherical bubble of initial radius R_0 carrying an electric change Q. A uniform electrostatic field of intensity **E** is applied to the dielectric, polarizing the bubble by means of the surface mobility B of electric charge carriers. The action of **E** on the charge Q stretches the bubble in the direction of **E** into a shape close to a spheroid of eccentricity e [5, 9], and the radius of the equivalent sphere increases to R while the gas pressure in the bubble becomes equal to P. As found in [4], an increase in Q and **E** can lead to a bubble instability, which manifests itself in the ejection of highly dispersed charged daughter bubbles from the bubble apexes. The instability can develop by different scenarios depending on the ratio of the bubble thermal oscillation period to the characteristic time of electric-potential relaxation over the bubble surface through the surface motion of charge carriers.

The characteristic time of electric-potential relaxation through the motion of charge carriers on a gas–fluid interface is $\tau_q = \varepsilon R/(E + BQ/R^2)$; and the period of bubble thermal oscillation is $\tau_u = [\rho R^3/\sigma\{1 - W^2 - w^2/(16\pi)\}]^{1/2}$, where $w^2 = \varepsilon E^2 R/\sigma$ is the parameter characterizing the Taylor instability of a conducting bubble with respect to surface polarization and $W^2 = Q^2/(16\pi\varepsilon\sigma R^3)$ is the Rayleigh parameter characterizing the stability of the bubble with respect to electric charge.

If the charge mobility B is so small that $\tau_u \ll \tau_q$, then the bubble surface can be treated as nonconducting in the course of instability development and the charge is "frozen" into the surface. When such a bubble is unstable with respect to the charge buildup on its surface, it breaks up into two equal daughter bubbles carrying equal charges [7].

When the charge mobility B is so high that $\tau_q \ll \tau_u$, the bubble surface can be treated as perfectly conducting. In this case, the bubble disintegrates into a host of highly dispersed daughter bubbles [1, 4, 10].

To determine the critical conditions for the instability of a charged bubble in a liquid dielectric, we write out the potential energy of a spheroidal bubble in a linear approximation with respect to e^2:

$$\Delta U = 4\pi\sigma R^2\left(1 + \frac{2}{45}e^4\right) - \frac{E^2R^3}{2\varepsilon}\left(1 + \frac{2}{5}e^2 + \frac{58}{175}e^4\right) + \frac{Q^2}{2\varepsilon R}\left(1 - \frac{1}{45}e^4\right) - PV\ln\frac{V}{V_0} + P_{at}(V - V_0) - 4\pi\sigma R_0^2, \quad (1)$$

where V_0 and V are the initial and final volumes of the bubble, respectively, and P_{at} is atmospheric pressure.

Since an equilibrium state of the bubble corresponds to a minimum of its potential energy, the derivatives of (1) with respect to e^2 and R must vanish. In a linear approximation with respect to e^2, one obtains the following equations describing the critical conditions for

the instability of a charged spheroidal gas bubble in field **E**:

$$e^2 = \frac{9w^2}{16\pi}\frac{1}{1-W^2},$$
$$\frac{(P-P_{at})R}{2\sigma} \equiv \beta = 1 - W^2\frac{3}{16\pi}w^2. \quad (2)$$

In contrast to the case of a liquid drop placed in a uniform electric field **E**, the critical conditions for the instability of a gas bubble in a field **E** depend on the gas pressure through the dimensionless parameter β [1, 5, 9].

2. As the bubble instability with respect to its surface charge (i.e., the sum of its intrinsic and polarization charges) develops, the spheroidal bubble begins to emit small charged daughter bubbles from one or both of its apexes, depending on charge value Q and external electric field **E**.

After an emitted bubble breaks away from the parent, the daughter-bubble volume changes from V_{ij}^0, to V_{ij} and the gas pressure inside it becomes equal to P_{ij}. The first subscript refers to an apex of the parent bubble: $i = 1$ corresponds to the apex from which a bubble is ejected in the direction of **E**, and $i = 2$ corresponds to the other apex. The subscript j is the number of an emitted bubble. The relative change in the daughter-bubble volume can be estimated by using the definition of the isothermal coefficient of compressibility

$$\frac{\Delta V_{ij}}{V_{ij}^0} = -\chi(P_{ij} - P). \quad (3)$$

Since $\chi \approx (10^{-7}$–$10^{-5})$ Pa^{-1} for gases, it is easy to show that the relative change in the bubble volume is on the order of 1–10^{-2}.

Figures presented in [4] show that the daughter bubbles are driven away from the parent bubble by forces of electrical repulsion; quickly lose their energy through friction; and then stop, making up two groups of daughter bubbles located at a distance $L = ma$ from the apexes of the parent bubble, where a is its semimajor axis and m is a parameter. These groups of charged bubbles generate an additional electric field in the neighborhoods of the apexes of the parent bubble, which hampers the breakaway of new daughter bubbles. To simplify the model calculations presented below, the electric field generated by a group of daughter bubbles is replaced with the field of a point charge located on the symmetry axis at a distance L from the corresponding apex of the parent bubble.

Let us consider the separation of the nth daughter bubble ejected from one apex of the parent bubble and the separation of the lth bubble ejected from the other apex, taking into account the fact that, by the current time moment, $n-1$ daughter bubbles have been ejected from the one apex of the parent bubble and $l-1$ daughter bubbles have been ejected from the other apex. The ejected daughter bubbles have charges $q_{ij} \ll (Q + ER^2)$ and radii $r_{ij} \ll R$. We assume that the time of daughter-bubble separation is on the order of the period of the principal eigenmode of capillary oscillation of a daughter bubble, $\sim(r_{ij})^{3/2}$. Then, k bubbles detach from one apex during the time required for one daughter bubble to break away from the other apex, where k is the integral part of $(r_{2l}/r_{1n})^{3/2}$. In the resultant electric field, which can be considered as quasi-uniform over a length comparable to the bubble size, a daughter bubble has the shape of a prolate spheroid with eccentricity e_{ij} [9]. In our calculations, the values e_{ij} are determined by means of an iterative procedure.

The breakup of an unstable bubble is assumed to take place at a constant temperature, since the heat capacity of the liquid is much greater than the heat capacity of the gas contained in the bubbles. Using the fact that the total charge of the system is constant, we find the change in the system's potential energy due to the ejection of a daughter bubble from an apex of the parent bubble:

$$\Delta U_{ij} = 4\pi\sigma r_{ij}^2 A(e_{ij}) + q_{ij}^2\frac{B(e_{ij})}{2\varepsilon r_{ij}}$$
$$- q_{ij}\frac{B(e)}{\varepsilon R}\left[Q - \sum_{j=1}^{n-1} q_{1j} - \sum_{j=1}^{l-1} q_{2j}\right]$$
$$+ q_{ij}\frac{K(\nu_{ij})}{\varepsilon R}\left[Q - \sum_{j=1}^{n-1} q_{1j} - \sum_{j=1}^{l-1} q_{2j}\right] \quad (4)$$
$$+ (-1)^{i+1}\frac{ER}{\varepsilon}q_{ij}\Omega(\nu_{ij}) + \frac{q_{ij}}{\varepsilon L}\sum_{j=1}^{n(i)-1} q_{ij}$$
$$- P_{ij}V_{ij}\ln\left[\frac{V_{ij}}{V_{ij}^0}\right] + P_{at}[V_{ij} - V_{ij}^0],$$

where

$$A(e_{ij}) = \frac{1}{2}\left((1-e_{ij}^2)^{1/2} + \frac{\arcsin e_{ij}}{e_{ij}}\right)(1-e_{ij}^2)^{-1/6},$$

$$B(e_{ij}) = \frac{(1-e_{ij}^2)^{1/3}}{e_{ij}}\operatorname{arctanh}(e_{ij}),$$

$$K(\nu_{ij}) = \frac{(1-e^2)^{1/3}}{e}\operatorname{arctanh}\left(\frac{e}{\nu_{ij}}\right), \quad \nu_{ij} = \left(1 + \frac{\xi_{ij}}{a^2}\right)^{1/2},$$

$$\Omega(\nu_{ij}) = \frac{e(\nu_{ij}-1) - \nu_{ij}\operatorname{arctanh}[e(\nu_{ij}-1)(\nu_{ij}-e^2)^{-1}]}{(1-e^2)^{1/3}(\operatorname{arctanh} e - e)},$$

$$n(i) = \begin{cases} n, & \text{if } i = 1 \\ l, & \text{if } i = 2 \end{cases},$$

where ξ_{ij} are the spheroidal coordinates of a daughter bubble at the moment of its separation from the parent bubble.

The first term in (4) characterizes the surface energy of a daughter bubble; the second and the third terms describe the change in the intrinsic electrostatic energy of the bubble system; the fourth one corresponds to the energy of electric interaction between the charges of daughter and parent bubbles; the fifth term is the energy of interaction between a daughter bubble and the parent-bubble polarization charge; the sixth one describes the energy of interaction between a daughter bubble and the group of bubbles emitted earlier; and the seventh and the eighth represent the work done by the gas during the isothermal variation of the daughter-bubble volume.

The emission of daughter bubbles continues as long as the Coulomb force that ejects a daughter bubble is larger than the counteracting Laplace force $2\pi\sigma r_{ij}^*$, where r_{ij}^* is the radius of the gas bridge connecting a daughter bubble with the parent. Assuming that the electrostatic field intensity at the point of daughter-bubble separation is determined by the fields generated by the parent bubble and the daughter bubbles ejected earlier, one obtains the following conditions for daughter-bubble separation from the apexes of the parent bubble:

$$\frac{\alpha_{ij} X_{ij}(1-e_{ij}^2)^{1/6}}{8} \le Y_{ij}\left(\frac{w}{(16\pi)^{1/2}} + W\right)^2 \times \left\{\left[\frac{W}{w(16\pi)^{-1/2} + W} - \sum_{j=1}^{n-1} Y_{ij} - \sum_{j=1}^{l-1} Y_{2j}\right] C(\nu_{ij}) + (-1)^{i+1}\frac{w}{w(16\pi)^{-1/2} + W} T(\nu_{ij}) - \frac{(1-e^2)^{2/3}}{m^2}\sum_{j=1}^{n(i)-1} Y_{ij}\right\}, \quad (5)$$

where

$$T(\nu_{ij}) = 1 - \frac{\operatorname{arctanh}(e\nu_{ij}^{-1}) - e\nu_{ij}(\nu_{ij}^2 - e^2)^{-1}}{\operatorname{arctanh}(e) - e},$$

$$C(\nu_{ij}) = \frac{(1-e^2)^{2/3}}{(\nu_{ij}^2 - e^2)}, \quad \alpha_{ij} = \frac{r_{ij}^*}{b_{ij}},$$

$$Y_{ij} = \frac{q_{ij}}{(Q + ER^2)}, \quad X_{ij} = \frac{r_{ij}}{R},$$

where X_{ij} is the dimensionless radius of a daughter bubble, Y_{ij} is its charge, and b_{ij} is the semiminor axis of a spheroidal daughter bubble.

The first and the second terms in the braces in (5) characterize the intensities of the electric fields generated by the intrinsic and polarization charges of the parent bubble at the daughter-bubble separation point, respectively; and the third term is the intensity of the electric field generated by the total charge of the group of bubbles emitted earlier at the same point.

Invoking Onsager's principle of minimum energy dissipation in nonequilibrium processes, we postulate that the variation of potential energy of the system associated with daughter-bubble emission be extremal; i.e., the conditions $\partial(\Delta U_{ij})/\partial q_{ij} = 0$ and $\partial(\Delta U_{ij})/\partial r_{ij} = 0$ are assumed to hold [10, 11]. In addition to the two equations in (5), this yields the following four equations for the dependent variables X_{1j}, Y_{1j}, ν_{1j}, X_{2j}, Y_{2j}, and ν_{2j}:

$$Y_{ij}\frac{B(e_{ij})}{X_{ij}} + \left[\frac{W}{w(16\pi)^{-1/2} + W} - \sum_{j=1}^{n-1} Y_{1j} - \sum_{j=1}^{l-1} Y_{2j}\right] \times [K(\nu_{ij}) - B(e)] + (-1)^{i+1}\frac{w}{w(16\pi)^{-1/2} + W}\Omega(\nu_{ij}) + \frac{(1-e^2)^{1/3}}{m}\sum_{j=1}^{n(i)-1} Y_{ij} = 0, \quad (6)$$

$$X_{ij}A(e_{ij}) - \left(\frac{w}{(16\pi)^{1/2}} + W\right)^2 Y_{ij}^2\frac{B(e_{ij})}{X_{ij}^2} - \eta_{ij}\beta X_{ij}^2 = 0,$$
$$\eta_{ij} = \frac{P_{ij} - P_{at}}{P - P_{at}}, \quad \beta = \frac{(P - P_{at})R}{2\sigma}. \quad (7)$$

3. In our numerical analysis of system (5)–(7), the parameters α_{ij} and η_{ij} were assumed to be equal for bubbles detaching from both apexes of the parent bubble and independent of the bubble number: $\alpha_1 = \alpha_2 = 0.9$ and $\eta_1 = \eta_2 = 0.6$. The analysis showed that solutions to this system depend not only on the values of its parameters but also on the sign of the parent-bubble charge Q.

In the plane (W^2, w^2), at constant values of other physical quantities, there are six domains of existence of solutions to system (5)–(7) shown in Fig. 1. In domain A_1, emission takes place only at one apex of the parent bubble. In domain A_2, emission takes place only at the other apex of the parent bubble. In domain B, the parent bubble is stable. In domains D_1 and D_2, emission takes place at both apexes and the charges of daughter bubbles emitted from both apexes of the parental bubble are of the same sign. In domain C, emission takes place at both apexes but the charges of daughter bubbles ejected from different apexes of the parent bubble have opposite signs. Note that the domains weakly depend on the value of β. For example, when $W^2 =$

const, the change in the Taylor parameter is $w^2(\beta = 0) - w^2(\beta = 0.75) \approx 10^{-3}$.

The curves separating the domains from each other were obtained in the following way. The values of $w^2 < 2.59$ and W^2 were chosen from domain A_1, where solutions describing daughter bubbles ejected from the second apex of the parent bubble do not exist. Solutions X_{11}, Y_{11}, and ν_{11} to the system of three equations for the first bubble ejection from the first apex were sought for a constant Rayleigh parameter and decreasing Taylor parameter. As the Taylor parameter reached a certain value, the solutions disappeared. In this way, the curve $w^2(W^2)$ separating domains A_1 and B was obtained as the Rayleigh parameter was varied from 0 to 0.6. Next, the values of $w^2 > 2.59$ and W^2 were chosen from domain C. Solutions X_{11}, Y_{11}, ν_{11}, X_{21}, Y_{21}, and ν_{21} to system (5)–(7) for the first emission event at both apexes of the parent bubble were sought. Again, the Rayleigh parameter was held constant and the Taylor parameter was decreased. As the Taylor parameter reached a certain value, the solutions X_{21}, Y_{21}, and ν_{21} disappeared. As a result, the curve $w^2(W^2)$ separating domains C and A_1 was calculated for the Rayleigh parameter varying from 0 to 0.225. Next, the parameters $W^2 \geq 0.6$ and w^2 were chosen from domain D_1. Solutions X_{11}, Y_{11}, ν_{11}, X_{21}, Y_{21}, and ν_{21} to the system of six equations for the first emission event at both apexes of the parent bubble were sought for a constant Rayleigh parameter and increasing Taylor parameter. As the Taylor parameter reached a certain value, the solutions X_{21}, Y_{21}, and ν_{21} disappeared. Thus, the curve separating domains D_1 and A_1 was obtained for constant values of the Rayleigh parameter lying in the interval from 0.6 to 2. All domains corresponding to $Q < 0$ were obtained by reflecting the domains calculated for $Q > 0$, because the equations for X_{1j}, Y_{1j}, and ν_{1j} take the form of those for X_{2j}, Y_{2j}, and ν_{2j} when Q is replaced by $-Q$ in the equations of system (5)–(7).

A. Suppose that the initial values of the bubble parameters W^2 and w^2 lie in A_1 or A_2. Then, emission takes place at only one apex (at the first one if $Q > 0$ and at the second one if $Q < 0$). Dispersion in domains A_1 and A_2 proceeds in the same manner, except that the daughter bubbles carry negative charges in domain A_1, while the charge of daughter bubbles in domain A_2 is positive. During emission, the Rayleigh parameter of the bubble decreases faster than the Taylor parameter, and the bubble can reach the boundary of domain A_1 or A_2 in the plane (W^2, w^2) if the total electric charge accumulated at the apexes of the parent bubble of the daughter bubbles is too small to stop the emission. Further development of the breakup process depends on the Taylor parameter. If $w^2 < 2.59$, the bubble falls into domain B of the (W^2, w^2) diagram and emission ceases completely. If $w^2 > 2.59$, the bubble falls into domain C and emission takes place at both apexes. Figure 2 shows the results of our calculations of unstable bubble breakup performed for $W^2 = 0.4$ and $w^2 = 0.4$.

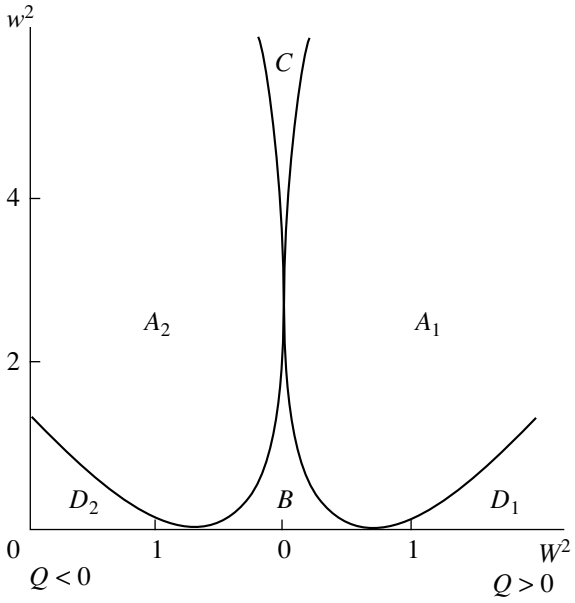

Fig. 1. Boundaries for domains in the plane (W^2, w^2) corresponding to various mechanisms of excessive surface-charge loss by a bubble for $e^2 = 0.7$, $\alpha_1 = \alpha_2 = 0.9$, $\beta = 0.75$, and $\eta_1 = \eta_2 = 0.6$.

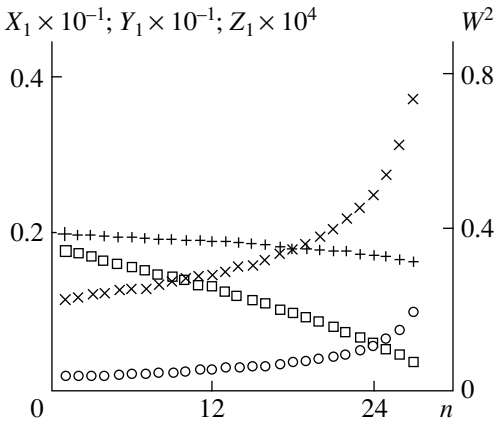

Fig. 2. Daughter-bubble number dependence of the radius X_1 (×), charge Y_1 (○), relative charge Z_1 (□), and Rayleigh parameter W^2 (+) for bubble emission from the first apex of the parental bubble for $Q > 0$ at $e^2 = 0.7$, $\alpha_1 = 0.9$, $m = 1$, $\beta = 0.75$, and $\eta = 0.6$.

B. If the initial values of W^2 and w^2 for the an unstable bubble lie in domain D_1 or D_2, emission takes place at both apexes. The signs of daughter bubbles detaching from both apexes are now the same. The Rayleigh parameter of the parent bubble decreases in the course of emission: it moves from domain D_i to domain A_i, whereupon the breakup process develops as described in subsection A. Figures 3 and 4 show the results calcu-

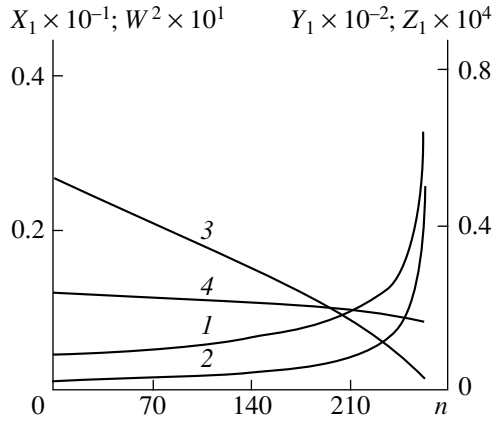

Fig. 3. The same as in Fig. 2 for $w^2 = 0.18$ and $W^2 = 1.2$; curves *1*, *2*, *3*, and *4* correspond to (×), (○), (□), and (+), respectively.

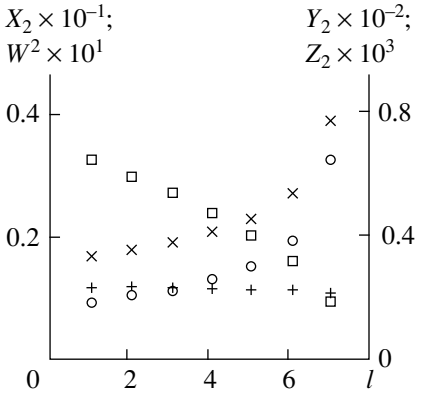

Fig. 4. Daughter-bubble number dependence of radius X_2 (×), charge Y_2 (○), relative charge Z_2 (□) and Rayleigh parameter W^2 (+) for bubble emission from the second apex of the parental bubble for $Q > 0$ at $e^2 = 0.7$, $\alpha_2 = 0.9$, $m = 1$, $\beta = 0.75$, and $\eta = 0.6$.

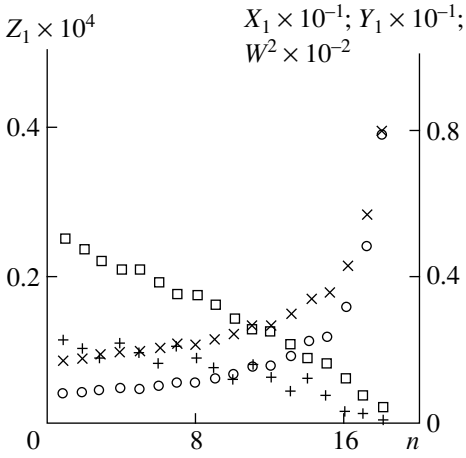

Fig. 5. The same as in Fig. 2 for $w^2 = 2.7$ and $W^2 = 0.0025$.

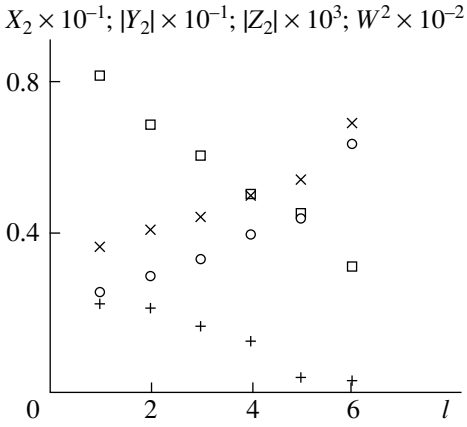

Fig. 6. Daughter-bubble number dependence of the dimensionless radius X_2 (×), magnitude of charge $|Y_2|$ (○), magnitude of relative charge $|Z_2|$ (□), and Rayleigh parameter W^2 (+) for bubble emission from the second apex of the parental bubble for $w^2 = 2.7$ and $W^2 = 0.0025$; other parameters are the same as in Fig. 4.

lated for $W^2 = 1.2$ and $w^2 = 0.18$. During the time required for one to seven daughter bubbles to break away from the second apex, the first one emits 8, 9, 9, 10, 11, 13, or 18 bubbles respectively. Then, the bubble enters domain A_1 in the plane (W^2, w^2) and emission continues only at the first apex of the parent bubble. The total charge of the daughter bubbles ejected earlier from the first apex of the parent bubble then becomes sufficiently large for emission from this apex to cease, although the bubble does not enter domain *B* in the plane (W^2, w^2).

C. If the initial values of W^2 and w^2 lie in domain *C*, emission takes place at both apexes, and the charges of daughter bubbles ejected from both apexes differ in both sign and value. The results calculated for $W^2 = 0.0025$ and $w^2 = 2.7$ are shown in Figs. 5 and 6. In this case, during the time required for six daughter bubbles to break away from the second apex, the first apex of the parent bubble emits 4, 3, 4, 3, 3, and 1 bubble, respectively.

The calculations revealed that the left-hand side of the second equation in (2) does not exceed 1.04 and remains almost constant during emission. This means that daughter bubbles are unstable with respect to expansion.

CONCLUSIONS

Depending on both external electrostatic-field intensity **E** and the value and sign of the intrinsic charge *Q*

of a surface-conducting bubble in a liquid dielectric, the instability of the bubble with respect to both intrinsic and induced surface electric charges can develop by different scenarios, with daughter bubbles ejected either from only one apex of the parent bubble or from both. During bubble breakup, a smooth change in the emission regime may occur.

REFERENCES

1. A. I. Grigor'ev, A. N. Zharov, V. A. Koromyslov, and S. O. Shiryaeva, Izv. Ross. Akad. Nauk, Mekh. Zhidk. Gaza, No. 5, 205 (1998).
2. S. O. Shiryaeva and A. N. Zharov, Pis'ma Zh. Tekh. Fiz. **24** (24), 30 (1998) [Tech. Phys. Lett. **24**, 959 (1998)].
3. A. I. Grigor'ev, S. O. Shiryaeva, and A. N. Zharov, Zh. Tekh. Fiz. **69** (2), 11 (1999) [Tech. Phys. **44**, 141 (1999)].
4. C. G. Garton and Z. Krasucki, Trans. Faraday Soc. **60**, 211 (1964).
5. K. J. Cheng and J. B. Chaddock, Phys. Lett. A **106** (1–2), 51 (1984).
6. K. J. Cheng and J. B. Chaddock, Int. J. Heat Fluid Flow **7** (4), 278 (1986).
7. A. I. Grigor'ev, V. A. Koromyslov, and A. N. Zharov, Pis'ma Zh. Tekh. Fiz. **23** (19), 60 (1997) [Tech. Phys. Lett. **23**, 760 (1997)].
8. A. N. Zharov, Pis'ma Zh. Tekh. Fiz. **24** (21), 49 (1998) [Tech. Phys. Lett. **24**, 849 (1998)].
9. A. I. Grigor'ev, S. O. Shiryaeva, and E. I. Belavina, Zh. Tekh. Fiz. **59** (6), 27 (1989) [Sov. Phys. Tech. Phys. **34**, 602 (1989)].
10. A. I. Grigor'ev and S. O. Shiryaeva, Zh. Tekh. Fiz. **61** (3), 19 (1991) [Sov. Phys. Tech. Phys. **36**, 258 (1991)].
11. S. O. Shiryaeva and A. I. Grigor'ev, Zh. Tekh. Fiz. **65** (2), 11 (1995) [Tech. Phys. **40**, 122 (1995)].

Translated by Vitaly V. Gursky

Technical Physics, Vol. 45, No. 6, 2000, pp. 710–719. Translated from Zhurnal Tekhnicheskoĭ Fiziki, Vol. 70, No. 6, 2000, pp. 43–51.

Mechanism for Propagation of a Positive Leader

A. V. Ivanovskiĭ

Received June 8, 1999

Abstract—A model of leader breakdown in air is considered. The channel is formed due to heating of the streamer trace in the field of the streamer zone. A previous model of a streamer is generalized with allowance for recombination of charged particles. A mathematical model of heating of the streamer trace is developed. It is demonstrated that, at a given potential, the ignition of the channel is provided by streamers that possess a certain charge and the corresponding propagation velocity. This velocity determines the propagation velocity of a steady leader. The dependence of the leader velocity on the cloud potential is found. The results obtained are compared with the data from in-situ observations and laboratory studies. © *2000 MAIK "Nauka/Interperiodica".*

INTRODUCTION

Based on the results of in-situ observations and laboratory studies, two discharge regions can be distinguished in the leader stage of a spark discharge: a streamer zone and a channel [1]. The channel is a region filled with a high-temperature plasma that provides charge transfer from the high-voltage electrode (cloud) to the leader head. The propagation velocity of the leader is $\vartheta_h \sim 10^6$–10^8 cm/s. The length of the channel can be as long as several kilometers, whereas its diameter is only a fraction of millimeter. A great number of streamers start from the leader head at the velocities ϑ_{st}, which can be much higher then ϑ_h. A family of streamers forms the streamer zone, whose typical length is tens of meters; the transverse size is several meters. The channel currents govern macroscopic processes in the leader discharge (charge transfer, propagation, and the formation of the streamer zone). However, the parameters of the channel are determined by the processes in the streamer zone. That is why the streamer zone plays an important role in the leader breakdown.

Although there is a general concept of the process, a self-consistent mathematical model of the leader stage of a spark discharge allowing one to establish the relationship between the propagation velocity of the leader, the parameters of the channel and the streamer zone, and the cloud potential V_{cl} is still lacking.

BASIC ASSUMPTIONS

By analogy with an arc discharge, we can assume that, at currents ≥10 A, the electric field inside the channel is about 1 kV/m [2]. For megavolt potential drops at distances of hundreds of meters, we can neglect the variation in the potential over the channel and consider a steady-state regime of penetration at the velocity ϑ_h corresponding to a potential V of the leader head equal to V_{cl}. Thus, the role of the channel reduces to the transfer of the potential V_{cl} from the cloud to the streamer zone.

We assume that the electric field E_{st} is constant along the streamer zone. The field is produced and sustained by charge transferred into the streamer zone by all the streamers starting from the leader head [1]. Streamers are plasma formations with a charge q_{st} and length determined by electron attachment [3] and electron–ion recombination. Due to polarization, the field at the head increases. Ionization in the increased field compensates for the loss of electrons due to attachment and recombination and ensures penetration of the streamer. At fixed E_{st}, the charge q_{st} unambiguously determines the velocity ϑ_{st}, the streamer radius a_{st}, and the concentration of electrons n_{st} [4].

The leader channel is formed during heating of the streamer trace in the field E_{st} by the current produced by ions, electrons detaching from negative ions, and electrons produced due to ionization by detaching particles. Electron detachment takes place in the interaction of negative ions with electronically excited molecules. At high temperatures, the processes of detachment due to the interaction with molecules in the ground state (at $T \geq 10^3$ K) and energy relaxation of vibrationally excited molecules (at $T \geq 2.5 \times 10^3$ K) become important [5, 6]. These processes determine the dynamics of the channel formation, but weakly influence the propagation velocity of the leader and the parameters of the streamer zone and the channel in the steady-state regime.

If the heating time t_{st} of the streamer trace is constant, then the potential of the channel formation $V_{st} \cong E_{st}\vartheta_{st}t_{st}$ increases with increasing ϑ_{st} or q_{st}. A decrease in q_{st} leads to a decrease in the streamer radius a_{st} and an increase in t_{st} due to the growth of thermal conductivity. An increase in t_{st} leads to an increase in V_{st}. We

1063-7842/00/4506-0710$20.00

can expect that, at fixed E_{st}, the $V_{st}(q_{st})$ dependence has a minimum V_m, the corresponding streamer velocity and charge being ϑ_m and q_m, respectively. This minimum determines the potential $V = V_m$ and the leader velocity $\vartheta_h = \vartheta_m$ in the steady-state regime, which means that, among the streamers starting from the leader head, only the streamers with the charge q_m form the channel. The other streamers starting from the leader head produce and sustain the field E_{st}.

The cloud potential V_{cl} determines the leader current $J = c_0\vartheta_h V_{cl}$, where c_0 is the capacitance per unit length. In turn, the leader current determines the steady-state parameters of the channel according to the arc-discharge theory. Below, we discuss the above statements in more detail.

A SOLITARY STREAMER DISCHARGE

We will characterize a streamer by a charge distribution over the length

$$q(z) = q_0\begin{cases}0, & z \geq z_f\\ \exp\left(\dfrac{z-z_f}{\lambda}\right), & z < z_f\end{cases} + q_1\delta(z-z_f), \qquad (1)$$

$$q_{st} = \int_{-\infty}^{+\infty} q(z)dz = q_0\lambda + q_1,$$

where z_f is the front coordinate, λ is the spatial scale of charge relaxation determined by attachment and recombination, and q_1 is the head charge.

In my previous paper [4], it was shown that, from the condition of continuity of the current density at the front, it follows that $q_1 = a_{st}q_0$. If $\lambda/a_{st} \gg 1$, then, for the charge distribution given by (1), the field E on the streamer axis is described by the equation

$$\frac{dE}{dx} - \tau\frac{\sigma}{\varepsilon_0}E = -E_{st}q_0'$$

$$\times\left\{1 - \frac{x-x_f}{\sqrt{(x-x_f)^2+1}} + \frac{1}{\left(\sqrt{(x-x_f)^2+1}\right)^3}\right\},$$

$$x \geq x_f,$$

$$\pi\tau\frac{d}{dx}(\sigma E) + C_0E$$

$$= C_0E_{st}\{1 + q_0'(E_1(\lambda/a_{st}, x) + E_2(x))\}, \qquad (2)$$

$$x < x_f,$$

where $x = z/a_{st}$, $x_f = z_f/a_{st}$, $q_0' = q_0/(2\pi\varepsilon_0 a_{st}E_{st})$ is a dimensionless charge per unit length, $\tau = a_{st}/\vartheta_{st}$ is the characteristic time, $E_1(\lambda/a_{st}, x)$ and $E_2(x)$ are the given functions of x and the parameters λ/a_{st}, $C_0 = 2\pi\varepsilon_0/\ln(2\lambda/a_{st} - \gamma + 0.5)$ is the capacitance per unit length, and $\gamma = 0.577215665$ is the Euler constant.

The conductivity is determined by electrons: $\sigma = e\mu_e ne$, where $\mu_e(E)$ is the electron motility. To determine the electron density n_e, it is necessary to solve the system of equations describing the ionization kinetics. For a streamer propagating at the velocity ϑ_{st} (in this case, we have $d/dt \longrightarrow -\vartheta_{st}d/dz = -\tau d/dx$), this system has the form

$$\frac{dn_e}{dx} = (\nu_{att} - \nu_{ion})\tau n_e + \alpha_{ei}\tau n_e n_+,$$

$$\frac{dn_-}{dx} = -\nu_{att}\tau n_e + \alpha_{ii}\tau n_- n_+, \quad n_+ = n_e + n_-, \qquad (3)$$

where n_+ and n_- are the densities of positive and negative ions, respectively; $\nu_{att}(E)$ and $\nu_{ion}(E)$ are the attachment and ionization rates, respectively; and α_{ei} and α_{ii} are the rate constants of electron–ion and ion–ion recombination, respectively.

System (3) is written under the assumption that the plasma is quasineutral, which is valid for $\vartheta_{st} \gg \vartheta_{dr}$, where ϑ_{dr} is the drift velocity of electrons.

For $x \geq x_f$, in the vicinity of the streamer head, where $E > E_{br}$ (here, $E_{br} \cong 30$ kV/cm is the breakdown field determined by the conditions $\nu_{att}(E) = \nu_{ion}(E)$), we have $\nu_{ion}(E) \gg \alpha_{ei}n_+$; as a result, equation (3) reduces to

$$\frac{dn_e}{dx} = (\nu_{att} - \nu_{ion})\tau n_e, \quad x \geq x_f. \qquad (4)$$

We assume that $\alpha_{ei} = \alpha_{ii} = \alpha_r$ (where $\alpha_r = \alpha_{ei}(E_{st})$) behind the ionization front (i.e., at $x \leq x_f$). In this case, ionization in the streamer trace is inessential and can be neglected, so that equation (3) takes the form

$$\frac{dn_e}{dx} = \nu_{att}\tau n_e + \alpha_r\tau n_e n_+,$$

$$\frac{dn_+}{dx} = \alpha_r\tau n_+^2, \quad x \leq x_f. \qquad (5)$$

The solution to equation (5) with the boundary condition $n_+(x = x_f) = n^+$ has the form $n_+(x) = n^+/(1 + \alpha_r\tau(x_f - x)n^+)$. The value of n^+ is determined from the equality $n^+ = n_e(x = x_f)$, where $n_e(x = x_f)$ is the solution to equation (4) (in the vicinity of the front, we have $n_e \gg n_-$ and $n_e \cong n_+$). Finally, we arrive at

$$\frac{dn_e}{dx} = \left(\nu_{att} + \frac{\alpha_r n^+}{1 + \alpha_r\tau(x_f - x)n^+}\right)\tau n_e, \quad x \leq x_f. \qquad (6)$$

When choosing the initial conditions for (4) and (6), we assume (as is usually done in numerical simulations of streamers; see, e.g., [7, 8]) that, when the electric

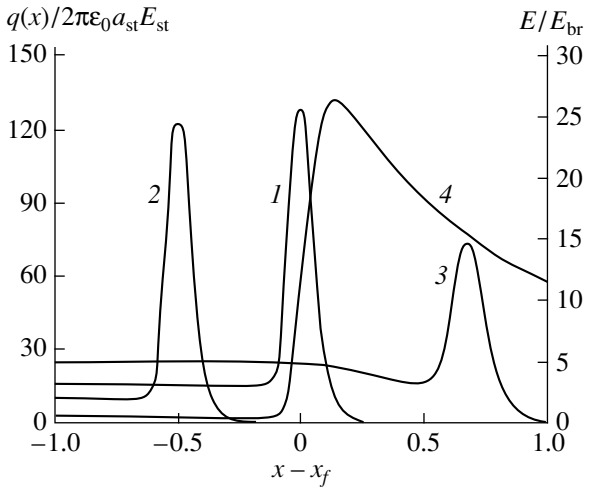

Fig. 1. The charge per unit length vs. x for $q_0' = (1)$ 21.4, (*2*) 15, and (*3*) 25, and (*4*) the field E vs. x for $q_0' = 21.4$.

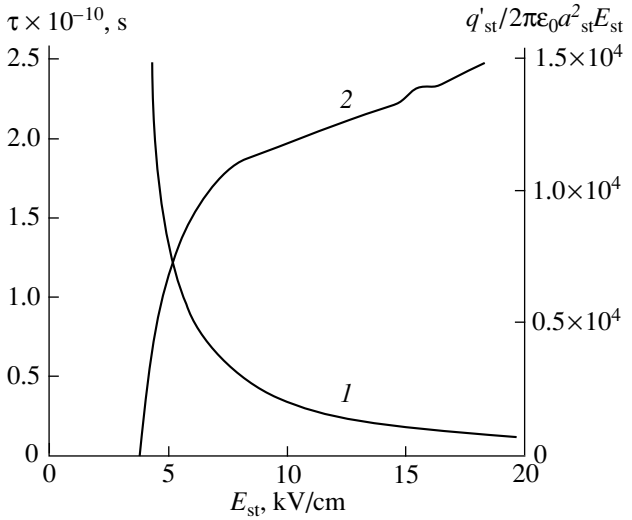

Fig. 2. (*1*) The time τ and (*2*) charge q'_{st} vs. the field E_{st}.

field reaches the value of E_{br}, the electron density is $n_e = n_0 \cong 10^5$ cm^{-3}.

The algorithm for solving equations (2), (4), and (6) was developed in [4]. At a given value of E_{st}, the unknown parameters q_0', τ, and λ/a_{st} are determined from the following conditions.

(i) The parameter q_0' is determined from the condition that the charge per unit length $q(x) = \pi a_{st}\tau\sigma E$ attains its maximum at the streamer head (at $x = x_f$). Figure 1 shows the curves $q(x)$ obtained by numerically solving equations (2) and (4) for $q_0' = 21.4$, 15, and 25; $E_{st} = 0.4E_{br}$; and $\tau = 1.8 \times 10^{-11}$ s. The true value of q_0' is 21.4, because $q(x)$ attains its maximum at $x = x_f$. Curve *4* illustrates the corresponding dependence $E(x)$.

(ii) The parameter τ is determined by equating the electron density at the front $n_e(x = x_f)$ (or $E(x = x_f)$) obtained from equations (2) and (6) under the conditions $n_e(x \longrightarrow -\infty) \longrightarrow 0$ and $E(x \longrightarrow -\infty) \longrightarrow E_{st}$ to the established electron density n^+ (or the field E^+) behind the front obtained from equations (2) and (4). For $E_{st} = 0.4E_{br}$ and $\tau = 1.8 \times 10^{-11}$ s, we have $E^+ = 0.497E_{br}$ and $n^+ = 4.6 \times 10^{15}$ cm^{-3} (Fig. 1).

(iii) The parameter λ/a_{st} is determined from the condition that the streamer charge obtained from equations (2), (4), and (6) be equal to q_{st}. Taking into account expression (1), this condition can be rewritten in the form

$$\frac{\lambda}{a_{st}} = \frac{q'_{st}}{q_0'} - 1, \qquad (7)$$

where $q'_{st} = q_{st}/(2\pi\varepsilon_0 a_{st}^2 E_{st})$ is a dimensionless streamer charge, which is determined by the values of σ and E obtained from equations (2), (4), and (6):

$$q'_{st} = \frac{1}{2\pi\varepsilon_0 a_{st}E_{st}}\int_{-\infty}^{+\infty} q(x)dx = \frac{\tau}{2\varepsilon_0 E_{st}}\int_{-\infty}^{+\infty}\sigma(x)E(x)dx. \quad (7')$$

The parameters q_0', τ, and λ/a_{st} satisfying conditions (i)–(iii) can be found by iteration.

Figures 2 and 3 show the plots of τ, q'_{st}, and the steady-state electron density behind the ionization front n^+ versus E_{st}. The streamer parameters corresponding to the field E_{st} and charge q_{st} can be found as follows. The radius $a_{st} = [q_{st}/(2\pi\varepsilon_0 q'_{st} E_{st})]^{1/2}$ is determined by q_{st} and $q'_{st}(E_{st})$ (Fig. 2). The velocity $\vartheta_{st} = a_{st}/\tau$ is determined by a_{st} and $\tau(E_{st})$.

The solutions obtained exist at E_{st} greater than the threshold field E_{th}, which corresponds to the minimum in the dependence of the attachment rate on the electric field ($E_{th} \cong 4$ kV/cm; Fig. 3, curve *2*) [4].

The data presented in Figs. 2 and 3 are the starting point for studies of the formation of a leader channel in the field of the streamer zone.

FORMATION OF THE LEADER CHANNEL

We assume that channel formation occurs at a constant pressure P_0 equal to atmospheric pressure. At low levels of dissociation (ionization), the pressure P_0 is determined by the density N and temperature T of neutral molecules. Hydrodynamic equations for N and T

have the form [2]

$$Nc_p\left(\frac{\partial T}{\partial \tau} + u\frac{\partial T}{\partial r}\right) = \frac{1}{r}\frac{\partial}{\partial r}\left(r\lambda\frac{\partial (kT)}{\partial r}\right) + q_t,$$
$$T\frac{1}{r}\frac{\partial}{\partial r}(ru) = \frac{\partial T}{\partial \tau} + u\frac{\partial T}{\partial r}, \quad P_0 = NkT, \tag{8}$$

where λ is the thermal conductivity at constant pressure [2] and the time is counted from the arrival of the streamer front: $\tau = t - z/\vartheta_{st}$.

In equations (8), we neglected kinetic energy as compared to thermal energy, the longitudinal heat flux as compared to the radial flux, and the longitudinal velocity as compared to the radial velocity u. By virtue of the high rate of relaxation of rotationally excited molecules, we assume that the translational and rotational temperatures are equal to each other. We neglect heating of the medium due to relaxation of vibrationally and electronically excited molecules. The heat capacity of air at constant pressure is $c_p = 7/2kT$. The source heating the medium (q_t) includes elastic collisions of electrons (q_{en}) and ions (q_{in}) with neutral molecules, excitation of the rotational degrees of freedom (q_r), energy dissipation due to electron–ion (q_{ei}) and ion–ion (q_{ii}) recombination, and dissipative attachment (q_{att}):

$$q_t = q_{en} + q_{in} + q_r + q_{ei} + q_{ii} + q_{att}. \tag{9}$$

The sources of the bulk energy deposition depend on the electron density n_e and the densities of positive (n_+) and negative (n_-) ions. Assuming that the plasma of the streamer trace is quasineutral, we determine n_e, n_+, and n_- from the equations

$$\frac{\partial}{\partial \tau}[n_e(1 - \vartheta_{dr}/\vartheta_{st})] + \frac{1}{r}\frac{\partial}{\partial r}(rn_e\vartheta_e) = (\nu_{ion} - \nu_{att})n_e - \lambda_{ei}n_en_+ + \nu_{det}n_-,$$
$$\frac{\partial n_-}{\partial \tau} + \frac{1}{r}\frac{\partial}{\partial r}(rn_-\vartheta_-) = \nu_{att}n_e - \lambda_{ii}n_-n_+ - \nu_{det}n_-, \tag{10}$$
$$n_+ = n_- + n_e.$$

Here, $\nu_{ion}(T_e, \delta)$ and $\nu_{att}(T_e, \delta)$ are the ionization and attachment rates determined by the electron temperature T_e and the relative air density $\delta = N/N_0$, where $N_0 = 2.5 \times 10^{19}$ cm^{-3}); ν_{det} is the detachment rate; and $\lambda_{ei}(T_e)$ and $\lambda_{ii}(T_i, \delta)$ are the rate constants of dissociative electron–ion and three-particle ion–ion recombination, respectively. Since the mass of an ion is close to that of a neutral particle, the ion temperature is $T_i \cong T$. At $\vartheta_{st} \gg \vartheta_{dr}$, we can neglect the drift of electrons along the electric field, assuming that $\vartheta_{dr} \equiv 0$ (for a positive leader, we have $\vartheta_{dr} < 0$).

The radial flows of charged particles are determined by the sum of the flows related to the motion of the medium (n_eu and n_-u) and diffusion. In a quasineutral plasma of a streamer trace, diffusion is ambipolar. Neglecting thermal diffusion and assuming that $T_e \gg T$, we obtain [9] (here, $\nabla = \partial/\partial r$)

$$n_e\vartheta_e = n_eu - \frac{\mu_e\mu_i(2n_- - n_e)kT_e\nabla n_e}{e\ \mu_en_e + 2\mu_in_i},$$
$$n_-\vartheta_- = n_-u - \frac{\mu_in_-}{e}\frac{2\mu_ikT\nabla n_- - \mu_ekT_e\nabla n_e}{\mu_en_e + 2\mu_in_i}. \tag{11}$$

We assume that electron detachment results from collisions of negative ions with electronically-excited molecules; i.e., $\nu_{det} = \alpha^*N^*$, where α^* is the detachment rate constant and N^* is the density of electronically excited particles. We will vary α^* and determine N^* from the equation

$$\frac{\partial N^*}{\partial \tau} + \frac{1}{r}\frac{\partial}{\partial r}(ruN^*) = \nu_{ex}n_e - \alpha^*N^*n_-, \tag{12}$$

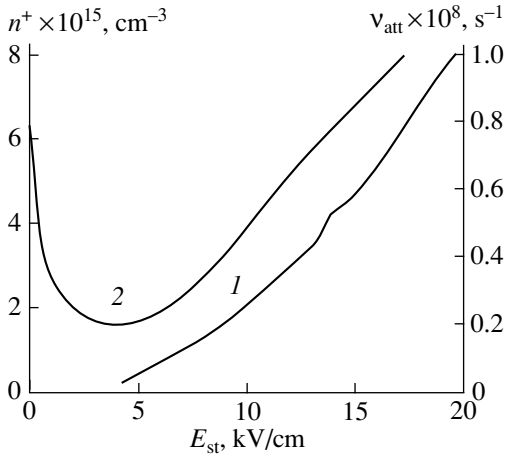

Fig. 3. (*1*) The electron density n^+ in the streamer channel and (*2*) the attachment rate ν_{att} vs. the field E_{st} of the streamer zone.

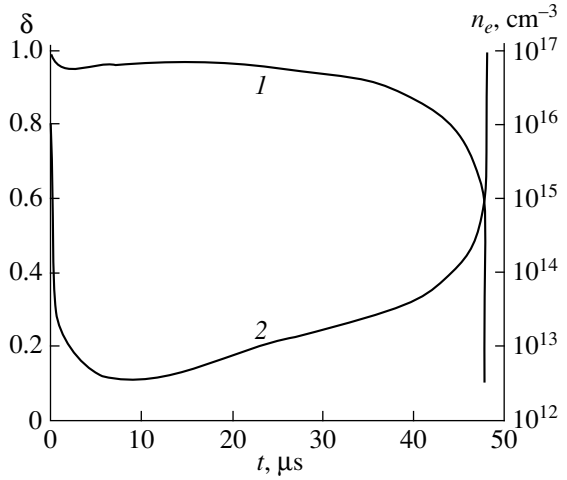

Fig. 4. (*1*) The relative air density δ and (*2*) the electron density n_e in the streamer trace vs. time for $E_{st} = 12.7$ kV/cm, $q_{st} = 0.33 \times 10^{-9}$ C ($\vartheta_{st} = 8.5 \times 10^7$ cm/s), and $\alpha^* = 10^{-8}$ cm^3/s.

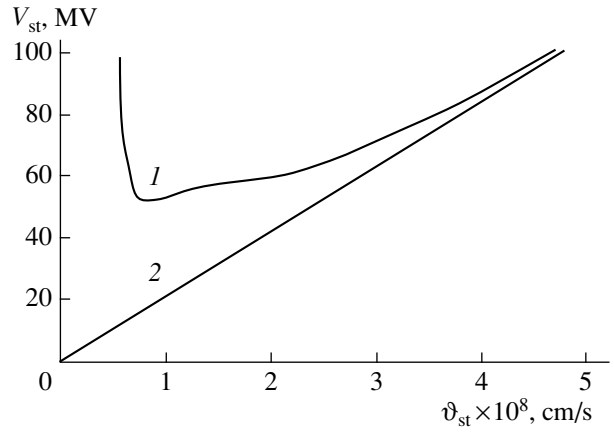

Fig. 5. The potential of channel formation V_{st} vs. the streamer velocity at E_{st} = 12.7 kV/cm in (*1*) the comprehensive model and (*2*) the model without allowance for the transfer processes.

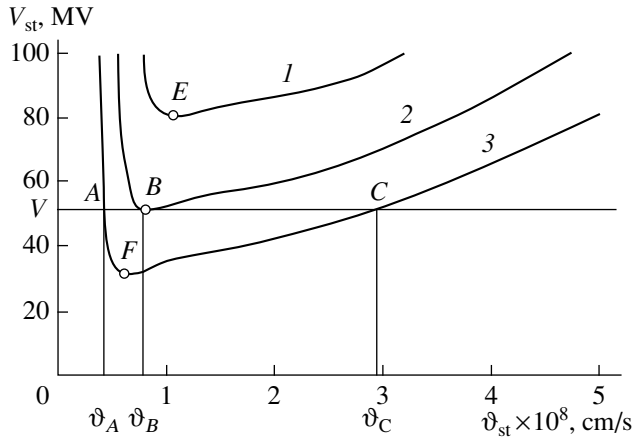

Fig. 6. The potential of channel formation V_{st} vs. the streamer velocity for E_{st} = (*1*) E_1, (*2*) E_2, and (*3*) E_3.

where $\nu_{ex}(T_e, \delta)$ is the excitation rate of the molecular electronic levels.

The electron temperature, which governs the rates of production and annihilation of charged particles, is determined from the energy balance for electrons [10]:

$$\frac{\partial}{\partial\tau}\left(\frac{3}{2}n_e kT_e\right) + u\frac{\partial}{\partial r}\left(\frac{3}{2}n_e kT_e\right) + \frac{5}{2}n_e kT_e\frac{1}{r}\frac{\partial}{\partial r}(ru) \tag{13}$$
$$= \frac{e^2 n_e}{m_e\nu_m}E_{st}^2 - q_{en} - q_r - q_v - q_{ex} - q_i + \frac{1}{r}\frac{\partial}{\partial r}\left(r\lambda_e\frac{\partial(kT_e)}{\partial r}\right),$$

where q_v, q_{ex}, and q_i are the energy losses due to vibrational and electronic excitation and ionization, respectively; $\lambda_e = 5/2 n_e kT_e/m_e\nu_m$ is the electron thermal conductivity; and ν_m is the frequency of elastic collisions.

Figure 4 shows the dynamics of streamer trace heating. The figure presents the time dependences of the relative air density δ and the electron density n_e at $r = 0$ obtained by numerically solving equations (8)–(13) at E_{st} = 12.7 kV/cm and $q_{st} = 0.33 \times 10^9$ C ($\vartheta_{st} = 8.5 \times 10^7$ cm/s) at $\alpha^* = 10^{-8}$ cm/s. The decrease in the electron density in the streamer trace due to attachment and recombination is followed by an increase in n_e, which is explained by accumulation of electronically excited molecules. The formation of the channel at $\tau = t_{st} \cong 48$ μs is characterized by a sharp increase in n_e and a decrease in δ. In order to describe the subsequent heating dynamics, it is necessary to take into account Coulomb collisions, relaxation of vibrationally excited molecules, dissociation of molecules, radiation transfer, etc. However, even without going into details, we can expect further growth of the conductivity and the channel current and, consequently, a sharp decrease in the field E_{st} of the streamer zone. This allows us to introduce the potential of channel formation $V_{st} \cong E_{st}\vartheta_{st}t_{st}$.

Figure 5 shows a typical plot of V_{st} versus $\vartheta_{st}(q_{st})$. Here, t_{st} is the time required for the relative air density to achieve the value $\delta = 0.1$. A comparison with the curve obtained for $\vartheta_e = \vartheta_- = u$, $\lambda_e = 0$, and $\lambda = 0$ shows that the increase in V_{st} at small velocities ϑ_{st} (small charges q_{st}) is related to the increase in the role of transfer processes (mainly heat conduction) with decreasing streamer trace radius a_{st}; i.e., the dependence of V_{st} on $\vartheta_{st}(q_{st})$ has a minimum determined by the heat conductivity of a medium.

STEADY-STATE LEADER DISCHARGE

Figure 6 shows the plots of the potential V_{st} of channel formation versus the streamer velocity ϑ_{st} for three values of the field E_{st} of the streamer zone at $\alpha^* = 10^{-8}$ cm^3/s. Let the cloud potential be V. In the steady-state regime, $V = V_{st}$ (we neglect the potential drop along the channel) and the leader velocity is $\vartheta_h = \vartheta_{st}$. At $E_{st} < E_2$, leader propagation is impossible. For $E_{st} \geq E_2$ (e.g., $E_{st} = E_3$), two groups of streamers correspond to each value of the field of the streamer zone. For $E_{st} = E_3$, these are the streamers propagating at the velocities ϑ_A and ϑ_C, which correspond to two possible velocities of leader penetration. Stable propagation at the velocity $\vartheta_h = \vartheta_A$ is impossible, because the streamers with the velocities $\vartheta_A < \vartheta_{st} < \vartheta_C$ form the channel at smaller potentials. Steady-state penetration at the velocity ϑ_C is also unstable, because the streamers with $\vartheta_{st} > \vartheta_C$ overtake the leader and decrease the field of the streamer zone. We can assume that the field $E_{st} = E_2$ and the velocities $\vartheta_h = \vartheta_{st} = \vartheta_B$ (point *B*) correspond to stable penetration of the leader. In this case, the decrease in the field E_{st} by the streamers with $\vartheta_{st} > \vartheta_B$ leads to the termination of propagation; as a result, the field E_{st} increases.

Thus, the minimum field of the streamer zone E_m that still allows the growth of the leader is established at a given cloud voltage V. A group of streamers with the charge q_m and velocity ϑ_m correspond to this field. The heating of the traces of these streamers results in channel formation.

Figure 7 shows the plots of the leader penetration velocity ϑ_h versus the cloud potential (Fig. 6; points *F*, *B*, *E*). The propagation velocity ϑ_h increases with increasing α^*. For natural lightning, the maximum velocity is about 2.6×10^8 cm/s and the maximum charge is about 20 C [11]. Assuming that the capacitance of the leader is 4×10^{-8} F (the length is about 5×10^3 m), we estimate the maximum potential to be ~500 MV. Close values result from calculations at $\alpha^* = (0.5\text{–}1) \times 10^{-8}$ cm^3/s (Fig. 7).

The drift of electrons along the field (Fig. 8) affects the leader parameters if the propagation velocity is comparable with the drift velocity. The increase in the conductivity at the stage of channel formation leads to a decrease in the field of the streamer zone. For a leader propagating at the velocity ϑ_h, the estimate for the decrease in the field $E_{st}(\tau)$ of the streamer zone can be found from the equations

$$\frac{\partial V}{\partial \tau} = \vartheta_h E_{st}(\tau), \qquad I = C_{st}\vartheta_h V, \quad I = (G_{tr} + G_{st})E_{st}(\tau), \tag{14}$$

where V is the potential, I is the total current of the streamers, $C_{st} = 2\pi\varepsilon_0/\ln(2\vartheta_h t_{st}/R_{st})$ is the capacitance per unit length of the streamer zone, $G_{tr} = 2\pi\int_0^\infty \sigma(r, \tau) r dr$ (where $\sigma = e\mu_e n_e + e\mu_i(n_+ + n_-)$) is the linear conductivity of the trace of a streamer that forms the channel, and G_{st} is the total linear conductivity of all the streamers.

From (14) we obtain the equation for the field of the streamer zone

$$\frac{\partial}{\partial \tau}[(G_{tr} + G_{st})E_{st}(\tau)] = C_{st}\vartheta_h^2 E_{st}(\tau). \tag{15}$$

For small conductivity of the streamer trace ($G_{tr} \longrightarrow 0$), the field is constant along the streamer zone ($E_{st}(\tau) = E_{st}(\tau = 0) = E_{st}$) if $G_{st} = C_{st}\vartheta_h^2 \tau$. The growth of G_{tr} in the stage of channel formation causes a decrease in the field. Note that the linear conductivity that is necessary to sustain the field of the streamer zone can be provided even by a solitary streamer, because the conducting zone widens due to the ionization of new areas by the transverse electric field [12].

Figure 8 presents the plots of the leader velocity versus potential obtained from equations (8)–(13) with field (15) for a ratio $\vartheta_h t_{st}/R_{st}$ between the length and radius of the streamer zone equal to 3 [1]. It is seen from the figure that taking into account the capacitance of the streamer zone results in the appearance of the threshold voltage V_{min} for leader breakdown, which

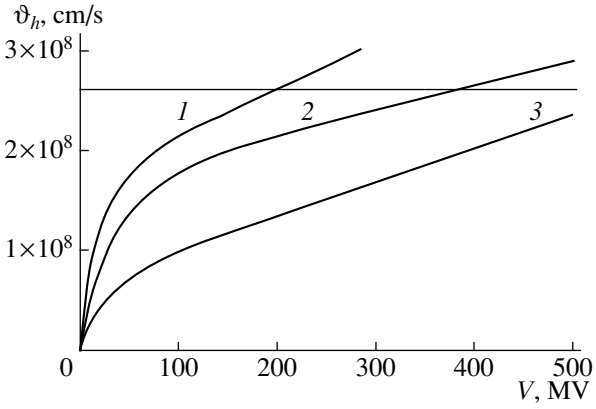

Fig. 7. The leader velocity vs. the potential V for $\alpha^* = (1)\ 2.5 \times 10^{-9}$, $(2)\ 5 \times 10^{-9}$, and $(3)\ 10^{-8}$ cm^3.

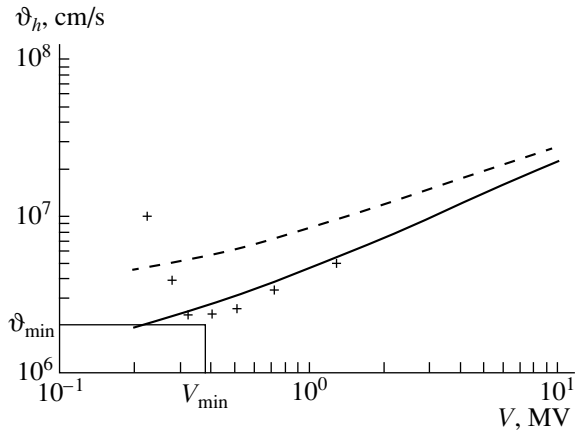

Fig. 8. The leader velocity vs. the potential V at $\alpha^* = 10^{-8}$ cm^3/s for $\vartheta_{dr} = 0$ and $C_0 = \infty$ (solid line), $\vartheta_{dr} \neq 0$ and $C_0 = \infty$ (dashed line), and $\vartheta_{dr} \neq 0$ and $C_0 \neq \infty$ (crosses).

corresponds to the minimum velocity ϑ_{min} of leader propagation. Laboratory studies yield the following minimum values of the leader velocity and potential: $\vartheta_{min} \sim 2 \times 10^6$ cm/s and $V_{min} \sim$ 300–400 kV [1].

In order to estimate the maximum leader length L_m, we present the cloud potential V_{cl} as a sum of the potential V of the streamer zone and the potential drop $V_c = E_c L$ along the channel. We assume that the field E_c is on the order of the arc field: $E_c(\text{V/m}) \cong A_1 J^{-0.5}$, where $J(\text{A}) = c_0\vartheta_h V_{cl}$ is the leader current, $c_0 \cong 8 \times 10^{-12}$ F/m, and $\vartheta_h(m/s) \cong A_2 V^{2/3}$. The value of $A_1 = 10^4(\text{VA}^{1/2})/\text{m}$ is obtained by interpolating the data from [13], and the value of $A_2 = 4.5\text{m}/(\text{V}^{2/3}\text{s})$ is obtained by interpolating curve *3* in Fig. 7. Finally, for the length and velocity of the leader, we obtain

$$L = \frac{\sqrt{c_0 A_2}}{A_1} V_{cl}^{11/6}\left(\frac{V}{V_{cl}}\right)^{1/3}\left(1 - \frac{V}{V_{cl}}\right), \qquad \vartheta_h = A_2 V^{2/3}. \tag{16}$$

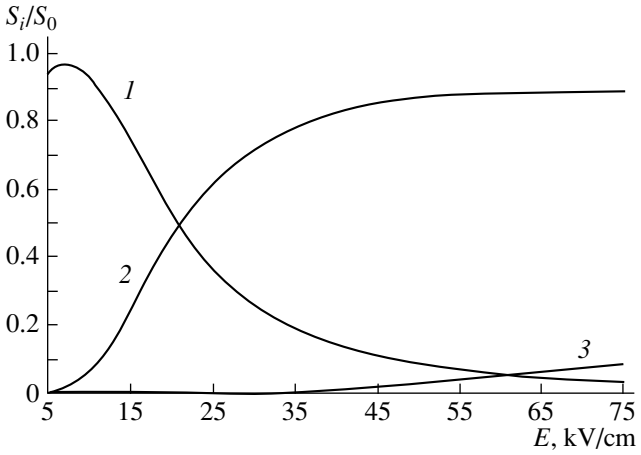

Fig. 9. The relative electron energy losses vs. the electric field: (*1*) vibrational excitation, (*2*) electronic excitation, and (*3*) ionization of air ($S_0 = \Sigma Si$).

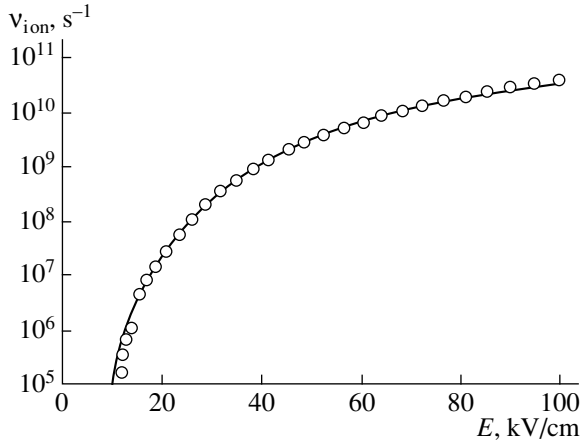

Fig. 10. The ionization rate vs. the electric field E: the solid line shows the experimental data from [35] and circles show the results of calculations by (A4).

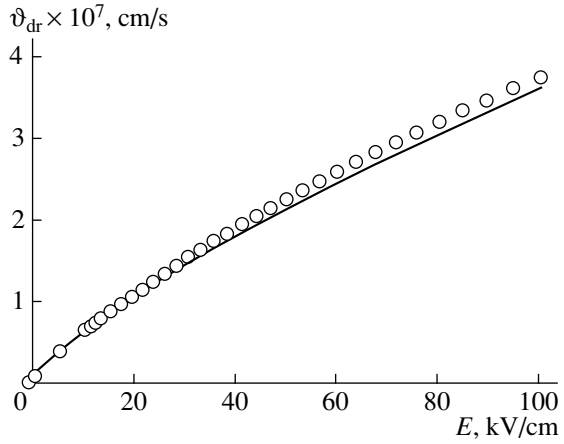

Fig. 11. The electron drift velocity vs. the electric field E. The notation is the same as in Fig. 10.

We estimate the maximum velocity of the leader assuming that $V = V_{cl}$, i.e., $\vartheta_m \cong 4.5 V_{cl}^{2/3}$. The length attains its maximum at $V = 0.25V_{cl}$: $L_m \cong 2.8 \times 10^{-10} V_{cl}^{11/6}$. Note that, for the leader length $L \ll L_m(V_{cl})$, we can neglect the potential drop along the channel and consider steady-state propagation.

For the maximum potentials of artificial lightning, we have $V_{cl} \cong 3$–5 MV, $L_m \cong 200$–500 m, and $\vartheta_m \cong 0.94$–1.3×10^5 m/s. The observed values are $L \cong 1000$ m and $\vartheta \cong 10^5$ m/s [1].

For the minimum lengths of natural lightning, we have $L \cong 10^3$ m, $V_{cl} \cong 7$ MV, and $\vartheta_m \cong 1.6 \times 10^5$ m/s. The observed value is $\vartheta \cong 10^5$ m/s [11].

For gigantic lightning, we have $V_{cl} \cong 500$ MV, $L_m \cong 2.5 \times 10^6$ m, and $\vartheta_m \cong 2.8 \times 10^6$ m/s.

DISCUSSION

The electron energy losses due to the excitation of electronic levels sharply increase in the fields $E \geq E^* \cong 10$ V/cm (Fig. 9). In the above analysis, the field E^* determines the threshold for leader breakdown in air. It is believed that the field in the streamer zone is $E_{st} \sim 5$ kV/cm [1]; i.e., E_{st} is close to the threshold for streamer breakdown E_{th} (Fig. 3, curve *2*). This is the main difference between the above concept and the generally accepted views [1].

Direct measurements of the field of the streamer zone in a rod–plane gap with a length up to 20 m [14] provide evidence of the validity of the relationship $E_{st} \sim E_{th}$. Those measurements were based on the Pockels effect; however, at the field strengths ≥2–3 kV/cm, correct measurements of the fields in air by detectors based on bismuth silicate crystals are hardly possible because of the field distortion by a local corona [1]. It is possible that multiple streamer breakdowns (corona) near the

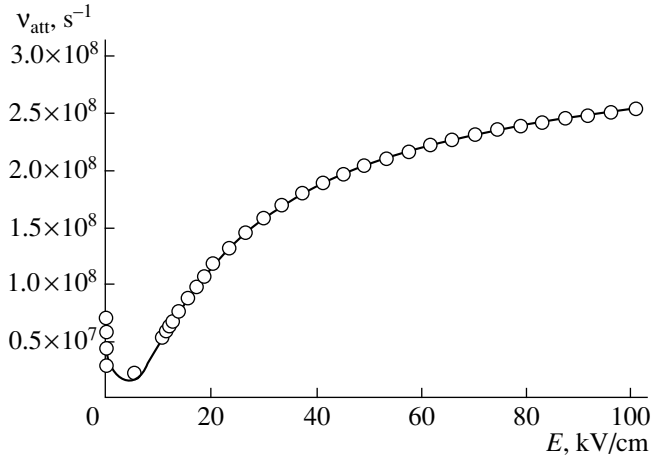

Fig. 12. The attachment rate vs. the electric field E. The notation is the same as in Fig. 10.

detector at the field strength $E > E_{th}$ decrease the local field strength to $E \sim E_{th}$. In this case, the results presented in [14] only allow one to be confident that the field in the streamer zone is greater than E_{th}.

The estimate $E_{st} \sim 1/\vartheta_{st} dV/dt \sim 12$ kV/cm obtained from an experimentally observed linear dependence of the velocity of a streamer starting from a point on the steepness of the front of the voltage pulse dV/dt at $\vartheta_{st} \geq 2 \times 10^5$ cm/s [3] provides indirect evidence in favor of the relationship $E_{st} \sim E^*$.

At fields of about E^*, the $N_2(A^2\Sigma_u^+)$ and $N_2(B^3\Pi_g)$ levels with the energies $I^* = 6.14$ and 7.3 eV, respectively, are mainly excited [15]. In the interaction with these molecules, the detachment rate constant is $\alpha^* \sim 2.5 \times 10^{-9}$ cm^3/s [1, 9]. An increase in α^* by a factor of 2–4 provides the best agreement with the experimental data. Additional channels of destruction of negative ions are provided by detachment in the interaction with molecules excited to higher electronic levels ($I^* \geq 10$ eV; the relative concentration of such particles is about 10%); detachment due to the interaction with resonant radiation; electron-impact detachment in the regions with high electron density, e.g., in the vicinity of the front of a streamer discharge (Fig. 3, curve *1*). This problem requires further investigation.

We did not manage to produce a similar steady-state regime of breakdown for a negative leader, because, in the stage of channel formation (Fig. 4), the electron drift velocity ϑ_{dr} exceeded the streamer velocity ϑ_{st}, which led to discharge termination [see the first equation in (10)].

CONCLUSIONS

We have considered a model of leader breakdown in air in which the channel is formed due to heating of the streamer trace in the field of the streamer zone, which is formed by a great number of streamers starting from the leader head [1]. The initial parameters of the plasma in the streamer trace are determined with the use of the previously developed model of streamer discharge [4], which was generalized by allowing for the recombination of charged particles. Detachment of electrons in the interaction of negative ions with electronically excited molecules plays the key role in the formation of the channel.

It is demonstrated that, in the steady-state regime, the channel is formed from streamer traces with a certain charge. The other streamers produce and sustain the field of the streamer zone.

We have found the penetration rate, the length of the streamer zone, and the length of the leader discharge as functions of the cloud potential. We have estimated the minimum potential that makes leader discharge possible and have found the corresponding propagation velocity.

It is the $N_2(A^3\Sigma_u^+)$ and $N_2(B^3\Pi_g)$ electronic levels that are mainly excited in the fields under consideration. The detachment rate constant in the interaction with these molecules is $\alpha^* \sim 2.5 \times 10^{-9}$ cm^3/s. An increase in α^* by a factor of 2–4 provides the best agreement with the experimental data. The problem of additional channels of destruction of negative ions requires further investigation.

For a negative leader, a similar steady-state regime of breakdown is impossible, because, in the stage of channel formation, the electron drift velocity is greater than the streamer velocity, which leads to current termination.

Within the model presented, the threshold (with respect to the formation of the leader discharge) field of the streamer zone, $E^* \cong 10$ kV/cm, is determined by a sharp increase in electron energy losses due to excitation of the electronic levels. Bazelyan and Raiser suggested [1] that the field of the streamer zone is close to the threshold field of the streamer discharge $E_{th} \cong 5$ kV/cm. There are arguments in favor of both hypotheses. In order to clarify this problem, further investigations are necessary.

APPENDIX

Reaction Rate Constants

The cross sections of interactions of electrons with molecular nitrogen and oxygen are studied in [16, 17]. Let us briefly describe the cross sections used in this paper. The dependences of the transport cross sections q_m of elastic collisions on the electron energy ε were taken from [18]. We follow [19, 20] in the description of rotational excitation. To determine the total cross sections, we take into account the smallness of the rotational constants ($B_0 = 2.5 \times 10^{-4}$ eV for N_2 and $B_0 = 1.8 \times 10^{-4}$ eV for O_2) and replace summation over the indices of the levels j with integration over j from $j = 0$ to $j = \infty$. For the deceleration cross section, we obtain

$$S_{in}^R = 4B_0\sigma_0\left(1 - \frac{kT}{\varepsilon}\right), \qquad \text{(A1)}$$

where $\sigma_0 = 8\pi/15(a_0)^2$, a_0 is the Bohr radius and Q is the quadrupole electric moment ($Q = 1.05$ for N_2 and $Q = 0.3$ for O_2).

When describing vibrational excitation, we only consider collisions of the first type, which means that we assume the molecules to be in the ground state. The excitation cross sections of the first eight levels of N_2 and four levels of O_2 can be found in [21] and [22], respectively.

The cross sections of the electronic excitation of molecular nitrogen are taken from [23] (for the $A^3\Sigma_u^+$ and $a^1\Pi_g$ states), [24] (for the $B^3\Pi_g$ and $C^3\Pi_u$ states), and [25] (for the $b^1\Pi_u$ and $b^1\Sigma_u^+$ states and the sum of

cross sections of the higher lying states). For molecular oxygen, the cross sections of the excitation of the $a^1\Delta_g$ and $b^1\Sigma_g^+$ states are taken from [15, 22] and the cross sections of the excitation of the $A^3\Sigma_u^+$ and $B^3\Sigma_u^-$ states and the sum of the cross sections of the higher lying states are taken from [25]. When describing electron-impact ionization, we restrict ourselves to the process starting from the ground state. The corresponding cross sections for N_2 and O_2 are taken from [26] and [27], respectively.

The cross sections of a three-particle attachment to O_2 are taken from [28], assuming O_2 to be the third particle. The dissociative attachment rates are determined based on the cross sections from [29].

The temperature dependences of the rates of production and annihilation of charged particles corresponding to the above cross sections are determined from the kinetic equation for the symmetric part of the electron distribution function f_0 [30],

$$\frac{\partial}{\partial\varepsilon}\left\{\left[\frac{e^2E^2}{N^2}\frac{\varepsilon}{3q_m(\varepsilon)}+kT\varepsilon^2\frac{m_e}{M}q_m(\varepsilon)\right]\frac{\partial}{\partial\varepsilon}f_0(\varepsilon)\right.$$

$$\left.+\varepsilon^2\frac{2m_e}{M}q_m(\varepsilon)f_0(\varepsilon)\right\}=\sum_i[\varepsilon Q_i(\varepsilon)f_0(\varepsilon)$$

$$-(\varepsilon+\varepsilon_i)Q_i(\varepsilon+\varepsilon_i)f_0(\varepsilon+\varepsilon_i)+\varepsilon Q_i^-(\varepsilon)f_0(\varepsilon) \qquad \text{(A2)}$$

$$-(\varepsilon-\varepsilon_i^-)Q_i^-(\varepsilon-\varepsilon_i^-)f_0(\varepsilon-\varepsilon_i^-)]+\varepsilon q_{\text{ion}}(\varepsilon)f_0(\varepsilon)$$

$$-2\int_{\varepsilon+I}^{\infty}\varepsilon' q_{\text{ion}}(\varepsilon')f_0(\varepsilon')\psi(\varepsilon',\varepsilon)d\varepsilon',$$

which is solved for various values of the ratio E/N according to the technique developed by Sherman [31]. From the distribution function f_0, we obtain the electron temperature

$$T_e=\frac{2}{3k}\int_0^{\infty}\varepsilon^{1/2}f_0(\varepsilon)d\varepsilon \qquad \text{(A3)}$$

and the corresponding rate constants of production and annihilation of charged particles, as well as the collision frequencies and the rates of energy losses [30, 32]. The obtained dependences of the rate constants on T_e are interpolated with the use of the analytical formulas ($[T_e]$ is in eV)

$$\nu_m=2.52\times10^{12}\delta\sqrt{T_e}[0.727$$

$$+T_e^{-2}\exp(-0.791/T_e^2)],\ \text{s}^{-1},$$

$$\nu_{\text{ion}}=8.975\times10^9\delta T_e^{9/2}(0.0018+T_e^{-11})$$

$$\times\exp(-10.13/T_e^2),\quad \text{s}^{-1},$$

$$\nu_{\text{ex}}=5.53\times10^6\delta T_e^2(1812.23+T_e^{-15})$$

$$\times\exp(-1.7835/T_e^2),\quad \text{s}^{-1},$$

$$\nu_{\text{att}}^3=3.075\times10^7\delta^2[0.08554$$

$$+T_e^{3/4}(1+16.23\exp(-0.734/T_e^2))]^{-1/2},\quad \text{s}^{-1}, \qquad \text{(A4)}$$

$$\nu_{\text{att}}^2=3.06\times10^8\delta$$

$$\times\exp\left[-\frac{69.6}{22.9T_e^{3/2}(1+10.1T_e^{-5.5}\exp(-2.53/T_e^2))}\right],\ \text{s}^{-1},$$

$$q_{\text{en}}+q_r=(8.15+6.39\times10^{-4}\nu_m\sqrt{T_e})$$

$$\times10^7\sqrt{T_e}(1-T/T_e)n_e,\ \text{eV/(s cm}^3),$$

$$q_V+q_{\text{ex}}=8.917\times10^{10}T_e^{-3}(9.93+T_e^5)$$

$$\times\exp(-2.36/T_e^3)n_e,\ \text{eV/(s cm}^3),$$

where ν_{att}^3 and ν_{att}^2 are the rates of three-particle and dissociative attachment, respectively: $\nu_{\text{att}}=\nu_{\text{att}}^3+\nu_{\text{att}}^2$.

We assume dissociative recombination and recombination in triple collisions to be the main channels of electron–ion and ion–ion recombination, respectively. The corresponding constants were determined from [33, 34]

$$\alpha_{\text{ei}}=3\times10^{-7}\left(\frac{300}{T_e}\right)^{1/2},\quad \text{cm}^3/\text{s},$$

$$\alpha_{\text{ii}}=2\times10^{-6}\delta\left(\frac{300}{T}\right)^{5/2},\quad \text{cm}^6/\text{s},\quad [T_e,T]=\text{K}, \qquad \text{(A5)}$$

where T_e and T are in K.

The rate of the bulk loss of electron energy due to ionization was determined from $q_i=I\nu_{\text{ion}}n_e$, where $I=14.9$ eV is the mean ionization potential of air molecules. We assume that the particles produced via electron–ion and ion–ion recombination and dissociative attachment remain in the ground state, so that all the released energy is transformed into heat. In this case, $q_{\text{ei}}=\alpha_{\text{ei}}(I_e+3/2kT_e)n_e^2$; $q_{\text{ii}}=\alpha_{\text{ii}}I_in_+n_-$, and $q_{\text{att}}=2\varepsilon_i\nu_{\text{att}}^2n_e$. The energies released in different elementary acts are assumed to be $I_e=6$ eV, $I_i=13.44$ eV, and $\varepsilon_i=1.35$ eV.

Figures 10–12 compare the ionization rates ν_{ion}, electron drift velocities ϑ_{dr}, and the attachment rates ν_{att} obtained from the experimental data [35] and from formulas (A4) at $\delta=1$. In the last case, the electric field E

corresponding to the temperature T_e was determined from [see (13), in which $\partial/\partial\tau$, $\partial/\partial r = 0$]:

$$\frac{e^2 n_e}{m_e \nu_m} E^2 = q_{\text{en}} + q_{\text{r}} + q_{\nu} + q_{\text{ex}} + q_i. \qquad \text{(A6)}$$

REFERENCES

1. É. M. Bazelyan and Yu. P. Raĭzer, *Spark Discharge* (Mosk. Fiz. Tekh. Inst., Moscow, 1997).
2. *The Theory of Electric Arc Columns*, Ed. by V. S. Éngel'sht and B. A. Uryukov (Nauka, Novosibirsk, 1990).
3. É. M. Bazelyan and A. Yu. Goryunov, Élektrichestvo, No. 11, 27 (1986).
4. A. V. Ivanovskiĭ, Zh. Tekh. Fiz. **66** (8), 59 (1996) [Tech. Phys. **41**, 778 (1996)].
5. I. Gallimberty, in *Proceedings of 2nd World Electrotechnical Symposium, Moscow, 1977*.
6. I. Gallimberty and A. Bondiou, J. Phys. D **27**, 1252 (1994).
7. S. K. Dhali and P. F. Williams, Phys. Rev. A **31**, 1219 (1985).
8. S. K. Dhali and P. F. Williams, J. Appl. Phys. **62**, 4696 (1987).
9. H. S. W. Massey, *Negative Ions* (Cambridge University Press, Cambridge, 1976; Mir, Moscow, 1979).
10. Ya. B. Zel'dovich and Yu. P. Raizer, *Physics of Shock Waves and High-Temperature Hydrodynamic Phenomena* (Nauka, Moscow, 1963; Academic, New York, 1966).
11. M. M. Uman, *Lightning* (McGraw-Hill, New York, 1969; Mir, Moscow, 1972).
12. A. V. Ivanovskiĭ, Zh. Tekh. Fiz. **65** (12), 48 (1995) [Tech. Phys. **40**, 1230 (1995)].
13. I. A. Krinberg, Zh. Tekh. Fiz. **38**, 1705 (1968) [Sov. Phys. Tech. Phys. **13**, 1382 (1968)].
14. N. I. Petrov, V. R. Avanskiĭ, and N. V. Bombenkova, Zh. Tekh. Fiz. **64** (6), 50 (1994) [Tech. Phys. **39**, 546 (1994)].
15. I. A. Krinberg, *Electron Kinetics in the Ionosphere and Plasmosphere of the Earth* (Nauka, Moscow, 1978).
16. N. L. Aleksandrov, A. M. Konchakov, and É. E. Son, Fiz. Plazmy **4**, 169 (1978) [Sov. J. Plasma Phys. **4**, 98 (1978)].
17. N. L. Aleksandrov, F. N. Vysikaĭlo, R. Sh. Islamov, *et al.*, Teplofiz. Vys. Temp. **19**, 350 (1981).
18. I. Shimamura, Sci. Pap. Inst. Phys. Chem. Res. (Jpn.) **82**, 1 (1989).
19. E. Gerjuoy and S. Stein, Phys. Rev. **97**, 1671 (1955).
20. E. Gerjuoy and S. Stein, Phys. Rev. **98**, 1848 (1955).
21. G. J. Schulz, Phys. Rev. A **135**, 988 (1964).
22. F. Linder and H. Schmidt, Z. Naturforsch. A **26**, 1617.
23. W. L. Borst, Phys. Rev. A **5**, 648 (1972).
24. P. N. Stantonf and R. M. S. John, J. Opt. Soc. Am. **59** (3), 252 (1969).
25. A. E. S. Green and R. S. Stolarski, J. Atmos. Terr. Phys. **34**, 1703 (1972).
26. D. Rapp and P. Englander-Golden, J. Chem. Phys. **42**, 4081 (1965).
27. J. T. Tate and P. T. Smith, Phys. Rev. **39**, 270 (1932).
28. D. Spence and G. J. Schulz, Phys. Rev. A **5**, 724 (1972).
29. D. Rapp and D. D. Briglia, J. Chem. Phys. **43**, 1480 (1965).
30. L. G. H. Huxley and R. W. Crompton, *The Diffusion and Drift of Electrons in Gases* (Wiley, New York, 1974; Mir, Moscow, 1977).
31. B. Sherman, J. Math. Anal. Appl. **1**, 342 (1960).
32. A. V. Ivanovskiĭ, Zh. Tekh. Fiz. **68** (6), 37 (1998) [Tech. Phys. **43**, 648 (1998)].
33. A. V. Eletskiĭ and B. M. Smirnov, Usp. Fiz. Nauk **136** (1), 254 (1982).
34. J. J. Tomson, Philos. Mag. **47**, 337 (1924).
35. A. I. Golubev, A. V. Ivanovskiĭ, A. A. Solov'ev, *et al.*, Vopr. At. Nauki Tekh., Ser.: Teor. Prikl. Fiz., No. 2, 17 (1985).

Translated by A. Chikishev

Technical Physics, Vol. 45, No. 6, 2000, pp. 720–726. Translated from Zhurnal Tekhnicheskoĭ Fiziki, Vol. 70, No. 6, 2000, pp. 52–57.

Porous Generator of Thermonuclear Fuel Pellets

I. V. Viniar and A. N. Shlyakhtenko

PELIN Laboratory, Moscow, 212125 Russia

Received June 21, 1999

Abstract—A model of solid hydrogen isotope pellet formation is proposed for an original porous generator employed in the system of periodic particle injection into the plasma of thermonuclear devices. The results of model calculations show that the frequency of 3-mm pellet formation in this system may reach up to 2, 1.3, and 1 Hz for hydrogen, deuterium, and tritium, respectively. © *2000 MAIK "Nauka/Interperiodica"*.

INTRODUCTION

A widely recognized method of maintaining thermonuclear reactions consists in injecting macroparticles (pellets) of solid hydrogen isotopes into the plasma of thermonuclear devices [1]. Many of these devices are equipped with pellet generators which, together with the gas injection valves, constitute a base of the fuel supply system. Most frequently employed are pneumatic injectors, in which the pellets are accelerated with compressed air (like projectiles in a gun barrel) up to a velocity of 1–3 km/s and injected into the plasma. The problem of injector development reduces to designing a device capable of generating solid pellets of hydrogen isotopes with a temperature of about 10 K at a steady-state production rate above 1 Hz and a reliability of operation exceeding 95%.

Several possible designs of the pellet generator have been proposed [2–7]. In the Zambony generator [2], the gas is continuously frozen onto the rim of a rotating disk and the ice is periodically cut off. However, this device provides pellet production in a steady-state regime at a frequency not exceeding 0.2 Hz. Another generator [3], consisting of a system of three switched piston extruders pressing a fuel ice rod cut into pellets, requires keeping a large stock of fuel, which is rather dangerous (especially when working with tritium). More promising systems are apparently offered by generators using "gas" or screw extruders [4, 5]. Here, obvious disadvantages are a rather high gas pressure (10 MPa) in the first case and a quite large necessary fuel stock (reaching several grams) in the latter case (again, undesired when dealing with tritium).

Recently [6], a new generator scheme was proposed in which the fuel pellets are formed upon melting a small volume of solid fuel continuously frozen in a porous sleeve, essentially representing a short part of the injector barrel, followed by the liquid phase leaking and freezing again in the barrel. The first tests showed [7] that solid hydrogen pellets 3 mm in diameter can be formed in such a system at a frequency of 0.1 Hz. To increase the rate of pellet production, it was necessary to optimize the system design. The task of this work was to develop a model of particle formation in the proposed porous generator and perform the optimization procedure based on this model.

PELLET FORMATION MODEL

Prior to estimating the minimum time required for pellet formation in the proposed generator, let us determine the maximum barrel diameter for which a liquid drop of fuel will not spread over the surface. Consider a liquid drop occurring in equilibrium inside a horizontal round barrel. The orthogonal coordinate axes x and y perpendicular to the barrel axis are conveniently oriented in the horizontal and vertical directions as depicted in Fig. 1. Let the saturated vapor pressure and the liquid-phase pressure at the point $y = R$ in the barrel be P_s and P_R, respectively, where R is the barrel radius. The free surface of the liquid is described by the function $u(x, y)$. A static equation for this system describes the balance of gravity and surface tension forces [8]:

$$\sigma_2 \operatorname{div}\left(\frac{\nabla u(x, y)}{\sqrt{1 + [\nabla u(x, y)]^2}}\right) = \rho_2 g(R - x) + (P_R - P_s), \quad (1)$$

where ρ_2 and σ_2 are the density and the surface tension coefficient of the liquid, respectively, and g is the accel-

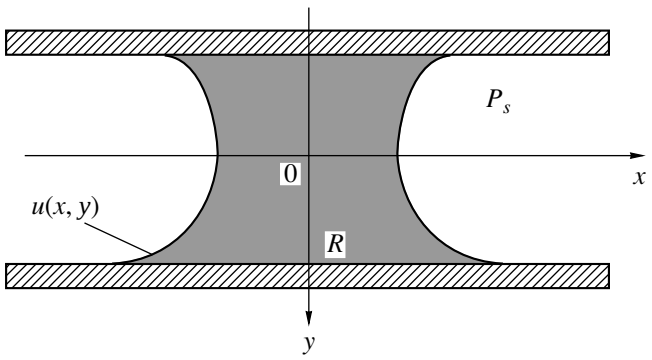

Fig. 1. Schematic diagram showing a liquid fuel drop in the injector barrel.

1063-7842/00/4506-0720$20.00 © 2000 MAIK "Nauka/Interperiodica"

eration of gravity; here and below, the indices 1–3 refer to the solid, liquid, and gas phases of the fuel, respectively.

Integrating equation (1) over the barrel cross section $x^2 + y^2 \le R^2$ and using the Ostrogradsky–Gauss theorem, we obtain a relationship

$$2\sigma_2 \cos\varphi = \rho_2 g R^2 + (P_R - P_s)R,$$

where φ is the contact angle for the liquid on the barrel surface. This relationship yields a formula for the barrel radius:

$$R = \sqrt{\frac{2\sigma_2 \cos\varphi}{\rho_2 g} + \left(\frac{P_R - P_s}{2\rho_2 g}\right)^2} - \frac{P_R - P_s}{2\rho_2 g}. \quad (2)$$

As is seen from this expression, the maximum possible radius is that corresponding to $P_R = P_s$. Taking into account that liquid hydrogen almost perfectly wets the barrel surface, we obtain a final expression for the maximum barrel radius R_{max} at which the fuel drop will not spread over the surface:

$$R_{max} = \sqrt{\frac{2\sigma_2}{\rho_2 g}}. \quad (3)$$

Calculations by formula (3) performed for the ρ_2 and σ_2 values taken from [9] showed that the surface tension would prevent drops of hydrogen, deuterium, and tritium with radii below 2.8, 2.1, and 1.85 mm, respectively, from spreading in the barrel. Of course, the liquid fuel can be frozen in a barrel of greater radius as well, but in this case the liquid would partly spread on the surface, vaporize, and condense again onto the surface of ice formed in the barrel. Increased duration of this process would render the system hardly applicable to periodic fuel injection.

The new principle of pellet formation consists essentially in pulsed heating and melting of the fuel in the pores of the injector, whereby the melted fuel would leak through the pores into the injector barrel to freeze there again [6]. Since a generator with fuel operating in this mode has to be periodically heated only by 5–10 K, the time of pellet formation would markedly decrease compared to the time usually required to freeze a portion of the gas in the barrel by cooling the fuel from 290 to 10 K.

As is seen from the scheme presented in Fig. 2, the accelerating gas, driving pellet *1* in barrel *2*, enters (at room or elevated temperature) via valve *4* and passes via tube *3* through pellet generator *5* (cooled down to approximately 10 K), thus heating this part of the injector. If the solid fuel, melted by heat delivered with the gas, penetrates through sleeve *6* into the barrel, the whole process of pellet formation will be self-sustaining, requiring no drives or mechanisms. This circumstance would render the generator simple in design and use, markedly increasing the reliability of the system. Liquid helium permanently circulating inside heat exchanger *7* cools the generator so that the accumulated liquid fuel freezes inside the injector barrel and in the porous generator. The volume of the porous sleeve, emptying when the liquid drop leaks into the barrel, is rapidly filled with a new portion of fuel condensing on the developed pore surface.

The purpose of developing the proposed model consists in evaluating the minimum time necessary for pellet formation, depending on the characteristic of the fuel and the parameters of the system design.

The amount of heat delivered to the generator with the accelerating gas can be evaluated by using, in the first approximation, a relationship between the Nusselt number (Nu) for a steady-state gas flow in a round tube and the Reynolds (Re) and Prandtl (Pr) numbers [10]:

$$\mathrm{Nu} = 0.023\mathrm{Re}^{0.8}\mathrm{Pr}^{0.4}. \quad (4)$$

The local Re and Pr values can be calculated using the cross-section-average parameters of a given accelerating gas with allowance for its adiabatic expansion upon entering the barrel from a shot valve volume of about 6 cm^3. Assuming the gas enthalpy variation to be small (despite the heat exchange with the barrel walls), the gas escape time t^* from the barrel can be estimated by the formula [11]

$$t^* = \frac{S}{8a_3}\left(\frac{P_0}{P_3}\right)^{1/7}\left[3 + 2\left(\frac{P_0}{P_3}\right)^{2/7} + 3\left(\frac{P_0}{P_3}\right)^{4/7}\right], \quad (5)$$

where P_0 and P_3 are the initial and final gas pressure in the barrel, a^3 is the sound velocity in the unperturbed gas, and S is the barrel length (including the inlet tube carrying the gas ejected from the shot valve).

Let us assume that the heat supplied to the system by the accelerating gas to the barrel and the inlet tube and removed in the steady-state regime by the injector cooling system is transferred only within small parts of the inlet tube *2*, barrel *3*, and the generator surface contacting the gas (Fig. 2). For definiteness, we also assume that the pellet length, porous sleeve thickness, and barrel diameter have equal values and the heat-exchange area between gas and generator is two times the pellet surface area. Under these assumptions, the heat transferred from gas to generator during every cycle can be calculated using the heat-exchange coefficient $\alpha_g(t)$ expressed via the Nusselt number (4), and the gas temperature can be determined using equation (5). We assume that the main heat exchange takes place within a time period during which the accelerating gas (helium) pressure in the barrel drops from 5 MPa to 10 kPa. The barrel length (with the gas inlet tube) is taken equal to $S = 460R$.

The amount of fuel that must be melted in the generator pores so as to form a pellet is equal to the sum of the mass of the liquid pellet and the mass of the saturated vapor in the barrel (necessary to provide for equilibrium of the drop). For a linear variation of the temperature from T_0 (room temperature) to the generator

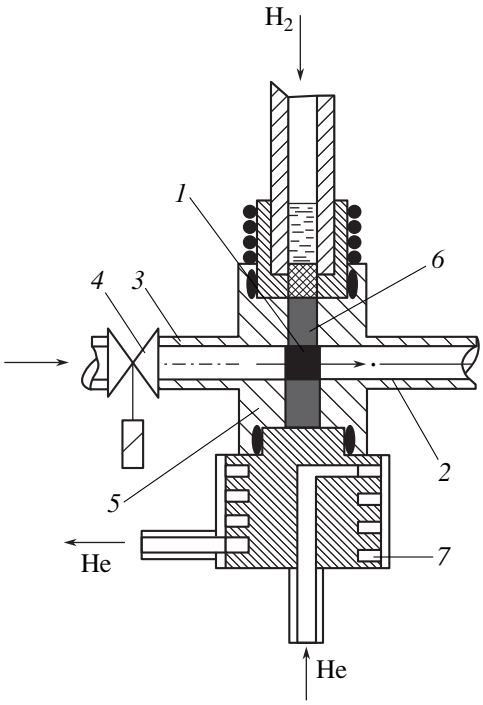

Fig. 2. Schematic diagram of a fuel injector with the proposed porous generator (see the text for explanations).

temperature T, the required mass of the melted solid fuel m^* is not less than

$$m^* = \pi R^2\left[2R\rho_2 + S\rho_s\frac{T}{T_0 - T}\ln\left(\frac{T_0}{T}\right)\right], \qquad (6)$$

where ρ_2 and ρ_s are the densities of the liquid fuel and its vapor at the melting point, respectively.

In order to ensure that a part of the fuel will freeze in the pores, preventing new portions from leaking into the barrel, the mass of the fuel inside the pores must somewhat exceed that calculated by formula (6):

$$m = nm^*. \qquad (7)$$

In order to estimate the minimum time required to form a new pellet, we will take $n = 1.2$. Estimates of the time required for heating and cooling the generator filled with solid fuel can be obtained using equations of the energy balance of a system including the generator, the solid and liquid fuel in the pores, and the pellet frozen in the barrel. We will use the approximation of spherical pores uniformly distributed over the sleeve volume and assume that the porous copper sleeve, owing to a high thermal conductivity, has the same temperature over the entire volume. Then, the generator cooled by liquid helium with a heat transfer coefficient α_{He} is descried by the following balance equation:

$$q_g + q_w + q_c - q_p - q_m - \alpha_{He}(T - T_{He})F = Mc\frac{dT(t)}{dt}, \qquad (8)$$

where q_g, q_w, q_c, q_p, and q_m denote the thermal fluxes from accelerating gas and additional heater, the constant heat supply, the heat delivered to the solid/liquid fuel in the pores and to the pellet frozen in the barrel; T_{He} is the constant temperature of helium in the heat exchanger; F is the heat exchanger area; and M and c are the intrinsic mass and heat capacity of the generator (without fuel in the pores).

The constant heat supply to the generator, which can be reduced down to a level below 0.1 W, will be neglected as compared to the other contributions entering into equation (8). The thermal flux to the pores is determined as

$$q_p = 4\pi r_p^2 N\lambda_i\frac{\partial\Theta_i(r,t)}{\partial r} \quad \text{at} \quad r = r_p,$$
$$N = \frac{3m}{4\pi r_p^3}, \qquad (9)$$

where $\Theta_i(r, t)$ is the temperature of the ith phase of fuel in the pores; N is the effective number of pores in the generator, equal to the ratio of the total volume of fuel in the pores to a single pore volume for the average pore radius r_p; λ_i is the thermal conductivity of the fuel; and $i = 1, 2$ for the solid and liquid fuel phase, respectively.

Let r_s be a radial coordinate of the spherical surface separating sold and liquid fuel phases inside a pore. The energies of both phases can be expressed as

$$\rho_i c_i\frac{\partial\Theta_i(r,t)}{\partial t} = \frac{1}{r^2}\frac{\partial}{\partial r}\left(\lambda_i r^2\frac{\partial\Theta_i(r,t)}{\partial r}\right), \qquad (10)$$

where c_i are the specific heat capacities of the fuel phases at constant pressure.

We assume that the generator temperature does not exceed the boiling temperature of the fuel, so that no vaporization takes place at the metal–fuel interface. Then, the boundary conditions can be formulated as

$$\Theta_i = T \quad \text{at} \quad r = r_p, \quad \frac{\partial\Theta_i}{\partial r} = 0 \quad \text{at} \quad r = 0,$$
$$\Theta_1 = \Theta_2 = T_s \quad \text{at} \quad r = r_s \qquad (11)$$

and the Stefan condition at the phase transition boundary as

$$\lambda_2\frac{\partial\Theta_2}{\partial r} - \lambda_1\frac{\partial\Theta_1}{\partial r} = \rho_1 L\frac{dr_s}{dt} \quad \text{at} \quad r = r_s, \qquad (12)$$

where T_s and L are the temperature and latent heat of fusion of the fuel.

As the fuel is melted, the liquid penetrates through the pores into the barrel. If the fuel is again frozen at the time instant when the amount of liquid in the barrel is m^*, then the pellet freezing time will be minimum and the porous sleeve will essentially play the role of a dosing valve for liquid fuel delivery to the barrel.

In order to estimate the time required for the liquid to leak into the barrel, it is necessary to consider the dynamics of liquid fuel flowing through the given porous medium. However, it is clear that the nonlinear character of the Navier–Stokes equations, together with the impossibility of determining the positions of surfaces at which the necessary boundary conditions can be formulated, hinder the obtaining of a rigorous solution for the flow velocities. However, provided that the Reynolds numbers are small, the effect of inertial forces can be neglected in comparison with the viscous forces and the flow of liquid in a porous medium can be described with sufficient precision by the following equation [12]:

$$U = \frac{1}{K\mu}\frac{\varepsilon^2}{A^2}\frac{\Delta P}{h}, \qquad (13)$$

where U is the mean rate of liquid filtration through the porous medium, $K = 5.0$ is the Kozeny empirical coefficient, μ is the coefficient of dynamic viscosity, ε is the ratio of the total pore volume to the porous sleeve volume, A is the total specific pore surface (per unit volume), ΔP is the driving pressure gradient, and h is the height of the porous sleeve above the barrel axis.

Using equation (13), we determine the filtration time required for the preset amount of liquid to accumulate in the injector barrel:

$$t_f = \frac{1}{4}K\mu\left(\frac{A}{\varepsilon R}\right)^2\frac{hm^*}{\rho_2\Delta P},$$

or after some transformations,

$$t_f = \frac{9K\mu}{n}\left(\frac{h}{r_p}\right)^2\frac{1}{\Delta P}. \qquad (14)$$

The cycle of pellet formation is terminated by freezing in the barrel. This process begins as soon as the generator temperature decreases below the melting point of the fuel and proceeds simultaneously with fuel cooling and freezing in the pores. Calculation of the time required for this process is based on solving the Stefan problem with boundary conditions of the third kind, which is analogous to the problem of fuel freezing in the pores. Thus, each phase of fuel in the barrel is described by the equation

$$\rho_i c_i\frac{\partial\Psi_i(r,t)}{\partial t} = \frac{1}{r}\frac{\partial}{\partial r}\left(\lambda_i r\frac{\partial\Psi_i(r,t)}{\partial r}\right) \qquad (15)$$

with the boundary conditions

$$\Psi_i = T \quad \text{at} \quad r = R,$$
$$\frac{\partial\Psi_i}{\partial r} = 0 \quad \text{at} \quad r = 0, \qquad (16)$$
$$\Psi_1 = \Psi_2 = T_s \quad \text{at} \quad r = r_c,$$

and the Stefan condition at the phase transition boundary

$$\lambda_2\frac{\partial\Psi_2}{\partial r} - \lambda_1\frac{\partial\Psi_1}{\partial r} = \rho_1 L\frac{dr_c}{dt} \quad \text{at} \quad r = r_c, \qquad (17)$$

where r_c is the radial coordinate of the spherical surface separating solid and liquid fuel phases in the barrel. The set of equations (4), (5), (8)–(12), (14), and (15)–(17) were solved by numerical methods. The mass of copper and the number of pores were selected so as to ensure that the heat transferred by the accelerating gas would not increase the temperature of the generator (with a given heat capacity) up to the boiling point of the fuel (to avoid undesired vaporization), while melting all the fuel filling the pores.

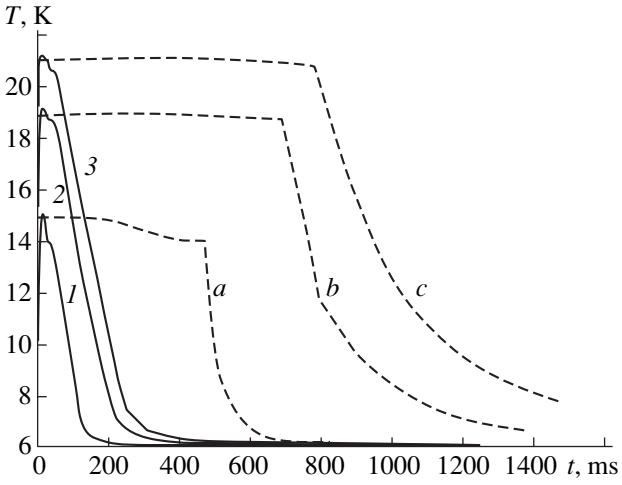

Fig. 3. Time variation of (*1–3*) the temperature of the porous generator sleeve filled with hydrogen, deuterium, and tritium, respectively, and (*a–c*) the temperature on the axis of the corresponding pellets.

Figure 3 (solid curves) shows the results of calculations of the temperature–time profiles during heating and cooling of the porous generator containing hydrogen or its isotopes in the pores. Also presented in Fig. 3 (dashed curves) are the profiles of temperature variation with time on the axis of pellets. The calculations were performed for a generator with a mass of 30 g and a pore diameter of 0.06 mm, forming pellets with a diameter and length of 3 mm. This size is of interest for thermonuclear setups such as JET (Great Britain), LHD (Japan), and Tore-Supra (France). The coolant (helium) temperature was taken equal to 6 K, the heat exchanger surface was 10 cm^2, and the coolant heat transfer coefficient was calculated for a helium flow rate of 10 h^{-1}. As is seen, heating of the generator with the pores filled with solid fuel takes about 20–30 ms, which is approximately equal to the time of accelerating gas escape from the barrel. Cooling the generator to the initial temperature level prior to every injection cycle (10, 16, and 19 K for hydrogen, deuterium, and tritium, respectively) proceeds at a threefold slower rate (because of the less effective heat exchange with liquid helium) and

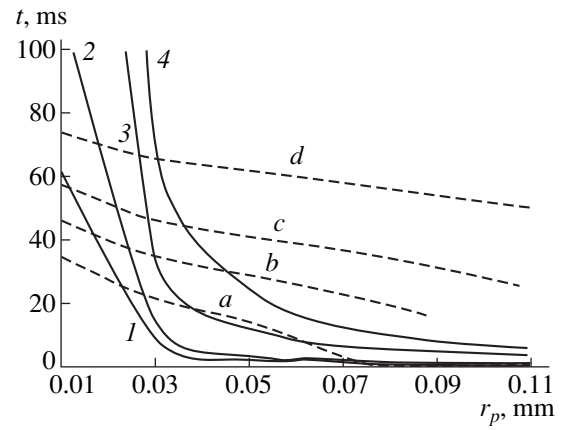

Fig. 4. The plots of (*1–4*) the time required for accumulation of a liquid hydrogen mass m^* in the injector barrel at an input fuel pressure of 0.1, 0.05, 0.02, and 0.01 MPa, respectively, and (*a–d*) the sleeve open state duration for an additional heating power of 0, 5, 10, and 20 W, respectively, versus the generator pore radius.

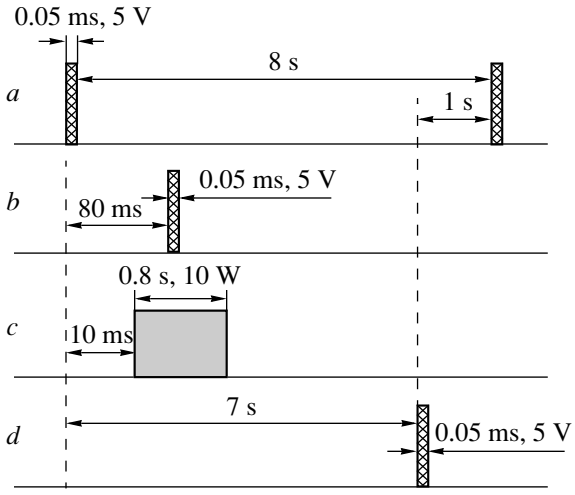

Fig. 5. Time schedule of pulses in a working cycle of pellet formation: (*a*) shot valve opened; (*b*) gate valve closed; (*c*) additional heater switched on; and (*d*) gate valve opened.

is less dependent on the fuel type. The longest stage in the pellet formation cycle is that of fuel freezing in the barrel, which takes about 0.45, 0.70, and 0.80 s for hydrogen, deuterium, and tritium, respectively. Another 50 ms are required for cooling the frozen fuel to a temperature 4–5 K below the solidification point.

The results of calculations presented in Fig. 3 show that the time of pellet solidification in the injector barrel exceeds the time of fuel melting and freezing in the pores. This is valid for the pore size below 0.2 mm. If the pore diameter increases, the liquid fuel penetrates into the barrel faster and it is difficult to provide for a dosed fuel admission at the expense of rapid cooling of the porous sleeve only. Oscillations in the gas pressure at the generator input or in the vapor pressure in the barrel readily break the conditions of liquid drop equilibrium (1), whereby an excess amount of liquid fuel may leak into the barrel. This circumstance increases the time of pellet formation and violates stable operation of the generator. Therefore, the pore size should be selected based on the optimum time of liquid fuel leakage into the barrel.

According to the results of numerical modeling, the time of accumulation of the required volume of liquid fuel for a generator pore radius from 0.01 to 0.05 mm is approximately equal to the time during which the sleeve temperature exceeds the fuel melting point. The latter state is called the open state of the porous sleeve. Figure 4 shows calculated plots of (*1–4*) the time t_f required for accumulation of the liquid fuel necessary to form a pellet and (*a–d*) the time of the open state of the sleeve versus the pore radius for various levels of the additional power supplied to heat the generator. The height of the porous sleeve was taken equal to 25 mm. The data presented in Fig. 4 indicate that, in order to increase stability of the system operation and facilitate control of pellet formation, it is necessary to ensure that the open state duration (i.e., the time of liquid fuel accumulation in the barrel) is sufficiently long (tens of milliseconds) at a minimum additional heating power (still sufficient to melt all fuel in the pores). The additional heating power strongly influences the open state duration and can be used, together with the fuel gas pressure, to effectively control the process of liquid fuel melting and filtration into the injector barrel.

An analysis of the calculated results showed that the following conditions have to be satisfied to reach the minimum time of pellet formation (for the pellet size below 4 mm): generator mass, $M < 50$ g; pore radius, $r_p < 0.05$ mm; total pore volume must not be greater than four times the pellet volume; and refrigerating capacity must be maximum (not less than 7 W at 4.2 K). For example, in a 20-g generator with a pore radius of 0.03 mm, a fuel stock coefficient of $n = 2$, and a refrigerating capacity of 7 W, the time required to form a 3-mm solid hydrogen pellet is 0.5 s, the corresponding values for deuterium and tritium being 0.8 and 1.0 s, respectively.

EXPERIMENTAL RESULTS

The purpose of our experiments was to determine the minimum time of pellet formation in a porous generator and to compare this value to the results of calculations based on the model described above. The experiments were performed with a generator weighing 77 g mounted in an injector [13] equipped with a programmed controller.

Figure 5 shows the time schedule of control pulses generated by the controller in a working cycle of pellet formation and injection. The cycle begins with a pulse opening the valve admitting the accelerating gas. Then, 10 ms after the valve opening, the additional heater was

switched on to operate for 0.4–0.8 s. During this period, the gate valve was closed (10–80 ms after the starting pulse) and solid fuel (hydrogen) melted in the pores and leaked into the injector barrel. During the whole experiment, gaseous hydrogen at a pressure of 0.1 MPa was supplied to the input tube of the porous generator. The injector design allowed visual monitoring of the barrel into which liquid hydrogen leaked through the porous sleeve. Within less than 0.5 s after the cycle started, hydrogen melted in the pores and leaked out to fill the barrel. This portion of liquid hydrogen was frozen within 6–7 s, and then the gate valve was opened. The next shot was produced 1 s after opening the gate. The accelerating gas and that formed upon pellet impact onto the diagnostic chamber flange and evaporation were evacuated by a pumping system, and the cycle was repeated.

Thus, in the steady-state regime of injector operation, the total time of pellet formation was about 8 s. Attempts at reducing this time showed that the generator was capable of producing pellets in a period of 6 s. However, the video record of flying pellets in this case frequently revealed a smeared, apparently snowy, axial trace. The probability of injecting intact pellets dropped from 80 to 50%.

Figure 6 shows plots of the generator temperature versus time over the working cycle. Curve *1* is the temperature variation measured by a sensor mounted near the porous sleeve, and curve *2* presents the results of calculation for the same generator. As is seen, the two plots are sufficiently close to each other, which confirms the applicability of the proposed model to a description of the process of pellet formation in the porous generator and minimization of the pellet formation time. The temperature profile measured by the sensor was reproduced from cycle to cycle, which is evidence of stable operation of the system. The video record of flying pellets allowed their quality, dimensions, and velocities to be evaluated. According to these data, the pellets appeared as transparent ice columns, containing no noticeable cracks or cleavages, with a diameter of 2.4 mm and a length of 3–4 mm. Some decrease in the pellet size as compared to the barrel diameter (2.7 mm) is explained by friction-induced sublimation of fuel from the side surface of pellets moving in the barrel, in agreement with the experiments using injectors of other types [3] and with the results of model calculations [14].

We have studied the system operation during several series of injection cycles, with the total number of pellets above one thousand. The pellet velocities were determined by monitoring their position relative to a measuring scale in the video frame and by measuring the delay time between the starting pulse and the instant when the pellet crossed a laser pulse focused on the photodetector. The experimental pellet velocities varied within 1.1–1.2 km/s for a system using acceleration with helium at a pressure of 7 MPa.

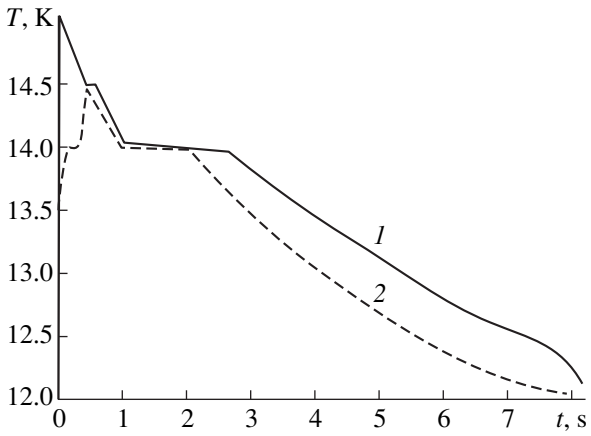

Fig. 6. Time variation of the generator temperature over the working cycle of hydrogen pellet formation: (*1*) experiment; (*2*) model calculation.

CONCLUSION

We have completed the first stage of tests on pellet generators of a new type, capable of producing an unlimited number of fuel pellets in a steady-state periodic operation mode. The generators are referred to as porous, since the main element is a porous metal sleeve filled with a thermonuclear fuel. A generator with a mass of 77 g formed solid hydrogen pellets with a diameter of 2.4 mm and a length of 3–4 mm at a frequency of 0.125 Hz. In order to design generators with increased injection frequency, we have developed a model for calculation of the regime of system operation, which allows the pellet formation time to be reduced by selecting optimum structural parameters of the porous generator. The results of model calculations showed that a generator with a mass below 50 g and a pore diameter below 0.1 mm may provide a pellet formation frequency of up to 1–2 Hz. In the second stage of this work, we are planning to perform the tests with generators weighing about 30 and 40 g.

An advantage of the new type of pellet generator is that the fuel stock in the system at each time instant does not exceed a few pellet volumes. This feature makes the new system more attractive for handling tritium as compared to existing extruders containing a fuel volume amounting to hundreds of pellets. The proposed generator involves no moving parts, which increases reliability of the system and makes it an acceptable part for the fuel injection systems in thermonuclear devices of long-term operation.

ACKNOWLEDGMENTS

The authors are grateful to S. Sudo (National Institute for Fusion Science, Japan) for his support and attention to this work, and for kindly providing the opportunity for performing some tests with our generator at the NIFS facilities.

REFERENCES

1. S. Milora, W. Houlberg, L. Lenguel, and V. Mertens, Nucl. Fusion **35**, 657 (1995).
2. S. Combs, Rev. Sci. Instrum. **64**, 1679 (1993).
3. S. Combs, C. Foust, and A. Qualls, Rev. Sci. Instrum. **69**, 4012 (1998).
4. I. V. Viniar, B. V. Kuteev, S. V. Skoblikov, *et al.*, Zh. Tekh. Fiz. **65** (7), 167 (1995) [Tech. Phys. **40**, 723 (1995)].
5. I. V. Viniar, S. V. Skoblikov, and P. Yu. Koblents, Zh. Tekh. Fiz. **68** (5), 117 (1998) [Tech. Phys. **43**, 588 (1998)].
6. I. V. Viniar, RF Patent No. 1611139, Otkrytiya, Izobret. **15**, 223 (1997).
7. I. Viniar and S. Sudo, Rev. Sci. Instrum. **68**, 1444 (1997).
8. R. Finn, *Equilibrium Capillary Surfaces* (Springer-Verlag, New York, 1986; Mir, Moscow, 1989).
9. P. C. Souers, in *Hydrogen Properties for Fusion Energy*, (University of California Press, Berkeley, 1986), p. 391.
10. *The Theory of Heat-and-Mass Transfer*, Ed. by A. I. Leont'ev (Vysshaya Shkola, Moscow, 1979).
11. *Gasodynamic Principles of Interior Ballistics*, Ed. by K. P. Stanyukovich (Oboronizdat, Moscow, 1957).
12. M. É. Aérov and O. M. Todes, *Fixed- and Fluidized-Bed Apparatuses: Hydraulic and Thermal Principles of Operation* (Khimiya, Moscow, 1968).
13. I. Viniar, A. Umov, and S. Sudo, Plasma Devices Op. **6** (1–3), 219 (1998).
14. I. V. Viniar and A. N. Shlyakhtenko, Izv. Ross. Akad. Nauk, Mekh. Zhidk. Gaza, No. 1, 3 (1999).

Translated by P. Pozdeev

Technical Physics, Vol. 45, No. 6, 2000, pp. 727–731. Translated from Zhurnal Tekhnicheskoĭ Fiziki, Vol. 70, No. 6, 2000, pp. 58–62.

A Modified Paschen Law for the Initiation of a DC Glow Discharge in Inert Gases

V. A. Lisovskiĭ and S. D. Yakovin

Kharkov State University, ul. Svobody 4, Kharkov, 310077 Ukraine

Received June 22, 1999

Abstract—Breakdown of inert gases in a homogeneous dc electric field is studied experimentally and theoretically at various distances L between the electrodes and radii R of the discharge tubes. It is shown that, for arbitrary geometric dimensions of the discharge chamber and cathode materials, the ratio of the breakdown electric field strength to the gas pressure holds constant at the breakdown curve minimum. A modified Paschen law is obtained, according to which the breakdown voltage is a function of both the product of the gas pressure by the distance L and the ratio L/R. *© 2000 MAIK "Nauka/Interperiodica".*

INTRODUCTION

The dc glow discharge is widely used for obtaining thin polymer and oxide films, cleaning surfaces of materials, pumping gas-discharge lasers, in plasma displays, voltage stabilizers, etc. Therefore, studying the conditions for glow discharge initiation is of significant interest. As is known [1–7], the dc glow-discharge breakdown curves are described by the Paschen law $U_{dc} = f(pL)$; i.e., the breakdown voltage U_{dc} is a function of the product of the gas pressure p and distance between the electrodes L. This means that the breakdown curves $U_{dc}(p)$ obtained for various distances L must be superimposed on each other when being plotted as the function $U_{dc}(pL)$. However, in some experimental studies it was revealed that, at equal values of the product pL, the breakdown voltage for a long discharge gap with flat electrodes is appreciably higher than for a short gap [4, 8–17].

In this work, we have studied experimentally and theoretically the breakdown of inert gases in a dc electric field in discharge chambers with various interelectrode distances L and interior radii R.

THEORY

The equation for gas breakdown in a homogeneous dc electric field derived in [18] takes into account electron-impact ionization of gas molecules, the drift of electrons and ions along the field direction, and the diffusive motion of electrons along the discharge-tube radius. However, the authors [18] neither analyzed the breakdown equation obtained, nor compared its solutions with the experimental results. Therefore, after simple transformations, equation (12) from [18] is written in the form

$$\alpha = \frac{D_2}{V_e}\left(\frac{2.4}{R}\right)^2 + \alpha\gamma\left\{\exp\left[L\left(\alpha - \frac{D_e}{V_e}\left(\frac{2.4}{R}\right)^2\right)\right] - 1\right\}, \quad (1)$$

where α and γ are the first and second Townsend coefficients, D_e is the transverse electron diffusion coefficient, and V_e is the drift velocity of electrons.

The following expressions can be written for V_e, D_e, and α in a wide range of the ratio E_{dc}/p (close to, and to the right of, the minima of the breakdown curves) for inert gases (argon, xenon, etc.) [19–22]:

$$V_e = \mu_e E_{dc} = \mu_{e0}\frac{U_{dc}}{pL}, \quad (2)$$

$$pD_e \approx \text{const} = D_{e0}, \quad (3)$$

$$\alpha = A_0 p \exp\left(-\frac{B_0 pL}{U_{dc}}\right), \quad (4)$$

where μ_{e0} is the electron mobility at $p = 1$ Torr and A_0 and B_0 are constants [3].

Substituting (2)–(4) into (1) and multiplying the left- and right-hand sides of (1) by L, we have the following equation for the breakdown:

$$A_0(pL)\exp\left(-\frac{B_0(pL)}{U_{dc}}\right) = \frac{D_{e0}}{\mu_{e0}}\frac{(2.4)^2}{U_{dc}}\left(\frac{L}{R}\right)^2$$

$$+ \gamma A_0(pL)\exp\left(-\frac{B_0(pL)}{U_{dc}}\right)\left\{\exp\left[A_0(pL)\right.\right. \quad (5)$$

$$\left.\left.\times \exp\left(-\frac{B_0(pL)}{U_{dc}}\right) - \frac{D_{e0}}{\mu_{e0}}\frac{(2.4)^2}{U_{dc}}\left(\frac{L}{R}\right)^2\right] - 1\right\}.$$

1063-7842/00/4506-0727$20.00

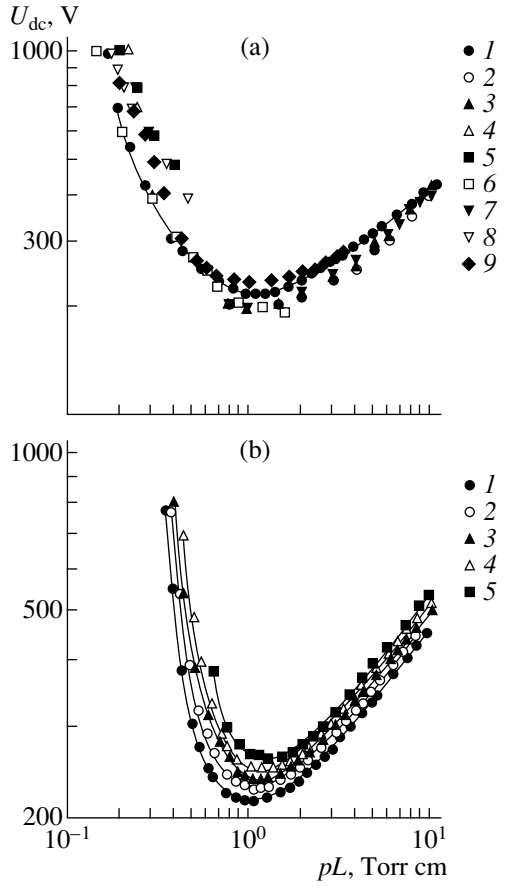

Fig. 1. (a) Experimental breakdown curves for a glow discharge in argon: (*1*) our measurements; (*2*, *3*) experiment [5] (Pt and Ni cathodes, respectively); (*4*) steel cathode [23]; (*5*) Ni cathode [24]; (*6*) steel cathode [25]; (*7*) Pt cathode [26]; (*8*) stainless steel cathode [27]; (*9*) Cu cathode [13]; (b) breakdown curves for a glow discharge in argon (R = 3.15 cm) at various distances between the electrodes L, cm: (*1*) 0.5; (*2*) 1; (*3*) 2; (*4*) 4; and (*5*) 6.

Since, as a rule, $\gamma \ll 1$, equation (5) can be simplified to the form

$$A_0(pL)\exp\left(-\frac{B_0(pL)}{U_{dc}}\right)\left\{\gamma\exp\left[A_0(pL)\right.\right.$$

$$\left.\left.\times\exp\left(-\frac{B_0(pL)}{U_{dc}}\right)-\frac{D_{e0}}{\mu_{e0}}\frac{(2.4)^2}{U_{dc}}\left(\frac{L}{R}\right)^2\right]-1\right\} \qquad (6)$$

$$+\frac{D_{e0}}{\mu_{e0}}\frac{(2.4)^2}{U_{dc}}\left(\frac{L}{R}\right)^2 = 0.$$

Equations (5) and (6) show that the breakdown voltage U_{dc} is a function not only of the product pL, but also of the ratio L/R. Let us differentiate (5) with respect to pL and equate the derivative $dU_{dc}/d(pL)$ to zero. Then, we derive two solutions for the breakdown curve minimum, one of which has no physical meaning and the other of which yields the relations

$$\left(\frac{U_{dc}}{pL}\right)_{min} = \left(\frac{E_{dc}}{p}\right)_{min} = B_0, \qquad (7)$$

$$\frac{A_0}{e}(pL)_{min} = \frac{D_{e0}}{\mu_{e0}}\frac{(2.4)^2}{B_0(pL)_{min}}\left(\frac{L}{R}\right)^2 + \frac{\gamma A_0}{e}(pL)_{min}$$

$$\times\left\{\exp\left[\frac{A_0}{e}(pL)_{min}-\frac{D_{e0}}{\mu_{e0}}\frac{(2.4)^2}{B_0(pL)_{min}}\left(\frac{L}{R}\right)^2\right]-1\right\}, \qquad (8)$$

$$\frac{A_0}{eB_0}U_{min} = \frac{D_{e0}}{\mu_{e0}}\frac{(2.4)^2}{U_{min}}\left(\frac{L}{R}\right)^2 + \frac{\gamma A_0}{e}\frac{U_{min}}{B_0}$$

$$\times\left\{\exp\left[\frac{A_0}{eB_0}U_{min}-\frac{D_{e0}}{\mu_{e0}}\frac{(2.4)^2}{U_{min}}\left(\frac{L}{R}\right)^2\right]-1\right\}, \qquad (9)$$

where e is the natural logarithmic base and $U_{min} = (U_{dc})_{min}$.

For $L/R \longrightarrow 0$, expressions (8) and (9) take the form [3]

$$(pL)_{min} = \frac{e}{A_0}\ln\left(\frac{1+\gamma}{\gamma}\right), \qquad (10)$$

$$U_{min} = \frac{eB_0}{A_0}\ln\left(\frac{1+\gamma}{\gamma}\right). \qquad (11)$$

From (7), it follows that, when the values of L, R, and γ are varied in discharge chambers, the breakdown curves are shifted in such a manner that the $(E_{dc}/p)_{min}$ value always remains constant, accompanied by the maximum electron ionizing power. Formulas (8) and (9) show that the coordinates of the minima $(pL)_{min}$ and U_{min} depend on the ratio L/R but not on L and R separately.

EXPERIMENTAL RESULTS

The above theoretical results were tested experimentally by measuring the breakdown curves for a glow discharge in argon at dc voltages $U_{dc} \le 1000$ V and pressures $p \approx 10^{-2}$–10 Torr. Discharge tubes with inner diameters of 9, 14, 27, 63, and 100 mm were used. Flat parallel electrodes were manufactured from stainless steel and occupied the entire cross section of the discharge tube.

Figure 1a shows one of the breakdown curves (L = 11 mm and R = 50 mm) and experimental curves obtained with argon in [5, 13, 23–27]. Our data are obviously in good agreement with the results of other authors. Figure 1b shows the breakdown curves measured by us at various distances L between the electrodes. These results prove that, as L increases, the breakdown curves are shifted not only to higher break-

down voltages U_{dc} (as was obtained in [8–17]) but also simultaneously to higher pL values. Such a conclusion can also be drawn from the experimental results shown in Fig. 3 of [13] for neon. Breakdown curves were obtained in [13] close to the minimum and to the left of it; it was pointed out that U_{dc} rises with increasing L. However, these results also show that the breakdown curves are shifted to higher pL values with increasing L (this fact was fully ignored in [13]). Hence, the departure from the Paschen law observed by us is well confirmed in independent measurements. Such a shift of the breakdown curves to the regions of higher U_{dc} and pL with an increase in the interelectrode distance L is apparently related to an increase in the loss of charged particles at the side (radial) walls of the discharge tube due to diffusion transverse to the electric field.

Figures 2 and 3 show U_{min} and $(E_{dc}/p)_{min}$ as functions of $(pL)_{min}$ and ratio L/R obtained from our experimental breakdown curves. Figure 2 shows that, for the measured coordinates of the breakdown curve minima, $U_{min} \propto (pL)_{min}$; from Figs. 2 and 3 it follows that $(E_{dc}/p)_{min} \approx \text{const} = 194 \pm 5$ V/(cm Torr) (this value is in satisfactory agreement with $B_0 = 180$ V/(cm Torr) [3]). Figure 2 also presents a straight line $U_{min} = 194(pL)_{min}$ describing the experimental points well. Therefore, the behavior of the coordinates of the breakdown curve minimum for a glow discharge, which was predicted by formula (7), is confirmed by our experimental results. Consequently, the ratio $(E_{dc}/p)_{min}$ at the breakdown curve minimum in an inert gas always remains constant for arbitrary experimental values of the interelectrode gap L and the tube radius R. The same rule is valid if the coefficient of ion–electron emission γ is varied (this was noted in [4, 5] and follows from the results of [28, 29]).

Figure 3 also shows that the U_{min} values obtained from experimental breakdown curves for various L and R fall satisfactorily on a single monotonically increasing curve. There is also a theoretical curve $U_{min}(L/R)$ in Fig. 3, which was calculated from (9) and agrees well with our experimental results (in these calculations, we used the values of α, V_e, and D_e from [3, 4, 19–22]). Therefore, the parameter L/R, as well as pL, is also important for the description of the glow-discharge breakdown curves. Figure 4 shows two breakdown curves in discharge chambers with different radii and interelectrode distances but equal ratios $L/R = 2.4$. As we see, the breakdown curves almost coincide in this case. Thus, the Paschen law can be written in the modified form

$$U_{dc} = f\left(pL, \frac{L}{R}\right). \qquad (12)$$

Let us formulate the modified law (12) in the following manner. Taking two discharge tube with L_1, R_1 and L_2, R_2, we measure the breakdown curves for them and

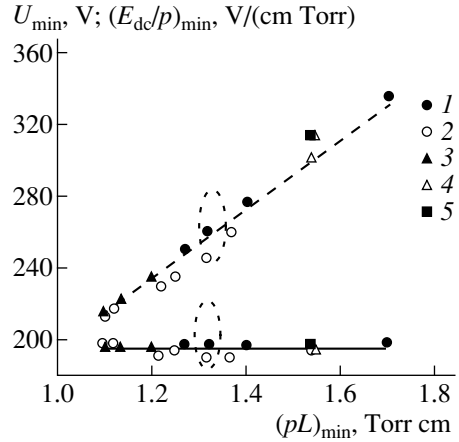

Fig. 2. Dependences of U_{min} and $(E_{dc}/p)_{min}$ on $(pL)_{min}$ for various R, cm: (*1*) 0.7; (*2*) 3.15; (*3*) 5; (*4*) 0.45; and (*5*) 1.35. Solid line: $(E_{dc}/p)_{min} = 194$ V/(cm Torr); dashed line: $U_{min} = 194(pL)_{min}$.

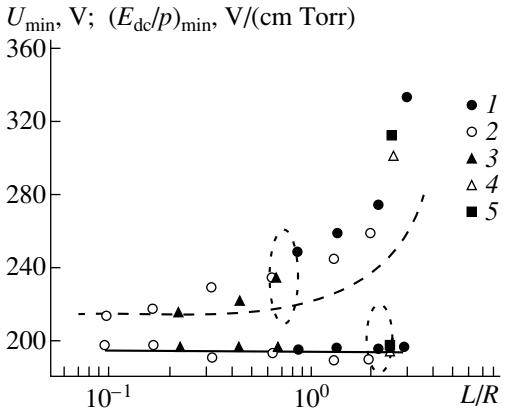

Fig. 3. Dependences of U_{min} and $(E_{dc}/p)_{min}$ on L/R; R values are the same as in Fig. 2. Solid line: $(E_{dc}/p)_{min} = 194$ V/(cm Torr); dashed line: calculations from (9).

plot these curves as $U_{dc1,2} = f(pL_{1,2})$. These two breakdown curves then coincide only in the case if $L_1/R_1 = L_2/R_2$. In other words, the conventional Paschen law $U_{dc} = f(pL)$ is valid only for discharge tubes with identical L/R. Discharges for which the dimensions of the electrodes and distances between them are geometrically similar and the gas pressures are inversely proportional to the interelectrode distances have equal discharge initiation voltages. In the general case with arbitrary L and R, the conventional Paschen law is not valid.

Note that with appropriately selected coordinate axes, we can achieve the coincidence of all the measured breakdown curves. For example, if we plot

$$pL^* = pL\Big/\left(1 + \left(\frac{L}{R}\right)^2\right)^a \qquad (13)$$

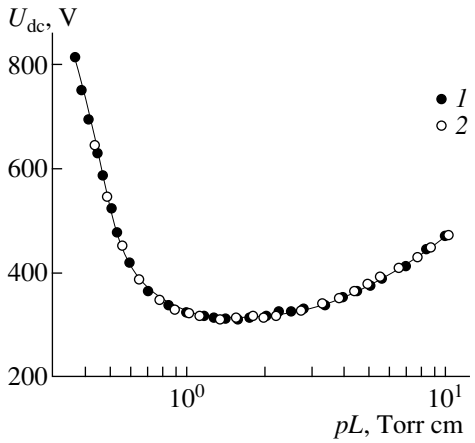

Fig. 4. Breakdown curves for L/R = 2.4: L = 1.1 (*1*) and 3.3 cm (*2*); R = 0.45 (*1*) and 1.35 cm (*2*).

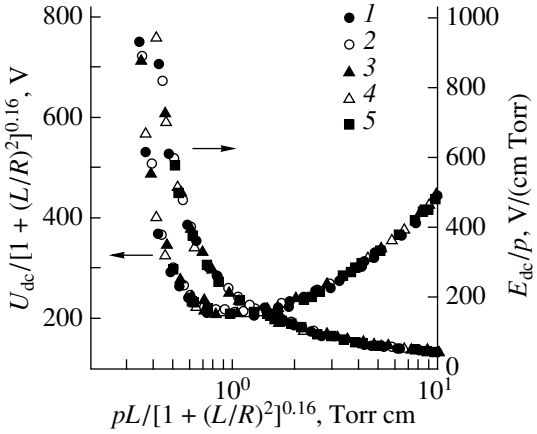

Fig. 5. Dependences of U_{dc}^* and E_{dc}/p on $(pL)^*$ in a discharge tube with R = 3.15 cm; L, cm: (*1*) 0.5; (*2*) 1; (*3*) 2; (*4*) 4; and (*5*) 6.

and

$$U_{dc}^* = U_{dc}/\left(1 + \left(\frac{L}{R}\right)^2\right)^a \qquad (14)$$

along the horizontal and vertical axes, respectively, where $a \approx 0.16$ for argon, then the breakdown curves in Fig. 1b are mutually superimposed to within an accuracy of ±5 V (Fig. 5). At $L/R \longrightarrow 0$, we obviously have a customary Paschen curve $U_{dc} = f(pL)$. Relations (13) and (14) show that $U_{dc}^*/(pL)^* = U_{dc}/(pL) = E_{dc}/p$; i.e., the dependences $E_{dc}/p = f((pL)^*)$ for different breakdown curves must also coincide (this is demonstrated in Fig. 5). By using relations (13) and (14) and breakdown voltage values shown in Fig. 5, we can predict to a high accuracy the breakdown curve in a discharge chamber for arbitrary L and R values. It follows from Fig. 5 that the Paschen law can be written in another modified form, $U_{dc}^* = f((pL)^*)$.

We will make one remark concerning the breakdown curve measurement technique. The glow-discharge breakdown curve is usually measured by two methods: (1) the distance L is fixed, and the breakdown voltages are then measured as a function of gas pressure; (2) breakdown voltages are measured at varied distances L and a fixed gas pressure. However, from the data obtained in this study, it follows that the second method of measuring the breakdown curve (at a fixed pressure and variable L) is not correct. The "breakdown curve" thus obtained represents a certain function, which is close to the Paschen curve at small L but is shifted to higher breakdown voltages with increasing L. In order to extract some valid information on discharge initiation, each experimental point obtained by this method should be recalculated by using relations (13) and (14).

CONCLUSIONS

In this study, glow-discharge initiation in inert gases was investigated experimentally and theoretically for variable interelectrode gaps and radii of the discharge tubes. It is shown that the ratio $(E_{dc}/p)_{min}$ holds constant at the minima of the breakdown curves for arbitrary interelectrode gaps, radii of the discharge chamber, and ion–electron emission coefficients. A modified Paschen law $U_{dc} = f(pL, L/R)$ is obtained; i.e., the breakdown voltage U_{dc} is a function of both the product of the gas pressure and gap width and the ratio L/R. It is shown experimentally that the conventional Paschen law $U_{dc} = f(pL)$ is valid only for discharge tubes in which the dimensions of the electrodes and the distances between them are geometrically similar. In the general case, the Paschen law is not valid.

REFERENCES

1. F. Paschen, Annalen der Physik und Chemie. Wiedemanns Annalen, Ser. 3, **37** (1), 69 (1889).
2. J. S. Townsend, *Electricity in Gases* (Clarendon, Oxford, 1915).
3. A. von Engel, *Ionized Gases* (Clarendon, Oxford, 1955; Fizmatgiz, Moscow, 1959).
4. J. Meek and J. Craggs, *Electrical Breakdown of Gases* (Clarendon, Oxford, 1953; Inostrannaya Literatura, Moscow, 1960).
5. S. Brown, *Elementary Processes in Gas Discharge Plasma* (Atomizdat, Moscow, 1961).
6. V. A. Lisovskiy and V. D. Yegorenkov, J. Phys. D **27**, 2340 (1994).
7. M. Sato, Bull. Yamagata Univ. **25** (2), 119 (1999).
8. J. S. Townsend and S. P. McCallum, Philos. Mag. **6**, 857 (1928).
9. H. Fricke, Z. Phys. **86**, 464 (1933).

10. S. P. McCallum and L. Klatzow, Philos. Mag. **17**, 279 (1934).
11. H. Buttner, Z. Phys. **111**, 750 (1939).
12. F. G. Heymann, Proc. Phys. Soc. London **63**, 25 (1950).
13. H. C. Miller, Physica **30**, 2059 (1964).
14. L. Jacques and W. Bruynooghe, in *Proceedings of the 15th International Conference on Phenomena in Ionized Gases, Minsk, 1981*, p. 609.
15. L. Jacques, W. Bruynooghe, R. Boucique, and W. Wieme, J. Phys. D **19**, 1731 (1986).
16. M. Yumoto, T. Sakai, Y. Edinuma, *et al.*, in *Proceedings of the 8th International Symposium on High Voltage Engineering, Yokohama, 1993*, p. 409.
17. G. Auday, P. Guillot, J. Galy, and H. Brunet, J. Appl. Phys. **83**, 5917 (1998).
18. V. I. Kolobov and A. Fiala, Phys. Rev. E **50**, 3018 (1994).
19. H. N. Kucukarpaci and J. Lucas, J. Phys. D **14**, 2001 (1981).
20. V. Puech and L. Torchin, J. Phys. D **19**, 2309 (1986).
21. M. Suzuki, T. Taniguchi, and H. Tagashira, J. Phys. D **23**, 842 (1990).
22. V. A. Lisovskiy and V. D. Yegorenkov, J. Phys. D **31**, 3349 (1998).
23. L. G. Guseva, Zh. Tekh. Fiz. **40**, 2253 (1970).
24. A. N. Dikidzhi and B. N. Klyarfel'd, Zh. Tekh. Fiz. **25**, 1038 (1955) [Sov. Phys. Tech. Phys. **15**, 1760 (1955)].
25. M. J. Schonhuber, IEEE Trans. Power Appar. Syst. **88** (2), 100 (1969).
26. F. Ehrenkranz, Phys. Rev. **55**, 219 (1939).
27. J. D. Pace and A. B. Parker, J. Phys. D **6**, 1525 (1973).
28. H. Jacobs and A. P. LaRocque, J. Appl. Phys. **18**, 199 (1947).
29. H. Jacobs and A. P. LaRocque, Phys. Rev. **74**, 163 (1948).

Translated by A.S. Seferov

Technical Physics, Vol. 45, No. 6, 2000, pp. 732–735. Translated from Zhurnal Tekhnicheskoĭ Fiziki, Vol. 70, No. 6, 2000, pp. 63–66.

SOLIDS

Reaction of a Dislocation–Impurity System to an Electromagnetic Excitation

V. I. Alekseenko

Donetsk Physicotechnical Institute, National Academy of Sciences of Ukraine, Donetsk, 340114 Ukraine

Received March 23, 1999

Abstract—In experiments on indium antimonide single crystals, the dynamic behavior of a screw dislocation–impurity ambient system was studied. It was found that local absorption of electromagnetic energy takes place in this system, leading to development of relaxation processes which change the system energy and, consequently, its dynamic properties. It is remarkable that the system can be activated by an electromagnetic field due to the presence of impurity ambient around otherwise inactive screw dislocations. © *2000 MAIK "Nauka/Interperiodica".*

INTRODUCTION

Until recently, weak electromagnetic (EM) fields ($U \ll kT$, where U is the energy of the electric or magnetic component of the field; and T is the temperature of an object) constituted the basis of scientific methods of investigating physical phenomena of materials and their properties. It had been considered that such exposure could not bring about an irreversible change in the structure or properties of condensed matter, as they did not affect the dynamic equilibrium in the concentration of defects. However, in nonequilibrium condensed systems, both crystalline [1–4] and amorphous [5], application of weak EM fields caused irreversible changes in their structure and properties. These facts have led to intensive developments in laboratory and industrial methods of EM processing of materials and products aimed at improvement of their physico-mechanical, electrophysical, and operational characteristics [4, 6]. Despite the applied nature of these research efforts, the immediate cause of the observed structural transformations has been identified: the relaxation processes triggered by EM stimulation of thermodynamically unstable materials.

Still, a question remains as to what elements of the system are responsible for the absorption of EM energy and the ensuing relaxation processes. Finding a solution to this problem can open prospects for efficient employment of EM fields in various applications. In order to solve such a problem, it is necessary to find a relation between macroscopic properties of a material and EM stimulation. Once this relation has been found, a scientific approach to employing weak EM fields can be formulated and their effect on the structure and properties of materials can be estimated both qualitatively and quantitatively. Guidelines for such an approach have been formulated by the present author [7]. Basically, these guidelines rely upon the knowledge of structural and energy states of a material that might be responsible for the relaxation processes and be directly involved in absorption of EM energy. In general, the nature of the structural and energy states can can differ by point defects, impurity atoms, linear defects, complexes, or volume defects. For example, it has been shown [1] that in NaCl single crystals treated in a magnetic field, the relaxation process is a result of decomposition of impurity phases $CdCl_2$ and $PbCl_2$. In [2], the relaxation process consisting of a periodic variation of the internal friction is linked to formation–disintegration processes of impurity ambients around dislocations as a result of magnetic field pulses applied to a polycrystalline structure. On the other hand, some authors [5] relate the relaxation process in disordered systems initiated by EM fields to alternating formation and disintegration of cluster structures. The above works, as well as many others, have a serious drawback. In none of the cases considered has the type of defects responsible for the EM energy absorption and relaxation processes been uniquely identified. In the objects studied, various types of defects can simultaneously be present, whereas the problem of their selection from the viewpoint of applying EM stimulation has not been addressed. This is probably the reason why a general model of relaxation processes caused by EM stimulation is still unavailable.

In this work, a serious attempt is undertaken to improve the general situation in this field. To identify the particular elements in a structure which absorb EM field energy and establish possible mechanisms of induced relaxation processes, a correct approach is required, namely, the appropriate choice of materials for study; formation in the chosen material of a particular system, of defects to be tested for the possibility of EM field absorption and initiation of a relaxation process, and, finally, the delineation of a technique for

1063-7842/00/4506-0732$20.00 © 2000 MAIK "Nauka/Interperiodica"

locally (*in situ*) controlling the behavior of this system of defects.

The system of defects chosen for this study consists of aged dislocations with an impurity ambient formed around them. It is understandable that the material should be monocrystalline, with controlled density of dislocations of a known type. In addition, the dislocation density should be such as to exclude their interaction and thus prevent uncontrolled delocalization of the process under study. To exclude the influence of the crystal bulk on initiation of the relaxation process, it is important that the crystal be diamagnetic, i.e., insensitive to external fields.

OBJECT OF STUDY AND EXPERIMENTAL TECHNIQUES

In conformity with the foregoing discussion, the studies were performed on initially dislocation-free ($\rho < 10^2$ cm^{-2}) monocrystalline indium antimonide (InSb) doped with tellurium to a concentration of 10^{15} cm^{-3}. The samples used had the form of a parallelepiped $2.5 \times 2.5 \times 15$ mm cut along crystallographic axes [111], [112], and [110], respectively. The studies were carried out for screw dislocations insensitive to EM stimulation, whose mobility was therefore unaffected by the EM field. The dislocations were introduced by scribing the (112) facet and then bending the sample placed on a four support in a transverse direction to the [111] axis. In a sample put under stress in this way, there forms after a time an ensemble of dislocations such as those seen in the micrograph in Fig. 1a of the (111) crystal face after a selective chemical etch. Figure 1b shows an X-ray topogram of an ensemble of dislocations introduced in the above manner. The topograms were registered using a technique of anomalous propagation of X rays. To increase the resolution, the topograms were taken in a one-crystal geometry with the use of Mo$K_{\alpha 1}$ radiation. The sample thickness for the topographic investigations was ~250 μm. X-ray topographic identification of an ensemble of dislocations for revealing the screw dislocations was performed using the condition of "invisibility" of dislocations on the topogram

$$(\bar{g} \times \bar{b}) = 0, \quad [\bar{g} \times \bar{n}] = 0, \qquad (1)$$

where $\bar{g}$ is the diffraction vector of a reflecting plane, $\bar{b}$ is the Burgers vector of a dislocation, and $\bar{n}$ is the dislocation line vector [8].

It is evident that a screw dislocation has a lot of planes meeting this condition and that an edge dislocation has a single reflecting plane. This fact makes possible identification of the type of dislocations introduced by sample deformation. A series of topograms of types {220}, {224}, and {004} have been obtained. Three of these topograms are shown in Figs. 1c–1e. Seen in the topogram of Fig. 1c are large segments

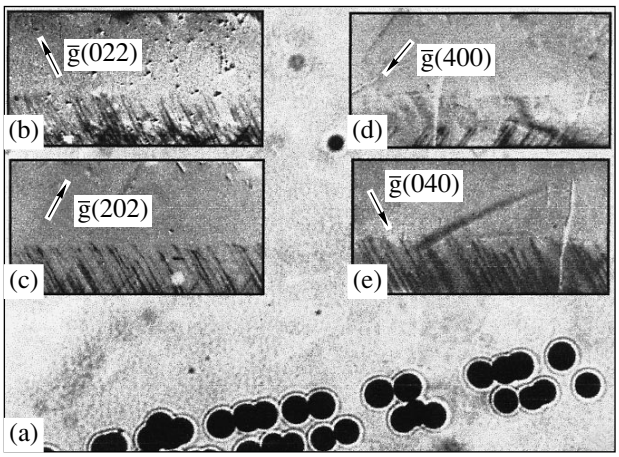

Fig. 1. (a) Micrographs of the (111) facet and (b–e) X-ray topograms showing screw dislocations in single crystals of deformed indium antimonide. Magnification in all topograms is ×28.5.

directed along two crystallographic axes, $[0\bar{1}1]$ and $[\bar{1}01]$. Dislocations aligned with $[0\bar{1}1]$ slip along the $(1\bar{1}1)$ axis and fade out in topogram 400 (Fig. 1d), which indicates that they are screw-type dislocations. Segments aligned with $[\bar{1}01]$ slide in the $(1\bar{1}1)$ plane and fade out in topogram 040 (Fig. 1e), which is also evidence that they are screw-type. It is to be emphasized that these dislocations are observed on the (111) sample face after a chemical etch (Fig. 1a). All of the work reported in this paper was performed on these dislocations, because their movement can be conveniently monitored using a chemical etch.

The impurity ambient around dislocations was produced by annealing the samples at a temperature of 300°C for 4 h. For EM field generation, an OIMP-101 oscillator was used that generated magnetic field pulses of amplitude 10^5 A/m at a repetition rate of 1 Hz. EM stimulation of samples with screw dislocations was carried out at room temperature.

As a parameter to be measured, the average displacement l of the ensemble of dislocations in the field of external mechanical stress σ was used, which is fairly sensitive to the condition of the dislocation ambient. Values of l were determined by averaging displacements of individual dislocations in the ensemble being investigated. Ensembles of 40–50 dislocations were studied. Mechanical strain in the sample was produced by bending a sample placed on four supports.

Using an optical microscope and the technique of a repeated selective sample etch, displacements of the aged screw dislocations were determined as a change of position of the respective etch pits. Variations of l with time t of sample loading were measured.

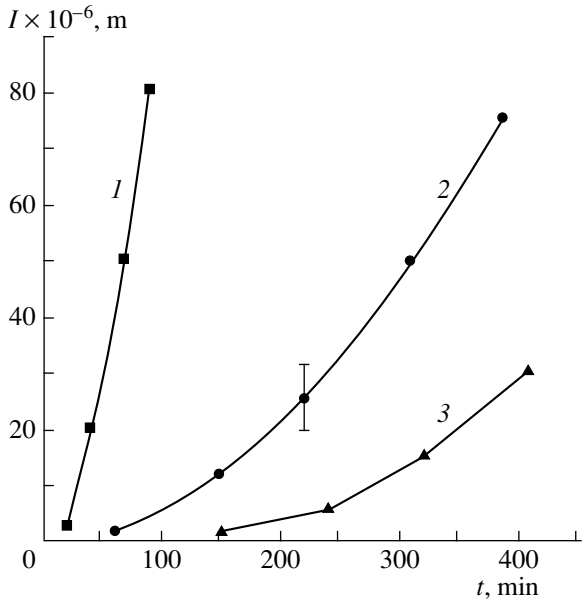

Fig. 2. Dependence of the average displacement of an ensemble of screw dislocations in an indium antimonide crystal on mechanical stress.

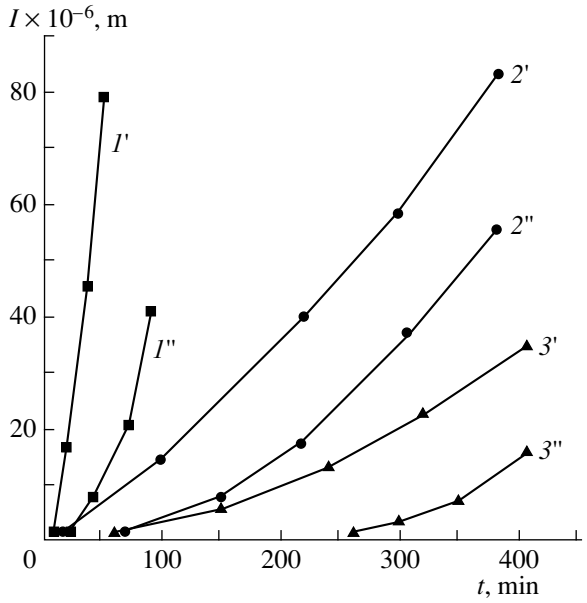

Fig. 3. Same as in Fig. 2, after EM stimulation.

RESULTS OF THE STUDY

Prior to studying the dynamic behavior of the screw dislocation–impurity system following EM stimulation of the sample, let us consider the system dynamics in the absence of EM stimulation. Figure 2 shows l as a function of applied mechanical stress duration for an indium antimonide sample after annealing in the regime described above. The curves were obtained at a bending stress of σ = 10 MPa and temperatures T_1 = 150 (curve *1*), T_2 = 130 (curve *2*), and T_3 = 115°C (curve *3*). In the curves shown, critical durations (t_{cr}) of mechanical stress can be distinguished within which l = 0. It should be noted that the $l(t)$ curves of annealed samples were measured taking into account zero displacements of the screw dislocations. It is owing to this fact that t_{cr} could be defined. As seen in Fig. 2, t_{cr} of a strained sample depends on temperature.

Using an expression for t_{cr} of a strained sample as a function of temperature [9],

$$t_{cr} = t_{cr}^{\circ}\sigma^{-m}\exp(U_a/kT), \qquad (2)$$

the activation energy for the breakaway of an impurity ambient from a dislocation under externally applied stress can be estimated. It was found to be equal to U_a = 1.0 ± 0.1 eV. Using a linear approximation of the function $U_a(\sigma)$ [9],

$$U_a = U_0 - \gamma\sigma \qquad (3)$$

(U_0 is the binding energy between the impurity ambient and the dislocation line; $\gamma = b^2L_c$ is the activation volume for the process of breaking a dislocation away from its ambient; b is the Burgers vector; and L_c is the distance between points where the dislocation is pinned by impurities), the energy of interaction between a dislocation and its ambient U_0 can be determined. For the indium antimonide single crystals studied, U_0 = 1.3 ± 0.1 eV at σ = 10 MPa and $L_c = 1/n = 2 \times 10^{-6}$ cm. The linear dislocation density along a dislocation line n was estimated using the Cottrell–Bilby expression [10]

$$n(t_T) = \alpha n_0(ADt_T/kT_T), \qquad (4)$$

where t_T and T_T are the annealing time and temperature, respectively, of the samples with screw dislocations; α = 6; $A = 10^{-7}$ eV cm; D is the impurity diffusion coefficient; and n_0 is the total number of atoms per unit volume of solution. The experimentally determined diffusion coefficient is equal to $D = 10^{-15}$ cm^2/s.

As the problem is to find out whether the EM field can influence the dynamic properties of screw dislocations, it appears that the characteristics to be investigated are t_{cr}, U_a, and U_0.

Figure 3 shows $l(t)$ curves at σ = 10 MPa and temperatures 150, 130, and 115°C immediately after EM stimulation of annealed indium antimonide containing screw dislocations (curves *1*'–*3*') and 24 h later (curves *1*''–*3*''). Immediately after EM stimulation, the number of dislocations with zero displacement is lower, resulting in shorter times t_{cr} under applied stress at all temperatures. In addition, the curves in question tend to straighten, because their nonlinearity is due to growth (with the time of exposure to stress) of the number of displaced dislocations. The estimated activation energy for the breakaway of a dislocation from its

impurity ambient under externally applied stress lowers to $U_a = 0.8 \pm 0.1$ eV. Similarly, the binding energy between dislocations and impurities lowers to $U_0 = 1.1$ eV. After being stored for 24 h at room temperature following EM stimulation, the situation is found to have changed in the reverse direction: t_{cr} at all temperatures is higher (Fig. 3, curves *1*"–*3*"), even compared with a material not subjected to EM stimulation (Fig. 2). It is remarkable that after storage for 24 h at room temperature, the dislocation–impurity system transformed in such a way that the energies increased as follows: $U_a = 1.1$ eV and $U_0 = 1.4$ eV. It will be recalled that in the initial sample, the impurity ambient (less tightly bound) formed after a 4-h hold at 300°C. With a diffusion activation energy of tellurium impurity of about 0.5 eV, the diffusion coefficients D_1 at $T_1 = 20$°C and D_2 at $T_2 = 300$°C differ by about four orders of magnitude. From the diffusion time relation $D_1t_1/D_2t_2 = 1$, it follows that the diffusion times t_1 and t_2 should also differ by about the same factor, but in this study this ratio was found to be less than an order of magnitude. It is thus evident that during a 24-h experiment, no ambient, let alone the one bound to a dislocation, can form as a result of impurity diffusion from the bulk. Qualitatively, this result can be understood in terms of the concept of diffusion instability produced by EM stimulation of the material [4]. Then, according to the above considerations, in the 24 h following EM stimulation, an impurity ambient should have formed around newly introduced screw dislocations at room temperature. Yet, no experimental evidence to confirm this was found: for screw dislocations induced in a sample after EM stimulation, no time delay of displacement was detected in the course of a few days, i.e., $T_{cr} = 0$.

CONCLUSIONS

The following important conclusions can be drawn from the analysis carried out in this work. As a result of EM stimulation of indium antimonide samples containing aged screw dislocations, a relaxation process is triggered, which transforms the impurity ambient in such a way as to make it more tightly bound to the dislocation. This in turn causes a lowering (relative to the initial state) of U_0, U_a, and t_{cr} values immediately after EM stimulation (apparently during its disruption), followed by an increase in these parameters; localization of the EM energy and the relaxation process takes place in a system consisting of dislocations and their impurity ambients, because in a system of dislocations devoid of impurity ambients, no relaxation processes are observed; the transition of the dislocation–impurity ambient system from one state to another as a result of EM stimulation is evidence of metastable states, which may be the states responsible for absorption of the EM field and the processes induced by this field.

The obtained results can serve as a basis for the development of electromagnetic methods of controlling the mechanical properties of materials.

REFERENCES

1. G. I. Distler, V. M. Kanevskiĭ, V. V. Moskvin, *et al.*, Dokl. Akad. Nauk SSSR **268** (3), 591 (1983) [Sov. Phys. Dokl. **28**, 43 (1983)].
2. O. I. Datsko, V. I. Alekseenko, and A. D. Shakhova, Fiz. Tverd. Tela (St. Petersburg) **38**, 1799 (1996) [Phys. Solid State **38**, 992 (1996)].
3. O. I. Datsko and V. I. Alekseenko, Fiz. Tverd. Tela (St. Petersburg) **39**, 1234 (1997) [Phys. Solid State **39**, 1094 (1997)].
4. *Treatment in Pulse Magnetic Fields*, Ed. by S. N. Postnikov (Gorki, 1989).
5. V. I. Alekseenko, G. K. Volkova, I. B. Popova, *et al.*, Zh. Tekh. Fiz. **66** (1), 49 (1996) [Tech. Phys. **41**, 24 (1996)].
6. S. N. Postnikov and V. P. Sidorov, in *Applied Problems of Strength and Ductility* (Gorki, 1981), pp. 150–154.
7. V. I. Alekseenko, Zh. Tekh. Fiz. **68** (10), 50 (1998) [Tech. Phys. **43**, 1181 (1998)].
8. A. B. Jenkinson and A. R. Lang, *Direct Observations of Imperfections in Crystals*, Ed. by J. B. Newkirck and J. H. Wernick (New York, 1962; Mir, Moscow, 1965).
9. V. I. Alekseenko and V. M. Mostovoĭ, Ukr. Fiz. Zh. **37**, 415 (1992).
10. A. H. Cottrell, *Dislocation and Plastic Flow in Crystals* (Clarendon, Oxford, 1953; Metallurgiya, Moscow, 1958).

Translated by B. Kalinin

Technical Physics, Vol. 45, No. 6, 2000, pp. 736–738. Translated from Zhurnal Tekhnicheskoĭ Fiziki, Vol. 70, No. 6, 2000, pp. 67–69.

SOLIDS

Influence of the Current Redistribution in the Matrix of a Composite Superconductor on Propagation of the Normal Zone

V. V. Lysenko

Russian Research Centre, Kurchatov Institute, pl. Kurchatova 1, Moscow, 123182 Russia

Received May 11, 1999

Abstract—Influence of the current redistribution in the stabilizing matrix of a composite superconductor with nonuniform distribution of the superconducting component over its cross section on the normal zone propagation is calculated. Analysis of the problem in dimensionless variables allows one to find parameters determining the import of the effect considered. Parametric relationships for the normal zone propagation velocity are obtained under cooling conditions inadequate for steady state stabilization. *© 2000 MAIK "Nauka/Interperiodica".*

Transition of a composite superconductor to the resistive state is accompanied by a flow of the transport current to the stabilizing matrix. The characteristic time for current redistribution in a nonuniform stabilizer of a large cross section may be as long as several seconds; therefore, this process can have significant effects on superconductor stability and the normal zone dynamics. A cable consisting of twisted wires of a composite superconductor surrounded by an additional aluminum stabilizer is an example of such conductors. Such conductors are intended, among other things, for magnetic systems of the detectors of particle accelerators where cryogenic stabilization of the winding is usually ensured by means of indirect cooling. Numerical and analytical methods were suggested [1, 2] to calculate current diffusion to the stabilizing matrix. The effect of current redistribution on superconductor stability was investigated under conditions of indirect cooling [3] as well as cooling by superfluid helium [4]. Other papers [5, 6] are devoted to studying moving normal finite-size regions in steady-state stabilized conductors of a large cross section.

Let us consider a composite superconductor of radius R_0, where superconducting filaments are uniformly distributed within the inner part of radius R_i surrounded by the region of an additional stabilizer, i.e., normal metal. Let us assume that the average specific resistance ρ of both parts of the conductor is equal at a temperature higher than critical. At the initial moment, the transport current I flows through the inner area of the conductor whose temperature is equal to the cooling medium temperature T_0 everywhere except for some length that instantly transforms to the normal state. Let us write the magnetic field diffusion equation (1) in cylindrical coordinates for an azimuthal component of the magnetic induction and the thermal balance equation (2) in the form

$$\mu_0 \frac{\partial B}{\partial t} = \frac{\partial}{\partial R}\frac{\rho}{R}\frac{\partial (RB)}{\partial R} + \frac{\partial}{\partial X}\rho\frac{\partial B}{\partial X}, \tag{1}$$

$$c\frac{\partial T}{\partial t} = \frac{\partial}{\partial X}\lambda\frac{\partial T}{\partial X} - \frac{hP}{A}(T - T_0) + W(X, t). \tag{2}$$

Here, c and λ are the mean volume thermal capacity and thermal conductivity of the conductor; A is the total cross section; P is the perimeter being cooled; h is the convective heat transfer coefficient; and $W = A^{-1}\int \rho j^2 dS$ is the heat release rate per unit conductor volume averaged over its cross section, where the current density j is found by differentiation with respect to the magnetic induction

$$j(R, X, t) = \frac{1}{\mu_0}\sqrt{\left(\frac{1}{R}\frac{\partial (RB)}{\partial R}\right)^2 + \left(\frac{\partial B}{\partial X}\right)^2}.$$

Let us adopt a "step" model of conductivity of a superconductor [7], where the resistivity of the composite changes abruptly at some temperature T_s, which is the mean between the current sharing temperature and the critical temperature. For simplicity, let us regard thermal and electrophysical parameters of the conductor constant. Let us introduce dimensionless variables (3) and write expressions for the characteristic magnetic induction, time, and length according to (4)

$$b = \frac{B}{B_0}, \quad \theta = \frac{T - T_0}{T_s - T_0}, \quad r = \frac{R}{L_m}, \quad x = \frac{X}{L_h}, \quad \tau = \frac{t}{t_h}, \tag{3}$$

1063-7842/00/4506-0736$20.00 © 2000 MAIK "Nauka/Interperiodica"

$$B_0 = \frac{\mu_0 I}{2\pi R_0}, \quad t_h = \frac{c(T_s - T_0)A^2}{\rho I^2},$$
$$L_h = \sqrt{\frac{\lambda t_h}{c}}, \quad L_m = \sqrt{\frac{\rho t_h}{\mu_0}}. \tag{4}$$

In this case, the magnetic field diffusion equation assumes the form (5) with boundary conditions (6) and initial conditions (7). Here, we neglected the second term on the right side of equation (1) associated with the radial component of current density. This approximation has practically no effect on the accuracy because of the small magnitude of the factor $(L_m/L_h)^2$ appearing in the second term in the dimensionless equation (typically10^{-3})

$$\frac{\partial b(r,\tau)}{\partial \tau} = \frac{\partial}{\partial r}\frac{1}{r}\frac{\partial (rb)}{\partial r}, \tag{5}$$

$$b(0,\tau) = 0, \quad b(r_0,\tau) = 1, \tag{6}$$

$$b(r,0) = \begin{cases} \beta^2 r/r_0, & r \le r_0/\beta \\ r_0/r, & r > r_0/\beta. \end{cases} \tag{7}$$

Here $r_0 = R_0/L_m$ and $\beta = R_0/R_i$. The parameter L_m is the depth to which the electric field will diffuse in the time period when some cross section of the conductor is heated by the passing normal zone front. Under the above assumptions, the current diffusion in every cross section of the conductor occurs independently, and the moment when the temperature reaches T_s represents the initial moment for the system (5)–(7). Using the solution of the system (5)–(7), we can calculate a variation with the time of the dimensionless specific heat release

$$w(\tau) = 0.5\int_0^{r_0}\left(\frac{\partial (rb)}{\partial r}\right)^2 \frac{dr}{r},$$

which we will use to analyze thermal processes in dimensionless variables. Equation (2) for this case can be written as

$$\frac{\partial \theta}{\partial \tau} = \frac{\partial^2 \theta}{\partial x^2} - \frac{\theta}{\alpha} + w(\tau - \tau_s), \tag{8}$$

where $\alpha = \rho I^2/(hP(T_s - T_0)A)$; and $\tau_s(x)$ is the moment when the dimensionless temperature at the point x reaches unity.

The stationary value of the dimensionless normal zone propagation velocity determined by the equations (5)–(8) depends on three dimensionless parameters: β, which is the relation between the conductor's overall dimensions and the size of an area containing the superconducting fraction, α characterizing the intensity of cooling, and r_0. The parameter r_0 is determined by the ratio between the characteristic times of transverse current diffusion $t_m = \mu_0 R_0^2/\rho$ and ohmic heating $r_0 = (t_m/t_h)^{1/2}$. In the case of instantaneous current redistribution over the matrix cross section, the problem has a well-known analytical solution [7] and the dimensionless normal zone propagation velocity is determined by the expression

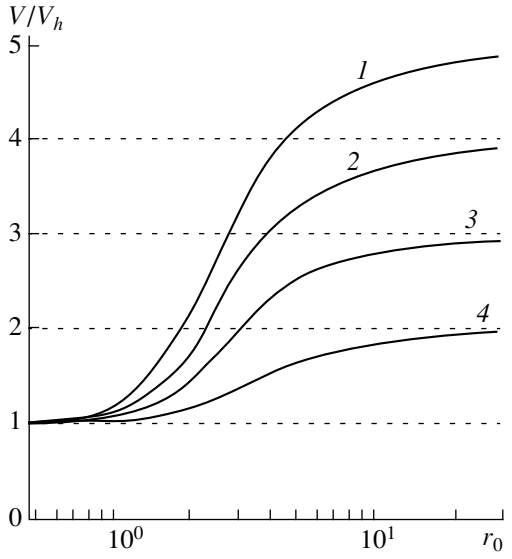

Fig. 1. Dimensionless normal zone propagation velocity versus parameter r_0 under adiabatic conditions. $\beta = 5$ (*1*), 4 (*2*), 3 (*3*), and 2 (*4*).

$$v_0 = \frac{\alpha - 2}{\sqrt{\alpha^2 - \alpha}}. \tag{9}$$

At first, numerical integration of the system (5)–(7) was carried out by the finite-difference method [8] to find the normal zone propagation velocities. Then, evolution of the initial thermal disturbance in the conductor was calculated using the obtained time dependence of heat release (tabulated in increments small enough to provide velocity calculations with an accuracy of about 1%), as well as the finite-difference method. The calculation results of the stationary normal zone propagation velocity without cooling are shown in Fig. 1. The denominate value of velocity can be obtained by multiplying the corresponding dimensionless value by a parameter $V_h = L_h/t_h = IA^{-1}(\rho\lambda/(T_s - T_0))^{1/2}$ s^{-1}. The dependence of the dimensionless velocity as a function of the dimensionless conductor radius has the characteristic form of a transition between two limiting cases: at low values of r_0, current redistribution over the entire cross section of the stabilizing matrix occurs fast enough so that this process does not affect the normal zone dynamics. At r_0 values higher than 10–30, the current is practically unable to flow to the region of the additional stabilizer in the transit time of the normal zone front, the specific heat release averaged over the cross section approaches $\beta^2\rho(I/A)^2$, and the dimensionless propagation velocity approaches β. Note that

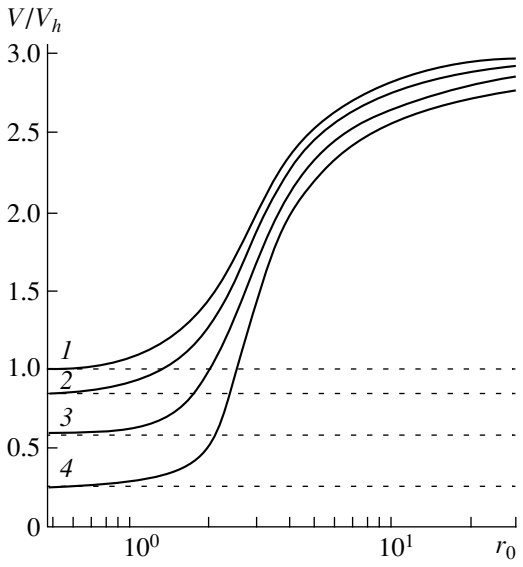

Fig. 2. Dimensionless normal zone propagation velocity versus parameter r_0. $\beta = 3$; $\alpha = \infty$ (*1*), 10 (*2*), 4 (*3*), and 2.5 (*4*).

within the framework of the model used, the dimensionless velocity does not depend on the matrix conductivity under adiabatic conditions (parameter L_m is independent of ρ). The reason is that the influence of current redistribution on the propagation velocity is determined by the ratio between the characteristic times of diffusion and ohmic heating, which depend on ρ in the same way. Let us estimate a typical transverse dimension of L_m. At $I/A = 10^8$ A/m^2, $c = 2 \times 10^3$ JK^{-1} m^{-3}, $T_s - T_0 = 2.5$ K, we obtain $L_m \approx 0.6$ mm.

The calculation results for the case of linear heat removal are presented in Fig. 2. The magnitudes of velocity for the case of a uniform distribution of the superconducting component over the stabilizer cross section are shown by dashed lines in Fig. 2. As well as in adiabatic conditions, at low values of r_0, the velocity is determined by the expression (9). With increasing r_0, the dimensionless velocity approaches βv_0; $\beta^2\alpha$ should be used as an effective stabilization parameter in calculating v_0.

To verify the obtained results, numerical simulation of normal zone propagation was carried out by the simultaneous solution of equations (1) and (2) using the finite-difference method. The differences in velocity magnitudes did not exceed 1–2%.

The results of the work demonstrate that analysis of the transition to the normal state of a superconducting magnet wound with a conductor of the type considered, and of the typical transverse dimension in the range of $(1–10)L_m$, must be carried out taking into account the finite time of current redistribution. For conductors with a typical transverse dimension larger than $(10–20)L_m$, the normal zone propagation velocity may be found if it is assumed that the heat release is due to the current flowing in that part of the stabilizer where the superconducting component is concentrated.

ACKNOWLEDGMENTS

This work was supported by the Russian Foundation for Basic Research (grant no. 96-15-98230).

REFERENCES

1. A. Devred, J. Appl. Phys. **65**, 3963 (1989).
2. A. A. Lee, R. H. Wands, and R. W. Fast, Cryogenics **32**, 863 (1992).
3. D. E. Baynham, N. V. Fetisov, and N. N. Martovetsky, IEEE Trans. Appl. Supercond. **3**, 805 (1993).
4. X. Huang and Y. M. Eyssa, IEEE Trans. Magn. **27**, 2304 (1991).
5. L. Dresner, in *Proceedings of the 11th International Conference on Magn. Tech., Tsucuba, Japan, 1989*, pp. 1084–1089.
6. R. Kupferman, R. G. Mints, and E. Ben-Jacob, J. Appl. Phys. **70**, 7484 (1991).
7. M. N. Wilson, *Superconducting Magnets* (Oxford Univ. Press, London, 1983; Mir, Moscow, 1985).
8. A. A. Samarskiĭ, *The Theory of Difference Schemes* (Nauka, Moscow, 1977).

Translated by M. Astrov

Technical Physics, Vol. 45, No. 6, 2000, pp. 739–742. Translated from Zhurnal Tekhnicheskoĭ Fiziki, Vol. 70, No. 6, 2000, pp. 70–73.

SOLIDS

Transversal Structure of Liquid Crystal in a Light Wave Field

M. V. Gol'dburt, V. P. Romanov, and D. O. Fedorov

St. Petersburg State University, Staryĭ Peterhof, 198904 Russia

Received June 3, 1999

Abstract—The change in the orientation of the director of a nematic liquid crystal in a light wave field under a uniform illumination is analyzed. A system of equations for the distribution of the director angle of inclination is derived for the case of normal incidence. This system accounts for the finite energy of interaction between the nematic and substrate. The dependence of the director distribution profile on the incident light intensity and cohesion energy is studied at fields considerably above the threshold. © *2000 MAIK "Nauka/Interperiodica".*

A remarkable feature of liquid crystals is their capability to reorient in relatively weak fields [1]. One such effect is the optical Frederix effect [1–5]. It implies a change in the orientation of the nematic liquid crystal director in the light wave field and could be of both threshold and nonthreshold character. Experimentally, it results in interference rings in the light wave field of sufficiently high intensity.

Special interest in the studies of this phenomenon in recent years is due to the discovery of a new effect. The threshold field decreases rapidly after a very small amount of dye is added to the liquid crystal [6, 7]. This phenomenon has the following physical explanation. The interaction potential of the excited dye molecule and nematic is changed, thus inducing an additional orienting moment [8, 9]. As a result, studies in fields considerably above the threshold become possible. This problem was discussed in papers [2, 10]. However, the problem was being solved for a simplified model. The authors worked under the single-constant approximation and strict boundary conditions.

In order to describe the experimental data quantitatively and to determine the liquid crystal parameters, a step-by-step description of the liquid crystal structure in the light wave field under the actual boundary conditions is treated. The present paper is devoted to this problem.

We now want to discuss a homeotropically oriented nematic liquid crystal sample of thickness d. Assume that it is located between two parallel plates. The light polarized along the plates' plane propagates normally to their surface parallel to the z-axis. Suppose that the layer is infinite in the xy-plane and the incident light produces a uniform illumination (Fig. 1).

Under these conditions, the effect of the director reorientation in the light wave field is of threshold character. The threshold value depends on the liquid crystal parameters, the thickness of the plate, and boundary conditions [2]. We investigate the distribution of the director angle of inclination in the fields much above the threshold. Free energy of the nematic is given by

$$F = \int_V \left\{ \left[\frac{K_1}{2} (\mathrm{div}\,\mathbf{n})^2 + \frac{K_2}{2} (\mathbf{n}, \mathrm{rot}\,\mathbf{n})^2 + \frac{K_3}{2} [\mathbf{n}, \mathrm{rot}\,\mathbf{n}]^2 \right] + F_e \right\} d^3\mathbf{r}. \quad (1)$$

Here $\mathbf{n}$ is the director vector, K_i (i = 1, 2, 3) are the Frank modules, and F_e is the contribution due to the interaction of the nematic with the light wave field [2]

$$F_e = -\frac{Sn_0}{c} (1 - p \sin u(\mathbf{r})^2)^{-1/2}, \quad (2)$$

where S is the Poynting vector projection on the normal to the liquid crystal layer, c is the velocity of light in a vacuum, $p = 1 - (n_0/n_e)^2$, $n_0 = \sqrt{\varepsilon_\perp}$, $n_e = \sqrt{\varepsilon_\parallel}$, $\varepsilon_\perp$ and $\varepsilon_\parallel$ are the transversal and longitudinal dielectric constants at the optical frequency relative to the director vector axis, and $u(\mathbf{r})$ is the angle between the wave propaga-

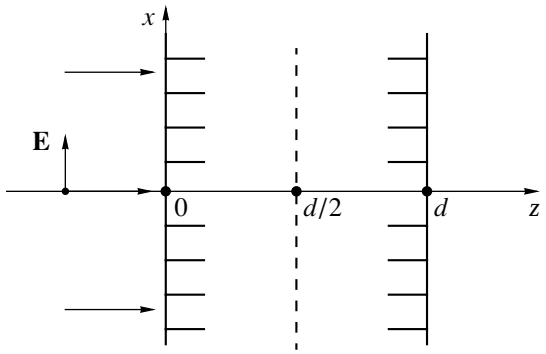

Fig. 1. The geometry of a homeotropically orientated liquid crystal layer in the field of a plane-polarized light wave at normal incidence with polarization along the x-axis.

1063-7842/00/4506-0739$20.00 © 2000 MAIK "Nauka/Interperiodica"

tion direction and the director. Under the uniform illumination of the sample, the problem is one-dimensional because the director distribution in the plates' plane is uniform and depends only on z. Suppose that the light is polarized along the x-axis. Then the director vector has components $\mathbf{n} = (\sin u(z), 0, \cos u(z))$, and the free energy of the liquid crystal transforms into

$$F = \int_V \left(\frac{1}{2}K_1 \sin^2 u\left(\frac{\partial u}{\partial z}\right)^2 + \frac{1}{2}K_3 \cos^2 u\left(\frac{\partial u}{\partial z}\right)^2 - \frac{Sn_0}{c}(1 - p\sin^2 u)^{-1/2}\right) d\mathbf{r}. \quad (3)$$

Minimizing the free energy, we get the equation for the distribution of the angle of inclination of the director at fields higher than the threshold:

$$\frac{d^2}{\pi^2}(1 + \delta\sin^2 u)\frac{\partial^2 u}{\partial z^2} + \frac{d^2}{\pi^2}\delta \sin u \cos u \frac{\partial u^2}{\partial z} + \frac{S}{S_c}\sin u \cos u (1 - p\sin^2 u)^{-3/2} = 0, \quad (4)$$

where $\delta \equiv (K_1 - K_3)/K_3$ and $S_c = K_3\pi^2 c/d^2 n_0 p$ is the threshold intensity under the strict boundary conditions ($u(0) = u/d = 0$).

For convenience, replace the variables in equation (4) $\tilde{z} = \pi z/d$. Then, we come to

$$(1 + \delta\sin^2 u)\frac{\partial^2 u}{\partial \tilde{z}^2} + \delta \sin u \cos u \left(\frac{\partial u}{\partial \tilde{z}}\right)^2 + \frac{S}{S_c}\sin u \cos u (1 - p\sin^2 u)^{-3/2}. \quad (5)$$

At fields close to the threshold, equation (5) is solved by expanding the term responsible for the interaction with the light in terms of u. But at strong fields, when the electromagnetic energy fluxes are considerably above the threshold, it is necessary to find an exact solution. This can be done after linearization of equation (5) if one replaces g by $(\partial u/\partial z)^2$. It results in

$$1/2(1 + \delta\sin^2 u)g' + \delta \sin u \cos u g + \frac{Sn_0 p \sin u \cos u^{3/2}}{(1 - p\sin^2 u)} = 0. \quad (6)$$

While solving this equation, let us take into account that $u(z)$ has a maximum at the center of the layer. Then,

$$g(z = d/2) = \left(\frac{\partial u}{\partial z}\right)^2 = 0,$$

and the solution to equation (6) is

$$g(u) = \frac{2S/S_c}{p(1 + \delta\sin^2 u)} \times \left(\frac{1}{(1 - p\sin^2 a)^{1/2}} - \frac{1}{(1 - p\sin^2 u)^{1/2}}\right), \quad (7)$$

where a is the angle of inclination of the director at the point $z = d/2$.

For $u(z)$,

$$\frac{\partial u}{\partial z} = \pm\sqrt{\frac{2S/S_c}{p(1 + \delta\sin^2 u)}} \times \left(\frac{1}{(1 - p\sin^2 a)^{1/2}} - \frac{1}{(1 - p\sin^2 u)^{1/2}}\right)^{1/2}, \quad (8)$$

where plus corresponds to the case of $\tilde{z} < \pi/2$ and minus to $\tilde{z} > \pi/2$. The integration of (8) results in the equation for u. Because of the problem's symmetry, we shall analyze this equation in the interval $0 \le z \le d/2$,

$$\int_{u_s}^{u} f(u, a)du = \sqrt{\frac{2S/S_c}{p}}\tilde{z}, \quad (9)$$

where

$$f(u, a) \equiv \frac{\sqrt{1 + \delta\sin^2 u}}{\sqrt{\frac{1}{(1 - p\sin^2 a)^{1/2}} - \frac{1}{(1 - p\sin^2 u)^{1/2}}}}$$

and u_s is the angle of inclination of the director at the boundary of the liquid crystal layer. Equation (9) characterizes the dependence of u on z with two parameters a and u_s. The relation between u_s and a under the fixed value of the electromagnetic energy flux S is given by the equation

$$\int_{u_s}^{a} f(u, a)du = \sqrt{\frac{2S/S_c}{p}}\pi/2. \quad (10)$$

In order to solve equation (9), one has to take into account directly the boundary conditions in explicit form. We take the surface energy density to be identical to the Rapini potential [11]:

$$F_{ss} = \frac{1}{2}W\sin^2 u_s, \quad (11)$$

where $u_s = u(0) = u(d)$ under the assumption that properties of both surfaces are identical.

At the same time, the volume density of the elastic energy also contributes to the surface energy. In the present case, it stems from the minimization of the free

energy containing the surface terms. As a result, the boundary conditions takes the form

$$W\sin u_s\cos u_s \pm K_3(1+\delta\sin^2 u_s)\frac{\partial u_s}{\partial z} = 0. \qquad (12)$$

Replacing the derivative $\partial u/\partial z$ by its expression (8), we derive

$$1/2\frac{W}{K_3}\sin 2u_s - \frac{\pi}{d}(1+\delta\sin^2 u_s)\sqrt{\frac{2S/S_c}{p(1+\delta\sin^2 u_s)}} \times\left(\frac{1}{\sqrt{1-p\sin^2 a}} - \frac{1}{\sqrt{1-p\sin^2 u_s}}\right) = 0. \qquad (13)$$

To derive the threshold value of the electromagnetic energy flux, we make the replacement $\sin u/\sin a = \sin x$ in equations (10) and (13). It results in

$$\sin a\int_{x_s}^{\pi/2}\frac{\sqrt{1+\delta\sin^2 a\sin^2 x}}{\sqrt{\frac{1}{(1-p\sin^2 a)^{1/2}} - \frac{1}{(1-p\sin^2 a\sin^2 x)^{1/2}}}} \times\frac{\cos x}{\sqrt{1-\sin^2 a\sin^2 x}}dx = \sqrt{\frac{2S}{pS_c}}\pi/2, \qquad (14)$$

$$\frac{W}{K_3}\sin x_s\sin a(1-\sin^2 a\sin^2 x_s)^{1/2} - \frac{\pi}{d}(1+\delta\sin^2 a\sin^2 x_s)^{1/2}\sqrt{\frac{2S}{pS_c}} \times\left(\frac{1}{(1-p\sin^2 a)^{1/2}} - \frac{1}{(1-p\sin^2 a\sin^2 x_s)^{1/2}}\right)^{1/2} = 0. \qquad (15)$$

Forcing a to zero transforms these equations into

$$\sqrt{S/S_c}\pi/2 = \pi/2 - x_s, \qquad (16)$$

$$\tan(x_s) = \frac{Wd}{\pi K_3}\sqrt{S/S_c}. \qquad (17)$$

To find the condition for the threshold intensity, we exclude x [2]:

$$\cot(\pi/2\sqrt{\tilde{S}_c/S_c}) = \frac{\pi K_3}{Wd}\sqrt{\tilde{S}_c/S_c}. \qquad (18)$$

Forcing W in (18) to zero results in

$$\tilde{S}_c = \frac{2Wd}{K_3\pi^2}S_c.$$

Thus, if the adhesion between the liquid crystal and a substrate is weak, the threshold flux of electromagnetic energy turns out to be proportional to the adhesion energy

$$\tilde{S}_c \sim W,\ W \longrightarrow 0.$$

Specifying the parameters of the system δ and p, the incident light intensity, and the cohesion energy and using equations (10) and (13), we calculated the slope angle of the director at the surface u_s and at the center of the layer a. After that, we determined from equation (9) the nematic transversal structure above the threshold. The parameters of the nematic liquid crystal used are the following: $K_1 = 6.95\times10^{-7}$ din, $K_3 = 8.99\times10^{-7}$ din, $n_0 = 1.544$, and $n_e = 1.758$. The results of calculations are shown in Figs. 2 and 3.

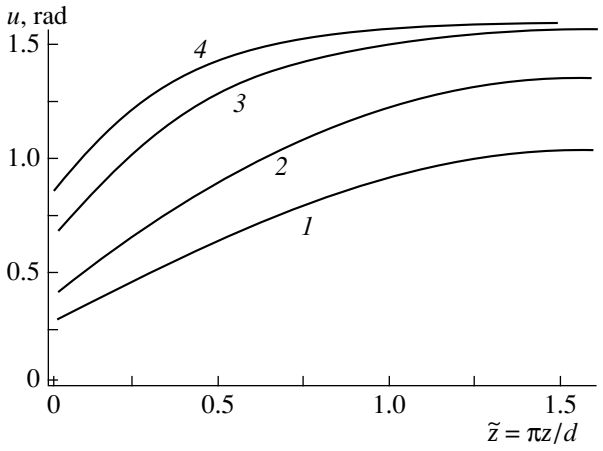

Fig. 2. The director angular distribution in the liquid crystal layer of thickness $d = 2\times10^2$ μm at cohesion energy $W = 5\times10^{-4}$ erg/cm^2 for light energy fluxes $S = 1.3\tilde{S}_c$ (*1*), $2\tilde{S}_c$ (*2*), $5\tilde{S}_c$ (*3*), and $8\tilde{S}_c$ (*4*), $\tilde{S}_c = 0.72S_c$.

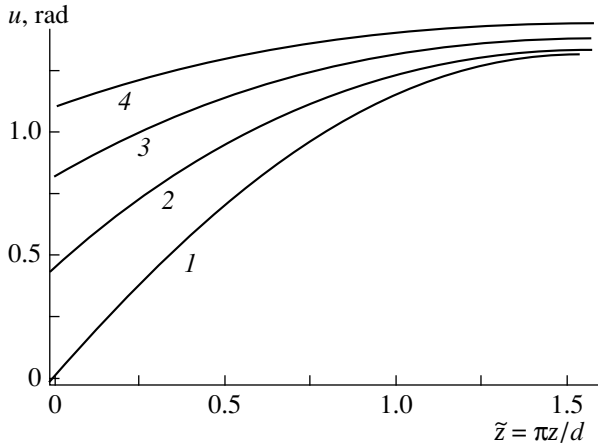

Fig. 3. The director angular distribution at different cohesion energy values for $S = 2\tilde{S}_c$; $W = 5\times10^{-2}$ (*1*), 4×10^{-4} (*2*), 2×10^{-4} (*3*), and 1.5×10^{-4} erg/cm^2 (*4*); layer thickness $d = 2\times10^2$ μm.

It is seen from Fig. 2 that, as the intensity increases, the thickness of the near-wall layer decreases. The shape of the distribution curve of angles of deflection from homeotropical orientation noticeably differs from sinusoidal, which is observed in relatively weak fields. It can also be seen that, at finite cohesion energy, the director deviation occurs not only in the volume but on the surface as well.

Figure 3 illustrates the distribution of the director angle of deviation at different values of cohesion energy for fixed radiation intensity. A very strong dependence of the results on W values deserves our attention.

It follows from the presented figures that the variation of local direction of the optical axis is sensitive to the radiation intensity values and nematic parameters. In particular, this enables one to determine liquid crystal parameters and, above all, cohesion energy with substrate from the dependence of the interference pattern on the radiation intensity.

REFERENCES

1. B. Ya. Zel'dovich and N. V. Tabiryan, Zh. Éksp. Teor. Fiz. **79**, 2388 (1980) [Sov. Phys. JETP **52**, 1210 (1980)].
2. H. L. Ong, Phys. Rev. A **28**, 2393 (1983).
3. S. M. Arakelyan, G. A. Lyakhov, and Yu. S. Chilingaryan, Usp. Fiz. Nauk **131** (1), 3 (1980) [Sov. Phys. Usp. **23**, 245 (1980)].
4. A. S. Zolot'ko, V. F. Kitaeva, N. Kroo, N. N. Sobolev, *et al.*, Pis'ma Zh. Éksp. Teor. Fiz. **32**, 170 (1980) [JETP Lett. **32**, 158 (1980)].
5. V. P. Romanov and D. O. Fedorov, Opt. Spektrosk. **78**, 274 (1995) [Opt. Spectrosc. **78**, 244 (1995)].
6. I. Janossy, L. Csillag, and A. D. Lloyd, Phys. Rev. A **44**, 8410 (1991).
7. I. Janossy, A. D. Lloyd, and B. S. Wherrett, Mol. Cryst. Liq. Cryst. **179**, 1 (1990).
8. L. Marrucci and D. Paparo, Phys. Rev. E **56**, 1765 (1997).
9. A. S. Zolot'ko, Pis'ma Zh. Éksp. Teor. Fiz. **68**, 410 (1999) [JETP Lett. **68**, 335 (1999)].
10. F. Marquis, P. Meystre, and E. M. Wright, Phys. Rev. A **36**, 875 (1987).
11. A. Rapini and M. Papoular, J. Phys. (Paris) **30**, 4 (1959).

Translated by S. Egorov

Technical Physics, Vol. 45, No. 6, 2000, pp. 743–746. Translated from Zhurnal Tekhnicheskoĭ Fiziki, Vol. 70, No. 6, 2000, pp. 74–77.

OPTICS, QUANTUM ELECTRONICS

Characteristics of Fourier Phase Holograms Recorded on Photopolymers

P. V. Ezhov, T. N. Smirnova, and E. A. Tikhonov

Institute of Physics, National Academy of Sciences of Ukraine, pr. Nauki 46, Kiev, 252650 Ukraine

Received December 17, 1998; in final form, September 3, 1999

Abstract—The results of the investigation of recording Fourier phase holograms on a self-developing photopolymer photosensitive in the range $\lambda = 400$–515 nm are presented. It has been found that, due to the transient energy transfer between the beams, noise gratings are recorded, and a corresponding sharp reduction in the signal-to-noise ratio occurs, while the diffraction efficiency of the hologram as a whole remains relatively high (above 50%). It has been found that the noise-grating recording can be substantially suppressed by increasing the intensity of the reference beam relative to the intensity of the object beam. In this way, the signal-to-noise ratio has been considerably improved for Fourier holograms of binary phase masks: at a reference to object beam intensity ratio $R = 26$, Fourier phase holograms are recorded with a diffraction efficiency $\eta = 15\%$ and signal-to-noise ratio $N = 20$ dB. © *2000 MAIK "Nauka/Interperiodica".*

INTRODUCTION

The application of Fourier holograms to solving spatial filtering problems and as matched filters in image-recognition systems [1, 2] makes the study of holographic media for these purposes important. One of the first papers where the advantages of photopolymer spatial filters were shown is [3]. The formation of holograms in the course of exposure (1–3 min) without the application of a wet chemical process allowed the authors of [3] to use this polymer successfully for the holographic recording of matched filters in van der Lugt's arrangement. To record the filters, they used the OmniDex material of the DuPont Company.

Substantial modulation of the average refractive index of the material accompanying the hologram formation on photopolymers is the cause of dynamic energy exchange between the recording and scattered beams [4], which may distort the interference pattern in the medium and considerably reduce the signal-to-noise ratio N. The role of dynamic effects is particularly great when holograms of diffuse objects are recorded. Therefore, the holographic recording on photopolymerizable compositions (PPC) requires a comprehensive study of the influence of recording conditions on the hologram parameters.

The objective of this work is to investigate and optimize the basic characteristics (diffraction efficiency η and signal-to-noise ratio N) of diffuse-object Fourier holograms using the FPK-488 photopolymerizable composition as the recording medium. It is known [5–7] that this photopolymer allows one to record spatial phase gratings with a spatial frequency of up to 6000 mm^{-1}, η practically up to 100%, and low noise level $N > 20$ dB. Unlike the OmniDex materials, photopolymerizable composition FPK-488 provides the maximal diffraction efficiency of holograms in the course of recording and does not require postexposure processing. The latter makes it more promising for use in image recognition systems as compared to photopolymer materials that require optical or thermal development.

In this paper, Fourier holograms of a particular class of objects, namely, random binary phase masks [8], were investigated. The dimensions of phase masks were 5×5 mm, and the number of phase elements were 256×256. Fourier spectra of these objects are characterized by the most uniform intensity distribution, which allows one to estimate correctly the ultimate diffraction efficiency η at a specified convergence angle between the reference and object beams.

EXPERIMENT

Fourier holograms were recorded by He–Cd laser radiation ($\lambda = 441.2$ nm) using a conventional arrangement (Fig. 1) [1]. The object was placed in the object plane P_{obj}, where it was illuminated by the transmitted collimated laser beam. The angle between the reference and object beams was $\alpha = 13°$. For a specified thickness of the recording film $d = 25$ μm, the Bragg recording mode was achieved for the mean spatial frequency. Selection of a random binary phase mask (RBPM) as the object allowed us to remove the problem of nonuniformity in intensity distribution in the plane of hologram recording, which often arises when Fourier holograms are recorded. The registering film was placed in the plane of recording, where a Fourier hologram of the phase mask was formed in the process of exposure.

The registering film was formed by introducing the initially liquid PPC between two glass substrates with spacers of calibrated thickness. In order to reduce the

1063-7842/00/4506-0743$20.00

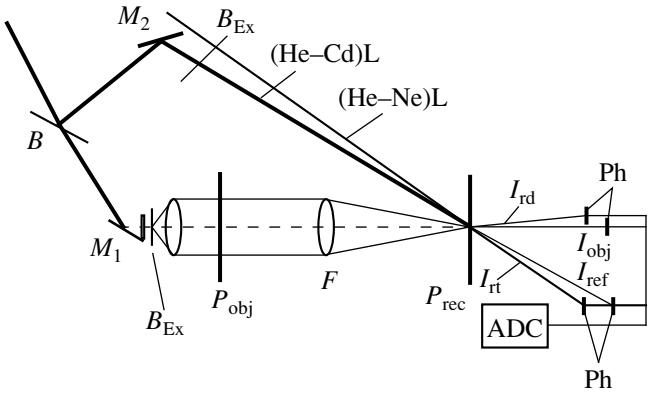

Fig. 1. Fourier-hologram recording arrangement with a registering system: (M_1, M_2) mirrors; (B) beamsplitter; (B_{Ex}) collimator with spatial filtering; (P_{obj}, P_{rec}) object plane and recording plane; (F) Fourier lens; (I_{rd}, I_{rt}) are the intensities of the diffracted and transmitted beams of the testing He–Ne laser [(He–Ne)L]; (I_{obj}, I_{ref}) intensities of the object beam and reference beam of He–Cd [(He–Cd)L] or Ar^+ laser; (ADC, Ph) analog-to-digital converter in the IBM-compatible computer and photodiodes of the registering system, respectively.

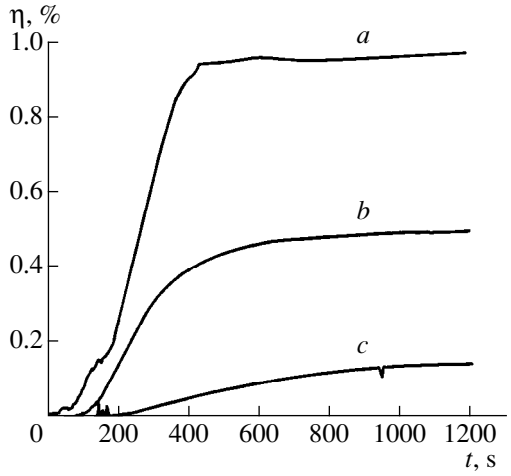

Fig. 2. Diffraction efficiency as a function of time for various R: (*a*) record of a grating, $R = 1$, $N > 20$ dB; (*b*) record of Fourier holograms, $R = 1$, $N = 4.8$ dB; and (*c*) record of Fourier holograms, $R = 26$, $N > 20$ dB.

noise, the PPC film was prepolymerized by an optimal dose of incoherent radiation in a wavelength range of 250–300 nm.

An automatic system detecting the intensity of the transmitted I_t and diffracted I_d beams of a He–Ne laser ($\lambda = 633$ nm) allowed one to record the dependence of diffraction efficiency on time as $\eta(t) = I_d(t)/(I_d(t) + I_t(t))$. A similar recording system was used to measure the kinetics of transient energy transfer between the interfering object and reference beams.

As the ratio of intensities of the object and reference beams R changed, the resulting intensity in the recording plane remained constant and was 4 mW/cm^2. In order to estimate the signal-to-noise ratio N, the hologram was placed in the object plane and the reconstructed image was analyzed by the procedure described in [9]. According to this procedure, in order to calculate N, signals I_0 and I_1 were measured. I_0 was a signal comprising the desired signal and a noise component, and I_1 was the desired signal. N was determined as $N = 10\log(I_1/(I_0 - I_1))$.

RECORDING OF FOURIER PHASE HOLOGRAMS

In order to determine the optimal conditions for recording Fourier holograms of the selected objects on the FPK-488, R was measured as a function of Fourier-hologram characteristics, such as $\eta(t)$, N, and maximum-efficiency attainment time t_m. The results of measurements are presented in the table and shown in Fig. 2. Initial values of such parameters as photopolymer-film thickness, ratio of the intensities of the hologram-forming beams, and total light intensity in the plane of hologram recording were taken that were optimized for recording transmission volume phase gratings [3–6].

Comparing the diffraction efficiency and signal-to-noise ratio for transmission volume phase gratings and Fourier holograms, one can see (Fig. 2) that the maximum efficiencies for the gratings and Fourier holograms with the same noise level ($N > 20$ dB) differ by more than a factor of 6.5.

Taking into account that, for the object used (RBPM), the uniformity of illuminance in the Fourier plane is maximal (Fig. 3a), we can say, without a loss in generality, that the obtained Fourier-hologram efficiency $\eta = 15\%$ is maximum for the given recording conditions and the medium. Attention is drawn to the steep rise of noise for Fourier holograms recorded at $R = 1$. This results from dynamic noise amplification and is considered in detail below. From the data obtained, one can draw a conclusion that, for recording thick phase holograms of diffuse objects on the photopolymer FPK-488 at $\alpha = 13°$ and $d = 25$ μm, the optimal parameters are the following: $R = 26$, $\eta = 15\%$, $N > 20$ dB, and $t_n = 5$–15 min (Fig. 2). An example of an image reconstructed from a Fourier hologram is shown in Fig. 3b.

In a number of papers [4, 10–13], it is shown that, for materials with sluggish response in which the image is formed in the process of recording, for FPK-488 in particular, transient energy transfer between interfering beams is characteristic because of changes in the refractive index during hologram recording. This results in (i) the amplification of weak noise gratings [11, 12] that occur due to the interference of the plane reference and spherical wave fronts (the consequence of the scattering of the plane wave by phase nonuniformities) [10]; (ii) amplification of the less intense wave

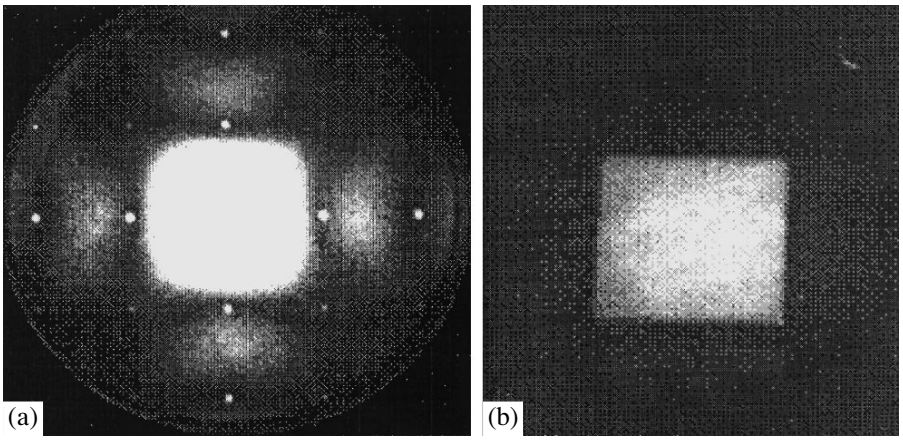

Fig. 3. (a) Spectrum of Fourier RBPM and (b) the image reconstructed from the Fourier hologram.

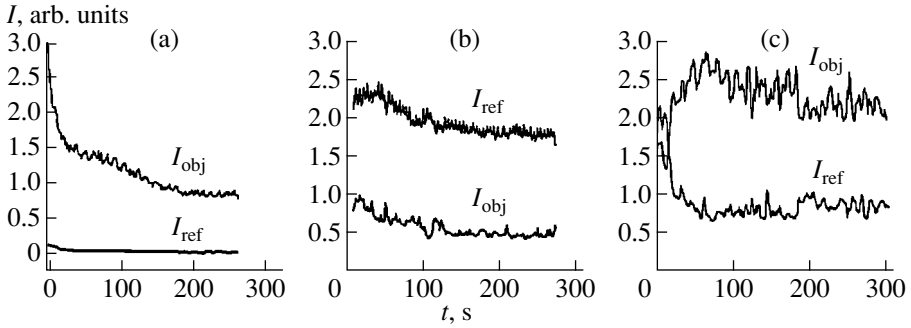

Fig. 4. Intensities of the reference and object beams as a function of time. I_{ref} and I_{obj} correspond to the transmission reference beam and object beam; (a) $R < 1$, (b) $R > 1$, and (c) $R \approx 1$.

[4] when gratings are recorded by plane waves with different intensities; and (iii) anomalous [13] amplification of the wave with greater intensity owing to the wave with lesser intensity which is observed during recording of diffuse objects.

The intensity of the energy transfer and its direction may [13] depend on such parameters as the ratio between the intensities of the object and reference beams, asymmetry in their incidence on the recording film, and total intensity of the recording field. In this paper, the energy transfer was investigated for various R, the other parameters being constant.

The dynamic effects may reduce the signal-to-noise ratio in the images reconstructed from holograms recorded on FPK-488. In principle, they cannot be removed. However, there is a possibility to minimize the noise level by either suppressing or counterbalancing the transient energy transfer [11, 12].

Since there is a need to minimize these noises for Fourier holograms, we measured, in the process of recording, the time dependences of the recording-beam intensities $I_r(t)$ and $I_{obj}(t)$ for the limiting cases: $R < 1$, $R > 1$, and $R = 1$. These dependences are shown in Figs. 4a–4c. The registration plane is located behind the hologram-recording plane P_{rec} (Fig. 1).

It is seen that, for $R < 1$ (Fig. 4a), a strong light scattering is observed at the initial moment without energy transfer between the recording beams. It is supposedly the result of amplification of noise gratings formed by the object beam (the presence of intermodulation noise in the image reconstructed from Fourier holograms). For $R > 1$ (Fig. 4b), a weak energy transfer occurs from the reference beam to the object beam. When $R \approx 1$ (Fig. 4c), a strong energy transfer is observed from the object beam to the reference beam against the background of dynamic noise amplification, as demonstrated by the asymmetry in the intensity variations of both beams.

Fourier-hologram recording parameters

No.	R	η, %	N, dB	t_m, s
1	1*	98	20	400
2	1	62	–4.77	–
3	4	52	–3.68	500
4	9	30	6.02	–
5	26	15	20	1000

* Recording of volume phase gratings [3–6].

From the results obtained, we may draw the conclusion that the region $R > 1$ is the one best suited to recording Fourier holograms of diffuse objects with $N > 20$ dB.

CONCLUSION

This paper presents the results of an investigation of recording thick Fourier holograms on FPK-488. It has been found that, due to a transient energy transfer between the beams, noise gratings are recorded and, respectively, a sharp reduction in the signal-to-noise ratio occurs, while the diffraction efficiency of the hologram as a whole remains relatively high (greater than 50%). It has been found that the noise-grating recording can be substantially suppressed by increasing the intensity of the reference beam relative to the intensity of the object beam. In this way, the signal-to-noise ratio has been considerably improved for the Fourier holograms of binary phase masks: for $R = 26$, Fourier phase holograms are recorded with the diffraction efficiency $\eta = 15\%$ and $N = 20$ dB.

ACKNOWLEDGMENTS

This work was supported by the Ukrainian Center of Science and Technology, project no. 559.

REFERENCES

1. R. J. Collier, C. B. Burckhardt, and L. H. Lin, in *Optical Holography* (Academic Press, New York, 1971), p. 672.
2. *Application of Optical Fourier Transforms*, Ed. by H. Stark (Academic Press, New York, 1982), p. 531.
3. R. W. Brandstetter and N. J. Fonneland, Proc. SPIE **1559**, 308 (1991).
4. V. I. Sukhanov and V. L. Korozinin, Pis'ma Zh. Tekh. Fiz. **18**, 1144 (1982) [Sov. Tech. Phys. Lett. **8**, 491 (1982)].
5. E. A. Tikhonov, T. N. Smirnova, and E. S. Gyul'nazarov, Kvantovaya Élektron. (Kiev), No. 40, 1 (1991).
6. E. A. Tikhonov, T. N. Smirnova, and E. S. Gyul'nazarov, Opt. Spektrosk. **67** (1), 175 (1989) [Opt. Spectrosc. **67**, 99 (1989)].
7. E. S. Gyul'nazarov, T. N. Smirnova, and E. A. Tikhonov, Zh. Tekh. Fiz. **57** (5), 932 (1987) [Sov. Phys. Tech. Phys. **32**, 565 (1987)].
8. M. V. Fitio, L. I. Muravsky, and A. I. Stefansky, Proc. SPIE **2647**, 224 (1995).
9. *Handbook of Optical Holography*, Ed. by H. J. Caulfield (Academic Press, New York, 1978; Mir, Moscow, 1982).
10. J. A. Jenney, Appl. Opt. **11** (6), 1371 (1972).
11. E. S. Gyul'nazarov, T. N. Smirnova, E. A. Tikhonov, and M. T. Shpak, Ukr. Fiz. Zh. **33** (1), 8 (1988).
12. E. S. Gyul'nazarov, T. N. Smirnova, and E. A. Tikhonov, Zh. Tekh. Fiz. **58**, 2405 (1989) [Sov. Phys. Tech. Phys. **33**, 1469 (1988)].
13. A. B. Mamaev, K. Orazov, N. F. Pilipetskiĭ, and V. V. Shkunov, Kvantovaya Élektron. (Moscow) **14** (2), 413 (1987).

Translated by I. N. Nikishin

Technical Physics, Vol. 45, No. 6, 2000, pp. 747–752. Translated from Zhurnal Tekhnicheskoĭ Fiziki, Vol. 70, No. 6, 2000, pp. 78–83.

RADIOPHYSICS

Generation of RF Oscillations in the Interaction of an Electromagnetic Shock with a Synchronous Backward Wave

A. M. Belyantsev and A. B. Kozyrev

Institute for Physics of Microstructures, Russian Academy of Sciences, Nizhni Novgorod, 603600 Russia

Received April 7, 1999

Abstract—A new mechanism for the transformation of video pulses into radio pulses during their propagation along a nonlinear transmission line with spatial dispersion—synchronism with a backward wave—is considered. Numerical simulations demonstrate that a substantial advantage of this mechanism over the interaction with a forward wave is the possibility of generating longer radio pulses at higher frequencies. © *2000 MAIK "Nauka/Interperiodica".*

INTRODUCTION

The possibility of the direct and efficient transformation of video pulses into radio pulses during their propagation along a nonlinear transmission line (TL) with spatial dispersion was considered in [1–3]. The method is based on the instability of the front of an electromagnetic shock (EMS) interacting with a synchronous wave ($v_s = v_p(\omega)$, where v_s is the EMS velocity and $v_p(\omega)$ is the phase velocity of the wave). The efficiency of transformation of an EMS propagating in synchronism with a forward wave ($v_p v_g > 0$, where $v_g(\omega)$ is the group velocity, $v_g < v_s$) was studied with account of high-frequency losses for various dispersion properties of the TL. In our previous paper [2], we have demonstrated that both the duration of a quasi-steady train of the generated oscillations and the TL length necessary for its formation depend on the choice of a "working point" at the TL dispersion curve upon saturation of nonlinearity. In particular, it was shown that, in the case of the generation of RF oscillations at the frequency corresponding to a minimum of v_g, when the dispersion broadening of the radio pulse is minimal, both the TL length that is necessary for the generation of a given number of oscillations and the damping rate of these oscillations depend strongly on the difference $v_p - v_g$. In the case of synchronism with a forward wave, this difference can be slightly increased by changing the TL dispersion. The situation changes drastically when v_p and v_g have opposite signs, i.e., when the EMS is in synchronism with either a backward harmonic of a periodic system or a normal backward wave ($v_g v_p < 0$). In this paper, we study the distinctive features of the generation of RF oscillations in a TL with ferrite in the case when the EMS is in synchronism with a backward wave or backward spatial harmonic and compare the results obtained with those for synchronism with a forward wave. Obviously, each particular electrodynamic system requires special study of spatial harmonics or normal waves and the efficiency of their excitation by a traveling source (EMS front). However, the main features of the synchronism between the EMS and a backward harmonic (or wave) can be establish based on general considerations using the simplest equivalent schemes of a TL with nonlinear ferrite elements. The analysis of the processes in such lines shows that, in the case of synchronism of an EMS with a backward spatial harmonic (or backward wave), the above mechanism can be used to generate longer radio pulses in a higher frequency range.

THE MODEL OF AN ELECTRODYNAMIC SYSTEM WITH FORWARD AND BACKWARD WAVES

It is well known that backward waves can exist in the media with anomalous spatial dispersion [4] and in various periodic systems, in particular, slow-wave electrodynamic systems (see, e.g., [5]), in which the propagating wave is spatially modulated. Such a wave can be considered as a wave group consisting of spatial harmonics whose amplitudes are coupled. The harmonics travel with different phase velocities, but the group velocity is the same for all of them. Some of the harmonics are forward, and some are backward. In different slow-wave systems, the fundamental (or zero) spatial harmonic, which has the largest absolute value of the phase velocity, can be either forward or backward [5]. If the wavelength is much longer than the period d of the system ($\lambda \gg d$), then the backward zero harmonic is dominating in the wave group [5]. This fact sometimes allows one to consider the wave group of a periodic system as a quasi-normal backward wave analogous to the backward wave in a system with anomalous spatial dispersion. The waves with zero backward harmonic propagate in slow-wave systems only within a

1063-7842/00/4506-0747$20.00

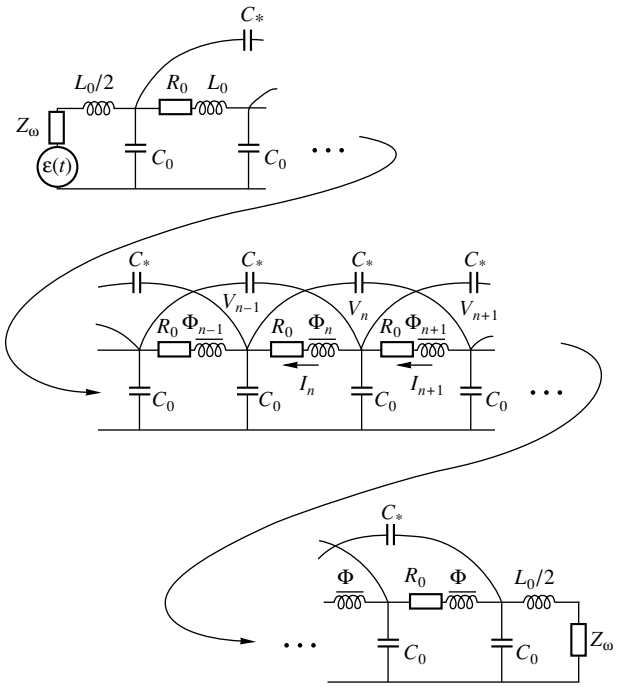

Fig. 1. The equivalent scheme of an *LC* nonlinear transmission line with ferrites and cross-coupling between the next nearest cells.

certain RF band, which makes impossible the propagation of shock waves in such systems (for the excitation of a shock wave, it is necessary that low-frequency waves can propagate in the system). However, if such a slow-wave system is coupled with another slow-wave system in which the forward zero harmonic dominates in the wave group propagating at low frequencies, then such an electrodynamic system allows both forward and backward quasi-normal waves, which makes possible the synchronism of an EMS with a backward wave. The use of a discrete equivalent chain (Fig. 1) allows simple description of such a situation. The discreteness of the equivalent chain gives rise to fundamental harmonics ($0 \le \varphi_0 \le \pi$ and $-\pi \le \varphi_0 \le 0$) traveling in the $+z$ and $-z$ directions and a set of harmonics $\varphi_n = \varphi_0 \pm 2\pi n$, where φ_n is the phase shift per cell or the wavenumber of the nth spatial harmonic normalized to the period d of the system. In contrast to real periodic slow-wave systems, these harmonics do not form wave groups, because the equivalent scheme does not provide the amplitude coupling between them. Hence, each harmonic can be regarded as a normal wave with the phase ($v_p^{(n)}$) and group ($v_g^{(n)}$) velocities

$$v_p^{(n)} = d\frac{\omega}{\varphi_n}, \quad v_g^{(n)} = d\frac{\partial\omega}{\partial\varphi_n} = d\frac{\partial\omega}{\partial\varphi_0}. \qquad (1)$$

This model allows us to study qualitatively the main features of the excitation of a wave group of a slow-wave system in the case of synchronism of the EMS front with one of the backward spatial harmonics. However, for each particular slow-wave system, the efficiency of excitation oscillations by an EMS front propagating in synchronism with a quasi-normal backward wave or backward spatial harmonic of the wave group depends strongly on the relationship between their fields and the currents of the traveling source (EMS front).

THE STRUCTURE OF A STEADY EMS IN A PERIODIC TL

1. General Considerations

The main features of the generation of RF oscillations in a TL with ferrite in the case of synchronism with a backward or forward wave (spatial harmonic) can be established based on the studies of the structure of a steady EMS.

If a TL has a periodic structure in the longitudinal direction z, then the alternating field behind the front of a steady EMS depends not only on the transverse coordinate $\mathbf{r}_\perp$ and the variable $\xi = (z - v_s t)/d$ related to the EMS front, but also on z. In particular, for synchronism of the EMS front with the nth spatial harmonic ($v_s = \mathrm{Re}\, d\omega/\varphi_n(\omega)$), the alternating component of the field behind the front upon saturation of nonlinearity can be represented qualitatively as [6]

$$\mathbf{E}_\sim \sim a_n(\omega)\mathrm{Re}\left[\exp(j\varphi_n\xi) \times \sum_m \mathbf{e}_m(\mathbf{r}_\perp, \omega)\exp\{j(\varphi_m - \varphi_n)z/d\}\right]. \qquad (2)$$

Here $\mathbf{e}_m(\mathbf{r}_\perp, \omega)$ is the electric field of the mth spatial harmonic and $a_n(\omega)$ is the excitation coefficient of the wave group, which is governed by the processes occurring at the EMS front, where the nonlinearity is not saturated. It follows from (2) that the oscillations in a steady wave damp with distance from the front as $\exp(-\varphi_n'' \xi)$ with the damping rate determined by the imaginary part of the wavenumber of the harmonic ($\varphi_n = \varphi_n' + i\varphi_n''$) that is in synchronism with the EMS front. In addition, the field is spatially modulated with the period equal to the period d of the structure. However, if the EMS is in synchronism with the dominating harmonic of one of the wave groups (waves) of a slow-wave system, then the periodicity over z is insignificant and the distribution of the alternating field of a steady EMS along the TL is governed mainly by the propagation constant of this harmonic.

At fixed $z = z_0$, relationship (2) describes the time behavior of the electric field of a steady EMS passing through a given section of a periodic slow-wave system. The electric field exhibits harmonic oscillations with the damping rate $-\varphi_n'' v_s/d$, which depends on both

the frequency of oscillations and the EMS velocity. It is clear that, for a steady EMS, the time behavior is identical for all the points $z = z_0 + nd$.

Evidently, the structure of a steady EMS in the case of synchronism with a forward harmonic is qualitatively the same as that for synchronism with a backward harmonic. However, such parameters as the damping rate and relative amplitude of oscillations can be substantially different. These differences can be established based on the consideration of a model problem using an equivalent scheme similar to that shown in Fig. 1.

2. Basic Equations

Nonlinear processes in an *LC* chain with capacitive cross-coupling (Fig. 1) are described by a system of differential difference equations,

$$\frac{d\Phi_n}{dt} = V_{n-1} - V_n - I_n R_0(\omega), \qquad \Phi_n = L_0(I_n + 4\pi\eta M_{hn}), \tag{3}$$

$$C_0\frac{dV_n}{dt} = I_n - I_{n+1} + C_*\frac{d}{dt}(V_{n-2} - 2V_n + V_{n+2}), \tag{4}$$

$$\frac{dM_{hn}}{dt} = -\frac{\alpha\gamma}{(1+\alpha^2)M}(M^2 - M_{hn}^2)H_n(I_n). \tag{5}$$

Here, Φ_n is the induction flux in the nth cell of the nonlinear TL, I_n is the current, V_n is the voltage, M_{hn} is the mean value of the magnetization vector (which is parallel to the magnetic field), $H_n(I_n)$ is the magnetic field, γ is the absolute value of the gyromagnetic ratio, M is the saturation magnetization ($4\pi M = B_s$), η is the ferrite space factor of the TL, α is the dissipation coefficient, C_0 is the capacitance of a unit cell of the TL, L_0 is the inductance of a unit cell upon saturation of nonlinearity, and C_* is the cross-coupling capacitance. The resistance $R_0(\omega)$ takes into account high-frequency losses in the TL that are related to dissipation in metal surfaces (due to skin effect) and high-frequency dielectric losses in the saturated ferrite. The frequency dependence of the resistance is given by

$$R_0 = k_0\sqrt{\omega} + \Gamma_0(\omega)\tan\delta(\omega), \tag{6}$$

where $\tan\delta$ is the tangent of dielectric losses in the saturated ferrite and the coefficients k_0 and $\Gamma_0(\omega)$ are determined by the TL structure. The frequency dependence of $\Gamma_0(\omega)$ is also determined by TL geometry and, in the general case, cannot be specified as a known function of frequency. However, for the estimates, we can assume that Γ_0 is constant within a wide frequency range. The frequency dependence of the tangent of dielectric losses $\tan\delta$, which is different for different ferrites, determines the frequency dependence of dielectric losses in the ferrite [see (6)]. Below, we assume that $\tan\delta \sim \omega^2$ (in particular, such a dependence approximates well $\tan\delta$ in the frequency range 500–1000 MHz for nickel–zinc ferrites).

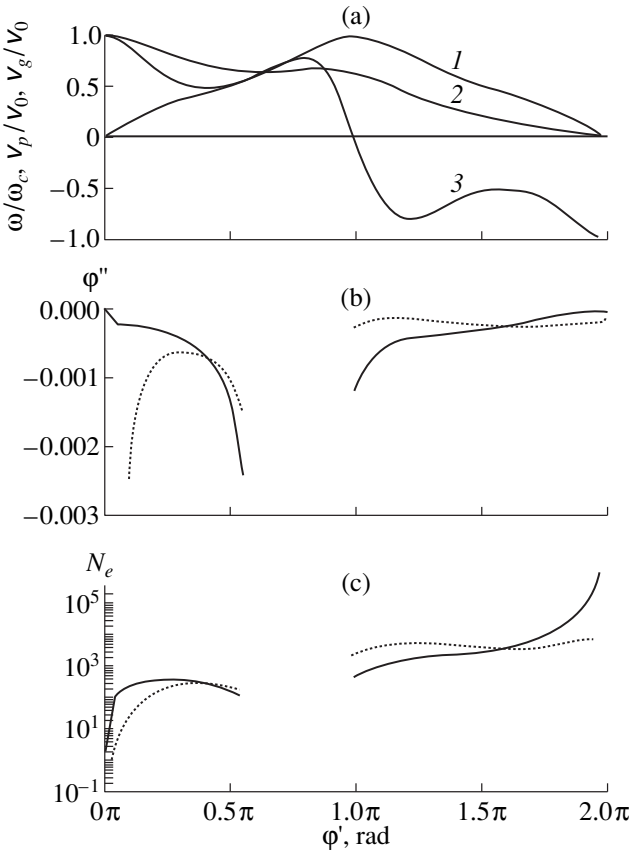

Fig. 2. (a) Dispersion characteristics of an *LC* chain with cross-coupling between the next nearest cells for the cross-coupling coefficient $\gamma_* = C_*/C_0 = 0.2$, (b) the imaginary part of the wavenumber φ", and (c) the duration of the generated radio pulse N_e versus the wavenumber φ'; for R_0/Z_0 = 0.000293 (dashed line) and $R_0 \sim \omega^2$ (for R_0/Z_0 (500 MHz) = 0.000293) (solid line).

Figure 2a presents the dispersion characteristics of the *LC* chain with a capacitive cross-coupling between the next nearest cells upon saturation of the ferrite and in the absence of losses. The figure shows the dependences of (*1*) the relative frequency ω/ω_c, (*2*) relative phase velocity v_p/v_0, and (*3*) relative group velocity v_g/v_0 on the wavenumber φ' for the forward wave ($0 \le \varphi_0 \le \pi$) and for the first spatial harmonic ($\varphi_1 = 2\pi - \varphi_0$). Here $\omega_c = 2/\tau_0$ is the critical frequency, $\tau_0 = (L_0C_0)^{1/2}$ is the time constant of a unit cell, and $v_0 = d/\tau_0$ is the characteristic velocity. It is seen that the synchronism of the EMS with a backward harmonic is possible near the minimum of the group velocity v_g but for values of $v_s = v_p(\omega)$ smaller than those in the case of synchronism with a forward wave.

As was mentioned above, in the case of saturated nonlinearity, the structure of a steady EMS is deter-

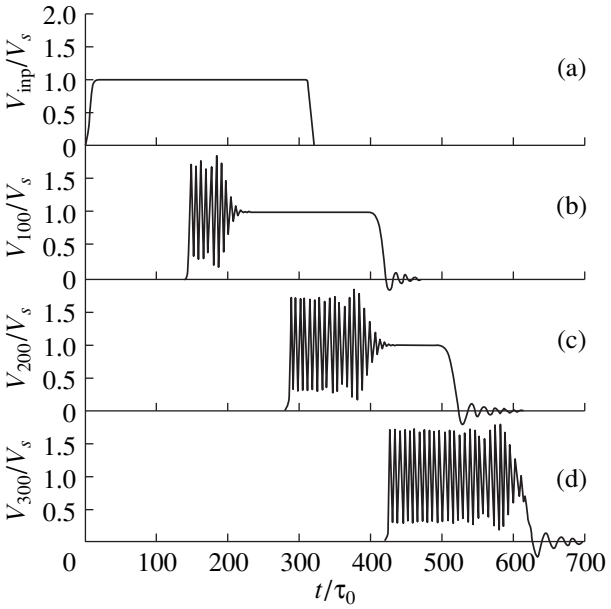

Fig. 3. Time dependences of the voltage (a) at the input cell (the input video pulse) and in the inductances of the (b) 100th, (c) 200th, and (d) 300th cells of a nonlinear TL with ferrites for synchronism of the EMS front with a forward wave at $\gamma_* = 0.2$; $\tau_0 = 6.4 \times 10^{-10}$ s; $\eta = 0.5$; $M = 300$ Oe; and $M_0/M = -0.8$, where M_0 is the initial magnetization. The dispersion characteristics of the synchronous wave are $\varphi = 1.264$, $\omega/\omega_c = 0.45$, $v_p/v_0 = 0.71$, $v_g/v_0 = 0.49$, and $Z_\omega/Z_0 = 0.61$.

mined by the wavenumber φ, which, in the case at hand, can be found by linearizing the system of equations (3)–(5) and passing over to the coordinate $\xi = (z - v_s t)/d$ related to the steady EMS. The unknown wavenumbers, which are the characteristic numbers φ of the linear differential difference equation obtained, are determined by

$$\varphi^2 \frac{v_s^2}{v_0^2} + i\varphi \frac{v_s}{v_0}\frac{R_0}{Z_0} - \frac{4\sin^2\varphi/2}{1 + 4\gamma\sin^2\varphi} = 0. \qquad (7)$$

Here, $\gamma_* = C_*/C_0$ and $Z_0 = (L_0/C_0)^{1/2}$. In the case of small losses, $\varphi''/\varphi' \ll 1$ ($\varphi = \varphi' + i\varphi''$), we arrive at

$$\varphi'' \approx \frac{R_0(\omega)/Z_0}{2\varphi'(v_g/v_0 - v_s/v_0)}. \qquad (8)$$

3. Calculation of the Parameters of a Steady-State Structure

Figures 2b and 2c show the dependences of the damping rate φ" and the duration of the steady radio pulse (the number N_c of oscillations in the oscillating part of the EMS front corresponding to an *e*-fold decrease in the amplitude) on the real part of the wavenumber φ' (or the wavenumber in the absence of losses) for frequency-independent resistance R_0 (dotted curve) and for the frequency dependence of R_0 typical of dielectric losses in ferrite ($R_0 \sim \omega^2$) (solid curve). In calculations, we used the values of the resistance R_0 that are typical of the frequencies of about 500 MHz.

Note that, for frequency-independent losses, the maximum duration of a steady radio pulse corresponds to a certain optimum value of the wavenumber near the minimum of v_g for both forward and backward waves. However, the maximum of N_e is less pronounced for backward waves, and it disappears completely under strong frequency dependence of R_0.

The duration of a steady radio pulse in the case of synchronism with a backward wave ($\pi < \varphi' < 2\pi$) is about one order of magnitude longer than that for synchronism with a forward wave (spatial harmonic). For frequency-dependent losses ($R_0 \sim \omega^2$), this is valid for any fixed frequency from the transmission band, and, for frequency-independent losses, this holds simultaneously for all the frequencies within the transmission band (Figs. 2b, 2c). Therefore, it is more advantageous to use the synchronism with a backward wave rather than with a forward wave in order to produce a long radio pulse with a higher carrier frequency.

It is seen from formula (8) that, in the case of synchronism with a backward wave, the smaller damping rate is explained, on one hand, by a relatively high rate of energy outflow (with the group velocity $v_s < 0$) from the EMS front and, on the other hand, by a greater value of the wavenumber φ'. An analogy with a traveling source provides a qualitative explanation of this fact. For synchronism with a backward wave, the energy of oscillations outflows fast from the EMS front, As a result, the damping of the generated radio pulse has no time to strongly affect the pulse envelope. This fact is also proved by numerical simulations of a nonsteady transformation of a video pulse into a radio pulse in the case of synchronism of the EMS front with a backward wave (harmonic) of a periodic TL.

NUMERICAL SIMULATIONS OF THE NONSTEADY GENERATION OF RF OSCILLATIONS BY AN EMS

1. Synchronism with a Forward Wave

Figure 3 shows the time dependences of the voltage in several cells of a TL with dispersion and ferrite nonlinearity in the case of synchronism with a forward wave. The EMS front is formed after the leading edge of the video pulse fed to the TL input (Fig. 3a) has passed three to four TL cells. After that, oscillations appear behind the front. The generated oscillations travel with a velocity lower than the EMS front velocity and gradually fall behind it (with the relative velocity equal to the difference of the phase and group velocities). The number of these oscillations is proportional to the distance covered by the EMS front (Figs. 3b–3d). The generation of the radio pulse is accompanied by a

decrease in the video pulse duration. The video pulse energy decreases due to dissipation at the EMS front and generation of oscillations behind it. In the nonsteady stage of the video pulse evolution shown in Fig. 3, the train of the generated oscillations can be divided into a train of quasi-steady oscillations, whose damping is determined mainly by the imaginary part of the wavenumber (which is the same as for a steady-state wave), and the trailing edge, where the damping of oscillations is determined mainly by the local dispersion of the group velocity. Note that the duration of the trailing edge and the dispersion broadening of the generated train are minimal when the working point corresponds to the minimum of the group velocity [2].

A train of oscillations can be output from the nonlinear TL to a matched load with Z_ω equal to the RF wave impedance ($Z_\omega = \mathrm{Re}(V_\omega/I_\omega)$, where V_ω and I_ω are the voltage and current amplitudes of the generated RF wave). An analogy with a traveling source allows us to determine the line length L (the number of cells) that is necessary for the formation of a train consisting of N oscillations [1, 2]:

$$L(N) = \frac{2\pi v_s N}{(v_s - v_g)\varphi'}. \qquad (9)$$

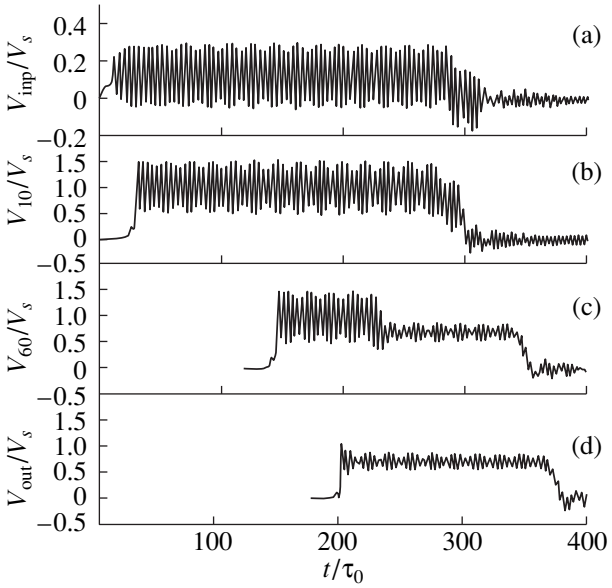

Fig. 4. Time dependences of the voltage (a) at the input load, in (b) the 10th and (c) 69th cells, and (d) at the output load of a nonlinear TL with ferrites for synchronism of the EMS front with a backward wave with the same parameters as in Fig. 3. The dispersion characteristics of the synchronous wave are $\varphi = 3.827$, $\omega/\omega_c = 0.82$, $v_p/v_0 = 0.43$, $v_g/v_0 = 0.78$, and $Z_\omega/Z_0 = 0.29$.

2. Synchronism with a Backward Wave

The nonsteady generation of RF oscillations by an EMS in the case of synchronism with a backward wave has some specific features. In contrast to the synchronism with a forward wave, in this case, the energy of RF oscillations travels in the direction opposite to the direction of propagation of the EMS front. Since, in this case, $v_g < 0$, the energy of the generated oscillations reaches the TL input very soon after the formation of the EMS front, and the further processes in the TL depend on the conditions at the input. In the general case, when there is no RF matching at the input, a part of the RF power is absorbed there and another part is reflected back into the line and, at $|v_g| > v_s$, experiences sequential reflections from the EMS front and the TL input. In the reflection from the moving boundary (EMS front), the double Doppler effect takes place. Consequently, the spectrum of a nonsteady EMS contains a set of frequencies, only one of which corresponds to the synchronous wave and appears in the steady-state structure of the EMS. Thus, several waves are generated simultaneously. The intensities of these waves depend on the boundary conditions at the walls of the formed "resonator" with a moving right boundary. Note that the character of the nonsteady processes during the generation of oscillations in the case of synchronism with a forward wave does not depend on the boundary condition at the input of a nonlinear TL. We omit the details of nonsteady processes related to the absence of RF matching at the TL input and consider the case when the spectrum contains only a wave synchronous with the EMS front and the load at the TL input Z_ω is matched at the frequency of the synchronous wave (see Fig. 1). Note that this case is most important for the development of generators of long radio pulses with a single carrier frequency.

We carried out numerical simulations of nonsteady processes for a TL with 85 nonlinear cells. Figure 4 shows the time dependences of the voltage at several TL cells and the matched input and output loads Z_ω. The sequence of nonsteady processes is as follows. The EMS front formed in the first cells travels along the TL and generates RF oscillations. The energy of these oscillations runs to the load at the TL input and is almost completely absorbed in it. The voltage pulse at the input load is the longest. As the cell number increases, the duration of the voltage pulse decreases, so that RF oscillations are almost absent at the matched output load.

The oscillograms in Fig. 4 also show the reflected signal that appears due to RF mismatch, which takes place even when the line input is loaded on the ohmic resistance equal to the wave impedance Z_ω. The reason for this mismatch is an uncompensated reactance resulting from breaking cross-coupling.

As for synchronism with a forward wave, the damping rate and TL dispersion determine the shape of the envelope of the generated radio pulse. The broadening of the trailing edge of the radio pulse is minimal when the synchronism corresponds to the minimum of the group velocity. Formula (9) can be used to estimate the

length of the line that is necessary for the formation of a given number of oscillations in the case of synchronism with a backward wave. This length appears to be 30 times smaller than that in the case of synchronism with a forward wave because of the negative group velocity and larger value of the wavenumber. As was expected, the damping of the *n*th oscillation of the voltage at the load is also smaller by one order of magnitude than that for synchronism with a forward wave.

3. Modulation Depth and Generation Efficiency

An important characteristic of the generated radio pulse is the modulation depth (i.e., the ratio of the amplitude of RF oscillations V_ω to the EMS amplitude V_s), which determines the generation efficiency for synchronism with both a forward and a backward wave. Modulation depth in the case of synchronism with a backward wave is smaller than that for synchronism with a forward wave (Figs. 3b, 3c, 4b, 4c).

An analytical expression for the modulation depth is given by

$$\frac{V_\omega^2}{V_s^2} = \frac{Z_\omega^2}{Z_0^2}\frac{1 - v_s^2/v_0^2}{1 - v_g/v_s}\left(1 - \frac{\tau_f}{T}\right). \quad (10)$$

Here, τ_f is the shock front width in a medium without dispersion calculated using the formula from [7], and T is the period of a synchronous wave. Relationship (10) is obtained based on the equation for the balance of the power fluxes [1] under the assumption that the mean power spent on remagnetization of ferrite in a TL with dispersion (i.e., for the front width comparable with the period of the generated oscillations) is $P_s\tau_f/T$. Two main factors determining the modulation depth V_ω/V_s are dispersion (specifically, the rate of the energy outflow from the EMS front) and the ratio τ_f/T of the EMS front width in a medium without dispersion to the period of a synchronous wave in a dispersive medium. The latter, along with high-frequency losses, determines the highest generation frequency, because the period of the synchronous wave can not be smaller than the EMS front width in a medium without dispersion.

Knowing the ratio V_ω/V_s, we can find the ratio of the power $P_\omega = 1/2\,\mathrm{Re}(I_\omega/V_\omega^*)$ of the generated RF oscillations to the EMS power $P_s = I_sV_s$ in a discrete TL (Fig. 1):

$$\frac{P_\omega}{P_s} = \frac{1}{2}\left(\frac{V_\omega}{V_s}\right)^2 \frac{1}{(Z_\omega/Z_0)^2 v_p/v_0} \times \left\{\frac{\omega/\omega_c}{\tan\varphi/2} - \frac{4\gamma_*\omega/\omega_c \sin 2\varphi}{1 + 4\gamma\sin^2\varphi}\right\}. \quad (11)$$

In the case of synchronism with a forward wave (harmonic) (Fig. 3), the ratio P_ω/P_s is about 0.47, whereas, for synchronism with a backward harmonic (Fig. 4), this ratio is about 0.27. However, the energy efficiency (the ratio of the mean energy of the generated radio pulse $P_\omega N$, where N is the number of oscillations in the radio pulse, to the total energy lost by the video pulse) is almost the same for synchronism with both a forward and a backward wave and, for comparable values of ω, ranges from 70 to 80%.

In other words, accelerating the RF generation process (by decreasing the EMS velocity and increasing the difference between the phase and group velocities) can substantially reduce the energy losses, thus lessening their influence. However, the fast energy outflow necessarily leads to the decrease in the modulation depth and power of the generated RF wave.

CONCLUSION

The study of the structure of an EMS propagating in synchronism with a backward wave (spatial harmonic) has shown that the regime in which a backward wave in coupled TLs or a wave group in a periodic electrodynamic system is excited is advantageous from the point of view of generating longer radio pulses at higher frequencies. This is due to the fact that, in this case, the damping rate of the generated RF oscillations and the required length of the line appear to be one order of magnitude smaller than those in the case when a forward wave is excited. The carrier frequency of the generated radio pulse can be controlled by varying the initial magnetization of the ferrite for synchronism with both a forward and a backward wave.

ACKNOWLEDGMENTS

This work was supported by the Russian Foundation for Basic Research, project no. 99-02-18046.

REFERENCES

1. A. M. Belyantsev, A. I. Dubnev, S. L. Klimin, *et al.*, Zh. Tekh. Fiz. **65** (8), 132 (1995) [Tech. Phys. **40**, 820 (1995)].
2. A. M. Belyantsev and A. B. Kozyrev, Zh. Tekh. Fiz. **68** (1), 89 (1998) [Tech. Phys. **43**, 80 (1998)].
3. A. M. Belyantsev and A. B. Kozyrev, Int. J. Infrared Millim. Waves **18**, 1169 (1997).
4. V. M. Agranovich and V. L. Ginzburg, *Crystal Optics with Spatial Dispersion and Exciton Theory* (Nauka, Moscow, 1965; Springer-Verlag, New York, 1984).
5. R. A. Silin and V. P. Sazonov, *Slow-Wave Systems* (Nauka, Moscow, 1966).
6. G. I. Freĭdman, Izv. Vyssh. Uchebn. Zaved. Radiofiz. **6**, 536 (1963).
7. A. M. Belyantsev, Yu. K. Bogatyrev, and L. I. Solov'eva, Izv. Vyssh. Uchebn. Zaved. Radiofiz. **6**, 561 (1963).

Translated by A. Chikishev

Technical Physics, Vol. 45, No. 6, 2000, pp. 753–758. Translated from Zhurnal Tekhnicheskoĭ Fiziki, Vol. 70, No. 6, 2000, pp. 84–89.

RADIOPHYSICS

The Measurement and Verification of Parameters of Pulse Electromagnetic Radiation Generated by a Large-Radius Ring Current

V. M. Fedorov, E. F. Lebedev, V. E. Ostashev, V. P. Tarakanov, A. V. Ul'yanov, V. E. Fortov, and B. D. Yankovskiĭ

High Energy Density Research Center, Joint Institute for High Temperatures, Russian Academy of Sciences, Izhorskaya ul. 13/19, Moscow, 127412 Russia

Received May 24, 1999

Abstract—Experimental and analytic studies of the generation and propagation of electromagnetic radiation due to repetitive current pulses of a nanosecond duration (peak power to 1 MW, current slew rate of 3.5 A/ns) are presented. The radiation source was a fine-wire ring antenna of large radius (ρ_a = 1.4 m). The antenna was driven along its full length instantaneously within the time τ shorter than the time of wave travel along the ring diameter ($\tau \le 2\rho_a/c$). Parameters of the emitted wave were measured. The experimental data are consistent with the calculated emitted-wave parameters that take into account radiation reflection from the conducting walls of the laboratory. The efficiency of transformation of drive pulse energy into ultra-wideband radiation was found to be approximately 15%. A ring antenna driven by repetitive current pulses (within the time $\tau \le 2\rho_a/c$) is suggested to be used as a reference ultra-wideband emitter. © *2000 MAIK "Nauka/Interperiodica".*

INTRODUCTION

The study of ultra-wideband (UWB) electromagnetic pulses is a new branch of scientific research holding much promise both for the extension of radar capabilities and for the simulation of the effect of lightning discharge and high-power electromagnetic pulses on nonlinear media and distributed electronic control systems [1, 2]. However, the lack of adequate measuring devices and processing algorithms makes it difficult to determine UWB radiation field parameters. Therefore, the development of a reference UWB pulse radiation source appears to be topical [3, 4]. A consistent set of calculated and experimental data would help to verify the results obtained in this field.

A fine-wire ring antenna can be used as a reference UWB emitter. The parameters of this antenna both as an emitter and as a receiver can be accurately calculated, because the spatial configuration of the current loop is well defined. As shown in [5] and experimentally demonstrated in [7, 8], if the antenna is driven simultaneously along its full length by a short current pulse ($\tau \ll \rho_a/c$), it emits with a high efficiency $\eta_a \sim \ln(\rho_a/c\tau)/\ln(\rho_a/r)$ (r is the antenna radius, $r < c\tau$) and a low angular divergence ($\Theta \approx c\tau/\rho_a \ll 1$) in an ultrawide frequency band ($\Delta f \sim f \sim \tau^{-1}$). The advent of high-current (~1 kA) semiconductor pulse generators with a short rise time (~1 ns) and a pulse rate of ~1 kHz [6, 9, 10] has given rise to the development of pulse drivers for efficiently emitting large-size current loops. Long-term (for hours) stable generation of nanosecond pulses significantly facilitates the detection of electromagnetic field parameters.

The goals of this work were (1) the fast ($\tau < 2\rho_a/c$) and instantaneous excitation of a large-radius (ρ_a = 1.4 m) ring antenna at each of its points, (2) direct measurements of the pulse-induced current in the antenna and the antenna field, (3) comparison of the experimental data with the calculations including radiation reflection from the conducting surfaces in the laboratory, and (4) the assessment of the methodical error involved in wideband field parameters of large-size open current loops.

DIPOLE RADIATION FIELD PARAMETERS IN AN UNSTEADY DRIVE MODE

The axial symmetry of a ring antenna (magnetic dipole) simplifies the calculation of its field parameters. Given the time dependence of the induced current and its distribution over the antenna, the radiation field parameters can be calculated with well-known analytic equations [5, 11].

The ring current was studied in a conducting-wall room of characteristic size ~15 m. For the antenna radius ρ_a = 1.4 m and the total rise time $\tau \approx 8$ ns ($c\tau \le 2\rho_a$), the antenna radiation wavelength was $\lambda_\sim \approx 2c\tau \approx 4\rho_a \approx$ 5–6 m, which is comparable to the laboratory size. The conducting surfaces in the laboratory (walls, screens, etc.) reflect electromagnetic waves. The time delay of a reflected wave at the point of observation depends on the position of this point relative to the

1063-7842/00/4506-0753$20.00 © 2000 MAIK "Nauka/Interperiodica"

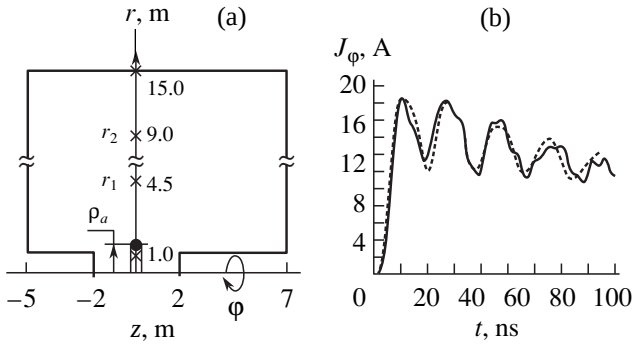

Fig. 1. (a) Axisymmetric model of the area of propagation (the ring antenna of radius ρ_a and points of observation r_1 and r_2 are shown) and (b) the time dependence of the induced current (solid curve, experiment; dashed curve, calculation).

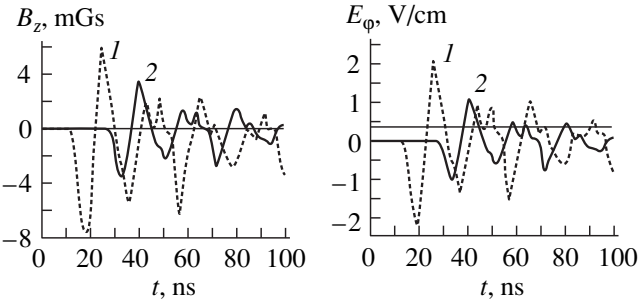

Fig. 2. Calculated lateral components of the magnetic and electric fields for the ring antenna emitting into free space. (*1*) $r_1 = 4.5$ and (*2*) $r_2 = 9$ m. Calculations were made for the actual value of induced current $J_\varphi(t)$.

antenna and reflecting surfaces. The radiation field parameters were preliminarily assessed using the KARAT electromagnetic program [12], which solves Maxwell's equations in the 2.5-dimensional approximation and allows experimental conditions to be taken into account.

Two geometrical axes passing through the center of the ring antenna are considered: the axis normal to the ring plane (z-axis) and any of the axes in the ring plane (r-axis). Strictly in the z direction, the emission is absent because of the ring symmetry. The point of observation is on the r-axis, because the angular dependence of the electromagnetic field parameters in this direction is weak. The position of this point depends on two mutually related, but inconsistent, factors: the conformity of the field lateral components to the plane wave condition $E_\varphi/B_z = c$ and the time delay of the reflected wave at the point of observation (as the distance r increases, the wave front shapes but the delay time decreases).

Oscillograms of induced current $J_\varphi(t)$ and an axisymmetric model for reflecting-boundary area of propagation (Fig. 1) were used as initial data for calculations. The current rise time was ≈8 ns; and the current slew rate, ~3.5 A/ns.

The dynamics of wave generation and propagation was simulated by calculating the parameters of antenna emission into free space (Fig. 2). The difference between the first (8 mGs) and second (6 mGs) half-wave amplitudes of the magnetic field that are generated by diametrically opposite parts of the ring at the point $r_1 = 4.5$ m ($\approx 3\rho_a$) on the radial axis shows that the point r_1 is close to the antenna. In contrast to plane waves, the lateral components of the electric and magnetic fields (E_φ and B_z, respectively) are not proportional to each other.

At the point $r_2 = 9$ m ($\approx 6\rho_a$), the components E_φ and B_z are much larger than the other field components: $\{B_r, B_\varphi\} \ll B_z$, $\{E_z, E_r\} \ll E_\varphi$. They are related as E_φ (V/cm) $\cong 3.3B_z$ (mGs), which is consistent with the plane wave condition. The electric field amplitudes for the first and second half-waves are ≈1 V/cm, and the radiation wavelength is 5–6 m; i.e., $\lambda_\sim \approx 4\rho_a$. Thus, a ring antenna driven within a time $\tau \le 2\rho_a/c$ generates a plane electromagnetic wave in the radial direction even at $r/\rho_a \ge 6$ and $r/\lambda_\sim \ge 1.5$.

The large-radius antenna is inductively coupled with the conducting surfaces of the area of propagation (Fig. 1). The antenna radiation induces eddy currents in them and, thus, reflected waves, which disturb the initial field configuration. The effect of reflection on the radiation field parameters is presented in Fig. 3 for the point r_2 where the plane wave has been already formed.

This effect is manifested in two ways (Fig. 3). First, a strong longitudinal magnetic field B_r (curve *2*) occurs ≈16 ns after the forward wave front (curve *1*) has reached the point of observation. This field is due to the different distances of the ring plane to the side reflecting screens ($z = -5$ and 7 m, respectively). Second, the first and second half-wave amplitudes become unequal. The second half-wave amplitude increases by 30% because of the "pump" effect from eddy currents induced by the antenna in the nearest symmetrically arranged screens ($z = \pm 2$ m). However, it should be noted that the condition $E_\varphi/B_z \cong c$ remains valid at least until the longitudinal component B_r of the magnetic field arises. Thus, the numerical simulation of the emission of the ring antenna driven for a short time $\tau \le 2\rho_a/c$ shows that the forward wave propagating in the radial direction can be detected at the point $r_2 \approx 6\rho_a \approx 1.5\lambda_\sim$ for a limited time (≈16 ns, or ≈2τ) determined by the reflecting screen geometry.

EXPERIMENTAL SETUP

Circuit. The current setting time τ in a circuit with an inductance L_a and an impedance R_a depends on the time of quasi-steady-state current relaxation $\tau_R \approx L_a/R_a$ and the rise time of a driving voltage pulse τ_g. If $\tau_g \ll \tau_R$, the time it takes for the current to reach 0.95 of the

amplitude value is $\tau \approx 3\tau_R$. The circuit impedance R_a (or the impedance introduced into the circuit) is related to the "rate" of ring antenna driving $2\rho_a/c\tau$ (the term used in [5]) as

$$R_a \approx 1.5\mu_0 c\left(\frac{2\rho_a}{c\tau}\right)\ln\frac{\rho_a}{r},$$

where $\mu_0 c = 377\ \Omega$ is the wave impedance of vacuum. If the parameter $2\rho_a/c\tau$ is fixed, R_a depends on the antenna radius ρ_a only slightly. If $\tau_g \ll \tau_R$, the unsteady mode of antenna driving ($2\rho_a/c\tau \geq 1$) is set at the circuit impedance $R_a \geq$ (4–5) kΩ (it is assumed that ρ_a/r = 200–500) regardless of the antenna radius. With the parameter $2\rho_a/c\tau$ fixed, the antenna radius ρ_a defines the upper boundary frequency of the radiation spectrum (the less the radius, the higher this frequency). At a given induced current amplitude, the antenna radius specifies the total energy of the radiation pulse. If $\tau_g \approx \tau_R$, the radius ρ_a of a "fast"-driven antenna should exceed $c\tau_g$.

The axial symmetry of the antenna implies the uniform distribution of the impedance and simultaneous change of the current at each point of the antenna. This requirement is met if the spatial longitudinal structure Δs of a ring antenna satisfies the condition $2\Delta s/c \leq 0.2\tau \ll \tau$; i.e., the permissible longitudinal discretization of the loop should be at least $\geq 10\pi(2\rho_a/c\tau)$. An experimental ring oscillator meeting this condition was developed in our laboratory. Its fragment is shown in Fig. 4.

Driver *1* is built on conventional drift diodes. Their blocking properties are sharply restored if the diode forward current is pumped in a special mode [6]. A series three-stage pulse shaper was used. The driver output stage consisted of 24 parallel channels. When the driver was made to pick up a matched load of 0.5 Ω, a trapezoidal voltage pulse with a rise time of $\tau_g \approx 3$ ns, amplitude up to 600 V, and a half-amplitude duration of approximately 20 ns was detected. The pulse power of the driver did not exceed 0.7 MW, and the pulse repetition rate was 100 Hz.

The ring antenna of radius ρ_a = 1.4 m consisted of N = 96 segments made of fine (r = 1 mm) copper wire. The length of each segment was 91 mm. The quasi-steady-state inductance of the antenna was L_a = 13.3 μH. Driver *1* was connected to wire segments *3* of the antenna with 1.6-m-long coaxials *2* with the wave impedance R_c = 50 Ω. The ring current alone was generated, since the radial currents in the cables were cancelled. The current rise time in the ring, $\tau \approx 8$ ns, was shorter than the doubled time of pulse travel through cables *2* (16 ns). Thus, within 16 ns, the driver is put under the optimum load $R_c/N \approx 0.5\ \Omega$ and the impedance $R_a \approx R_c N \approx 5$ kΩ, necessary for fast driving, is uniformly distributed over the antenna loop. When the output voltage of the driver was 510 V, the amplitude of

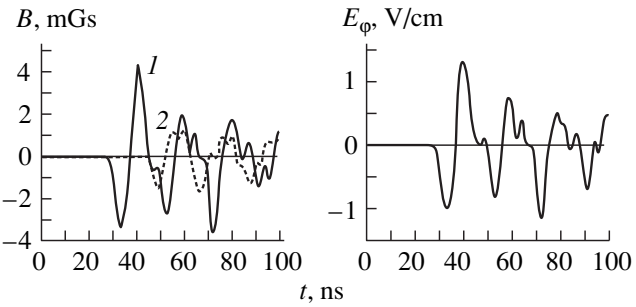

Fig. 3. Time dependence of the lateral, B_z (*1*) and longitudinal, B_r (*2*) magnetic field components at the point r_2 = 9 m. Reflection from the conducting surfaces.

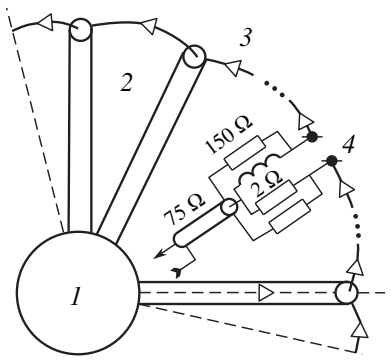

Fig. 4. Fragment of the ring oscillator: (*1*) driver, (*2*) coaxials, (*3*) elements of the ring antenna, and (*4*) current meter.

current pulses in the antenna was found to be $(J_\varphi)_{max}$ = 18.7 A; and the slew rate, 3.5 A/ns (Fig. 1). The resistance of the entire circuit (antenna and 96 feed cables) was assessed from the characteristic current decay time $\tau_d \approx 150$ ns at $L_a/\tau_d \approx 100\ \Omega$. Oscillations during the current decay are caused mainly by poor matching of antenna elements *3* with feed cables *2*. Direct current measurements at various points of the ring (both in its normal position and at various angles to the radial axis of suspension) in the conducting-wall room gave the same results within the accuracy of detection. Thus, the non-steady-state driving of the ring antenna within the time $\tau \leq 2\rho_a/c$ has been shown to be a possibility. The difference between current setting times along the antenna was $\ll\tau$.

Probing. Measurements of the driver voltage and that across the load (at the ends of cables *2*) was performed using a resistive voltage divider with a time resolution better than 0.5 ns. The induced current was measured in the loop by means of resistive shunt *4* with a compensating inductance (Fig. 4). The measurement results coincide well with the calculated values taking into account the actual voltage shape at the output of the loaded driver (Fig. 1).

Magnetic field oscillations in the emitted wave were measured with a differential-output probe based on a conventional symmetric magnetic dipole and an *LR*

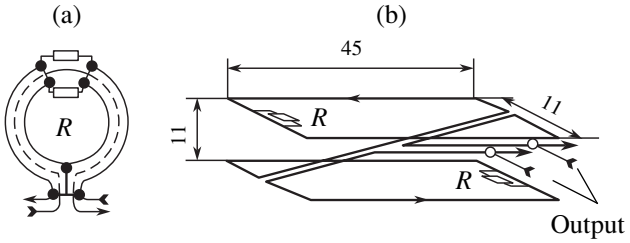

Fig. 5. Magnetic probes: (a) conventional symmetric magnetic probe with integrating resistors *R* and (b) symmetric double-dipole probe with increased immunity to electric parasitics.

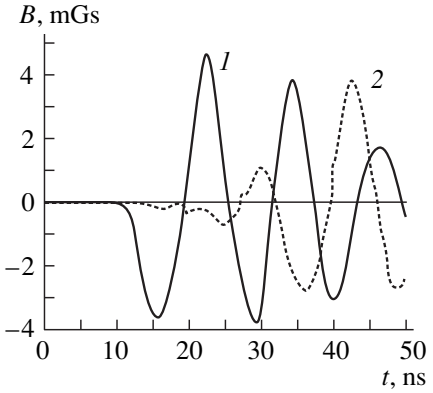

Fig. 6. (*1*) Lateral and (*2*) longitudinal components of the magnetic field of the emitted wave at the point of observation $r_2 = 9$ m.

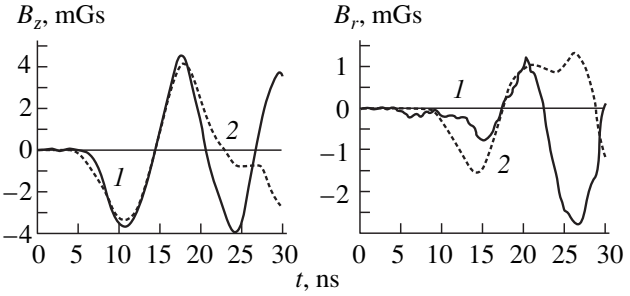

Fig. 7. (*1*) Measured and (*2*) calculated lateral and longitudinal components of the magnetic field of the emitted wave. The time axis is shifted for convenience.

integrator (Fig. 5a). However, such a probe (50×20 cm rectangular frame) turned out to be inappropriate because of electric-field-induced parasitics. The parasitic signals were measured by reversing the probe phase (by turning the probe through 180°), and their level was found to be 200%.

To avoid this disadvantage, a special probe of higher symmetry was developed (Fig. 5b). It consists of two identical rectangular (45×11 cm) symmetric magnetic dipoles with *LR* integrators. The planes of the series-connected dipoles are 11 cm apart. For the characteristic antenna radiation wavelengths $\lambda_\sim \approx 5$–6 m, the probe can be considered as a lumped (local) sensor.

The probe sensitivity is 33 mGs/V. For a forward wave of amplitude 3–4 mGs, the probe response was ≈0.1 V, which was reliably detected. The time constant of the *LR* integrator is ≈150 ns. This allowed direct measurement of the magnetic field of the forward wave for ≤20 ns with an accuracy of ≤10%.

Detection and processing of signals. A number of known ways to provide interference immunity during the measurements in an ac electromagnetic field [13, 14] were used: the coaxials were further shielded and passed through ferrite rings, decoupling filters were inserted into the supply circuit of the instruments, differential recording was applied, etc. S1-97 and S9-4A oscilloscopes with a frequency band of 0.45 and 1 GHz, respectively, were employed to record the signals. The oscillograms were photographed with a digital camera. A single oscillogram contained up to 400 data points. In further calculations, these data were interpolated with Newton and spline interpolation algorithms. The instrumental and methodical errors did not exceed 10%. The problem of accuracy improvement was beyond the scope of this article.

RESULTS AND DISCUSSION

The direct measurements of the lateral, B_z, and longitudinal, B_r, components of the magnetic field at the far point of observation ($r_2 = 9$ m) are presented in Fig. 6. The magnetic field amplitude detected by the probe is 3–4 mGs; the oscillation period is 16–20 ns. The second half-wave of B_z exceeds the first half-wave by 30%. The longitudinal component B_r lags behind the lateral component by ≈16 ns. The longitudinal (parasitic) component is due to reflection radiation from the metal surfaces of the laboratory. The appearance and level of parasitics were verified by detecting the magnetic field strictly along the *z*-axis of the antenna, where the emission is absent because of the ring symmetry.

Calculated and experimental data for the lateral, B_z, and longitudinal, B_r, components of the magnetic field at the point r_2 are compared in Fig. 7. For the lateral component B_z, the curves agree well for the initial ~16 ns, during which the forward wave is not yet disturbed by reflected waves. For B_r, the curves correlate both quantitatively (the same time of wave appearance at the point r_2) and qualitatively (the same signal variation) within the initial 15–20 ns. The difference between the measured and calculated values of B_r arises from the inaccurate simulation of the actual arrangement of the reflecting surfaces.

The consistency between the calculated and measured data for B_z makes it possible to determine the lateral component of the electric field E_φ from the magnetic induction: $B_z - E_\varphi = cB_z$. At the point of observa-

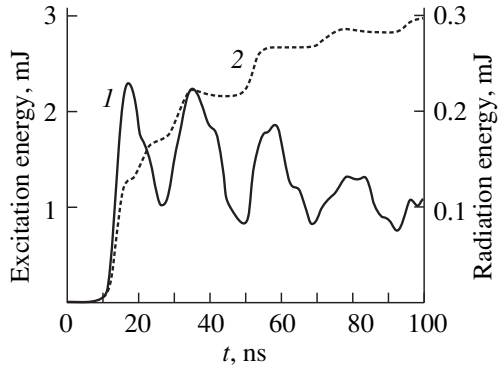

Fig. 8. Calculated data for the (*1*) induced and (*2*) radiant energy of the ring antenna.

tion r_2, the amplitude of E_φ was ≈1.1–1.4 V/cm, and the radiation energy flux density $E_\varphi B_z$ was ≈30–50 W/m^2.

The obtained results allow us to estimate the efficiency of transformation of induced current energy into radiant energy. This is also of some methodical significance, because it is well known that the antenna efficiency η_a in the quasi-steady-state ($\tau \gg 2\rho_a/c$) mode of driving a magnetic dipole is $\eta_a \sim (\rho_a/c\tau)^3/\ln(\rho_a/r) \ll 1$ [11]; and in the nonsteady-state mode ($\tau \ll 2\rho_a/c$), $\eta_a \leq 1$ [5].

Calculated data for the induced energy and total radiant energy are presented in Fig. 8. The antenna efficiency η_a (i.e., the ratio between the radiant energy and the sum of the induced and radiant energies) is seen to be 5–6% by the end of the first half-wave (the first peak in curve *1*) and 15–17% by the end of the second half-wave (the first minimum in curve *1*).

CONCLUSION

The experimental bench for studying the radiation of large-size current loops driven simultaneously along their full length within the time interval $\tau < 2\rho_a/c$ (nonsteady-state driving mode) was developed. The setup can also be used for examining the effect of UWB radiation on nonlinear media. The choice of such an antenna was dictated by the fact that the field of radiation from a fine-wire loop can be accurately calculated from the value of the drive current and that a current loop efficiently emits under the non-steady-state driving mode.

The fast ($\tau \approx 8$ ns) pulse driving of the ring antenna of radius 1.4 m was accomplished. The difference in the current setting times over the loop was ≈0.5 ns $\ll \tau$.

The high-current (≈1 kA) semiconductor generator was used as a driver. The low output impedance of the driver allowed the multipoint in-phase excitation of the antenna. The continuous (for hours) stable generation of UWB radiation pulses (pulse repetition rate up to 100 Hz) made the detection of the electromagnetic field parameters much easier.

The magnetic probe consisting of two identical symmetric dipoles was developed. The dipole leads are connected so that the signals induced in the dipoles by the magnetic field add up, whereas those induced by the electric field are canceled. Thus, the parasitics due to the electric field are eliminated, and the magnetic component of the UWB radiation is reliably detected. A conventional magnetic dipole cannot be used in the measurements because of the incomplete cancellation of signals induced by the electric field (the error is ~200%).

The time dependence of the magnetic induction showed that an electromagnetic wave emitted by the antenna in the radial direction turns into a plane wave even at a distance $4\rho_a$ away from the antenna center. Thus, experiments with such an antenna can be performed in a limited space. The electric field strength near the antenna was found to be 6 kV/m; and at a distance of 9 m away from the antenna, 110–140 V/m.

The results were verified by both analytical and numerical calculations. The KARAT computer program was used to assess the effect of radiation reflection from the metal surfaces in the laboratory. The measured UWB radiation parameters agree well with the calculated data both in the amplitude and variation of the magnetic component of the forward wave and in the time delay with which the reflected wave comes to the point of observation. The efficiency of transformation of drive pulse energy into radiant energy was found to be 15–17% for the oscillation period.

The instruments used in these experiments provide reliable information on the parameters of a UWB electromagnetic field generated by open current loops of large size. The possibility of these parameters being measured in a reflecting-wall room was demonstrated.

The proposed methods of UWB generation and radiant field detection can be used in the development of a reference emitter of nanosecond electromagnetic pulses.

ACKNOWLEDGMENTS

We are grateful to L.P. Feoktistov and V.V. Klimov (Lebedev Institute of Physics, Russian Academy of Sciences) for cooperation and valuable discussion.

REFERENCES

1. H. F. Harmuth, *Antennas and Waveguides for Nonsinusoidal Waves* (Academic Press, New York, 1984).
2. R. Godman, S. Tummala, and W. Carrara, in *Proceedings on IEEE International Radar Conference, 1995, Israel*, p. 479.
3. V. Fortov, L. Ivanov, S. Kovalenko, *et al.*, in *Program and Abstracts of the 11th International Conference on High-Power Electromagnetics EUROEM'98, Tel Aviv, 1998, Israel*, p. 117.

4. W. A. Radasky, in *Program and Abstracts of the 11th International Conference on High-Power Electromagnetics EUROEM'98, Tel Aviv, 1998, Israel*, p. 118.
5. Yu. V. Afanas'ev, V. V. Klimov, A. L. Feoktistov, and L. P. Feoktistov, Zh. Éksp. Teor. Fiz. **101**, 1118 (1992) [Sov. Phys. JETP **74**, 596 (1992)].
6. V. S. Belkin, O. Yu. Marin, and G. I. Shul'zhenko, Prib. Tekh. Éksp., No. 6, 120 (1992).
7. V. M. Fedorov, V. E. Fortov, V. E. Ostashev, *et al.*, in *Program and Abstracts of the 11th International Conference on High-Power Electromagnetics EUROEM'98, Tel Aviv, 1998, Israel*, p. 244.
8. V. M. Fedorov, E. F. Lebedev, V. E. Ostashev, *et al.*, in *Proceedings of the 5th All-Russia Scientific Conference "Electromagnetic Compatibility of Technological Tools and Biologic Objects," St. Petersburg, Russia, 1998*, p. 441.
9. V. M. Tuchkevich and I. V. Grekhov, *Novel Principles of High-Power Switching by Semiconductor Devices* (Nauka, Leningrad, 1988).
10. Yu. A. Kotov, G. A. Mesyats, S. N. Rukin, *et al.*, in *Proceedings of the 9th IEEE International Pulsed Power Conference, Albuquerque, 1993*, p. 134.
11. I. E. Tamm, *Principles of the Theory of Electricity* (Nauka, Moscow, 1989).
12. V. P. Tarakanov, *User's Manual for Code "KARAT"* (Berkeley Research Associates, Springfield, 1992).
13. P. P. Deĭchulli and V. M. Fedorov, Vopr. At. Nauki Tekh., Ser. Termoyader. Sintez **3** (16), 22 (1984).
14. A. J. Schwab, *Elektromagnetische Vertraeglichkeit* (Springer, Berlin, 1990; Énergoatomizdat, Moscow, 1995).

Translated by K. Chamorovskiĭ

Technical Physics, Vol. 45, No. 6, 2000, pp. 759–765. Translated from Zhurnal Tekhnicheskoĭ Fiziki, Vol. 70, No. 6, 2000, pp. 90–97.

RADIOPHYSICS

Effect of Heat on the Nonlinearity of Plane Strontium Titanate Film Capacitors on Sapphire in a Microwave Field

T. B. Samoĭlova and K. F. Astaf'ev

St. Petersburg Electrical Engineering University, St. Petersburg, 197376 Russia

Received May 26, 1999

Abstract—Nonlinear characteristics of plane strontium titanate film capacitors operating at microwave frequencies are investigated by measuring the power of a capacitor signal generated at the third-order intermodulation distortion (IMD) product frequency when the capacitor is excited by a two-tone microwave signal. Measurements are performed at 4 GHz at temperatures of 78 and 300 K. At T = 300 K, the nonlinear response of the capacitor corresponds to the nonlinearity determined from the low-signal capacitance–voltage characteristic (CVC). At T = 78 K, the nonlinear response to a two-tone microwave signal is greatly amplified when the signal components have equal amplitudes and close frequencies. It is demonstrated that this effect is due to the beat-frequency modulation of the strontium titanate film temperature, because the thermal time constant of a $SrTiO_3$ film on sapphire is small (~10^{-8} s). An analytical expression for third-order IMD product power generated by a $SrTiO_3$ capacitor is obtained with regard for the heat-induced nonlinearity. *© 2000 MAIK "Nauka/Interperiodica".*

INTRODUCTION

The nonlinearity of the permittivity of ferroelectric materials has been used in microwave technology for a long time [1, 2]. At present, the progress in thin-film technology of oxygen-containing ferroelectrics ($SrTiO_3$, $Ba_xSr_{1-x}TiO_3$), which have a highly nonlinear permitivity ε at relatively low dielectric losses ($\tan\delta \sim 10^{-2}$) in the paraelectric phase, has rekindled interest in these films as a material of passive (phase inverters and tunable filters [3, 4]) and active (frequency converters [4, 5]) microwave devices.

The discovery of high-temperature superconductivity (HTSC) in composite metal oxides (1987) has stimulated special interest in strontium titanate, a low-temperature paraelectric. The structural and chemical compatibility of superconductive oxides (in particular, $YBa_2Cu_3O_7$) and $SrTiO_3$ provides the high-quality interface between an HTSC electrode and a strontium titanate film. This decreases losses in the capacitor and offers considerable scope for the implementation of cryogen microwave integrated circuits using the unique properties of nonlinear dielectrics and superconducting materials [6]. However, the applications of nonlinear capacitors in linear microwave devices may be limited by undesirable nonlinear effects (the generation of harmonics and false signals at IMD product frequencies).

In this paper, we investigate and simulate the nonlinear responses from plane strontium titanate capacitors (STO capacitors) to a high-intensity microwave signal. The transfer ratio of a resonator containing an STO capacitor and the third-order IMD product power generated by the capacitor excited by a two-tone microwave signal were measured for different levels of the incident microwave signal. Experiments were performed at the temperatures 78 and 300 K.

SAMPLES AND LOW-SIGNAL CHARACTERISTICS

Samples used were nonlinear plane capacitors (Fig. 1) based on thin strontium titanate films of thickness h = 1 μm. They were deposited on a sapphire substrate of thickness H = 0.3 mm by microwave magnetron sputtering [7]. A 8-μm-thick copper film applied to

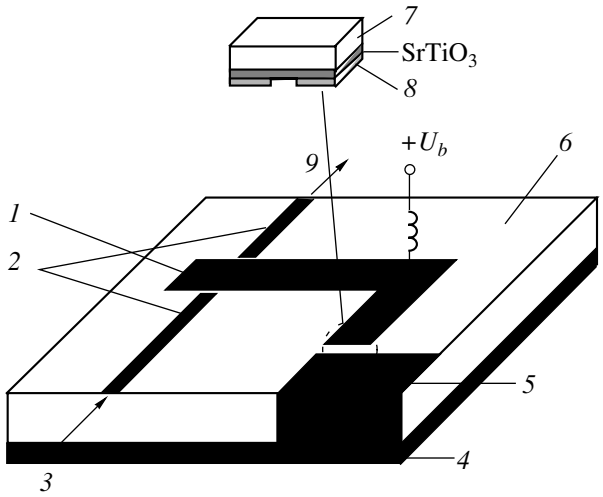

Fig. 1. Measuring microstrip resonator: (*1*) microstrip resonator, (*2*) feed lines, (*3*) microwave input, (*4*) ground line, (*5*) grounded pad, (*6*) substrate (alumina), (*7*) sapphire, (*8*) Cu electrodes, and (*9*) microwave output. The insertion shows the plane capacitor.

1063-7842/00/4506-0759$20.00 © 2000 MAIK "Nauka/Interperiodica"

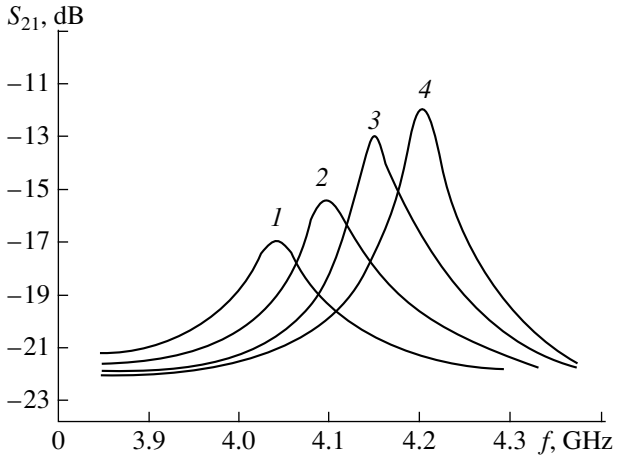

Fig. 2. Resonance curves of the measuring resonator: U_b = (*1*) 0, (*2*) 30, (*3*) 60, and (*4*) 100 V.

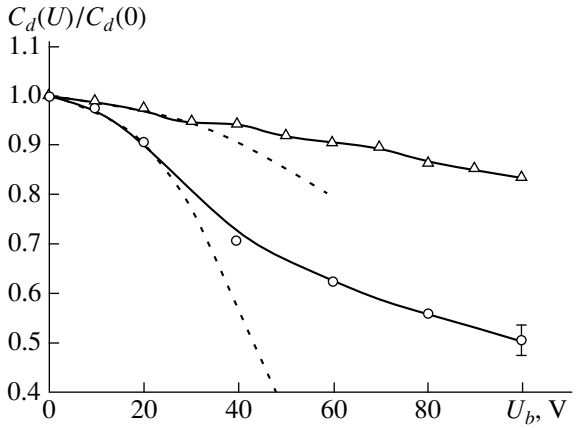

Fig. 3. Low-signal CVCs of the STO capacitors (solid lines) at T = (○) 78 and (△) 300 K. Dashed lines are approximation (3) for $U_0^2 = 1.2 \times 10^4$ and 8×10^4 V^2 at T = 78 and 300 K, respectively.

the film served as the capacitor electrodes. The width and length of the capacitor gap were s = 4–6 μm and W = 0.6 mm, respectively, and the overall dimensions of the capacitor were $0.5 \times 0.3 \times 1.5$ mm. The low-signal microwave parameters were measured at a frequency of about 4 GHz by the resonance method with an R4-38 complex-transfer-ratio meter. The measuring microstrip resonator (Fig. 1) was a copper microstrip (of length l and impedance Z_S = 21 Ω) with open- and short-circuited ends. The capacitor was inserted into a conductor break near the shorted end. The resonator was coupled with the external circuits through the capacitive gap, which provides a transfer ratio of –9 dB when a linear low-loss ($\tan\delta < 10^{-3}$) capacitor with an intrinsic quality factor Q_{00} = 200 is used. Depending on the capacitance and losses of the capacitors being investigated, transfer ratio S_{21}, resonance frequency f_0, and intrinsic Q_0-factor of the resonator varied from –13 to –24 dB, from 3.5 to 4.2 GHz, and from 60 to 100, respectively.

Figure 2 shows the resonance curves of the measuring resonator when the STO capacitor is biased by a dc voltage U_b. From the resonance curves for the STO capacitor, we derived the low-signal capacitance $C_0 = -\tan(\beta l)(\omega_0 Z_S)^{-1}$, dielectric loss tangent $\tan\delta = \xi^{-1}(Q_0^{-1} - Q_{00}^{-1})$, and low-signal amplitude of the microwave voltage [7]

$$U_c = \sqrt{4P_{\text{inc}}\xi(\omega_0 C_0)^{-1}Q_0|S_{21}|(1-|S_{21}|)}, \qquad (1)$$

where P_{inc} is the incident microwave power and ξ is the tapping factor (the parameter characterizing the insertion of the capacitor into the resonator):

$$\xi = 2\left[1 + [\omega_0 C_0 Z_S + (\omega_0 C_0 Z_S)^{-1}] \times \left[\frac{\pi}{2} + \arctan(\omega_0 C_0 Z_S)^{-1}\right]\right]^{-1}.$$

For all of the investigated capacitors, $\tan\delta$ = 0.01–0.02 and 0.02–0.04 at room (T = 300 K) and nitrogen (T = 78 K) temperatures, respectively. The low-signal characteristics of the resonator for two of them are summarized in the table.

Table

Sample no.	T, K	C_0, pF	ζ	$\tan\delta$	Q_0	S_{21}, dB	f_0, GHz	U_0^2, V^2
1	78	0.92	0.25	0.04	66	–16.8	3.872	1.2×10^4
2	300	0.66	0.19	0.02	91	–13.0	4.130	8.0×10^4

Measuring the shift of the resonance frequency of the resonator with the STO capacitor biased, one can construct the capacitance–voltage characteristics (CVCs) of the capacitor. Figure 3 demonstrates differential capacitance C_d versus U_b for samples 1 and 2 in the table. The bias voltage U_b = 100 V (corresponding to the averaged field intensity in the gap $E = U_b/s \approx 10^7$ V/m) is seen to decrease the capacitance of the STO capacitor by factors of about 2 and 1.2 at T = 78 and 300 K, respectively.

THE NONLINEAR BEHAVIOR OF THE $SrTiO_3$ CAPACITOR IN A MICROWAVE ENVIRONMENT

The nonlinear response of the STO capacitor to a microwave signal was investigated with the microstrip resonator (Fig. 1) in harmonic (one-tone) and biharmonic (two-tone) excitation modes.

In the one-tone mode, the microwave signal power at the output of the resonator (P_{out}) was measured as a function of the incident power (P_{inc}) at the low-signal

resonance frequency f_0. The experimental transfer functions were measured at T = 78 and 300 K (Fig. 4). At T = 78 K, the resonator transfer ratio decreases when $P_{inc} > +26$ dBm, which corresponds to the microwave amplitude of the capacitor voltage $U_c > 12$ V. This effect is typical of an oscillatory circuit with a nonlinear capacitance. At T = 300 K, the transfer ratio remains constant in the same range of incident power.

The response of the STO capacitor to a two-tone microwave signal was investigated with the standard technique for IMD measurement [8]. Two harmonic microwave signals of equal power ($P_{1inc} - P_{2inc}$) and close frequencies ($f_1 = f_0 + \Omega$ and $f_2 = f_0 - \Omega$) were applied to the measuring resonator. Due to the nonlinear frequency dependence of the capacitance of the STO capacitor, the response signals are generated at IMD product frequencies $f_S = \pm mf_1 \mp nf_2$ (m, n = 0, 1, 2, …). They were recorded by a spectrum analyzer at the output of the resonator. The output powers P_{1out} and P_{3out} were measured, respectively, at the fundamental (f_1) and third-order IMD product ($f_3 = 2f_1 - f_2$) frequencies versus power P_{1inc} of the harmonic component of the incident signal at the temperatures 78 and 300 K and different bias voltages U_b. All the measurements were performed under the condition $\Omega \le 1$ MHz, which confines all the recorded signals to a frequency band much smaller than the resonator passband.

Figures 5 and 6 present the measured nonlinear responses of the plane STO capacitor to the two-tone signal. In Fig. 5 are shown the resonator transfer functions at the fundamental and third-order IMD product frequencies for T = 78 and 300 K. The influence of a dc bias voltage on the transfer functions at nitrogen temperature is depicted in Fig. 6. The amplitude of the microwave voltage across the capacitor U_{c1} calculated by (1) for the fundamental frequency and $U_b = 0$ is given on the additional abscissa axis.

In the whole range of the incident microwave power (P_{1inc} = 0…+26 dBm), the cubic and linear dependences of P_{3out} and P_{1out}, respectively, on P_{1inc} are observed at T = 300 K. At 78 K, the transfer functions are cubic and linear at the fundamental and IMD product frequencies, respectively, only within the initial part of the incident power range. Here, the value of P_{3out}/P_{1out} exceeds the corresponding quantity at T = 300 K by approximately 50 dB. As P_{1inc} increases at 78 K, the dependence of the output power on the incident power weakens at both frequencies. A dc bias voltage applied to the capacitor noticeably suppresses the third-order IMD product signal and extends the incident power range where the function $P_{3out}(P_{1inc})$ remains cubic.

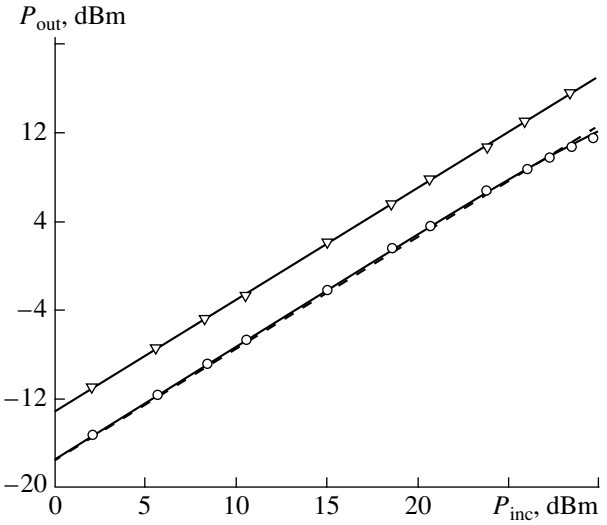

Fig. 4. Output power of the resonator vs. incident power in the one-tone excitation mode: (○) data points for sample 1 at T = 78 K and (▽) those for sample 2 at T = 300 K. Solid lines are calculated by (5) for U_0^2 found from the CVC approximation; dashed line is calculated $P_{out}(P_{inc})$ at T = 78 K for $U_0^2 = \infty$ (linear capacitor).

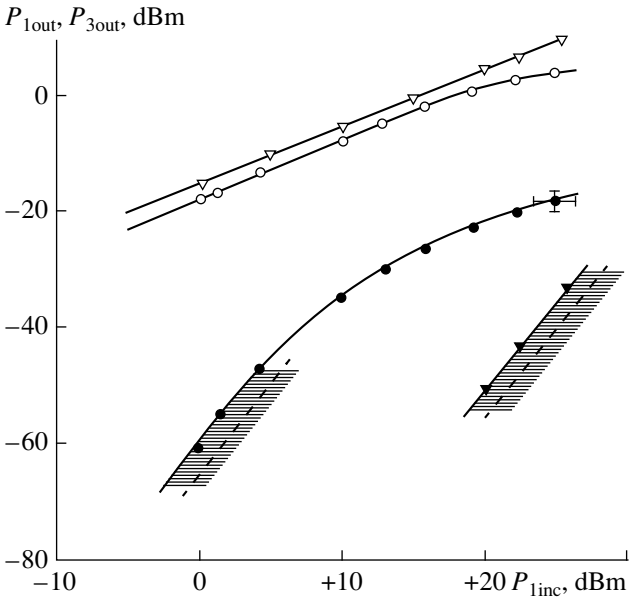

Fig. 5. (○) P_{1out} and (●) P_{3out} vs. P_{1inc} dependences taken at T = (○, ●) 78 and (▽, ▾) 300 K. Dashed lines are calculated by (9) and (17) for T = 300 and 78 K, respectively. Dashed regions are experimental errors for the quantities in (9) and (17).

RESULTS AND DISCUSSION

As the nonlinearity of the STO capacitor is due to the dependence of the capacitance on the instant microwave voltage across the capacitor, the experimental results will be discussed in terms of CVCs. Since the amplitude of the microwave voltage across the capacitor at the fundamental frequency does not exceed 30 V, it suffices to consider only the CVC initial section, where the nonlinear voltage dependence of the capacitance $C(U)$ can be represented by two terms of the

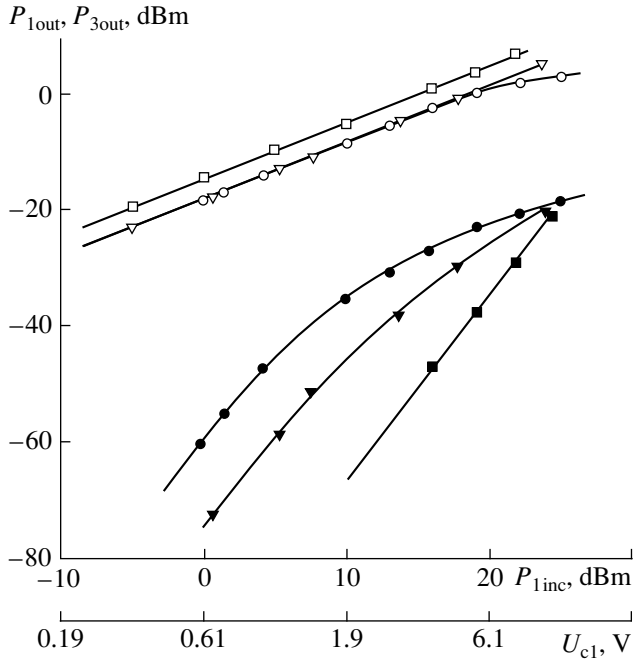

Fig. 6. The same as in Fig. 5 for capacitor bias voltages U_b = (○, ●) 0, (▽, ▼) 20, and (□, ■) 50 V.

power series:

$$C(U) = C_0\left(1 - \frac{U^2}{U_0^2}\right), \tag{2}$$

where U_0 is a phenomenological parameter that has dimension of voltage and quantitatively determines $C(U)$.

Since the differential capacitance C_d is measured at microwave frequencies, the initial section of experimental CVCs should be described by the expression

$$C_d(U) = C_0\left(1 - 3\frac{U^2}{U_0^2}\right). \tag{3}$$

Approximation (3) of experimental CVCs enables one to estimate the parameter U_0^2. For our capacitors, $U_0^2 \sim 10^5$ and $\sim 10^4$ V^2 at T = 300 and 78 K, respectively. For two capacitors, U_0^2 is given in the table and the CVC initial section approximated by (3) is shown in Fig. 3 (dashed curves).

From (2), we can obtain the transfer functions of the resonator operating in the one- and two-tone excitation modes.

Near the resonance frequency, the equivalent electric circuit of the measuring resonator can be represented by a parallel oscillatory circuit shown in Fig. 7a, where X_{coupl} is the impedance of the element coupling the resonator with the external circuits; L', C', and G' are, respectively, equivalent inductance, capacitance, and conductance of the resonance microstrip segment; and C and $g = \omega_0 C_0 \tan\delta$ are the capacitance and conductance of the STO capacitor. The equivalent parameters of the circuit are determined from the expressions

$$\omega_0^2 = \frac{1}{L'(C' + C_0)}, \quad Q_{00} = \frac{1}{\omega_0 L' C'}, \quad \xi = \frac{C_0}{C' + C_0}.$$

In the case of the one-tone excitation, the equivalent circuit of the resonator symmetrically coupled with the external circuits is further simplified to a circuit with an equivalent generator producing the current of amplitude $I = 2mI_{inc}$ (Fig. 7b). Here, $I_{inc} = \sqrt{2Z_0^{-1}P_{inc}}$ is the amplitude of an incident current wave, Z_0 is the wave impedance of external transmission lines, and m is the ratio of impedance transformation from the external lines to the resonator (for weak coupling, $m \approx Z_0/X_{coupl}$). The differential equation for forced oscillations in the equivalent parallel circuit,

$$\frac{di}{dt} = \frac{u_c}{L'} + \left[G' + g + \frac{2m^2}{Z_0}\right]\frac{du_c}{dt} + C'\frac{d^2u_c}{dt^2} + \frac{d^2}{dt^2}[C(u_c)u_c], \tag{4}$$

where $i = I\cos(\omega t + \varphi)$, is reduced to the known Duffing equation [9]. For frequencies f close to the low-signal resonance frequency f_0, the solution to the Duffing equation for a resonance circuit is a harmonic oscillation $u_c = U_c\cos(\omega t)$. Then, solving (4) and taking into account the expression $U_c = m^{-1}\sqrt{2Z_0P_{out}}$ and (2), we obtain the dependence of the output power on the incident power at a fixed frequency:

$$P_{out} = 4\frac{m^4}{Z_0^2}\frac{P_{inc}}{\left\{\frac{1}{\omega L'} - \omega\left[C' + C_0\left(1 - \frac{3}{2}\frac{Z_0}{m^2}\frac{P_{out}}{U_0^2}\right)\right]\right\}^2 + \left(G' + g + \frac{2m^2}{Z_0}\right)^2}. \tag{5}$$

Figure 4 demonstrates the transfer functions (solid curves) of the measuring resonator operating in the one-tone mode that were calculated by (5) for U_0^2, s found from CVC approximation (3). The experimental and calculated characteristics are in good agreement for both T = 78 and 300 K. Obviously, at T = 300 K, the

nonlinearity of the STO capacitors is weak and cannot noticeably distort the resonance curve in the range of incident power up to +30 dBm (which corresponds to $U_c \approx 27$ V for sample 2 at $T = 300$ K). At $T = 78$ K (sample 1), the observed decrease in the transfer ratio at a given frequency f_0 is caused by the shift of the resonance frequency due to the decrease in the average capacitance $\bar{C} = C_0[1 - (3/4)(U_c^2/U_0^2)]$ of the capacitor charged by the microwave voltage. This means that the permittivity of the strontium titanate film inertialessly follows the variation of the 4-GHz electric field.

When the resonator operates in the two-tone excitation mode and the voltage across the capacitor is $u_c(t) = U_{c1}(\cos(\omega_1 t) + \cos(\omega_2 t))$ (U_{c1} is the voltage amplitude at the fundamental frequency), the current

$$i_c = \frac{d}{dt}[C(u_c(t))u_c(t)] \quad (6)$$

flowing through the nonlinear capacitor contains the component generated i_{c3} at the third-order IMD product frequency $\omega_3 = 2\omega_1 - \omega_2$:

$$i_{c3} = \frac{3}{4}\omega_3 C_0 \frac{U_{c1}^3}{U_0^2}\sin(\omega_3 t). \quad (7)$$

Then, the amplitude of the third-order IMD product voltage across the capacitor is expressed by

$$U_{c3} = \frac{3}{4}\frac{U_{c1}^3}{U_0^2\sqrt{1 + \tan^2\delta}}. \quad (8)$$

Taking into account the condition $\omega_3 \approx \omega_0$, we can assume that the resonator parameters (ξ, Q_0, and S_{21}) and the distributions of voltages and currents along the resonator are identical at both frequencies. Then, combining (1) and (8) yields the IMD product power at the output of the resonator:

$$P_{3\,\mathrm{out}} = \frac{9\xi^2 Q_0^2 |S_{21}|^4 (1 - |S_{21}|)^2}{\omega_0 C_0 (1 + \tan^2\delta)}\frac{P_{1\mathrm{inc}}^3}{U_0^4} = A\frac{P_{1\mathrm{inc}}^3}{U_0^4}. \quad (9)$$

According to (9), in the range of incident power where transfer ratio $|S_{21}|$ of the resonator can be assumed to be constant at the fundamental frequency, the third-order IMD product transfer function of the resonator in log–log coordinates is linear with a slope of 3. This was observed experimentally in the whole range of $P_{1\mathrm{inc}}$ at $T = 300$ K and in the initial section of the characteristic at $T = 78$ K (Figs. 5, 6). The variation of the slope of the log–log transfer function with increasing power at $T = 78$ K can be attributed to a variation of the transfer ratio of the nonlinear resonator at a fixed frequency.

At $T = 300$ K, $P_{3\mathrm{out}}$ that is calculated by (9) for U_0^2 found from the low-signal CVC is in good agreement with the experimental data. Figure 5 shows $P_{3\mathrm{out}}(P_{1\mathrm{inc}})$

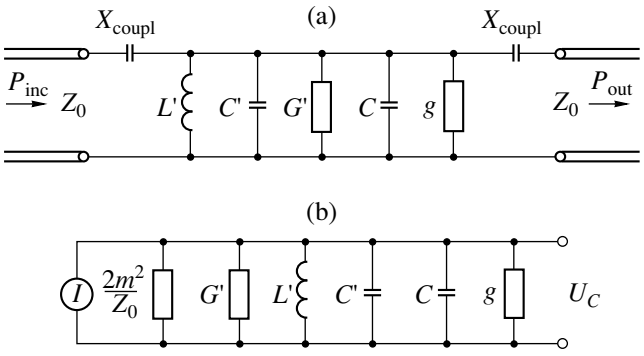

Fig. 7. Equivalent electric circuit of the measuring resonator.

for $T = 300$ K (dashed lines). At nitrogen temperature, the value of $P_{3\mathrm{out}}$ calculated by (9) is approximately 30 dB smaller than the experimental result.

The increased nonlinear response of the STO capacitor to the two-tone microwave signal at nitrogen temperature can be attributed to capacitance modulation when the capacitor temperature periodically varies (with the beat frequency $2\Omega = f_1 - f_2$) due to microwave power dissipation. The contribution of this mechanism is essential if $2\pi(2\Omega)\tau < 1$, where τ is the thermal relaxation time of the capacitor. We estimated the capacitor overheat due to the microwave power dissipated in the strontium titanate film and the thermal relaxation time from the solution of the heat conduction equation. It was assumed that heat exchange at the $SrTiO_3$ film–air interface is absent, the heat flux at the interface is continuous, and the temperature of the substrate back side is constant. Under these conditions, the overheat of the strontium titanate film can be expressed as

$$T - T_0 = \frac{P_{\mathrm{dis}}}{2W\lambda_f}\left[\frac{h}{s} + \frac{2}{\pi}\frac{\lambda_f}{\lambda_{\mathrm{sub}}}\ln\left(\frac{\pi H}{s}\right)\right], \quad (10)$$

where T_0 is the ambient temperature; P_{dis} is the microwave power dissipated in the strontium titanate film; and λ_f and λ_{sub} are the heat conductivities of the film and substrate, respectively.

Using an analogy between the electric and heat conduction equations, expression (10) can be written as

$$T - T_0 = \frac{P_{\mathrm{dis}}\tau}{C_T}, \quad (11)$$

where $C_T = C_v V$ is the specific heat of the capacitor, C_v is the specific heat of strontium titanate, and $V = shW$ is the volume of the active region of the capacitor.

Comparing (10) and (11), we obtain the expression for thermal relaxation time

$$\tau = \frac{C_v h^2}{2\lambda_f}\left[1 + \frac{2}{\pi}\frac{\lambda_f s}{\lambda_{\mathrm{sub}} h}\ln\left(\frac{\pi H}{s}\right)\right]. \quad (12)$$

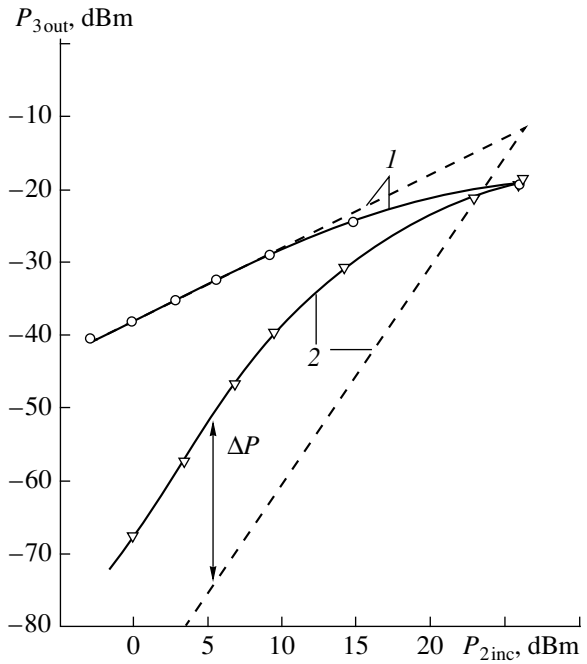

Fig. 8. P_{3out} vs. P_{2inc}. (○, ▽) data points at equal values of U_0. For curves *2*, the difference in the IMD product signals is responsible for U_0 variation caused by the capacitor temperature modulation with the frequency $2\Omega = f_1 - f_2$.

The heat conductivities of single-crystal sapphire and strontium titanate are, respectively, 900 and 20 Wm^{-1} K^{-1} at $T = 78$ K and 25 and 6 W m^{-1} K^{-1} at $T = 300$ K [1]. Then, the thermal relaxation times for the capacitors are $\tau \approx 10^{-7}$ and 10^{-8} s at $T = 300$ and 78 K, respectively. Thus, in our experiments (at $2\Omega \leq 2 \times 10^6$ Hz), the inequality $2\pi(2\Omega)\tau \leq 1$ is satisfied at nitrogen temperature.

If the capacitance is modulated because of moderate variations of the film electric field and temperature, it can be represented as

$$C(U, T) = C_0\left[1 - \frac{U^2}{U_0^2} - K_T(T - T_0)\right], \qquad (13)$$

where the factor K_T characterizes the temperature dependence of the capacitance near $T = 78$ K, where the behavior of the strontium titanate films differs from the Curie–Weiss law.

Experimental temperature dependences for the capacitances of STO capacitors similar to those considered in this paper are presented in [7]. From these results, K_T is estimated as 10^{-2} K^{-1} at $T = 78$ K.

In the two-tone mode, the microwave power dissipated in the strontium titanate film oscillates with the beat frequency 2Ω:

$$P_{dis} = \omega_0 C_0 \tan\delta U_{c1}^2(1 + \cos(2\Omega t)). \qquad (14)$$

Using (6) and (13) in view of (11) and (14), we obtain the third-order IMD product component of the current flowing through the nonlinear capacitor because of the thermal modulation of the capacitance:

$$i_{c3}^T = \frac{1}{2}\frac{K_T\omega_0 C_0\tau\tan\delta}{C_v V}\omega_3 C_0 U_{c1}^3 \sin(\omega_3 t). \qquad (15)$$

Introducing the notation

$$U_{0T}^2 = \frac{3}{2}\frac{C_v V}{K_T\omega_0 C_0\tau\tan\delta}, \qquad (16)$$

we bring (15) to form (7). Eventually, at $T = 78$ K, the IMD product power at the output of the resonator is expressed by

$$P_{3out} = AP_{1inc}^3\left(\frac{1}{U_0^2} + \frac{1}{U_{0T}^2}\right)^2, \qquad (17)$$

where A is determined in (9).

In particular, for sample 1, $U_{0T}^2 \approx 10^3$ V^2, so that taking account of the thermal nonlinearity of the capacitance adds approximately 20 dB to the calculated P_{3out} value. Figure 5 shows the dependence $P_{3out}(P_{1inc})$ (dashed lines) calculated by (17) for $T = 78$ K. With regard for errors in determining the quantities involved in (17), our estimates are in satisfactory agreement with the experimental data. The application of a dc bias voltage weakens the temperature dependence of the capacitance (by decreasing K_T) and, thus, causes U_{0T} to grow. This effect shows up in the experimental transfer functions of the resonator (Fig. 6) as a decrease in the IMD product signal P_{3out} relative to P_{1inc} and an extension of the incident power range where the transfer ratio remains constant and the dependence $P_{3out}(P_{1inc})$ is cubic.

To further verify the correctness of this result, we measured (at $T = 78$ K) the IMD product power P_{3out} at the output of the resonator that was excited by two-tone signals with different depths of amplitude modulation. During the measurements, the power of one component of the incident signal (P_{2inc}) varied from –10 to +26 dBm, while that of the other (P_{1inc}) remained constant and equaled +26 dBm. The results of these measurements are presented in Fig. 8 (data points on curve *1*). When $P_{2inc} \ll P_{1inc}$ and the modulation of the microwave voltage across the capacitor can be ignored, the dependence $P_{3out}(P_{2inc})$ has the following analytical form:

$$P_{3out} = AP_{1inc}^2 P_{2inc}\frac{1}{U_0^4}. \qquad (18)$$

The dependence $P_{3out}(P_{2inc})$ calculated by (18) at a constant transfer ratio S_{21} is shown in Fig. 8 (dashed part of curve *1*). In addition, Fig. 8 shows the already discussed dependence $P_{3out}(P_{2inc})$ for the case when the

resonator is excited by the two-tone signal with equal powers of its components ($P_{1\text{inc}} = P_{2\text{inc}}$) (curves *2*). Triangles are data points, and dashed curve *2* shows $P_{3\text{out}}$ calculated by (9) for U_0 that was used in constructing curve *1*. One can see that, at $T = 78$ K, when the modulation depth of the microwave signal incident on the resonator increases to 1, the nonlinear response of the STO capacitor noticeably grows. In Fig. 8, we show the difference $\Delta P \approx 22$ dB between the experimental and calculated IMD product signals. This difference is due to the modulation of the capacitor temperature with the beat frequency $\Delta P \cong 10 \log(U_0^4 / U_{0T}^4)$. The value of U_{0T} found from these measurements is consistent with the above estimates.

It is significant that the increased nonlinear response of the STO capacitor to the two-tone microwave signal at $T = 78$ K can be suppressed using a substrate with a heat conductivity lower than that of sapphire. The reason is that, in this case, the thermal relaxation time increases and the higher-than-T_0 steady-state temperature of the strontium titanate film is set.

CONCLUSION

The nonlinear responses of the plane capacitors to a high-intensity microwave field were analyzed at $T = 78$ and 300 K. The capacitors were made of thin strontium titanate films on single-crystal sapphire substrates. It was demonstrated that, at $T = 300$ K, the nonlinear behavior in the microwave range can be predicted from the low-signal capacitance vs. dc voltage curve in view of expression (9). At $T = 78$ K, due to the small thermal relaxation time of the STO capacitor, the nonlinear behavior depends on the exciting microwave signal. The response of the STO capacitor to the one-tone microwave signal corresponds to the nonlinearity of the low-signal CVC. However, the periodic (with the beat frequency) thermal modulation of the capacitance considerably amplifies the nonlinear response to the two-tone microwave signal with close frequencies of its components. The expressions for nonlinear behavior of STO capacitors in the microwave range at $T = 300$ and 78 K were derived.

Our results can be useful in designing microwave microelectron devices, specifically, in optimizing the layout of microwave circuits with nonlinear STO capacitors to reduce undesired nonlinear distortions.

ACKNOWLEDGMENTS

We are grateful to A.M. Prudan, V.E. Loginov, and Prof. O.G. Vendik for useful discussions.

REFERENCES

1. O. G. Vendik, *Ferroelectrics in Microwave Technology* (Sov. Radio, Moscow, 1979).
2. M. DiDomeniko, D. A. Johnson, and R. H. Pantell, Appl. Phys. **33**, 1697 (1962).
3. A. B. Kozyrev, V. N. Keis, G. Koepf, *et al.*, Microelectron. Eng. **29**, 257 (1995).
4. A. T. Findikoglu, Q. X. Jia, and D. W. Reagor, IEEE Trans. Appl. Supercond. **7**, 2925 (1997).
5. A. T. Findikoglu, Q. X. Jia, D. W. Reagor, and K. D. Wu, Electron. Lett. **31**, 1814 (1995).
6. S. S. Gevorgian, D. I. Kaparkov, and O. G. Vendik, IEE Proc., Part H: Microwaves Antennas Propag. **141**, 501 (1994).
7. A. B. Kozyrev, T. B. Samoĭlova, A. A. Golovlov, *et al.*, J. Appl. Phys. **84**, 3326 (1998).
8. J. H. Jacobi, Microwaves RF **119** (1986).
9. E. Philippow, *Nichtlineare Electrotechnik* (Akademische Verlagsgeselschaft Gest und Portig, Leipzig; Énergiya, Moscow, 1976).

Translated by I. Efimova

Technical Physics, Vol. 45, No. 6, 2000, pp. 766–769. Translated from Zhurnal Tekhnicheskoĭ Fiziki, Vol. 70, No. 6, 2000, pp. 98–101.

Sputtering Characteristics of Fullerene C_{60} Films under Bombardment with 0.1–1-keV Argon Ions and Atoms

I. P. Soshnikov*, A. V. Lunev*, M. É. Gaevskiĭ*, L. G. Rotkina*, and V. T. Barchenko**

** Ioffe Physicotechnical Institute, Russian Academy of Sciences, St. Petersburg, 194021 Russia*

*** St. Petersburg State Electrical Engineering University, St. Petersburg, 197376 Russia*

Received September 28, 1998; in final form December 21, 1998

Abstract—The sputtering of fullerene C_{60} films under bombardment with Ar^+ ions was studied. In thin films, blistering effects related to diffusion of the implanted argon ions along the layer and substrate interface have been found to occur. A threshold behavior was observed for sputtering at ion energies around 0.2 keV, which is much higher than in graphites. It has been shown that dependence of the work function on ion energy can be described in the framework of Zigmund–Falcone's approximation, which takes into account anisotropic effects in cascade collisions, and with Yudin's approximation for the sputtering of elemental materials. The obtained surface binding energy for fullerenes is $U_s \cong 6.7$ eV, which is less than the value for graphites, $U_{s\,\mathrm{graph}} = 7.7$ eV.

INTRODUCTION

One of the most interesting modern materials are fullerenes, which can find application in microelectronics and in nuclear and space technology. Fluxes of fast atomic particles encountered in nuclear and space technology and the wide use of ion (atom) bombardment in microelectronics technology and in modern techniques of structural analysis of materials stimulate studies of sputtering of fullerene films (fullerides) and modification of their structure, properties, and surface morphology as a result of bombardment with ion (atom) beams.

The few known studies of the interaction of fullerenes with accelerated atomic particles deal with problems of structural modifications resulting from bombardment with Ar^+ atoms ($E = 2$ keV) [1], ion and photon emission produced by bombardment with hydrogen and helium ions [2], and emission of clusters containing large numbers of atoms from surfaces of fullerides bombarded with (16.5 keV) Cs^+ ions [3, 4]. Unfortunately, important problems of sputtering and modification of the structure and properties of fullerene films are not quite understood. For example, Hoffman *et al.* [1] used in their work the method of electron energy loss spectroscopy (EELS), whereas it is known that the electron bombardment of fullerides can cause their polymerization [5–7].

In this study, sputtering and modification of the structure and surface morphology of fullerene C_{60} films under bombardment at normal incidence with monochromatic Ar beams of energy from 0.1 to 1 keV were investigated.

EXPERIMENTAL TECHNIQUE

The experiments were carried out on C_{60} films of thickness 100–2000 nm deposited by vacuum sputtering in VUP-5M apparatus. Purity of the fullerene soot used in the sputtering experiments was 99.98% or higher. As substrates, GaAs(100) and Si(100) wafers were used of grades AGChT-4 and KÉF-4.5, respectively, and were treated by chemical-dynamic methods prior to sputtering [8]. It has been shown in [9–12] that C_{60} films obtained under similar conditions have a polycrystalline structure.

The bombardment of the samples having an area of 0.25–1.5 cm^2 was carried out in a specially designed installation with a neutral Ar beam ~60 mm in diameter at a flux of $j \sim 10^{15}$ part $cm^{-2}\,s^{-1}$ up to fluences of around $\Phi \sim 10^{19}$ part cm^{-2}. The energy of the particles was varied in the range from 0.1 to 1 keV, and the sample temperature during bombardment did not exceed $T \sim 75$°C. The residual pressure in the working chamber was not higher than $P \sim 2 \times 10^{-6}$ torr and increased to $P \sim 3 \times 10^{-4}$ torr during operation of the source of accelerated particles. Detailed description of the particle source is given in [13–16]. The ion beam density was measured with a Faraday cup. The sputtering yield of the fullerene films $Y_{C_{60}}$ and the fluence Φ were determined from measured thicknesses of the layers sputtered from investigated films and GaAs control targets, $h_{C_{60}}$, and h_{GaAs}, respectively. The interrelationship between these quantities is given by the formula

$$\begin{aligned} Y_{C_{60}} &= \rho_{C_{60}} h_{C_{60}} / \Phi M_{C_{60}}, \\ \Phi &= \rho_{GaAs} h_{GaAs} / M_{GaAs} Y_{GaAs}, \end{aligned} \qquad (1)$$

1063-7842/00/4506-0766$20.00 © 2000 MAIK "Nauka/Interperiodica"

where Y_{GaAs} is the sputtering yield of gallium arsenide determined from data given in [14–19]; $\rho_{C_{60}}$ and ρ_{GaAs} are the densities of C_{60} and gallium arsenide films equal to 1.7 and 5.32 g/cm^3, respectively [9, 20]; and $M_{C_{60}}$ and M_{GaAs} are the average atomic masses of carbon and gallium arsenide, 12 and 72.4, respectively.

RESULTS AND DISCUSSION

Examination of the surface morphology resulting from bombardment of the fullerene films using scanning electron microscopy techniques revealed two types of surface relief: (i) shallow, randomly oriented ripples and (ii) blisters (Fig. 1). Characteristic dimensions of the random ripples are 0.01 and 0.1 μm in height and width, respectively. The orientation of the ripples is apparently affected by the specific etching pattern at the boundaries of microcrystallites. Characteristic dimension of the blisters is about 1 μm. The formation of blisters appears to be a result of accumulation of the implanted argon. Analysis of the blisters in samples bombarded with different doses shows that there is a step behavior in the blister density variation with increasing fluence. Samples with an initial C_{60} film thickness of about 0.1 μm after an exposure of $\Phi \sim 1 \times 10^{18}$ ion/cm^2 had a blister density of around 1.5×10^4 cm^{-2}, whereas, in samples bombarded with a dose of $\Phi \sim 3 \times 10^{18}$ ion/cm^2, the density of blisters was about twice as high, reaching a value of $\sim 3 \times 10^4$ cm^{-2}.

Comparison of the surface morphologies formed under identical bombardment conditions on samples with different C_{60} film thicknesses shows that in films with larger initial thickness, the resulting blister density is lower. Analysis of the obtained results indicates that the processes leading to the formation of blisters can be related to diffusion along the C_{60}/substrate interface.

It is known that fullerene can be polymerized as a result of various irradiations [9, 21–23]. In order to determine the condition of the C_{60} films after bombardment, their solubility in toluene was tested, and it was found that the fullerene films underwent polymerization as a result of sputtering with a neutral argon beam. Detailed results of the study of this effect will be presented elsewhere.

The measurement results of the sputtering yield of C_{60} films are presented in Figs. 2 and 3. Their analysis shows that, in films having the residual thickness less than 40 nm, there is a deviation of the C_{60} sputtering yield from the dependence observed in thick films (Fig. 2). This dependence is probably due to the effect of the substrate on the propagation of the cascade collisions; i.e., at film thicknesses comparable to the cascade size, some collisions will occur with atoms of the substrate instead of carbon atoms. Because the ratio of the masses of the primary particles and substrate atoms is closer to unity than that of the primary particles and carbon atoms, the efficiency of energy dissipation will be higher in the substrate material. Therefore, lower yields ought to be expected for films of thickness comparable to the size of a collision cascade, as observed in the experiment.

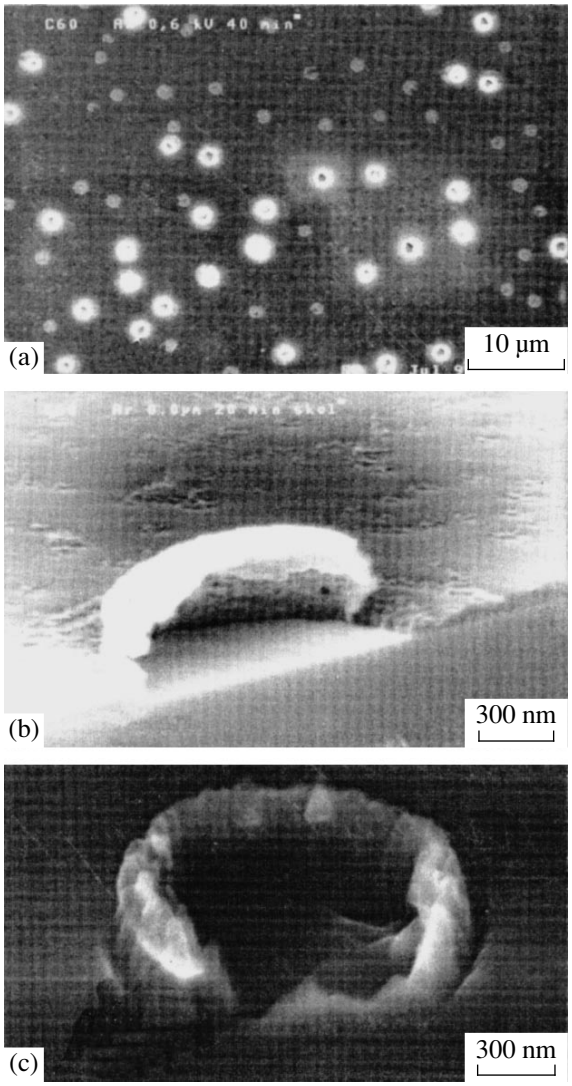

Fig. 1. Surface morphology of the C_{60} film with the initial thickness of $d \sim 0.2$ μm after bombardment with a neutral argon beam of energy $E = 0.6$ keV at flux density $j \sim 10^{14}$ part/s cm^2 up to fluences of around $\Phi \sim 3 \times 10^{-18}$ part/cm^2. (a) general view, (b) cross section of a closed cavity, and (c) cross section of an open blister.

Comparison of the scattering yields between films that were first polymerized and the polycrystalline films showed no dependence on the initial condition of the film. This is probably the consequence of the higher rate of film polymerization by the ion beam compared with the sputtering rate.

Dependence of the sputtering yield of thick C_{60} films on the particle energy is shown in Fig. 3. This dependence features a high value of the sputtering

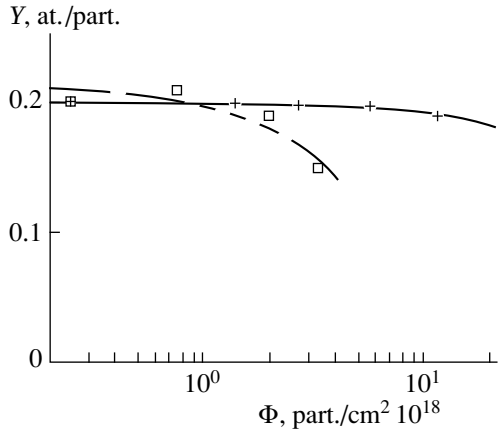

Fig. 2. Dependence of the C_{60} film sputtering yield on film thickness for bombardment with a 0.6-keV argon beam.

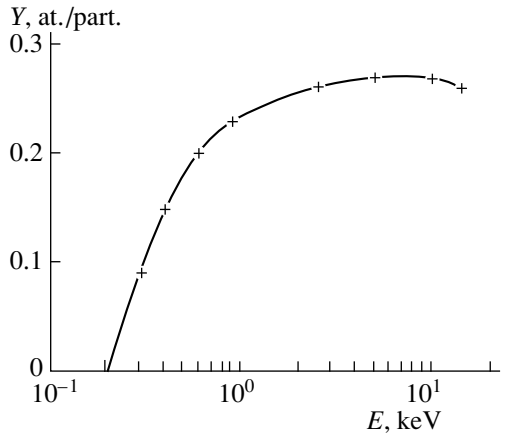

Fig. 3. Dependence of the sputtering yield of thick (>0.05 μm) C_{60} films on particle (argon) energy at normal incidence.

threshold energy $E_{th} \sim 0.2$ keV and considerable variation of the sputtering yield in the range of energies up to 1 keV. In the energy range from 1 to 15 keV, the sputtering yield rises slowly reaching a maximum of $Y \sim 0.3$ atoms per ion at $E = 9.5$ keV. Comparison of the sputtering yields for fullerene films, graphites, and carbon films shows that the values for fullerenes are intermediate between the other two materials. This discrepancy of data can be indicative of the effect of porosity on the results of determinations; i.e., the deposited carbon films may have a very porous structure, and, therefore, higher sputtering yield values are obtained compared with bulk graphite. The fullerene films possibly have lower porosity, and their sputtering yield, therefore, differs less from the data for bulk graphite.

Comparison of the sputtering yield values for fullerides with corresponding data for the most important microelectronics materials Si, SiO_2, and GaAs [14–19, 21, 22] shows that the efficiency of sputtering of fullerides by argon ions with energies 0.3–1 keV is lower by a factor of 3–10 (depending on the target material and bombardment conditions). In addition, in the sputtering of fullerenes, a threshold behavior is observed at a particle energy $E \sim 200$ eV, which is commonly used in plasmochemical etching, because this is a considerably higher value than that for graphite, Si, SiO_2, and GaAs [14–19, 21, 22].

Fitting the obtained dependence to various approximations has shown that the best results are obtained with the use of Zigmund–Falcone's model [23], which takes into account anisotropic effects in sputtering,

$$Y = Y_i[1 - (E_{th}/E)^2], \tag{2}$$

where E_{th} is the sputtering threshold energy determined from the experimental graph and equal to about 200 eV, which is considerably higher than the known values for most of the basic materials of microelectronics. Y_{is} is the sputtering yield neglecting the anisotropy effects, calculated with the use of the Yudin's approximation [24],

$$Y_i = \frac{2Y_{max}(E/E_{max})^{1/2}}{1 + E/E_{max}}, \tag{3}$$

where E_{max} is the energy of incident particles corresponding to the maximum value of the sputtering yield Y_{max}.

E_{max} and Y_{max} are defined as

$$E_{max} = 0.3E_{tf} = \frac{0.3Z_1Z_2(1 + M_i/M_t)}{6.92 \times 10^6 a}, \tag{4a}$$

$$Y_{max} = \Lambda(Z_1, Z_2)\frac{n\pi a^2 E_{tf}}{U_s}, \tag{4b}$$

where E_{tf} is the Thomas–Fermi energy; a is the interaction potential screening radius; and Λ is a material constant given by the formula

$$\Lambda(Z_1, Z_2) = \Lambda(Z_2) - 4.65 \times 10^{-12}(Z_1 - 18), \tag{4c}$$

$$\Lambda(Z_2) = 1.3 \times 10^{-10} Z_2^{1/2} \times \left[1 + 0.25\sin\left(2\pi\frac{Z_2 + Z + Z_0/4}{Z_0}\right)\right], \tag{4d}$$

where $Z_0 = 8$ and $Z = 0$ for $Z_2 \le 18$ and $Z_0 = 18$ and $Z = 2$ for $Z_2 > 18$.

The surface binding energy U_s determined from the best fit of the theory and experiment is equal to 6.7 eV, which is slightly less than for graphite ($U_s = 7.7$ eV [21, 24]).

The value of the sputtering threshold energy E_{th} is approximately 200 eV (Fig. 3), which is considerably higher than for graphite [17, 21]. This high sputtering threshold is probably related to the lower atomic density of fullerenes compared to graphite and, as a conse-

quence, lower retardation efficiency in the near-surface layer of fullerene, on which the sputtering is largely dependent.

CONCLUSIONS

In this work, sputtering of C_{60} films by a neutral argon beam has been carried out. It has been shown that under the experimental conditions, the fullerene films undergo polymerization. The sputtering is accompanied with a number of phases of blister formation, apparently as a result of diffusion processes at the layer and substrate interface. In thick films, the formation of blisters is less intensive. A threshold behavior has been observed in the dependence of sputtering on particle energy at energies around 0.2 keV. The experimental sputtering yield curves are found to be in satisfactory agreement with Zigmund–Falcone's model [23], which takes into account the anisotropy effects in the collisions of target atoms and ions, and with Yudin's approximation for the sputtering coefficients of simple targets [24].

ACKNOWLEDGMENTS

We are grateful to A. Ponomarev and ZAO Astrin for making the sample of fullerene soot available to us.

This study was supported in part by the Russian Foundation for Basic Research, project no. 02-98-18117.

REFERENCES

1. A. Hoffman, P. J. K. Paterson, S. T. Johnson, *et al.*, Phys. Rev. B **53**, 1573 (1996).
2. A. I. Bazhin, G. M. Druzhinin, and V. N. Ryzhov, in *Proceedings of the XIII International Conference "Ion-Surface Interaction," Moscow, 1997*, Vol. 2, p. 26.
3. N. Kh. Dzhemilev, I. V. Verevkin, S. E. Maksimov *et al.*, in *Proceedings of the International Conference "Emission Electronics," Tashkent, 1997*, p. 135.
4. N. Kh. Dzhemilev, I. V. Verevkin, S. E. Maksimov, *et al.*, Izv. Ross. Akad. Nauk, Ser. Fiz. **60** (7), 121 (1996).
5. T. Tada and T. Kanayama, Jpn. J. Appl. Phys. **80**, L63 (1996).
6. Y. B. Zhao, D. M. Poirier, R. J. Pechman, and J. H. Weaver, Appl. Phys. Lett. **64**, 577 (1994).
7. M. Matus, J. Winter, and H. Kuzmany, in *Solid State Science*, Ed. by J. Fink, H. Kuzmany, M. Mehrig, and R. Roth (Springer Ser., 1993), Vol. 117.
8. S. Sangwal, *Etching of Crystals. Theory, Experiment, and Application* (Elsevier, Amsterdam, 1987; Mir, Moscow, 1992).
9. S. V. Kozyrev and V. V. Rotkin, Fiz. Tekh. Poluprovodn. (St. Petersburg) **27**, 1409 (1993) [Semiconductors **27**, 777 (1993)].
10. L. Akselrod, H. J. Byrne, T. E. Sutto, and S. Roth, Chem. Phys. Lett. **233**, 436 (1995).
11. W. Krakow, N. M. Rivera, R. A. Roy, *et al.*, Appl. Phys. A **56**, 185 (1993).
12. D. M. Chen, H. Xu, W. N. Creager, and P. Burnet, J. Vac. Sci. Technol. B **12**, 1910 (1994).
13. V. T. Barchenko and A. Yu. Sokolovskiĭ, Izv. Leningr. Élektrotekh. Inst. **303**, 42 (1982).
14. N. A. Bert and I. P. Soshnikov, Fiz. Tverd. Tela (St. Petersburg) **35**, 2501 (1993) [Phys. Solid State **35**, 1239 (1993)].
15. I. P. Soshnikov, N. A. Bert, Yu. A. Kudryavtsev, and A. V. Lunev, Poverkhnost', No. 3, 83 (1997).
16. I. P. Soshnikov, N. A. Bert, Yu. A. Kudrjavtsev, and A. V. Lunev, Nucl. Instrum. Methods Phys. Res. B **127/128**, 115 (1997).
17. J. B. Malherbe, Sol. St. Mater. Sci. **19**, 55 (1994).
18. J. Comas and C. B. Cooper, J. Appl. Phys. **38**, 2956 (1967).
19. G. Betz and G. Wener, in *Sputtering by Particle Bombardment*, Ed. by R. Behrishe (Springer, Heidelberg, 1983; Mir, Moscow, 1986), Vol. 2.
20. *Physicochemical Properties of Semiconductors*, Ed. by A. V. Novoselova (Nauka, Moscow, 1978).
21. I. Itoh, Y. Yamamura, *et al.*, At. Data Nucl. Data Tables **80**, 3 (1984).
22. H. Bach, I. Kitzmann, and H. Schroeder, Radiat. Eff. **21**, 31 (1974).
23. J. Falcone, Usp. Fiz. Nauk **162** (4), 71 (1993).
24. V. V. Yudin, Élektron. Tekh. Ser. Poluprovodn. Prib. **6** (172), 3 (1984).

Translated by B. Kalinin

Technical Physics, Vol. 45, No. 6, 2000, pp. 770–775. Translated from Zhurnal Tekhnicheskoĭ Fiziki, Vol. 70, No. 6, 2000, pp. 102–107.

EXPERIMENTAL INSTRUMENTS AND TECHNIQUES

Peculiarities of the Growth Kinetics of Silicon–Germanium Alloy Layers from Silane and Germane with an Additional Heated Element in the Vacuum Chamber

L. K. Orlov, A. V. Potapov, and S. V. Ivin

Institute for Physics of Microstructures, Russian Academy of Sciences, Nizhni Novgorod, 603600 Russia

Received May 18, 1999; in final form December 1, 1999

Abstract—To study the disintegration of the molecules of hydrides at the surface of the growing layer and their influence on the rate of the epitaxial process a model of the growth kinetics of $Si_{1-x}Ge_x$ alloy layers from silane and germane by the molecular beam epitaxy method with SiH_4 and GeH_4 gas sources is considered. Through comparison of numerical simulation data and experimental relationships, the steady-state growth kinetics has been studied and a comparative analysis carried out of the efficiency of entry of Ge(Si) atoms into the growing layer both in the presence of Si and Ge atomic flows in the reactor (the so-called hot-wire method) and in their absence. The growth rates obtained with this method of epitaxial growth and with one of its modifications where the use is made of a sublimating silicon bar as an additional heated element have been compared. Peculiarities in the behavior of the dependence of the layer growth rate on its composition have been revealed and explained.

INTRODUCTION

In recent years in connection with the prospects of applying alloyed heterostructures in devices of microelectronics and microwave electronics, a considerable interest is seen in both improvement of the structure growth techniques and in development of physicochemical and mathematical models, which can provide an adequate description of the epitaxial process. In the majority of basic studies, the growth of strained Si–Ge heterostructures had been performed by the traditional method of molecular beam epitaxy (MBE). In the last decade, however, in connection with practical requirements, vacuum methods of epitaxy with gas sources (GSMBE) that use hydrides of silicon and germanium have been intensively developed. This growth method, which has considerably higher yield compared with MBE, features better area uniformity of layers and compares well with the traditional MBE in the possibility to form abrupt heterointerfaces, which is important in the growth of nanometer scale structures.

At the present time, in the literature, there is already a considerable number of experimental studies on vacuum hydride epitaxy of $Si_{1-x}Ge_x$ [1–5] with the use of both molecular and atomic flows in the reactor. However, the theoretical grounds of this method are at present not sufficiently developed [1, 2, 6–11]; as a result, the paths of the hydride disintegration reactions proceeding at the surface of the growing layer are not properly understood and there is little knowledge of the surface concentrations of different components of the disintegration products and their interaction. The main difficulty in modeling the kinetics of the layer growth from hydrides is the multiplicity of intermediate disintegration reactions and their paths [3, 12], which results in the appearance of a great many uncertain kinetic constants in the kinetic equations.

In the present study, a physicochemical model of the kinetics of the steady-state layer growth from the atomic flows of silicon and germanium as well as from the molecular flows of silane and germane [9] is developed. The model is the extension of the results obtained in [6–8, 10, 11] to the case of a mixture of two gases and contains a minimal number of parameters that have to be determined from the experiment. The numerical simulation of the technological processes on the basis of the proposed model has been carried out in a wide range of the growth parameters in both their presence in the reactor of additional atomic flows (hot-wire method) and in their absence. A comparative analysis of the growth rates for GSMBE and the hybrid Si–GeH_4 MBE method of layer growth studied earlier [6–8, 10] has been carried out. The latter is a modification of the GSMBE method with an additional hot source in the form of a silicon bar instead of the commonly used tungsten wire. The use of the sublimating silicon source, although involving some technological restrictions, allows one to obtain in the growth chamber silicon atomic flows without the use of the molecular silane source. Analysis of the model of surface processes for different technological modifications revealed the origin of the unusual behavior of the dependence of the layer growth rate on composition for different versions of the technology.

1063-7842/00/4506-0770$20.00

THE MODEL OF THE PHYSICO-CHEMICAL PROCESSES AT THE LAYER SURFACE

To describe the growth kinetics of the alloy layers, we use the approach proposed in [6–8, 10] for Si–GeH_4 MBE. In order to reduce the arbitrariness in the choice of kinetic constants and their number, the scheme of the disintegration of silane and germane molecules both at the substrate and at the additional hot source will be considered in the following simplified form using the notion of an effective frequency coefficient ν_{MH_3} of the full disintegration of the MH_3 molecules

$$\underline{M}H_4(gas) + \underline{2} \longrightarrow \underline{M}H_3 + \underline{H},\ \underline{M}H_3 + \underline{3} \longrightarrow \underline{M} + 3\underline{H},$$
$$M(gas) + \underline{1} \rightleftharpoons \underline{M},\quad \underline{M} \longrightarrow M(cr), \qquad (1)$$
$$\underline{H} \longrightarrow SH_2(gas).$$

Here M = Ge, Si; underlining denotes atoms bonded to the surface. The possible intermediate disintegration reaction paths of the MH_3 molecule were discussed in [3, 12]. They ought to be taken into account in the study of thermal desorption spectra [11]. In the present paper, the disintegration of the MH_2 molecules is not considered in detail. Below, the corresponding system of kinetic equations for monomolecular adsorption ($\Theta_{Si} + \Theta_{Ge} + \Theta_H + \Theta_{SiH_3} + \Theta_{fr} = 1$) is presented, which allows one to calculate concentrations of the adparticles averaged over the surface $\Theta_i = n_i/n_s$ (i = MH_3, M, H; n_i is the density of the ith particle's pieces; and $n_s = 6.78 \times 10^{14}$ cm^{-2} is the density of the adsorption centers at the surface [1]), and of the free adsorption sites $\Theta_{fr} = \Theta_{bl} + \Theta_{nbl}$ both blocked by MH_3 molecules ($\Theta_{bl} = 3\Theta_{SiH_3} + 3\Theta_{GeH_3}$), and nonblocked Θ_{nbl}

$$d\Theta_{MH_3}/dt = 2(S_{MH_4}F_{MH_4}/n_s)\Theta_{nbl}^2 - 24\nu_{MH_3}\Theta_{MH_3}\Theta_{fr}^3,$$
$$d\Theta_H/dt$$
$$= \sum_M \{2(S_{MH_4}F_{MH_4}/n_s)\Theta_{nbl}^2 + 72\nu_{MH_3}\Theta_{MH_3}\Theta_{fr}^3\} \qquad (2)$$
$$- \nu_H(x)\Theta_H - r_H\Theta_H,$$
$$d\Theta_M/dt = 24\nu_{MH_3}\Theta_{MH_3}\Theta_{fr}^3 + g(S_{MH_4}F_{MH_4}/n_s)\Theta_{fr}$$
$$- \nu_M\Theta_M - r_M\Theta_M.$$

Here, $F_{MH_4(M)}$ is the molecular (atomic) flux incident on the substrate; S_{MH_4} is the sticking coefficient of the MH_4 molecule at zero coverage and temperature T at the substrate surface (the sticking coefficient of the M atoms is assumed to be unity); $\nu_{M(H)}$ is the frequency coefficient of desorption of M(H) atoms from the surface ($\nu_{Si} = \nu_{Ge} = 10^{13}\exp(-2.3/kT)$ [13]); $r_{M(H)}$ is the crystallization rate; and g is the transfer coefficient of atoms from an additional hot source to the substrate. Here, we suppose that hydrogen is delivered at the surface only by hydride molecules, because it is effectively evacuated from the reactor volume and has a small value surface sticking coefficient compared with S_{MH_4} ($S_{H_2} \approx 0.01 S_{MH_4}$ [1]). Below, it is also assumed that the removal of hydrogen from the surface proceeds mainly due to desorption ($\nu_H(x) \gg r_H$) and that the concentration of hydrogen incorporated into the lattice is substantially lower than the concentration of host atoms ($r_M\Theta_M \gg r_H\Theta_H$). The third equation of system (1) takes account of the atomic flow from the additional heated element in the growth chamber (the hot-wire method). With known surface densities Θ_i it is easy to calculate the experimentally obtainable growth rate

$$V_{gr} = (r_{Si}\Theta_{Si} + r_{Ge}\Theta_{Ge})n_s/n_0 \qquad (3)$$

and the average composition of the deposited $Si_{1-x}Ge_x$ epitaxial layer

$$x = r_{Ge}\Theta_{Ge}/(r_{Si}\Theta_{Si} + r_{Ge}\Theta_{Ge}). \qquad (4)$$

Here $n_0 = 5.5 \times 10^{22}$ cm^{-3} is the number of the $Si_{1-x}Ge_x$ alloy atoms per unit volume. The value of the sticking coefficient S_{GeH_4} was estimated in [8, 10] on the basis of experimental data available in the literature. The value for S_{SiH_4} is given in [1]. Below, the sticking coefficient S_{GeH_4} is taken equal to $S_{GeH_4} = 3S_{SiH_4} = 2 \times 10^{-2}$ and independent of the temperature (in the temperature range of interest here, 550–750°C) and on the surface composition.

To accurately describe the growth process, it is necessary to take into account the dependence of the rate of crystallization (generally speaking, non-linear) on the density of adatoms condensed at the surface. Approximately, the dependence $r_{Si}(\Theta_{Si}, T)$ can be obtained by analyzing MBE growth of a silicon layer. From the balance equations for silicon atoms, it is easy to obtain the following expressions relating r_{Si} and Θ_{Si} [10]

$$r_{Si} = (F_{Si} + \nu_{Si}n_s)V_{gr}n_0/(F_{Si} - \nu_{Si}n_0)n_s;$$
$$\Theta_{Si} = (F_{Si} - \nu_{Si}n_0)/(F_{Si} + \nu_{Si}n_s). \qquad (5)$$

The typical form of the dependence of $r_{Si}(\Theta_{Si})$ on Θ_{Si} calculated for several temperatures with the use of an empirical plots of the flux of Si atoms and Si epitaxial layer growth rate versus source and substrate temperatures was given in [9, 10] (for instance, $r_{Si} \sim 1$ at T = 600°C and $\Theta_{Si} = 10^{-4}$–10^{-2}). Because of the absence of similar data for germanium we assumed below $r_{Ge} = r_{Si}$ and, thus, ignored the effect of germanium and silicon surface segregation.

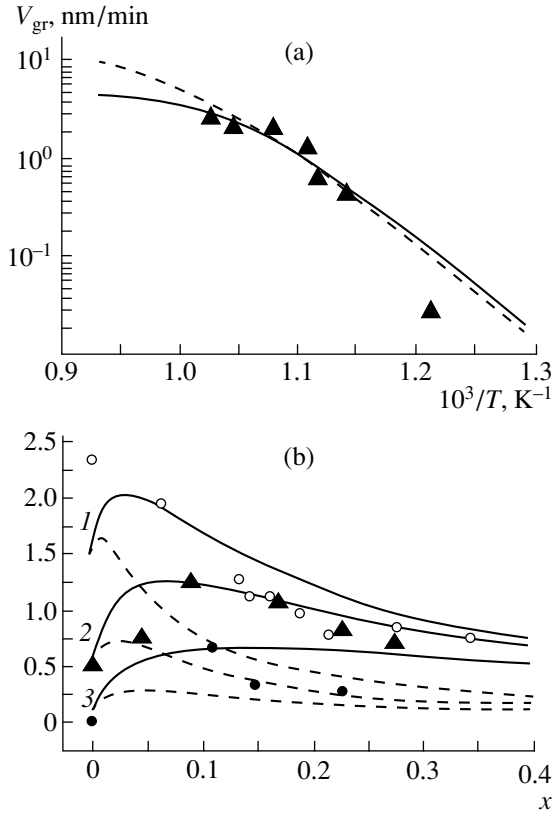

Fig. 1. (a) Temperature dependence of the silicon layer growth rate by MBE and (b) dependence of the $Si_{1-x}Ge_x$ layer growth rate by GSMBE on composition (germane pressure in reactor) at a constant silane pressure of 6.5×10^{-4} Torr. Experimental data [4] denoted as follows: T, °C: (●) 550, (▲) 600, (○) 650; curves represent simulations at $\nu_0 = 0.7$ s^{-1}, $E_{SiH_3} = 0.08$ eV (solid lines) and at $\nu_0 = 500$ s^{-1}, $E_{SiH_3} = 0.6$ eV [6] (dashed line).

The hydrogen desorption essentially influences the epitaxial layer growth rate, especially at low temperatures. For the alloy the rate of hydrogen, desorption will depend on surface composition as well, since the activation energies for hydrogen desorption from silicon ($E_{H-Si} = 2.08$ eV) and from germanium ($E_{H-Ge} = 1.56$ eV) differ considerably [2]. Usually, a linear approximation is used in calculations, obtained under an assumption that the hydrogen adatoms are equiprobably distributed over Si and Ge sites for adsorption [2]. However, surface migration can appreciably change the adatom distribution over the lattice sites due to the difference in Si–H and Ge–H bond energies. In its movement on the surface, an adatom will stay most of the time at the sites with a greater binding energy. Therefore, it should be expected that the effective desorption frequency will be lower. The strongest deviation is most likely to occur at small x. This shortcoming can be readily overcome if this factor is taken into account at least in the approximation of high particle mobility [9]. In this case, it is not difficult to obtain an expression for the frequency coefficient of hydrogen desorption from the surface of $Si_{1-x}Ge_x$ alloy

$$\nu_H(x) = \nu_{H-Ge}\Theta_{H-Ge}(x) + \nu_{H-Si}\Theta_{H-Si}(x),$$

$$\Theta_{H-Si}(x) = \{-\beta + (\beta^2 + 4\alpha(1-\gamma)\Theta_H)^{0.5}\}/2(1-\gamma),$$

$$\alpha = \gamma(1-x)(1-\theta_Z), \qquad (6)$$

$$\beta = \alpha + x(1-\Theta_Z) - (1-\gamma)\Theta_H,$$

$$\gamma = \nu_{GeSi}/\nu_{SiGe}, \quad \Theta_H = \Theta_{H-Si} + \Theta_{H-Ge},$$

where $\Theta_Z = 1 - \Theta_H - \Theta_V$, Θ_V is the density of free adsorption sites at the surface, and ν_{ij} is the frequency of transfer of hydrogen adatoms between sites of types i and j.

DETERMINATION OF THE EFFECTIVE RATE OF DISINTEGRATION OF THE HYDRIDES AT THE GROWING SURFACE FROM OBSERVED GROWTH PROCESS RELATIONSHIPS

In the foregoing, we discussed the meanings of several kinetic coefficients in the system of equations (2). In order to derive the effective disintegration rate of the hydride molecules MH_3 at the surface, it is necessary, apart from adjustment of other model parameters, to compare the theoretical calculations with experimental data available in the literature. The easiest way of obtaining an expression for the frequency coefficient of full disintegration of silane molecules at the growing surface is by comparing the calculated curves with temperature dependences of the rate of silicon layer growth from silane, of which a lot can be found in the literature (see, for example, [4]). A typical plot of $V_{gr}(T)$ for silicon is presented in Fig. 1a, from which it follows that a satisfactory agreement between theory (solid line) and experiment is achieved at $\nu_{SiH_3} = \nu_0 \exp(-E_{SiH_3}(\text{eV})/kT)$ s^{-1}, $\nu_0 = 0.7$ s^{-1}, $E_{SiH_3} = 0.08$ eV (at $T = 600$°C $\nu_{SiH_3}^{-1} \approx 5$ s). The change of slope of the $V_{gr}(T)$ curve is caused by the fact that at $T < 600$°C the growth rate is limited by an increase of the surface coverage by hydrogen (in simulations, we used $E_{H-Si} = 2.08$ eV) while at $T > 600$°C it is limited by the hydride disintegration rate at the surface. Here and below, we used the same values of the process parameter ν_0 and E_{SiH_3} as given in [12] for the rate of the reaction $\underline{Si}H_3 + \underline{1} \longrightarrow \underline{Si}H_2 + \underline{H}$. It can, therefore, be stated that at the growth temperature higher than 550°C, the disintegration rate of the surface hydride radicals can be limited by this reaction. Analysis of mass spectrometry data on surface composition [11] confirms that this reaction mainly determines the effective disintegration time of the $\underline{Si}H_3$ molecule (the concentration of $\underline{Si}H_3$ molecules at the growing surface far exceeds that of the $\underline{Si}H_2$ molecules; rapid disintegration of the latter is assumed to

proceed by the reaction $2\underline{Si}H_2 \longrightarrow 2\underline{Si}H + H_2$ [12]). In particular, from Fig. 1a, it is seen that the activation energy of the $\underline{Si}H_3$ molecule markedly affects the slope of the curves in the low temperature region. The use in simulations of different values of the process parameters ($\nu_0 = 500\ s^{-1}$, $E_{SiH_3} = 0.6$ eV [5]) associated with a different, more involved disintegration path of the SiH_2 molecules at the surface ($\underline{Si}H_2 + \underline{1} \longrightarrow \underline{Si}H + \underline{H}$ [12]) and sometimes used for the analysis of experimental data [6, 10] results, in the case under consideration, in a discrepancy between theoretical and experimental dependences (Fig. 1, dashed curves).

To determine the value of ν_{GeH_3} and ascertain some other system parameters, let us use an experimental dependence of the growth rate of $Si_{1-x}Ge_x$ layers on their composition (Fig. 1b) [4]. The numerical simulation (solid curves) has shown that the disintegration rate of the GeH_3 molecules determines the layer growth rate at a constant silane pressure. In our case, it is equal to $\nu_{GeH_3} = 0.03\exp(-0.04\ (\text{eV})/kT)\ s^{-1}$ (at $T = 600°C$ $\nu_{GeH_3}^{-1} \approx 1$ min). In our calculations of the silane disintegration rate, we assume the following values of the parameters: $\nu_0 = 0.75\ s^{-1}$, $E_{SiH_3} = 0.08$ eV. The maximum on the $V_{gr}(x)$ curve is associated with the dependence of the hydrogen desorption rate on surface composition. In the region of small x, the growth rate increases with germanium content since the hydrogen desorption from the surface is enhanced ($E_{H-Ge} < E_{H-Si}$) and the density of the free adsorption sites is increased. The further increase of x by means of increasing the germane pressure causes a covering of the surface by products of germane disintegration and, as a result, a lowering of the growth rate. The behavior of the curve can be easily understood by analyzing the dependences of surface concentrations of disintegration products of different hydrides on the germane concentration in the reactor chamber (Fig. 2a). It is seen that at low germane pressures ($P_{GeH_4} < 10^{-5}$ Torr), the surface concentration of hydrogen drops sharply with pressure while at elevated germane pressures ($P_{GeH_4} > 10^{-5}$ Torr), a drop in the concentration of silicon atoms is observed.

However, it should be noted that the use for $V_{gr}(x)$ calculations of a model that does not take into account the influence of surface migration of particles on the distribution of hydrogen adatoms over that surface, results in a shift of the maximum of the theoretical curve to the region $x = 0.02$–0.04 [2] while the maxima on the experimental curves have positions around $x \approx 0.1$ at $T_{gr} = 550$–$600°C$ (Fig. 1b). Taking into account the surface migration of H adatoms [see (6)] considerably improves an agreement between theoretical and experimental curves (Fig. 1b).

A maximum in the $V_{gr}(x)$ dependence occurs only in a temperature range from 500 to 700°C. Outside of this range, the growth rate is a monotonously sloping curve [1]. The reason is that at high temperatures, hydrogen desorption from the surface proceeds rather effectively and the addition of germane only results in the reduction of the number of the free adsorption sites. At low growth temperatures, the contribution of the silicon component to the growth rate is insignificant and the addition of germane results in a monotonous increase of $V_{gr}(x)$.

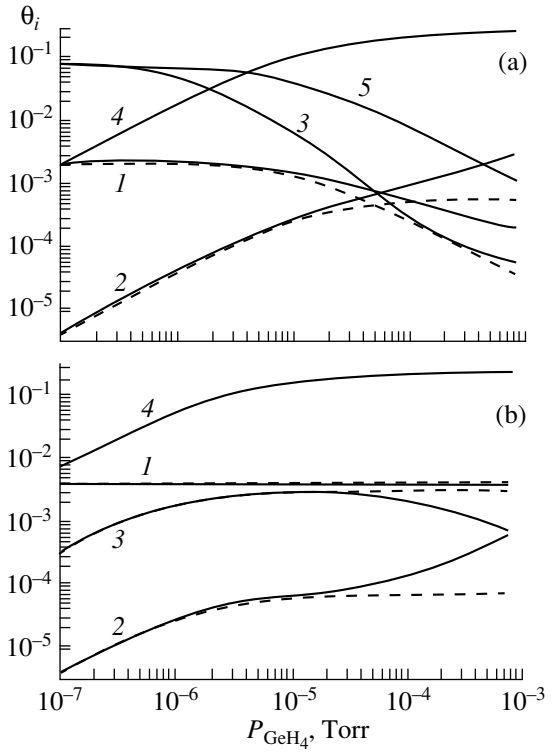

Fig. 2. Dependences of surface densities of hydride disintegration products on germane pressure in the reactor (a) for GSMBE method at $P_{SiH_4} = 10^{-4}$ Torr, $T = 700°C$, $g = 0$, 0.1 and (b) for Si–GeH_4 MBE method at $J_{Si} \approx 1 \times 10^{15}\ cm^{-2}\ s^{-1}$, $T = 700°C$, $g = 0$, 0.037. Dashed and solid lines correspond to $g = 0$ and $g > 0$, respectively. (*1*) Θ_{Si}, (*2*) Θ_{Ge}, (*3*) Θ_H, (*4*) Θ_{GeH_3}, and (*5*) Θ_{SiH_3}.

EFFECT OF AN ADDITIONAL HEATED ELEMENT IN THE GROWTH CHAMBER ON THE RATE OF THE EPITAXIAL PROCESS

One of the limitations of MBE with gas sources is the extremely low layer growth rate, which in some instances becomes an obstacle in fabrication of device structures. Using monosilane and monogermane, it is impossible to obtain a maximum growth rate exceeding 2–3 nm/min (Fig. 1). The growth rate can be increased through the use of digermane and disilane; however, in both cases, it decreases exponentially with a lowering of temperature, which is due to the very nature of thermally activated physicochemical processes at the growing surface.

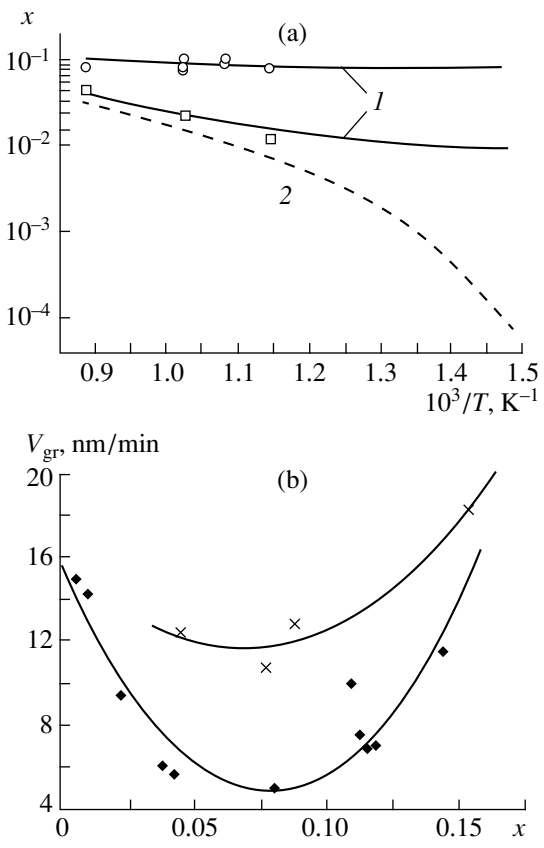

Fig. 3. (a) Experimental (signs) and theoretical (for g = 0.037—curves *1* and g = 0—curve *2*) dependences of germanium content in $Si_{1-x}Ge_x$ layers on growth temperature at P_{GeH_2}, Torr: (○) 5×10^{-4}, (□) 5×10^{-5}. (b) Growth rate of $Si_{1-x}Ge_x$ layers as a function of alloy composition at T, °C: (◆) 700, (×) 850; curves are polynomial fits; $J_{Si} = 1 \times 10^{15}$ cm^{-2} s^{-1}.

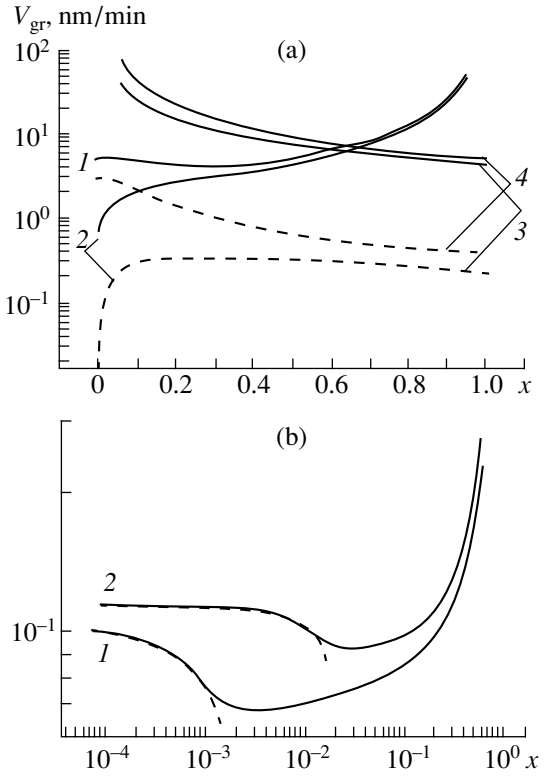

Fig. 4. Calculated growth rate $V_{gr}(x)$ of $Si_{1-x}Ge_x$ layers as a function of composition without ($g \neq 0$) (dashed lines) and with (g = 0.1 (a), 0.037 (b)) an additional hot source (dotted lines) in the growth chamber. (a) – GSMBE at a constant silane pressure (*1*, *2*) or constant germane pressure (*3*, *4*); $P_{SiH_4, GeH_4} = 10^{-4}$ (*1*, *4*), 10^{-3} (*2*, *3*) Torr; partial pressure of the second gas component was varied from 10^{-7} to 10^{-2} Torr. (b) Si–GeH_4 MBE method at $J_{Si} \approx 1 \times 10^{15}$ cm^{-2} s^{-1}, 600 (*1*), and 700°C (*2*); $P_{GeH_4} = 10^{-8}$–5×10^{-2} Torr.

One of the most simple methods for the acceleration of the pyrolysis process in the reactor is a hot-wire method [14], which essentially consists in placing in front of the substrate of an element heated to a high temperature, for instance, a tungsten wire spiral resistively heated to 1200°C. Such an element can play a role of its own as a source of the flow of atoms if a sublimating silicon bar is used instead of the tungsten wire as in the hybrid S–GeH_4 MBE method [6–8, 10]. The process of disintegration of hydrides of silicon and germanium proceeds effectively at a surface heated to temperatures exceeding 1000°C. The produced Si and Ge atoms desorb and arrive at the substrate. This way of delivering atoms of the growing material indirectly by increasing the coverage of the layer surface, appreciably increases the growth rate, which, in this case, is independent of the substrate temperature.

The presence of additional atomic flows can affect both the shape of the $V_{gr}(x)$ curves and the effective rate of disintegration of the hydride molecules at the growing surface. To see that this is indeed the case, we considered an example of a simple technology that uses only one source of gaseous germane and an additional hot source of the sublimating monocrystalline silicon (Si–GeH_4 MBE [6–8, 10, 15]). The silicon bar heated by electric current is the source of both silicon and germanium atomic flows. With this technology, the only unknown parameter of the model, ν_{GeH_3} can be determined by fitting the calculated dependences $x(T, P_{GeH_3})$ to the experimental curves (Fig. 3a) obtained with our direct participation [15]. From the $x(T)$ dependence, we have found that for Si–GeH_4 MBE, the best agreement of theory and experiment is achieved at $\nu_{GeH_3} = 2\exp(-0.47\ (\text{eV})/kT)$ s^{-1}. A similar ν_{GeH_3} value is defined from an analysis of the $x(P_{GeH_3})$ dependence [7]. It is seen that the activation energy for disintegration of a GeH_3 molecule in the considered case differs essentially from the value obtained above for the

GSMBE method. This can be explained by the rate-determining effect of the disintegration process of the molecule $\underline{Ge}H_2 \longrightarrow \underline{Ge}H + \underline{H}$. The dominating role of different chemical reactions in different techniques is possibly related both to the influence of the atomic flows on the rate of chemical reactions at the surface, and to the dependence of the rate of these reactions on the concentration of the reactants. The low concentration of GeH_2 molecules at the growing surface precludes their disintegration by the faster bimolecular reaction $2GeH_2 \longrightarrow 2GeH + H_2(gas)$.

Varying contributions of atomic and molecular flows in different experimental conditions in the reactor can considerably affect the shape of the $V_{gr}(x)$ dependence as well. The corresponding curves obtained at a constant flux of silicon atoms from the sublimating Si source in the Si–GeH_4 MBE [6, 7] are presented in Fig. 3b. It is seen that the behavior of the curves in Figs. 1b and 3b differs greatly. The reasons for the behavior of the curves in Fig. 1b were discussed above, while the reasons for the behavior of the curves in Fig. 3b will be considered below.

COMPARATIVE ANALYSIS OF THE BEHAVIOR OF THE GROWTH PROCESS DEPENDENCES FOR GSMBE METHOD WITH AND WITHOUT ATOMIC FLOWS IN THE REACTOR

Having determined the kinetic coefficients, the dependence of the layer growth rate on its composition can be calculated in a more general case for a wide range of technological parameters. The behavior of the curves reflects the role of different physicochemical processes in the conditions of a given technological experiment. First, let us consider the case of GSMBE with gaseous silane and germane sources. The use in the growth of only molecular flows ($g = 0$) results in theoretical $V_{gr}(x)$ curves of Fig. 4a similar to curves in Fig. 1b. The behavior of the curves at a constant partial silane pressure was already discussed. The reasons for the specific shape of the curves at a constant partial germane pressure are similar. Comparison of the curves for $g = 0$ (solid lines) and $g \neq 0$ (dashed lines) in Fig. 4a shows that the introduction of the hot source considerably influences the growth rate, especially in the composition ranges where the content of one of the alloy components is low. The introduction of additional atomic flows with rising pressure of the varying component $GeH_4(SiH_4)$ considerably changes the effective hydride disintegration rates (Fig. 4a) due to an increase in the concentration of condensing adatoms Θ_{Ge} and Θ_{Si} (Fig. 2a).

Let us compare the obtained dependences with similar curves calculated for the Si–GeH_4 MBE method with a single gas source of germane and sublimating hot silicon source (Fig. 4b). Curves in Fig. 4b can be easily interpreted if it is noted that at the zero value of P_{GeH_4}, all $V_{gr}(x)$ curves should meet at a point $V_{gr}(Si)$ corresponding to the growth of a pure silicon layer. In contrast to the previous, casehydrogen in this growth process takes no part whatsoever. As the GeH_4 pressure rises, the growing surface becomes blanketed by the products of germane disintegration (Fig. 2b), which results in decreased density of adsorbed Si atoms and, consequently, in lower growth rates. In this case, the lower is the substrate temperature, the more noticeable is the decrease of the growth rate (Figs. 3b, 4b). A further increase in the germane pressure, and accordingly the germanium content, results in a more intensive flow of Ge atoms from the hot source and the concentration of Ge atoms at the growing surface (Fig. 2b). Therefore, the growth rate increases (Figs. 3b, 4b).

ACKNOWLEDGMENTS

The authors wish to thank the interindustrial scientific research program, "Physics of Solid State Nanostructures" (grant no. 97-2023) and INTAS (grant no. 96-0580) for their financial support.

REFERENCES

1. D. W. Greve, Mater. Sci. Eng. B **18**, 22 (1993).
2. D. J. Robbins, J. L. Glasper, A. G. Cullis, *et al.*, J. Appl. Phys. **69**, 3729 (1991).
3. B. Cunningham, J. O. Chu, and S. Akbar, Appl. Phys. Lett. **59**, 3574 (1991).
4. L. T. Vinh, V. Aubry-Fortuna, Y. Zheng, *et al.*, Thin Solid Films **294**, 59 (1997).
5. T. R. Bramblett, Q. Lu, N. E. Lee, *et al.*, J. Appl. Phys. **77**, 1504 (1995).
6. L. K. Orlov, V. A. Tolomasov, A. V. Potapov, *et al.*, Inst. Phys. Conf. Ser. **155** (3), 205 (1997).
7. L. K. Orlov, V. A. Tolomasov, A. V. Potapov, *et al.*, Izv. Vyssh. Uchebn. Zaved., Ser. Mat. Élektron. Tekh. **2**, 30 (1998).
8. L. K. Orlov, V. A. Tolomasov, A. V. Potapov, *et al.*, IEEE SIMC **9**, 215 (1996).
9. A. V. Potapov, L. K. Orlov, and S. V. Ivin, Thin Solid Films **336** (1–2), 191 (1998).
10. L. K. Orlov, A. V. Potapov, V. A. Tolomasov, *et al.*, in *Proceedings of the 2nd Russia Symposium "Heat-and-Mass Transfer and Growth of Single Crystals and Thin Film Structures," Obninsk, Russia, 1997*, Ed. by V. P. Ginkin, p. 288.
11. A. V. Potapov and L. K. Orlov, in *Proceedings of the International Symposium "Nanostructures: Physics and Technology," St. Petersbrug, Russia, 1998*, p. 487.
12. S. M. Gates, C. M. Greenlief, D. B. Beach, *et al.*, J. Chem. Phys. **93**, 7493 (1990).
13. H. C. Abbink, R. M. Broudy, and G. P. McCarthy, J. Appl. Phys. **39**, 4673 (1968).
14. P. Brogueira, J. P. Conde, S. Arekat, *et al.*, J. Appl. Phys. **78**, 3776 (1995).
15. V. A. Tolomasov, L. K. Orlov, S. P. Svetlov, *et al.*, Kristallografiya **43**, 535 (1998) [Crystallogr. Rep. **43**, 493 (1998)].

Translated by M. Lebedev

Technical Physics, Vol. 45, No. 6, 2000, pp. 776–779. Translated from Zhurnal Tekhnicheskoĭ Fiziki, Vol. 70, No. 6, 2000, pp. 108–112.

EXPERIMENTAL INSTRUMENTS AND TECHNIQUES

Reversible Polarization of Ferroelectric Ceramics in a Rapid-Growing Electric Field

S. A. Sadykov[1], V. Z. Borodin[2], and A. Sh. Agalarov[2]

[1] *Dagestan State University, Makhachkala, 367025 Dagestan, Russia*

[2] *Research Institute of Physics, Rostov State University, pr. Stachki 194, Rostov-on-Don, 344090 Russia*

Received December 1, 1998; in final form, October 19, 1999

Abstract—The complex permittivity of ferroelectric PZT ceramics with different compositions was measured in a pulsed rapid-growing electric field. The time dependence of the real component exhibits three peaks. The dips between them correlate with imaginary component peaks. Domain mechanisms that contribute to the ferroelectric polarization and are responsible for the time dependences are considered. © *2000 MAIK "Nauka/Interperiodica".*

During polarization reversal in ferroelectrics subjected to an electric field, the domain walls are displaced, leading to a significant increase in the complex permittivity ε*. Up to now, nonlinear features of ε* have been investigated mostly in crystalline ferroelectrics for repolarization due to rectangular bipolar voltage pulses. As shown in [1, 2], the permittivity is ambiguously related to the reversing current and strongly depends on frequency. The peak of the real component ε' of permittivity has been found to lag behind that of the reversing current i_r, whereas the imaginary component ε'' and i_r vary synchronously. Similar results have been obtained for PZT polycrystalline samples polarized by a pulse electric field with a controllable buildup rate [3]. With such a reversal method, an ε'(t) curve has three distinct peaks and ε''(t), two smeared ones. It has been suggested [1–3] that the components of ε* depend not only on the total area of the domain walls; otherwise, the ε'(t) and ε''(t) curves would be similar. It appears that relaxation processes associated with domain wall displacement also influence the permittivity of ferroelectrics.

In ceramics, the microscopic nature of polarization in an external electric field is much more complicated than in single crystals. This is particularly true for intense rapid-growing fields, when, even at normal temperatures, the macroscopic polarization of ceramics reaches values typical of standard methods within microseconds [4]. The physical mechanism of ε* growth in ceramic ferroelectrics has not yet been completely understood, though it is of importance in applications. Little is also known about the dynamics of the domain structure and its relaxation in pulse fields.

In this work, we pursue our study on the reversibility of ε'(t) and ε''(t) in PZT ferroelectrics [3]. The reverse characteristics can shed light upon the domain dynamics in external electric fields at various stages of fast (microsecond) polarization switching.

EXPERIMENT

Conventional ferroelectric ceramics PKR-1 and PZT-19 [5] with a low coercive field E_c (0.6–1.0 and 1.2 kV/mm, respectively) were used as samples. PKR-1 is a three-component solid solution of complex oxides (like $PbTiO_3$–$PbZrO_3$–$Pb\,B'_{1/2}B''_{1/2}\,O_3$) that has the rhombohedral phase near the morphotropic region. PZT-19 also belongs to the morphotropic region and has a relatively high permittivity $\varepsilon_{33}^{T} = 1600$ (compare with $\varepsilon_{33}^{T} = 700$ for PKR-1). One-mm-thick disc-shaped samples 10 mm in diameter were prepared by hot pressing. Flat silver electrodes were applied to the disk faces.

The experimental setup is shown in Fig. 1. Preannealed samples were subjected to electrical pulses whose rise rate, controlled by plug-in inductors, was chosen such that the complete polarization period t_p lasted 50–100 μs. This time interval is optimum for

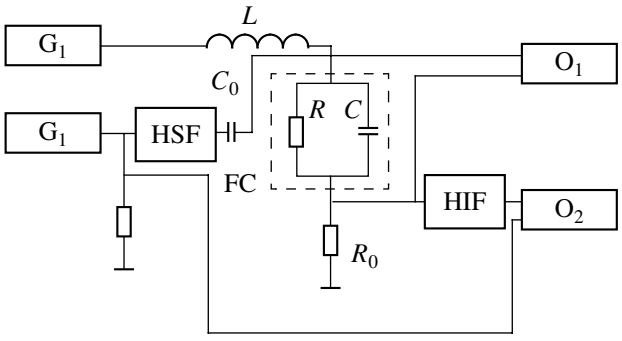

Fig. 1. Experimental setup. G_1, high-voltage pulse generator; G_2, sinusoidal voltage generator; HSF, high-frequency separation filter; HIF, high-frequency in-line filter; O_1 and O_2, oscillographs; FC, ferroceramic.

1063-7842/00/4506-0776$20.00

oscillographic measurements of the permittivity at 0.3–1.5 MHz. The real, ε', and imaginary, ε", parts of the reverse permittivity, which are effective kinetic parameters of polarization, were calculated from the measured instantaneous low-voltage input signal U_0; sample signal U at the instant of switching; and phase difference φ between them, which is related to dielectric losses. In the calculations, a ferroelectric sample was represented as a capacitance C and a resistance R connected in parallel. The analysis of this circuit by the method of conductivities gives the following computing formulas:

$$C = \left(\frac{R}{A} - 1\right)^{1/2} (\omega R)^{-1}, \quad (1)$$

$$R = \left(A\tan\varphi - \frac{1}{\omega C_0}\right)^2 A^{-1} + A, \quad (2)$$

where $A = (U_0 R_0 U^{-1})(1 + \tan^2\varphi)^{-1/2}$, C_0 is the stopping capacitance (1 nF), R_0 is the load resistance (6.3 Ω), and ω is the circular frequency of the measuring voltage. ε' and ε" were calculated from expressions (1) and (2), respectively ($\sigma = \varepsilon_0\varepsilon''\omega$, where σ is the equivalent parallel conductance).

The accuracy of the C and R calculation was checked by replacing the sample by discrete capacitance and resistance of known values.

Potential and current oscillograms for three times of polarization reversal are presented in Fig. 2. Also shown is the output measuring voltage for one of the reversal period. The input signal voltage was 5 V. It is seen that polarization proceeds mostly under the constant electric field (dynamic coercive field $E_c' > E_c$) and is completed when the field monotonically rises for the second time and reaches $2–3E_c'$. The reversing current curves have a specific asymmetric shape with a smoothed peak and sharp fall. Such a variation of the field is defined by that of the polarization current, which in turn depends on the initial rise rate of the field and properties of a ferroelectric sample. Thus, the sample potential is controlled by the polarization current, while the switching processes take place under the self-consistent electric field.

A variation of the high-frequency output signal is a direct result of the variation of the sample impedance during polarization. As soon as the domain walls are rearranged and a new polarization state is formed, the output signal stops growing, though the field in the sample continues to increase. Therefore, the polarization period t_p was defined as an interval between the application of a high-voltage pulse and the instant when the low-voltage output signal ceases to vary.

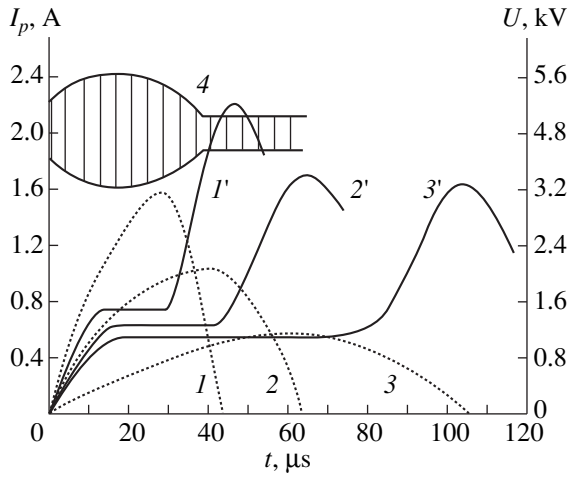

Fig. 2. (*1'–3'*) Typical high-voltage electric pulses and (*1–3*) reversing current for PKR-1 at t_p = (*1*) 40, (*2*) 60, and (*3*) 100 μs; (*4*) output measuring voltage with a frequency of 1 MHz for t_p = 40 μs.

RESULTS AND DISCUSSION

Time dependences of the real part ε' for PKR-1 during polarization are plotted in Fig. 3. During the reversal period, ε' goes through three peaks with different amplitudes. Note that, when t_p decreases from 100 to 40 μs, the shape of the ε'(t) curve does not change.

The first and highest peak occurs at the leading edge of a voltage pulse and corresponds to low dielectric losses. In [3], this peak is associated with the elastic vibrations of the domain walls about their equilibrium positions. The domain walls fixed at defects are considered as damped oscillators.

At the first stage of reversal, 180° domain walls become unstable and their mobility increases, but the initial structure does not change. Then, 180° tapered domains arise and extend along the electric field. As the number of domains involved in polarization and their mobility increase, so does ε'. Concurrently, conditions for piezoelectric domain contraction are set, which results in a decrease in ε'. Thus, the effect of negative Δε' can be attributed to domain contraction due to the piezoelectric deformations of individual domains by the high-frequency measuring field. When these processes are balanced, ε' peaks (the first peak) at $E \approx E_c'$. As the electric field in the sample grows faster (i.e., the polarization rate increases), both the magnitude of ε' and its rate of change increase.

The second peak of ε' can be associated with the lateral motion of expanding 180° domains. The subsequent monotone decrease in ε' may result from a number of factors. The most probable ones are a reduction of the number of 180° reversals and enhanced domain

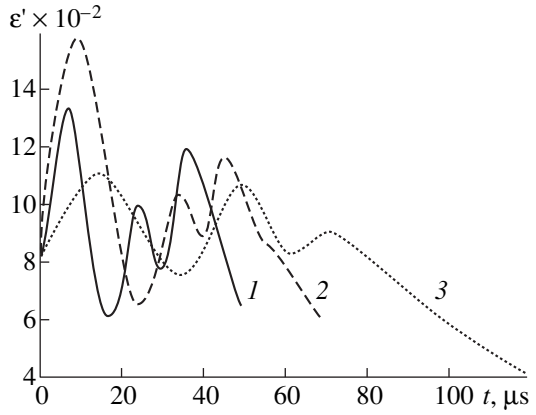

Fig. 3. ε'(*t*) curve for PKR-1. t_p = (*1*) 40, (*2*) 60, and (*3*) 100 μs.

contraction. Screening by bulk and surface charges also produces a noticeable effect on the domain dynamics. Different mobile point defects are known to pin the domain walls, thus markedly affecting their mobility [6]. The rate of wall screening depends on both the point defect mobility and the strength of their interaction, causing defects to drift. In the case of superfast field reversal, the bulk charges do not keep pace with the domain walls. Having broken free of the influence of the bulk charges, the walls become more mobile in the high-frequency field and contribute more to ε'. However, experimental results [4] indicate the complete screening of the polarization charge during microsecond reversal; i.e., when the characteristic polarization periods are significantly less than the times of Maxwellian relaxation of the bulk charges. We will consider this situation below.

As shown in [7], the interaction of walls with point or linear defects during repolarization produces field concentrators near pinning points. The concentrators are areas of anomalously high internal field. The field amplification factor can reach ~10^3 for linear defects. In strong local fields, $E \approx 10^5$–10^6 V/cm, impact ionization of impurities generates free carriers, which screen bound charge and cause radiative recombination [8]. Because of the small relaxation time ($\tau < 10^{-6}$ s), the excess charges compensate the depolarizing fields even at the nucleation stage. As a result, the walls slow down and ε' decreases. The electron subsystem influences the domain dynamics throughout the period of repolarization. It is supported by the fact that electroluminescence from ferroelectric ceramics in a self-consistent field appears at the beginning of repolarization and has several peaks similar to those in the ε'(*t*) curve [8].

At the final stage of reversal, the third peak due to 90° domain walls arises. Transmission electron microscopy studies of ceramics polarized in a self-consistent field have shown that their domain structure is a set of 90° lamellas with the walls oriented largely perpendicularly to the applied field and crossing grain boundaries (Fig. 4). In partially polarized ceramic samples, the rearrangement of 90° domain walls starts nearly simultaneously with the appearance of the second peak but becomes dominant only near the third peak of ε'. As the reversal time t_p shrinks, the third peak grows and tends to saturation. Thus, each of the ε' peaks behaves in a different manner.

Both ε' and ε'' drop as the measuring voltage frequency *f* grows from 0.3 to 1.5 MHz (Fig. 5). This decrease was most pronounced for the second and third ε' peaks. The ε' value in the first minimum does not depend virtually on frequency and remains close to the

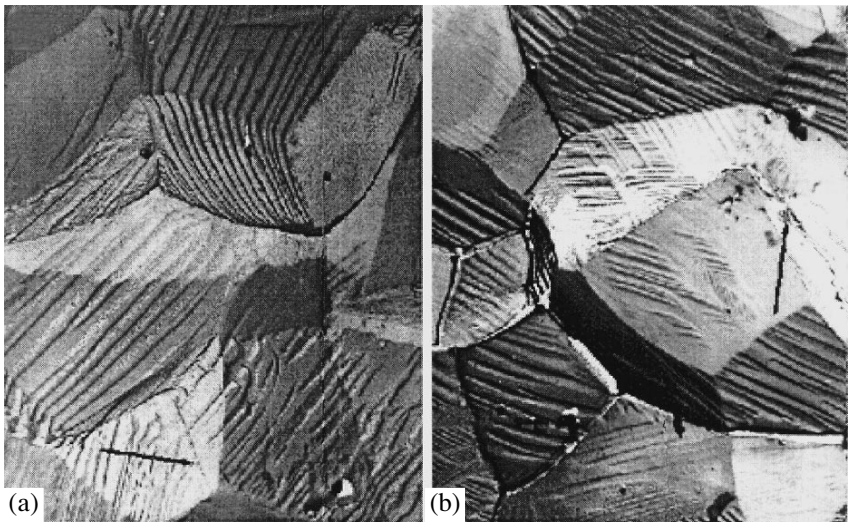

Fig. 4. Domain structure of PKR-1 after pulse polarization. Arrows indicate the direction of the applied field. (a) Orientation texture of 90° domain lamellas on the lateral sides of grains for t_p = 40 μs; ×11800. (b) Oriented 90° domain lamellas, *t* = 20 μs at t_p = 40 μs; ×7250.

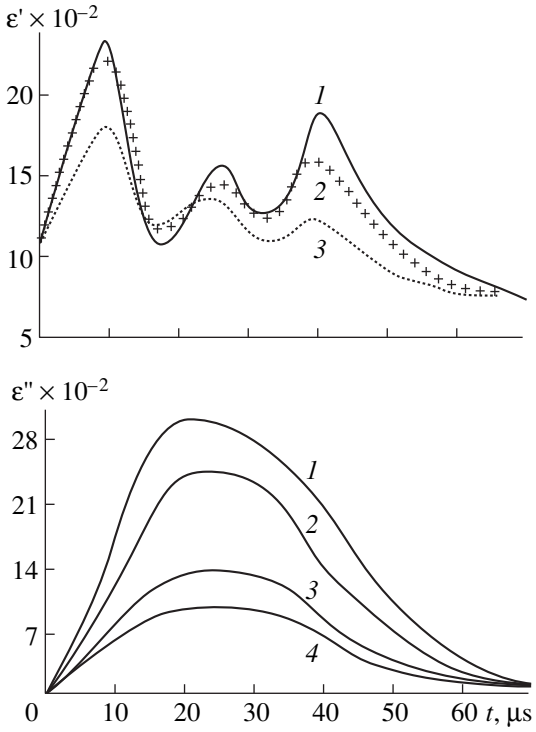

Fig. 5. ε'(*t*) and ε"(*t*) for PZT-19 at t_p = 60 μs and *f* = (*1*) 0.3, (*2*) 0.5, (*3*) 1.0, and (*4*) 1.5 MHz.

initial value of ε' (at *t* = 0), because domain contraction suppresses domain vibrations. The increase in ε' with decreasing frequency is associated with relaxation processes, among which 90° wall rearrangement proves to be the slowest. The different frequency dependences of ε* at different polarization stages imply the presence of a set of relaxation oscillators with different relaxation times. This should be kept in mind while interpreting the experimental results.

A change in the domain wall mobility during polarization significantly affects the ε"(*t*) dependence, since the motion of domains accounts for dielectric losses to a large extent. The dielectric viscosity for the lateral motion of 180° and 90° walls is larger than that for direct propagation. An increase in the domain mobility due to depinning from defects diminishes dielectric losses.

CONCLUSION

The time dependences of the reversible characteristics ε'(*t*) and ε"(*t*) of ferroelectric ceramics indicate different contributions from 180° and 90° domain walls to the permittivity at various stages of switching. The frequency dependence of ε* suggests the relaxation character of domain wall rearrangement, with the relaxation time varying in a broad interval. The relaxation time of domain walls can be estimated as

$$\tau = \frac{\sigma}{\varepsilon_0 \omega^2 \varepsilon'},$$

which gives ≈0.2 μs for PZT-19 and 0.3–0.45 μs for PKR-1. These values are approximately one order of magnitude less than those for crystals [1]. Presumably, the mobility of domains in a self-consistent field is governed not only by their interaction with defects and contraction but also by their screening owing to impact ionization of impurities during reversal.

REFERENCES

1. E. Fatuzzo, J. Appl. Phys. **33**, 2588 (1962).
2. A. Fouscova and V. Janousek, J. Phys. Soc. Japan **20**, 1619 (1965).
3. S. A. Sadicov, A. Sh. Agalarov, and V. Z. Borodin, Ferroelectrics **86**, 127 (1996).
4. S. A. Sadykov, E. I. Bondarenko, and A. Sh. Agalarov, Zh. Tekh. Fiz. **63** (11), 60 (1993) [Tech. Phys. **38**, 965 (1993)].
5. Yu. N. Venevtsev, E. D. Politova, and S. A. Ivanov, *Ferroelectrics and Antiferroelectrics in the Barium Titanate Family* (Khimiya, Moscow, 1985).
6. L. I. Dontsova, N. A. Tikhomirova, and L. A. Shuvalov, Kristallografiya **39**, 158 (1994) [Crystallogr. Rep. **39**, 140 (1994)].
7. B. M. Darinskiĭ and A. S. Sidorkin, Fiz. Tverd. Tela (Leningrad) **26**, 1634 (1984) [Sov. Phys.—Solid State **26**, 992 (1984)].
8. S. A. Sadykov and A. Sh. Agalarov, Pis'ma Zh. Tekh. Fiz. **16** (17), 32 (1990) [Sov. Tech. Phys. Lett. **16**, 655 (1990)].

Translated by A. Sidorova

Technical Physics, Vol. 45, No. 6, 2000, pp. 780–782. Translated from Zhurnal Tekhnicheskoĭ Fiziki, Vol. 70, No. 6, 2000, pp. 113–115.

BRIEF COMMUNICATIONS

Resonance Fluorescence in a Radio Frequency Field for a System of Two Nuclear Levels

V. V. Lomonosov and M. Yu. Talantov

Kurchatov Institute Russian Research Centre, pl. Kurchatova 1, Moscow, 123182 Russia

Received October 23, 1998; in final form, June 1, 1999

Abstract—The quantum-mechanical theory of resonance fluorescence in a radio frequency (RF) field is developed for a system of two mixed nuclear levels. The case when the resonant γ ray absorption is permitted only for a single level is considered. It is shown that the bare energies of nuclear states vary simultaneously with the parameters of the mixing RF field, and an additional quasilevel appears in the system. The time-dependent probabilities of the corresponding transitions are calculated. © *2000 MAIK "Nauka/Interperiodica".*

It was qualitatively shown in [1, 2] that the interference resulting from the quantum coherence of crossing Zeeman levels may significantly suppress the resonant γ ray absorption by one of them, whereas the emission probability remains significant under certain conditions. This property can be applied to the development of γ ray lasers and in other fields of γ ray optics.

The resonance fluorescence of photons at the Zeeman levels was analyzed in [3] for the case when the atomic system is affected by dc and ac magnetic fields. The temporal dynamics of the nuclear system should be described accurately taking into complete account the radiation widths of nuclear levels. In fact, the contribution of these levels can become significant.

For this purpose, we use in our paper the quantum-mechanical formalism developed in [4, 5] and used in [6] for describing the temporal dynamics of multilevel systems.

Let us consider two adjacent or degenerate nuclear levels with energies ε_1 and ε_2, and the ground state with energy ε_0 (Fig. 1). To prepare the system of this type for ^{5}Fe, the authors of [1] used dc magnetic field directed along the *EFG* axis of the quadrupole. When the magnetic field slightly deviates from this axis, the Zeeman interaction causes the mixing of levels 1 and 2 owing to the field component perpendicular to the *EFG* axis.

In contrast to this case, for mixing the levels, we use a radio frequency ac magnetic field directed perpendicular to the *EFG* axis. Thus, we consider a system of two adjacent levels under the effect of the RF magnetic field mixing these levels and an external radiation field. Let us assume that these fields are switched on simultaneously at the moment $t = 0$. This assumption allows us to describe correctly the phases of quantum states.

Following a conventional approach, we separate the system's Hamiltonian into two parts, H and H^1. The former includes nuclear effects, the RF field, and the free radiation field. The latter is related to the interaction responsible for the transitions between the pure states $|\psi_p\rangle$ of the free Hamiltonian. For the corresponding amplitudes $Q_p(t)$ of these states, we have the set of coupled equations [5]

$$i\frac{d}{dt}Q_p(t) = \sum_m Q_m(t) \times \exp[-i(\varepsilon_p - \varepsilon_m)t]\langle\psi_p|H^1|\psi_m\rangle + i\delta_{po}\delta(t), \quad (1)$$

where δ_{po} is the Kronecker delta and $\delta(t)$ is the delta-function.

The set of all possible states for the system is described by five amplitudes: (1) $A(t)$ corresponds to the ground state of a nucleus with N **s** photons having energies from the specified distribution; (2) $B_1^k(t)$ corresponds to the first excited state of the nucleus with energy ε_1 (there are $N - 1$ **s** photons, and one **k** photon with energy $\omega_{\mathbf{k}}$ is absorbed); (3) $B_2^k(t)$ corresponds to the first excited state of the nucleus with energy ε_2

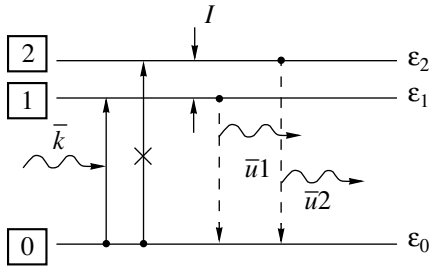

Fig. 1. The diagram illustrating the arrangement of nuclear energy levels considered in the problem of resonance fluorescence in the system with two adjacent levels in the presence of a mixing RF field *I*.

1063-7842/00/4506-0780$20.00

(there are $N-1$ **s** photons, one **k** photon with energy $\omega_{\mathbf{k}}$ is absorbed, direct transitions from the initial state to $B_2^k(t)$ are forbidden); (4) $C_1^{ku1}(t)$ corresponds to the ground state of the nucleus (there are $N-1$ **s** photons, one **k** photon is absorbed, and one **u1** photon with energy $\omega_{\mathbf{u1}}$ is emitted); (5) $C_2^{ku2}(t)$ corresponds to the ground state of the nucleus (there are $N-1$ **s** photons, one **k** photon is absorbed, and one **u2** photon with energy $\omega_{\mathbf{uz}}$ is emitted). Applying the Fourier transform to (1), we come to the following set of equations:

$$(\omega - E_0 + \omega_k + i\delta)a(\omega) = 1 + \sum_k H_k^* b_1^k(\omega), \quad (2)$$

$$\begin{aligned}(\omega - \varepsilon_1 - E_0 + \omega_k + i\delta)b_1^k(\omega) &= H_k a(\omega) \\ &+ 1/2V_{12}[b_2^k(\omega+\Omega) + b_2^k(\omega-\Omega)] \\ &+ \sum_{u1} H_{u1}^* c_1^{ku1}(\omega),\end{aligned} \quad (3)$$

$$\begin{aligned}(\omega - \varepsilon_2 - E_0 + \omega_k + i\delta)b_2^k(\omega) &= 1/2V_{21} \\ \times [b_1^k(\omega+\Omega) + b_2^k(\omega-\Omega)] &+ \sum_{u2} H_{u2}^* c_2^{ku2}(\omega),\end{aligned} \quad (4)$$

$$(\omega - \varepsilon_2 - E_0 + \omega_k - \omega_{u1} + i\delta)c_1^{ku1}(\omega) = H_{u1}^* b_1^k(\omega), \quad (5)$$

$$(\omega - \varepsilon_2 - E_0 + \omega_k - \omega_{u2} + i\delta)c_2^{ku2}(\omega) = H_{u2}^* b_2^k(\omega). \quad (6)$$

Here, all capital letters denoting the amplitudes are replaced by small letters denoting the corresponding Fourier components, E_0 is the energy of the system as a whole (further on, it is convenient to set $E_0 = 0$), δ is an infinitesimal positive parameter specifying the rule of the path tracing around the poles, H_s is the matrix element of the transition induced by the external radiation field and accompanied by absorption or emission of an **s** photon, V_{12} is the matrix element of transitions between levels *1* and *2* induced by the RF field (below, we assume that $V_{12} = V_{21} = V$), and Ω is the frequency of the RF magnetic field. Solving set (2)–(6) at large Ω (the actual small parameter will be specified below), we derive

$$a(\omega) = 1/(\omega + i\Gamma_0), \quad (7)$$

$$\begin{aligned}b_1^k(\omega) &= \\ &= \frac{H_k(\omega+\Omega-\varepsilon_2+\omega_k+i\gamma_2)(\omega-\Omega-\varepsilon_2+\omega_k+i\gamma_2)}{(\omega-E_1+\omega_k)(\omega-E_2+\omega_k)(\omega-E_3+\omega_k)(\omega+i\Gamma_0)},\end{aligned} \quad (8)$$

$$b_2^k(\omega) = \frac{V}{2}\frac{b_1^k(\omega+\Omega) + b_1^k(\omega-\Omega)}{\omega - \varepsilon_2 + \omega_k + i\gamma_2}, \quad (9)$$

$$c_{1(2)}^{ku1(u2)}(\omega) = \frac{H_{u1(u2)}^* b_{1(2)}^k(\omega)}{\omega - \varepsilon_2^k - \omega_{u1(u2)} + \omega_k + i\varepsilon}. \quad (10)$$

Here, Γ_0 is the half-width of the initial state or the absorption probability that can be set constant, and γ_1 and γ_2 are the half-widths of the corresponding levels defined in the standard way [5]. We assume that condition $\Gamma_0 < \gamma_1, \gamma_2$, usual for such a problem, is met. The energies in (8) are the solutions to a cubic equation. Under the condition $(\Delta\varepsilon_{12} + \Delta\gamma_{12})/(V^2 + \Omega^2) \ll 1$, they have a simple form

$$\begin{aligned}\Delta\varepsilon_{12} &= \varepsilon_2 - \varepsilon_1, \quad \Delta\gamma_{12} = \gamma_2 - \gamma_1, \\ E_1 &= \varepsilon + (1/6)\Delta\varepsilon_{12}(1 + 2F(V,\Omega)) \\ &- i(\gamma + 1/6)\Delta\gamma_{12}(1 + 2F(V,\Omega)),\end{aligned} \quad (11)$$

$$\begin{aligned}E_{23} &= \varepsilon \pm (1/6)\Delta\varepsilon_{12} \pm [\Omega^2 + V^2/2]^{1/2} \\ &- i(\gamma + (1/6)\Delta\gamma_{12}),\end{aligned} \quad (12)$$

where $\varepsilon = (\varepsilon_1 + \varepsilon_2)/2$, $\gamma = (\gamma_1 + \gamma_2)/2$, and $F(V, \Omega) = (2\omega^2 - V^2/2)(\Omega^2 + V^2/2)$.

Expressions (7)–(12) determine a solution to set (2)–(6) under the condition $\omega \gg |E_j(V,\Omega) - \omega_k|$ ($j = 1$–3). In this case, additional level E_1 arises in the system. If we just formally set $\Omega = 0$ in equations (7)–(11) and replace $V^2/2 \longrightarrow V$ in (11)–(12), then the expressions for the corresponding amplitudes will coincide with those governing the temporal dynamics in the constant magnetic field.

After transition to the time representation for state amplitudes (7)–(10), the normalization condition can be written in the following form:

$$\begin{aligned}|A(t)|^2 + \sum_k |B_1^k(t)|^2 + \sum_k |B_2^k(t)|^2 \\ + \sum_k \sum_{u1} |C_1^{u1}(t)|^2 + \sum_k \sum_{u2} |C_2^{u2}(t)|^2 = 1.\end{aligned} \quad (13)$$

Let us perform the summation over all energies of **k** photons from the initial distributions for the case of a broad line retaining unchanged the energies of emitted photons. We find

$$\begin{aligned}|A(t)|^2 + |B_1(t)|^2 + |B_2(t)|^2 \\ + \sum_{u1} |C_1^{u1}(t)|^2 + \sum_{u2} |C_2^{u2}(t)|^2 = 1.\end{aligned} \quad (14)$$

The time dependence of modules squared for the calculated amplitudes characterizes the dynamics of the corresponding states. It is presented in Fig. 2 for several realistic values of parameters.

In conclusion, let us briefly discuss the obtained results. Note first that the external radiation field and

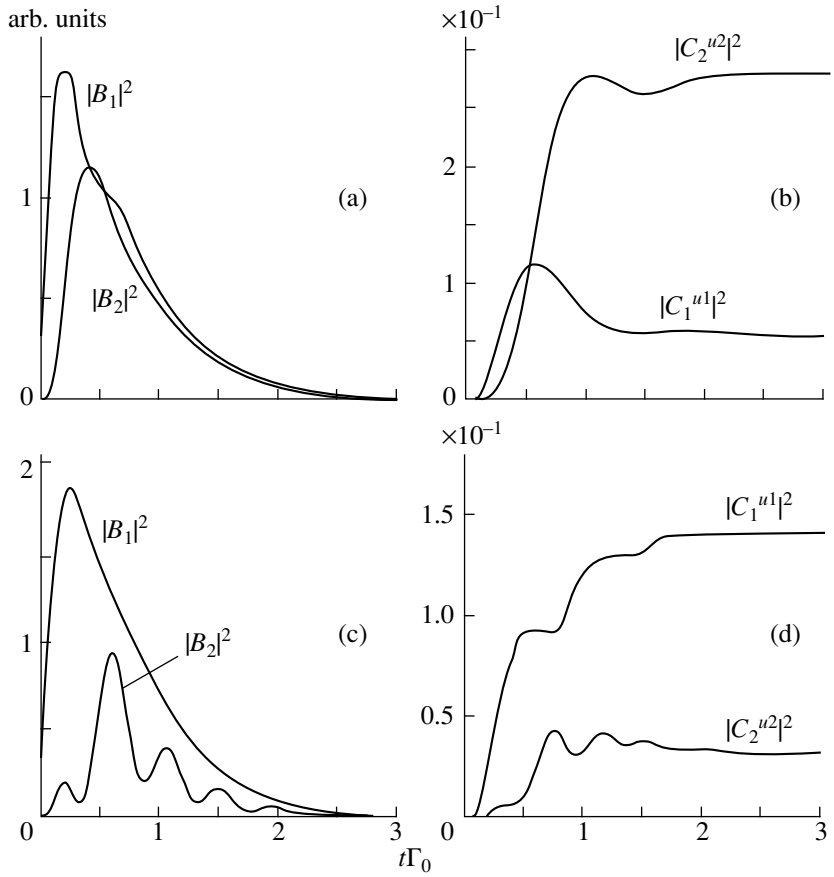

Fig. 2. Time dependences of moduli squared for amplitudes $|B_1(t)|^2$, $|B_2(t)|^2$, $|C_1^{u1}(t)|^2$, and $|C_2^{u2}(t)|^2$. $\varepsilon_1 = \varepsilon_2 = \varepsilon = 1.44 \times 10^{12}\Gamma_0$, $\gamma_1 = \gamma_2 = \gamma = 2.2\Gamma_0$, $v = 5\Gamma_0$, $\omega_{u1} = \omega_{u2} = \omega_u$, $\omega_u - \varepsilon = 1 \times 10^{-1}\Gamma_0$; $\Omega = 0$ (a, b) and $7\Gamma_0$ (c, d).

the RF field simultaneously switched on because of not only of a pushing apart of bare nuclear levels *1* and *2*, but also the creation of an additional level disappearing in the limiting case of the constant field at $\Omega = 0$. In addition, expressions (11) and (12) demonstrate the dependence of the features characterizing the arising states on the RF field parameters. This result can be used for the control and for providing the favorable development of experimental situation. Note also that the behavior of quantum-emission probabilities $|C_1^{u1}(t)|^2$ and $|C_2^{u2}(t)|^2$ (Figs. 2b, 2d) strongly depends on the photon energy.

ACKNOWLEDGMENTS

This work was supported by the Russian Foundation for Basic Research, project no. 98-02-16729.

REFERENCES

1. R. Coussement, M. van Den Bergh, G. S'heeren, *et al.*, Hyperfine Interact. **80**, 1307 (1993).
2. R. Coussement, M. van Den Bergh, G. S'heeren, *et al.*, Phys. Rev. Lett. **71**, 1824 (1993).
3. N. B. Delone, V. P. Kraĭnov, and V. A. Khodovoĭ, Usp. Fiz. Nauk **117** (1), 187 (1975) [Sov. Phys. Usp. **18**, 749 (1975)].
4. V. Weisskopf and E. Wigner, Z. Phys. **63**, 54 (1930).
5. W. Heitler, *The Quantum Theory of Radiation* (Clarendon Press, Oxford, 1954; Inostrannaya Literatura, Moscow, 1956).
6. V. V. Lomonosov and M. Yu. Talantov, Zh. Éksp. Teor. Fiz. **105** (2), 271 (1994) [JETP **78**, 144 (1994)].

Translated by K. I. Kugel

Technical Physics, Vol. 45, No. 6, 2000, pp. 783–785. Translated from Zhurnal Tekhnicheskoĭ Fiziki, Vol. 70, No. 6, 2000, pp. 116–118.

BRIEF COMMUNICATIONS

Preparation of Monolayers of Nanoparticles for Transmission Electron Microscopy

A. B. Vorob'ev, A. K. Gutakovskiĭ, V. Ya. Prinz, and V. A. Seleznev

Institute of Semiconductor Physics, Siberian Branch, Russian Academy of Sciences, Novosibirsk, 630090 Russia

Received November 16, 1998; in final form, December 8, 1999

Abstract—A novel procedure of sample preparation for transmission electron microscopy of nanoparticles is proposed yielding a monolayer of nanoparticles. The procedure offers the possibility of sorting nanoparticles by size and studying the influence of external fields on their arrangement. This technology can also be applied for the creation of ordered arrays of nanoparticles in ultrathin polymer films. © *2000 MAIK "Nauka/Interperiodica".*

High-resolution transmission electron microscopy (HRTEM) is the only technique for direct study of the structure of nanoparticles and nanoobjects on an atomic scale. Usually, ultradisperse materials for transmission microscopy are prepared by deposition on an object net (by sputtering or placing a drop of colloid solution). With all its simplicity, this procedure has a serious drawback, namely, the impossibility of obtaining a monolayer of nanoparticles, which is required for studying their structure. In this paper, we propose a procedure of sample preparation for the transmission electron microscopy of nanoparticles, which affords the possibility of (1) forming a monolayer of nanoparticles; (2) grading of nanoparticles by size; (3) studying the influence of external electric and magnetic fields on the arrangement of nanoparticles.

Magnetite (Fe_3O_4) nanoparticles were chosen for this study. Two alternative methods of sample preparation were used. In the simpler of the two methods, cracks in the [110] direction were produced in 300–400 μm-thick standard GaAs substrates by a mechanic indenter. Since cracking of gallium arsenide in this case occurs along cleavage planes, the crack has perfectly straight boundaries and its width smoothly decreases from the mouth of the crack to its apex. Then, a drop of suspension of the magnetite nanoparticles in solution of polystyrene solution in toluene is placed in the crack. Due to capillary forces, the solution containing nanoparticles fills the crack and after the drying of the solvent, a polystyrene film with embedded magnetite particles forms inside the crack. The crack volume acts as a "mould." Since the width of the formed crack is comparable with the size of particles (hundreds and tens of angstroms) [1], the particles are forced to arrange as a monolayer. Furthermore, because of the gradual decrease of the crack width, down to several angstroms near the apex, only the smallest particles can be accommodated close to the apex. Therefore, size grading of the particles along the crack takes place. It should be noted that the time of solvent evaporation is long because of the small area of contact with air; therefore, it is possible to influence particle distribution along the crack by application of external electric or magnetic fields. After solvent evaporation, the particles are found rigidly fixed in a polymer matrix and retain their mutual arrangement after removal of the field. In order to make the polymer film with embedded nanoparticles suitable for microscopy, the GaAs wafer was cleaved carefully along the crack and the film lifted off by its edges. The lifting-off was carried out in a liquid (water or alcohol), whence it was picked up by an object net and dried.

In the HRTEM images (Fig. 1), separate crystalline particles with lateral dimensions 40–200 Å and their agglomerates are seen. The lattice stripes of these particles correspond to the cubic structure of magnetite. Stripes corresponding to the {111} planes (the distance between stripes is 4.8 Å), {200} (4.2 Å), and {220} (2.9 Å) were observed.

A drawback of such an approach is the risk of damaging the film during lift-off as well as a rather small area of the portion of the film where its thickness is less than 400 Å thick and transparent to an electron beam, because cracks in thick GaAs wafers have small enough width only in a small region near the apex. Therefore, it is preferable to use as a "mould" cracks in thin (<10 μm) epitaxial GaAs films in which thin, ideally level crevices with sharp near-atomically-flat boundaries can be created [1].

In the second case, epitaxial GaAs/AlAs structures were used for sample preparation. On a GaAs substrate, a thin (100 Å) AlAs layer was grown and, atop of it, a GaAs layer of a thickness between 2–10 μm in different structures. The GaAs film was undercut and lifted off the substrate by a selective HF : H_2O etchant, which removed AlAs (the ratio of etching rates of AlAs and GaAs is more than 10^9 [2]). Then, a rectangular sample was cleaved out of the film (instead of cleaving photolithography can be used). A narrow crack was made in

1063-7842/00/4506-0783$20.00

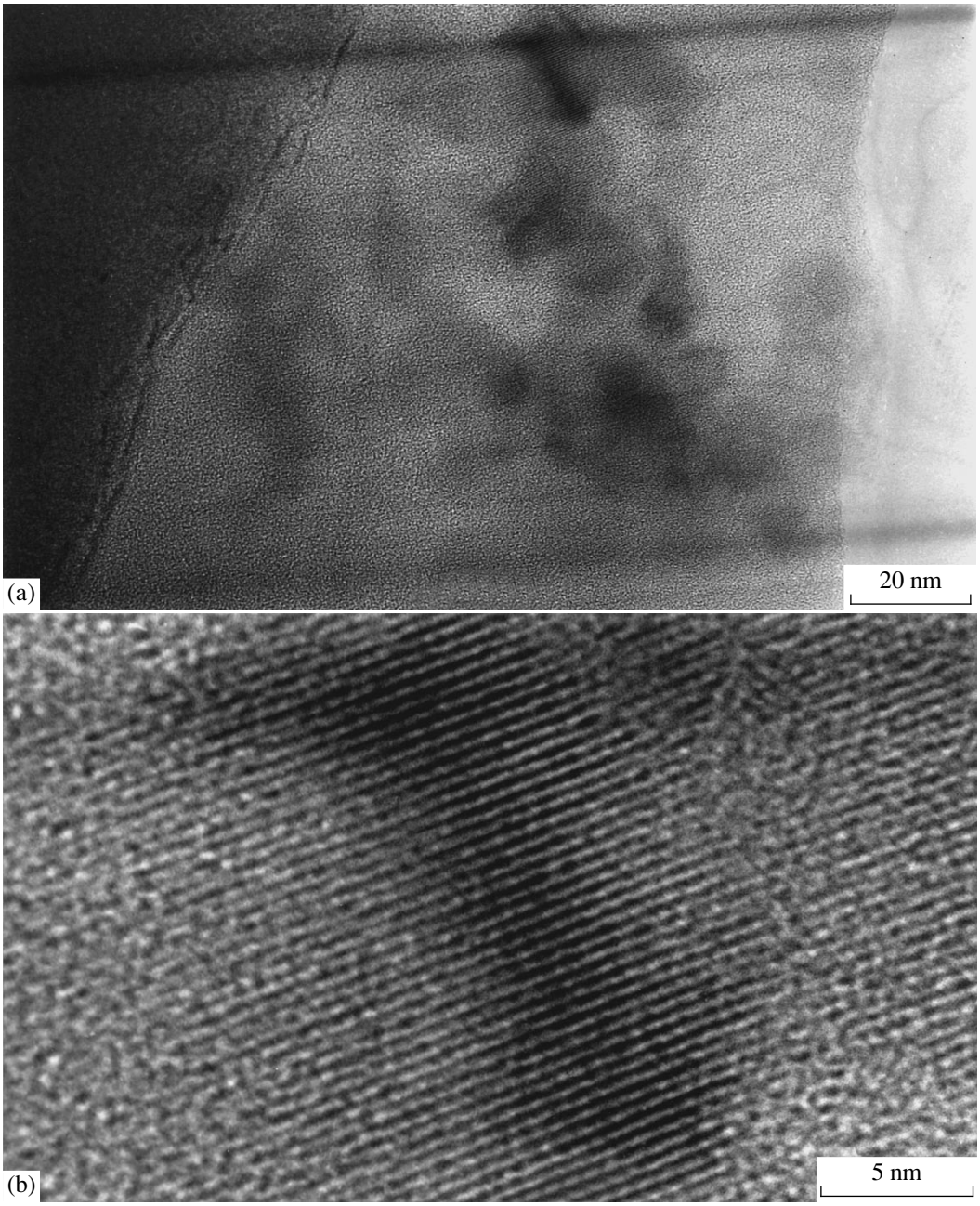

Fig. 1. (a) Electron microscopy image (dark field) of magnetite nanoparticles in a polymer film and (b) a part of an image in *a* (at higher magnification). A separate particle with lattice stripes associated with the {111} planes is seen.

the sample with a mechanical indenter parallel to its long side. Load on the indenter was gradually increased until the crack apex reached the center of the sample. Then, the sample with the produced crack was cemented by a conducting glue to a standard copper ring in such a way that the crack was above the ring opening. The sample plane was perpendicular to the ring plane while the direction of the crack was parallel to it. To manipulate the sample, we used a waxed needle.

For filling of the crack capillary, an iron oxide colloid solution in toluene with an addition of polystyrene was used. After toluene evaporation, the sample was immersed in an $H_3PO_4 : H_2O_2 : H_2O$ (3 : 1 : 50) etch for one and a half minutes. On both sides of the GaAs, film layers of a thickness of about 0.1 μm were etched away to partially expose the polystyrene film and, thereby, render it suitable for examination in a transmission electron microscope (Fig. 2). Immediately after etching, the sample was rinsed in isopropanol and then

dried in air. Water should not be used for rinsing since it has a rather high surface tension and while drying, it would break exposed edges of the thin polymer film.

In HRTEM experiments with such samples, we examined polymer films with embedded crystalline particles transparent to an electron beam. The film was jutting out of the GaAs wafer on both sides and had no damage over several hundreds of micrometers. Compared with the first case, the particle size distribution was narrower (70–100 Å), more uniform over the film area, without large agglomerates and with the particles arranged as a monolayer, at nearly equal distances from each other (about 200 Å). The thinnest part of the film was free of particles, which can be explained by insufficient crack width for particle penetration (the crack acts as a filter). It should be noted that image registration was hampered by drift and vibration of samples due to charge accumulation. This problem can be overcome using heavily doped GaAs films, which provide better electric contact between the polymer film and the copper ring.

The proposed procedure yields monolayer arrays of nanoparticles. Such objects are of interest not only for structural studies, but for transport studies as well. Nanoparticles are found sandwiched between crack sides in a semiconductor monocrystal, which can act as closely spaced electrodes if doped GaAs films are used. An influence of external electric and magnetic fields can further modify the properties of nanoparticle array due to formation of ordered structures. As an example, let us consider the magnetite Fe_3O_4 particles. At sizes less than 100 Å, they exhibit superparamagnetic properties. Alignment of their own magnetic moments follows the direction of the externally applied magnetic field. By placing a thin film with embedded superparamagnetic particles into a strong-enough magnetic field, two-dimensional arrays of identically oriented magnetic dipoles can be created. If the particles have a possibility to move in the film plane (before evaporation of the solvent from the crack), the interaction of magnetic dipoles can result in ordered arrangement of particles in the film, which will be retained after removal of the field, since the particles will be rigidly fixed in the polymer.

To conclude, a novel procedure of sample preparation for transmission electron microscopy of nanoparticles is proposed by which, in contrast to the standard technique, it is possible to obtain a monolayer of particles, as demonstrated in the example of iron oxide particles, as well as to grade them by size (filtration) and to study the influence of external fields on their arrangement. The procedure is suitable for particles from hundreds of angstroms down to several angstroms in size. The technological solutions used can be applied for the fabrication of structures containing ordered arrays of nanoparticles in a polymer matrix.

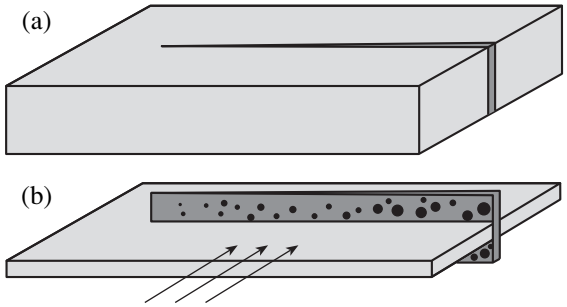

Fig. 2. Scheme of the sample preparation procedure for transmission electron microscopy: (a) the narrow crack creates a "mould" in the GaAs film, which is then filled with a colloid solution of nanoparticles with added polymer; (b) chemical etch of GaAs partially exposes the polymer film with nanoparticles making it suitable for electron beam microscopy (arrows show beam direction).

ACKNOWLEDGMENTS

The authors thank Yu. V. Butenko, V. L. Kuznetsov, and A. B. Sharoĭ for providing ultradisperse iron oxide samples for the study.

The study was supported in part by the Russian Foundation for Basic Research (grant no. 97-02-18479) and by the State research and development program "Promising Technologies and Devices for Micro- and Nanoelectronics" (project no. 208/67).

REFERENCES

1. V. Ya. Prinz, V. A. Seleznev, and A. K. Gutakovskiĭ, Surf. Sci. **361/362**, 886 (1996).
2. E. Yablonovitch, T. Gmitter, T. Harbison, and J. Bhat, Appl. Phys. Lett. **51**, 2222 (1987).

Translated by M. V. Lebedev

Technical Physics, Vol. 45, No. 6, 2000, pp. 786–788. Translated from Zhurnal Tekhnicheskoĭ Fiziki, Vol. 70, No. 6, 2000, pp. 119–121.

BRIEF COMMUNICATIONS

Pseudoelasticity of the Ti–Ni Alloy Subjected to Omnidirectional Pressure

S. A. Egorov and I. N. Lobachev

Smirnov Institute of Mathematics and Mechanics, St. Petersburg State University (Petrodvorets Branch), Universitetskiĭ pr. 2, Petrodvorets, 198904 Russia

Received April, 19, 1999

Abstract—Under certain (not just any) conditions, omnidirectional pressure applied to the Ti–Ni alloy is shown to change its superelastic properties, similar to the application of deforming force. © *2000 MAIK "Nauka/Interperiodica".*

It is known that the application of omnidirectional pressure to materials prone to thermoelastic martensite transformation may cause various deformational and force phenomena, such as transformation plasticity, shape-memory effect, reversible shape-memory effect on temperature cycling, and the generation and relaxation of reactive stresses [1–3]. However, the influence of pressure on superelasticity yet remains a mystery. Investigation into this effect appears to be topical since it would provide a better insight into martensite inelasticity in general and superelasticity in particular. In this work, we studied the effect of pressure on the superelasticity of the Ti–Ni alloy prone to thermoelastic martensite transformation.

Tests were performed in a high-pressure chamber (Fig. 1). Cantilevered specimen *1* 15 mm long and 1.8 mm in diameter is loaded by steel spring [2]. The displacement of the upper end of the spring was controlled by screw *3* with a pitch of 0.5 mm, and that of the lower end (or the bend of the free end of specimen *1*) was determined with slide-wire rheostat *4*, connected to digital ohmmeter *5*. From these two displacements, one can easily calculate the force experienced by specimen *1* from spring *2*. Our test chamber admits loading to 100 N. Unloading can be accomplished irrespective of the operating pressure, which ranged from atmospheric to 240 MPa. Machine oil was used as a working liquid. Absolute errors in measuring the force F and the bend f of the free end of the specimen with the spring–rheostat system were found to be 2 N and 0.06 mm, respectively. The temperature inside the chamber was varied from room temperature to 360 K by heating the body of the chamber with heater *6*.

All experiments were performed in the temperature interval 335–337 K. The desired temperature was set after 3-h heating. Due to the high thermal inertia of the chamber (the weight of the liquid-filled chamber is 80 kg), the temperature was maintained within 1 K throughout the experiment.

Test objects were specimens of the $Ti_{44.2}Ni_{54.4}Co_{0.52}Cr_{0.43}$ alloy. As-prepared specimens were annealed at 750 K for 40 min and cooled first to 290 K in the furnace and then to liquid-nitrogen temperature. The same procedure was applied after each run.

Thermomechanic atmospheric-pressure torsion tests showed that cooling and heating under a constant shear stress of 60 MPa lead to the transformation plasticity effect and the shape memory effect with the participation of an intermediate phase (possibly, R-phase [4]). The characteristic temperatures are M_s = 345 K, M_f = 265 K, A_s = 303 K, and A_f = 416 K.

The experiments were subdivided into three groups. In the first group, we studied the effect of omnidirectional pressure on the pseudoelastic properties of the Ti–Ni alloy. After the specimen had been placed in the high-pressure chamber and the temperature had been brought to 335–337 K under atmospheric pressure, we applied to it a force P and recorded the deformation. At a certain value of P, the pressure p was raised to 200 MPa at a rate of 6 MPa/min. As the pressure grew, the deformation was built up in the direction of the

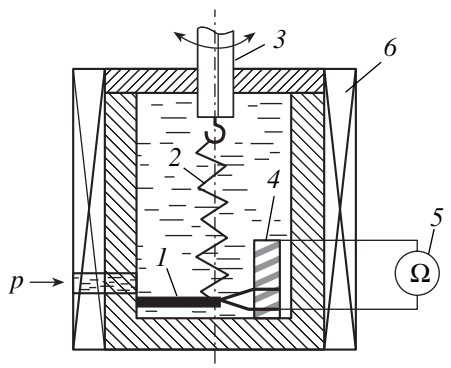

Fig. 1. High-pressure chamber: (*1*) specimen; (*2*) elastic spring; (*3*) measuring screw; (*4*) slide-wire rheostat; (*5*) ohmmeter; and (*6*) furnace.

1063-7842/00/4506-0786$20.00 © 2000 MAIK "Nauka/Interperiodica"

applied force, so that the bend f increased by 0.2–0.4 mm. At p = 200 MPa, we loaded the specimen again and recorded deformation buildup.

At f = 4–7 mm, the specimen was unloaded to some value of P and the pressure was decreased to atmospheric. In response to the pressure drop, f additionally went down by 0.2–0.4 mm in proportion to p. With further unloading, the specimen behaved in a usual manner for these conditions. A typical curve is shown in Fig. 2, where portions *AB*, *BC*, *CD*, *DE*, *EF*, and *FM* correspond to different stages of the experiment. As follows from this figure, a pressure increase at the loading stage results in a deformation buildup (portion *BC*) and a pressure drop at the unloading stage leads to additional deformation recovery (portion *EF*). It is noteworthy that these baromechanic effects are absent if the pressure is varied at the elastic portions of the $f(P)$ curve. This holds for both load increase and decrease.

In the second group of experiments, the specimen was placed in the chamber at 290 K, the pressure was raised to 200 MPa, the specimen was heated to 335–337 K and loaded by some value of *P*, and then the pressure was decreased to atmospheric. The pressure drop was found to be accompanied by severe material disordering (the deformation force became 5 to 15 N, or 15 to 50%, smaller). The value of f increased by 0.5–1.0 mm in proportion to the pressure variation. Further atmospheric-pressure loading deformed the specimen. This is illustrated in Fig. 3a, where portions *AB*, *BC*, and *CD* describe the different behavior of the Ti–Ni alloy under loading.

In subsequent experiments from the second group, the specimen was deformed by f = 5 mm under atmospheric pressure at 337 K, then it was unloaded to some value of *P*, and the pressure was raised to 200 MPa (Fig. 3b). In this case, the pressure rise causes deformation buildup, and f linearly increases with pressure by 0.2–0.4 mm (portion *BC*). In other words, in this case, the pressure increase reverses the sign of deformation relative to that before the pressure conditions were changed (note that the pressure rise at the elastic stage of unloading does not deform the material). The further decrease in P under a pressure of 200 MPa leads to usual pseudoelastic recovery.

The obtained results suggest that pressure cycling at the loading stage deforms the specimen at each cycle. This supposition was verified with the third group of experiments. The specimen was inelastically deformed at 336 K, and at some *P*, the pressure was raised to 200 MPa and then decreased to atmospheric. At each pressure cycle, the deformation builds up the deformation (Fig. 4a). Portions *BC* and *CD* refer to the pressure increase and decrease, respectively. Thus, our supposition proved to be valid.

Our data indicate that both an increase and a decrease in pressure cause material deformation at both the loading and unloading stages. However, the behavior of the material depends on which stage the pressure

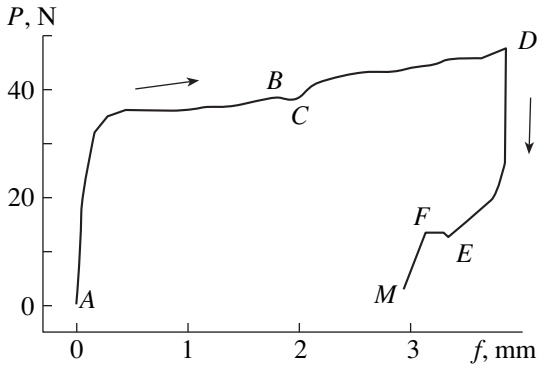

Fig. 2. Deforming force vs. bend under constant atmospheric pressure (portions *AB* and *FM*), for an increase in the pressure from atmospheric to 200 MPa (portion *BC*), under the constant pressure 200 MPa (portion *CDE*), and for a decrease in pressure from 200 MPa to atmospheric (portion *EF*).

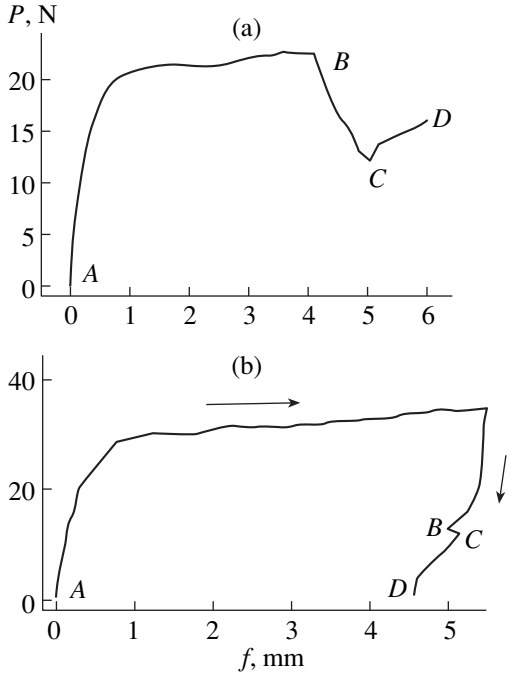

Fig. 3. $P(f)$ curves under different pressure conditions. (a) *AB*, constant pressure 200 MPa; *BC*, pressure drops from 200 MPa to atmospheric; and *CD*, constant atmospheric pressure. (b) *AB*, constant atmospheric pressure; *BC*, pressure rises from atmospheric to 200 MPa; and *CD*, constant pressure 200 MPa.

changes and the sign of change of pressure. The reason for such an unusual effect has not yet been fully understood. It seems likely that a pressure change induces various transformations depending on its sign. In the alloy under study, the direct and reverse martensite transformations involve the intermediate *R*-phase. If the $B2 \rightleftharpoons R$ and $R \rightleftharpoons B19'$ transformations have the opposite signs, a change in pressure in one direction may induce one phase transition, while a change in the

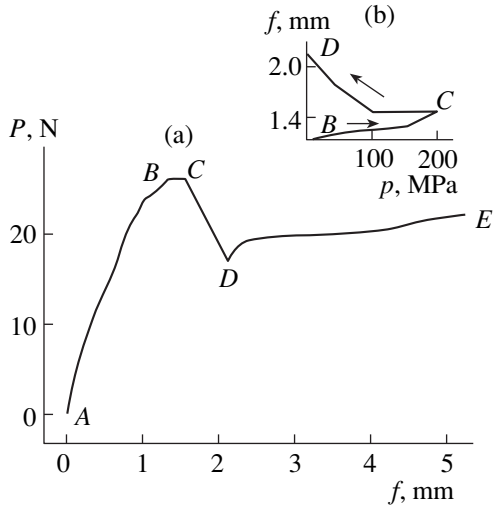

Fig. 4. (a) Deforming force vs. bend under different pressure conditions and (b) bend vs. pressure. *AB* and *DE*, constant atmospheric pressure; *BC*, pressure rises from atmospheric to 200 MPa; and *CD*, pressure drops from 200 MPa to atmospheric.

other direction may cause the other transition (according to the Clausius–Clapeyron equation). A comparison of Figs. 3a and 4b favors the afore-said. In the latter case, the decrease in pressure immediately after its rise from atmospheric to 200 MPa initiates deformation only at 100 MPa, while the $f(P)$ curve in Fig. 3a is almost linear.

The reason for the softening of the material due to pressure increase at the unloading stage (Fig. 3b) also remains unclear. If, at the loading stage, a pressure decrease initiates some phase transition ($B2 \rightleftharpoons R$ or $R \rightleftharpoons B19'$), as a result of which the material considerably softens (Fig. 3a), one might expect that, at the unloading stage, a pressure rise will cause reverse transition and, accordingly, the hardening of the alloy. Instead, the material softens, as demonstrated in the experiments. This suggests that the effect of pressure on the superelastic behavior of the material is not fully identical to that of a deforming force. This point calls for further investigation.

Our experimental results can be summarized as follows.

(1) In the Ti–Ni alloy studied in this work, an increase in pressure at the stage of loading results in a deformation buildup. At the stage of unloading, a decrease in pressure causes pseudoelastic recovery. In these cases, the effect of pressure on the superelastic properties of the material is identical to that of deforming force.

(2) A decrease in pressure at the stage of pseudoelastic deformation buildup and a rise in pressure at the stage of pseudoelastic recovery lead to a softening of the material.

(3) Our findings indicate that the effect of omnidirectional pressure on the superelasticity of the Ti–Ni alloy is not fully identical to that of a deforming force.

ACKNOWLEDGMENTS

The authors are indebted to A. E. Volkov for his valuable consultations.

This work was supported by the school of thought of Academician V. V. Novozhilov.

REFERENCES

1. S. P. Belyaev, S. A. Egorov, V. A. Likhachev, and O. E. Ol'khovik, Zh. Tekh. Fiz. **66** (11), 36 (1996) [Tech. Phys. **41**, 1102 (1996)].
2. V. A. Likhachev, S. P. Belyaev, and S. A. Egorov, in *Proceedings of the XXXII Seminar "Topical Problems of Strength," St. Petersburg, Russia, 1997*, p. 171.
3. S. P. Belyaev, S. A. Egorov, and I. N. Lobachev, in *Proceedings of the I Seminar "Topical Problems of Strength" dedicated to V. A. Likhachev*; in *Proceedings of the XXXIII Seminar "Topical Problems of Strength," Novgorod, Russia, 1997*, Vol. 2, Part 1, p. 60.
4. V. N. Khachin, V. G. Pushchin, and V. V. Kondrat'ev, *Titanium Silicide: Structure and Properties* (Nauka, Moscow, 1992).

Translated by V. A. Isaakyan

Technical Physics, Vol. 45, No. 6, 2000, pp. 789–793. Translated from Zhurnal Tekhnicheskoĭ Fiziki, Vol. 70, No. 6, 2000, pp. 122–125.

BRIEF COMMUNICATIONS

Linear Dispersion and Solitons in a Liquid-Filled Cylindrical Shell

A. N. Koren'kov

Received March 18, 1999

Abstract—The case of linear dispersion is investigated and a soliton solution is constructed for the problem of wave propagation in a system consisting of a liquid-filled elastic cylindrical shell. The dependence of the solution on the parameter characterizing the mutual influence of the shell and the liquid inside it is studied. *© 2000 MAIK "Nauka/Interperiodica".*

BASIC EQUATIONS

This paper considers the problem of wave propagation in a physical system consisting of an infinitely long circular cylindrical shell filled with an ideal incompressible liquid. The nonlinear equations that describe the dynamics of a membrane cylindrical shell in the coordinate system (r, z, φ) have the following dimensionless form [1]

$$\frac{\partial T_1}{\partial z} = \frac{\partial^2 u}{\partial t^2}, \quad T_2 - \frac{\partial^2 w}{\partial z^2} T_1 + \frac{\partial^2 \omega}{\partial t^2} = \gamma^2 p,$$

$$T_1 = \frac{\partial u}{\partial z} + \nu w + \frac{1}{2}\left[\left(\frac{\partial u}{\partial z}\right)^2 + \left(\frac{\partial w}{\partial z}\right)^2 + \nu w^2\right], \qquad (1)$$

$$T_2 = w + \nu\frac{\partial u}{\partial z} + \frac{1}{2}\left[w^2 + \nu\left(\left(\frac{\partial u}{\partial z}\right)^2 + \left(\frac{\partial w}{\partial z}\right)^2\right)\right],$$

where $\gamma^2 = R\rho_0/h\rho$; R is the shell radius; h is the shell thickness; ρ is the density of the shell material; ν is Poisson's ratio; ρ_0 is the density of liquid; u, v, and w, are the vector components of the shell surface displacement; and p is the pressure at the shell surface.

The Euler equations [2] have the form

$$\frac{\partial^2 \varphi}{\partial t \partial r} + \frac{\partial \varphi}{\partial r}\frac{\partial^2 \varphi}{\partial r^2} + \frac{\partial \varphi}{\partial z}\frac{\partial^2 \varphi}{\partial r \partial z} = -\frac{\partial p}{\partial r},$$
$$\frac{\partial^2 \varphi}{\partial t \partial z} + \frac{\partial \varphi}{\partial r}\frac{\partial^2 \varphi}{\partial r \partial z} + \frac{\partial \varphi}{\partial z}\frac{\partial^2 \varphi}{\partial z^2} = -\frac{\partial p}{\partial z}. \qquad (2)$$

Here, p is the pressure in liquid and $\varphi(r, z, t)$ is the velocity potential: $u = \mathrm{grad}\varphi$. The velocity potential satisfies the continuity equation

$$\frac{1}{r}\frac{\partial}{\partial r}\left[r\frac{\partial \varphi}{\partial r}\right] + \frac{\partial^2 \varphi}{\partial z^2} = 0. \qquad (3)$$

At the shell surface ($r = 1$), the normal component of the velocity of liquid is related to the transverse displacement by the no-leak condition

$$u_r(1, z, t) = \left.\frac{\partial \varphi}{\partial r}\right|_{r=1} = \frac{\partial w}{\partial t}. \qquad (4)$$

We assume that, at infinity $z \longrightarrow +\infty$, the shell is not moving, and the motion of liquid is unperturbed: $u_r = u_z = 0$, $p = 0$. The system of equations (1)–(4) forms a contact problem of hydroelasticity. This problem contains the dimensionless parameter γ characterizing the degree of the mutual influence of the shell and the liquid. We will call this parameter the coupling parameter of the problem.

LINEAR DISPERSION

Below, we construct the solutions to the contact problem (1)–(4) in the form of low-amplitude nonlinear waves with an infinite period. The leading term of the expansion of the phase velocity of such waves in powers of the small parameter (amplitude) coincides with the phase velocity of linear waves. To determine the latter quantity, we construct a dispersion relation that corresponds to the linearized problem.

We assume that the dependence of all functions on the z coordinate and the time t has the form $\exp[i(\kappa z - \omega t)]$, where κ is the wave number and ω is the cyclic frequency of the oscillations. The phase velocity of the wave is determined by the expression $c = \omega/\kappa$.

From the condition of the existence of nontrivial solutions to the linearized system (1)–(4), we derive the dispersion relation

$$c^4(\kappa^2 + \gamma^2\delta) - c^2(1 + \kappa^2 + \gamma^2\delta) + (1 - \nu^2) = 0,$$
$$\delta(\kappa) = \kappa I_0(\kappa)/I_1(\kappa). \qquad (5)$$

1063-7842/00/4506-0789$20.00

Here, $I_0(\kappa)$ and $I_1(\kappa)$ are the Bessel functions of the first kind. Equation (5) has two positive roots c_1^2 and c_2^2. Thus, for every wave number, there exist two waves propagating with the phase velocities c_1 and c_2 in the positive or negative direction.

By formally setting $\gamma = 0$ in equation (5), we obtain the dispersion relation corresponding to a "dry" shell. If $\kappa \ll 1$, i.e., only long-wave oscillations are considered, the roots of this equation take the form

$$c_1^2 = 1 - \nu^2 + O(\kappa^2),$$

$$c_2^2 = 1/\kappa^2 + O(1).$$

Let us study the dependence of the phase velocities c_1 and c_2 on the coupling parameter of the problem γ with allowance for the fact that $\delta(\kappa) = O(1)$ for $0 \le \kappa < \infty$. The case $\gamma \ll 1$ at $\kappa = O(1)$ reduces to the study of the dispersion relation for the "dry" shell. When $\kappa \longrightarrow 0$, equation (5) singularly degenerates. The root c_1^2 is determined by the same expression as above, whereas the root c_2^2 depends on the relation between the parameters γ and κ.

Now, we consider the case $\gamma \longrightarrow \infty$. We seek the solutions to equation (5) in the form of expansions in inverse powers of γ^2. Then, we obtain

$$c_1^2 = \gamma^{-2}(1-\nu^2)(1/\delta - \gamma^{-2}(\kappa^2+\nu^2)/\delta^2 + O(\gamma^{-4})),$$
$$c_2^2 = 1 + \gamma^{-2}\nu^2/\delta + O(\gamma^{-4}).$$

These representations are uniform in κ.

For the case of the propagation of long ($\kappa \ll 1$) waves, we assume that $\gamma = O(1)$ and seek the phase velocity in the form of a series expansion in powers of κ^2. Then, within $O(\kappa^2)$, the phase velocity is determined from the equation

$$2\gamma^2 c^4 - (1-2\gamma^2)c^2 + (1-\nu^2) = 0.$$

The discriminant of this equation is positive, and the equation has two positive roots, which satisfy the inequalities $0 \le c_1^2 \le 1-\nu^2$ and $1 \le c_2^2$.

WAVES WITH AN INFINITE PERIOD

We consider the propagation of long waves with low amplitude. To construct the leading term of the asymptotic expansion of the solution, we use the formal small parameter ε and introduce new variables $\xi = \varepsilon(z - ct)$ and $\eta = \varepsilon^3 t$. We seek the solution to the problem in the form

$$w(\xi,\eta) = \varepsilon^2[w^{(0)}(\xi,\eta) + \varepsilon^2 w^{(1)}(\xi,\eta) + O(\varepsilon^4)],$$

$$u(\xi,\eta) = \varepsilon[u^{(0)}(\xi,\eta) + \varepsilon^2 u^{(1)}(\xi,\eta) + O(\varepsilon^4)],$$

$$T_i(\xi,\eta) = \varepsilon^2[T^{(0)} - i(\xi,\eta) + \varepsilon^2 T_i^{(1)}(\xi,\eta) + O(\varepsilon^4)],$$
$$p(r,\xi,\eta) = \varepsilon^2[p^{(0)}(r,\xi,\eta) + \varepsilon^2 p^{(1)}(r,\xi,\eta) + O(\varepsilon^4)], \quad (6)$$

$$\varphi(r,\xi,\eta) = \varepsilon[\varphi^{(0)}(r,\xi,\eta) + \varepsilon^2\varphi^{(1)}(r,\xi,\eta) + \varepsilon^4\varphi^{(2)}(r,\xi,\eta) + O(\varepsilon^6)].$$

Note that, to obtain the first approximation to the solution, we have to consider the expansion of the velocity potential up to the term $\varphi^{(2)}$ inclusive. We substitute expansions (6) in equations (1)–(4) and set the coefficients multiplying identical powers of ε equal to zero. Then, the continuity equation (3) yields

$$\frac{1}{r}\frac{\partial}{\partial r}\left[r\frac{\partial\varphi^{(n)}}{\partial r}\right] = -\frac{\partial^2\varphi^{(n-1)}}{\partial\xi^2}; \quad n = 0, 1, 2. \qquad (7)$$

Here, we assume that $\varphi^{(-1)} = 0$. System (7) can be easily integrated. From the condition of the boundedness of the velocity potential at $r = 0$, it immediately follows that the initial approximation does not depend on the radial coordinate; the following approximations are polynomials of different degrees in r:

$$\varphi^{(0)} = \bar\varphi^{(0)}(\xi,\eta), \quad \varphi^{(1)} = -\frac{r^2}{4}\frac{\partial^2\bar\varphi^{(0)}}{\partial\xi^2} + \bar\varphi^{(1)}(\xi,\eta),$$
$$\varphi^{(2)} = \frac{r^4}{64}\frac{\partial^4\bar\varphi^{(0)}}{\partial\xi^4} - \frac{r^2}{4}\frac{\partial^2\bar\varphi^{(1)}}{\partial\xi^2} + \bar\varphi^{(2)}(\xi,\eta). \quad (8)$$

Here, $\bar\varphi^{(0)}(\xi,\eta)$, $\bar\varphi^{(1)}(\xi,\eta)$, and $\bar\varphi^{(2)}(\xi,\eta)$ are the functions that result from the integration with respect to r and are to be determined using the contact condition. The substitution of expressions (6) into the contact condition (4) yields

$$\left.\frac{\partial\varphi^{(0)}}{\partial r}\right|_{r=1} = 0; \quad \left.\frac{\partial\varphi^{(1)}}{\partial r}\right|_{r=1} = -c\frac{\partial w^{(0)}}{\partial\xi},$$
$$\left.\frac{\partial\varphi^{(2)}}{\partial r}\right|_{r=1} = -c\frac{\partial w^{(1)}}{\partial\xi} + \frac{\partial w^{(0)}}{\partial\eta}. \quad (9)$$

Solutions (8) allow us to write the expressions

$$\left.\frac{\partial\varphi^{(1)}}{\partial r}\right|_{r=1} = -\frac{1}{2}\frac{\partial^2\bar\varphi^{(0)}}{\partial\xi^2},$$
$$\left.\frac{\partial\varphi^{(2)}}{\partial r}\right|_{r=1} = \frac{1}{16}\frac{\partial^4\bar\varphi^{(0)}}{\partial\xi^4} - \frac{1}{2}\frac{\partial^2\bar\varphi^{(1)}}{\partial\xi^2}. \quad (10)$$

Finally, from the comparison of expressions (9) and (10), we obtain

$$\frac{\partial^2\bar{\varphi}^{(0)}}{\partial\xi^2} = 2c\frac{\partial w^{(0)}}{\partial\xi},$$
$$\frac{\partial^2\bar{\varphi}^{(1)}}{\partial\xi^2} = 2c\frac{\partial w^{(1)}}{\partial\xi} - 2\frac{\partial w^{(0)}}{\partial\eta} + \frac{c}{4}\frac{\partial^3 w^{(0)}}{\partial\xi^3}. \quad (11)$$

From the Euler equations (2), we derive

$$\frac{\partial}{\partial r}\left[p^{(0)} - c\frac{\partial\varphi^{(0)}}{\partial\xi}\right] = 0, \quad \frac{\partial}{\partial\xi}\left[p^{(0)} - c\frac{\partial\varphi^{(0)}}{\partial\xi}\right] = 0. \quad (12)$$

$$\frac{\partial}{\partial r}\left[p^{(1)} - c\frac{\partial\varphi^{(1)}}{\partial\xi}\right] = 0,$$
$$\frac{\partial}{\partial\xi}\left[p^{(1)} - c\frac{\partial\varphi^{(1)}}{\partial\xi}\right] = -\frac{\partial^2\varphi^{(0)}}{\partial\xi\partial\eta} - \frac{\partial\varphi^{(0)}}{\partial\xi}\frac{\partial^2\varphi^{(0)}}{\partial\xi^2}. \quad (13)$$

Using the first equation from (11) and the second equation from (12), which in particular is valid at the surface $r = 1$, we obtain

$$\left.\frac{\partial p^{(0)}}{\partial\xi}\right|_{r=1} = 2c^2\frac{\partial w^{(0)}}{\partial\xi}. \quad (14)$$

Taking into account the conditions at infinity, by virtue of equations (12), we obtain

$$\left.\frac{\partial\varphi^{(0)}}{\partial\xi}\right|_{r=1} = 2cw^{(0)}.$$

We use this expression to eliminate $\varphi^{(0)}$ from the right-hand member of the second equation (13), which we consider at $r = 1$. We also eliminate the function $\varphi^{(1)}$ by using expressions (8) and (11). Then, we obtain an expression for the tangential derivative of the pressure at the shell surface:

$$\left.\frac{\partial p^{(1)}}{\partial\xi}\right|_{r=1} = 2c^2\frac{\partial w^{(1)}}{\partial\xi} - 4c\frac{\partial w^{(0)}}{\partial h} - 4c^2w^{(0)}\frac{\partial w^{(0)}}{\partial\xi} - \frac{c^2}{4}\frac{\partial^3 w^{(0)}}{\partial\xi^3}. \quad (15)$$

We substitute expansions (6) into shell equations (1), which in the initial approximation yield the expressions

$$\frac{\partial T_1^{(0)}}{\partial\xi} = c^2\frac{\partial^2 u^{(0)}}{\partial\xi^2}, \quad T_2^{(0)} = \gamma^2 p^{(0)},$$
$$T_1^{(0)} = \frac{\partial u^{(0)}}{\partial\xi} + \nu w^{(0)}, \quad T_2^{(0)} = w^{(0)} + \nu\frac{\partial u^{(0)}}{\partial\xi}. \quad (16)$$

With allowance for relation (14), equations (16) reduce to a system of equations that is homogeneous in the derivatives of the functions $w^{(0)}$ and $u^{(0)}$:

$$(1 - 2\gamma^2c^2)\frac{\partial w^{(0)}}{\partial\xi} + \nu\frac{\partial^2 u^{(0)}}{\partial\xi^2} = 0,$$
$$(1 - c^2)\frac{\partial^2 u^{(0)}}{\partial\xi^2} + \nu\frac{\partial w^{(0)}}{\partial\xi} = 0.$$

The condition of the existence of nontrivial solutions to this system yields the equation for the velocity c of the coordinate system (ξ, η):

$$2\gamma^2c^4 - (1 + 2\gamma^2)c^2 + (1 - \nu^2) = 0, \quad (17)$$

which coincides with the equation that determines the initial approximation to the phase velocity of long waves in the case of linear dispersion.

The study of the next approximation yields

$$\frac{\partial T_1^{(1)}}{\partial\xi} = c^2\frac{\partial^2 u^{(1)}}{\partial\xi^2} - 2c\frac{\partial^2 u^{(0)}}{\partial\xi\partial\eta},$$
$$T_2^{(1)} = \gamma^2 p^{(1)} - c^2\frac{\partial^2 w^{(0)}}{\partial\xi^2},$$
$$T_1^{(1)} = \frac{\partial u^{(1)}}{\partial\xi} + \nu w^{(1)} + \frac{1}{2}\left[\left(\frac{\partial u^{(0)}}{\partial\xi}\right)^2 = \nu w^{(0)^2}\right], \quad (18)$$
$$T_2^{(1)} = w^{(1)} + \nu\frac{\partial u^{(1)}}{\partial\xi} + \frac{1}{2}\left[w^{(0)^2} + \nu\left(\frac{\partial u^{(0)}}{\partial\xi}\right)^2\right].$$

With allowance for the condition at infinity, we have

$$\frac{\partial u^{(0)}}{\partial\xi} = -\frac{\nu}{1 - c^2}w^{(0)}.$$

Differentiating the second equilibrium equation (18), using expression (15), and eliminating the longitudinal forces $T_1^{(1)}$ and $T_2^{(1)}$, we obtain

$$(1 - 2\gamma^2c^2)\frac{\partial w^{(1)}}{\partial\xi} + \nu\frac{\partial^2 u^{(1)}}{\partial\xi^2} = -4c\gamma^2\frac{\partial w^{(0)}}{\partial\eta} - (1 + 4c^2\gamma^2)\omega^{(0)}\frac{\partial w^{(0)}}{\partial\xi} - \nu\frac{\partial u^{(0)}}{\partial\xi}\frac{\partial^2 u^{(0)}}{\partial\xi^2} - c^2(1 + \gamma^2/4)\frac{\partial^3 w^{(0)}}{\partial\xi^3},$$
$$(1 - c^2)\frac{\partial^2 u^{(1)}}{\partial\xi^2} + \nu\frac{\partial w^{(1)}}{\partial\xi} = -\frac{\partial u^{(0)}}{\partial\xi}\frac{\partial^2 u^{(0)}}{\partial\xi^2} - 2c\frac{\partial^2 u^{(0)}}{\partial\xi\partial\eta} - \nu w^{(0)}\frac{\partial w^{(0)}}{\partial\xi}.$$

This inhomogeneous system of equations, which are linear in the derivatives of the functions $w^{(1)}$ and $u^{(1)}$,

has a zero determinant by virtue of equation (17). The requirement for this system of equations to have a solution leads to the Korteweg–de Vries equation

$$\frac{\partial w^{(0)}}{\partial \eta} + a w^{(0)} \frac{\partial w^{(0)}}{\partial \xi} + b \frac{\partial^3 w^{(0)}}{\partial \xi^3} = 0. \quad (19)$$

The solution to equation (19) has the form of a single soliton of amplitude U [3, 4]

$$w^{(0)} = U \operatorname{sech}^2[(\xi - V\eta)/L], \quad V = Ua/3, \quad L = 2\sqrt{3b/aU}. \quad (20)$$

The coefficients a and b are determined by the formulas

$$a = \frac{(1+4\gamma^2 c^2)(1-c^2)^3 - \nu^2(1-c^2)^2 - \nu^3 c^2}{2c(1-c^2)(\nu^2 + 2\gamma^2(1-c^2)^2)},$$

$$b = \frac{c(1-c^2)^2(1+\gamma^2/4)}{2(\nu^2 + 2\gamma^2(1-c^2)^2)}.$$

The velocity c of the moving coordinate system is determined from equation (17). Using the linearized equations of a membrane shell, we obtain the expression for the coefficient a involved in the Korteweg–de Vries equation:

$$a = \frac{2c\gamma^2(1-c^2)^2}{\nu^2 + 2\gamma^2(1-c^2)^2},$$

The coefficient b will be determined by the same expression as above.

SOLITON SOLUTION

Using expressions (20) and going back to the coordinates z, t, we write the solution in the form

$$w = W \operatorname{sech}^2[\kappa(z - vt)], \quad p = P \operatorname{sech}^2[\kappa(z - vt)], \quad u = U\{1 - \tanh[\kappa(z - vt)]\}, \quad (21)$$

where

$$\kappa = \frac{1}{2}\sqrt{\frac{aW}{3b}}, \quad P = 2c^2 W, \quad U = \frac{2\nu}{1-c^2}\sqrt{\frac{3bW}{a}}.$$

The wave velocity v is a sum of the velocity of linear waves c and the correction depending on the wave amplitude: $v = c + V$ and $V = Wa/3$.

From equation (17), it follows that, in the presence of liquid inside the shell, for a given amplitude, we always have two solitons that differ in their propagation velocities: a "slow" soliton and a "fast" one. In this respect, the situation is analogous to that observed in the case of linear waves where, for a given κ, two waves with the phase velocities c_1 and c_2 were obtained. Since the signs of the coefficients a and b are identical, both solitons have the form of a shell bulging whose propagation velocity is somewhat higher than the velocity of linear waves.

The coefficients a and b, which determine the contributions of each of these effects, essentially depend on the single parameter γ, which determines the type of the interaction between the shell and the liquid inside it. The case $\gamma \ll 1$ corresponds to a light liquid or gas; for a heavy liquid and a thin shell, we have $\gamma \gg 1$. Let us consider the behavior of the soliton solution obtained above in these limiting cases.

Assuming that, in the problem under study, $\gamma = 0$ and considering the solution corresponding to the "slow" soliton, we arrive at the case of a shell without liquid. Then, $c^2 = 1 - \nu^2$, and we obtain

$$a = -\frac{\sqrt{1-\nu^2}}{2\nu}, \quad b = \frac{\nu^2}{2}\sqrt{1-\nu^2},$$

$$\kappa = \frac{1}{2}\sqrt{-W/3\nu^3}, \quad V = 1 - \nu^2 - \frac{W}{6\nu}\sqrt{1-\nu^2}.$$

Since κ is real, we have $W < 0$, and the wave has the form of an impression of depth W with the characteristic length $1/\kappa$ and the propagation velocity also exceeding the phase velocity of linear waves.

Using the linear relations for the slow soliton, we obtain $a \longrightarrow 0$ and $b = O(1)$. In this case, the effect of dispersion predominates, which leads to "smearing" of the wave profile.

Now, let $\gamma \longrightarrow \infty$. Then, for the solution corresponding to the root c_1 of the characteristic equation (17), we have

$$a = \gamma^{-1} a_0 + O(\gamma^{-3}), \quad b = \gamma^{-1} b_0 + O(\gamma^{-3}), \quad c = \gamma^{-1} c_0 + O(\gamma^{-3}),$$

where the coefficient a_0 takes different values for the shells described by linear and nonlinear relations:

$$a_0 = \begin{cases} \dfrac{\sqrt{1-\nu^2}}{\sqrt{2}} & \text{for a linear shell} \\ \dfrac{3\sqrt{1-\nu^2}}{2\sqrt{2}} & \text{for a nonlinear shell;} \end{cases}$$

$$b_0 = \frac{2\sqrt{1-\nu^2}}{32}, \quad c_0 = \frac{\sqrt{1-\nu^2}}{\sqrt{2}}.$$

Expressions (21) show that, in the case under study, the pressure p at the shell surface is of a higher order of smallness than the displacements u and w: the pressure tends to zero as $O(1/\gamma^2)$. The velocity v of the soliton is also a quantity of the order of $O(1/\gamma^2)$.

As for the behavior of the "fast" soliton in the limiting cases of interest, its study with the help of the expansions obtained above is impossible. At $\gamma \longrightarrow 0$,

equation (17) singularly degenerates, and, for the initial approximation to the wave velocity, we obtain $c_2 \longrightarrow \infty$.

In the case $\gamma \longrightarrow \infty$, for the second root of the dispersion relation, we obtain $c_2 = 1 + O(1/\gamma^2)$, and formula (21) for the longitudinal displacement yields $U \longrightarrow \infty$. This case of the degeneracy of the coupling problem may also be called a singular one in view of the analogy with the structure of the expansions of the solutions to the boundary-value problems for differential equations with boundary layers.

REFERENCES

1. P. E. Tovstik, *Stability of Thin Envelopes* (Nauka, Moscow, 1995).
2. L. I. Sedov, *A Course in Continuum Mechanics* (Nauka, Moscow, 1983; Wolters-Noordhoff, Groningen, 1971), Vol. 1.
3. J. L. Lamb, *Elements of Soliton Theory* (Wiley, New York, 1980; Mir, Moscow, 1997).
4. P. S. Landa, *Nonlinear Oscillations and Waves* (Nauka, Moscow, 1997).

Translated by E. M. Golyamina

Technical Physics, Vol. 45, No. 6, 2000, pp. 794–796. Translated from Zhurnal Tekhnicheskoĭ Fiziki, Vol. 70, No. 6, 2000, pp. 126–127.

BRIEF COMMUNICATIONS

The Effect of the Concentration Dependence of a Diffusion Coefficient on the Stability of a Growing Spherical Particle

L. M. Martyushev and E. M. Sal'nikova

Institute of Industrial Ecology, Ural Division, Russian Academy of Sciences, Yekaterinburg, 620219 Russia

Received May 11, 1999

Abstract—The influence of the concentration dependence of the diffusion coefficient on the stability of a spherical particle growing from a supersaturated solution was studied with the Mullins–Sekerka approximation. The critical radius of stability was found, and it was shown that its value may increase by a factor of more than 1.5 if the concentration dependence of the diffusion coefficient is taken into consideration. © *2000 MAIK "Nauka/Interperiodica".*

Loss of stability and structure formation during crystallization are basic theoretical and practical issues [1, 2]. Their extensive investigation dates back to the pioneering work of Mullins and Sekerka [3], devoted to the growth of a spherical particle from supersaturated solution. The approach suggested in [3] has found wide application. Reports are available that concern growth stability [1, 4], the anisotropy of surface tension and kinetic coefficient of crystallization [5], the use of small quantities of second or higher orders in stability analysis [6], etc. All of them ignore the dependence of diffusion coefficient D on the concentration of supersaturated solution C: D is assumed to be constant. However, D is a complex function of C, as follows from physicochemical studies of salt solutions. This dependence shows up most vividly in the metastable region (for example, $D(C)$ falls down to zero at the point separating the metastable and labile regions) [7–9]. Since the major reason for loss of growth stability is diffusion field nonuniformity [3], stability analysis with regard for the concentration dependence of the diffusion coefficient seems to be burning.

In this work, the growth of a spherical particle from supersaturated solution is analyzed. The problem is stated as in [3], but D is assumed to be C-dependent. Since this relationship is generally unknown in an explicit form, we, following [9], take that

$$D(C) = D_\infty(1 + A(C - C_\infty));$$
$$A = \frac{1}{D_\infty}\frac{\partial D(C)}{\partial C}\bigg|_{C = C_\infty}, \qquad (1)$$

where C_∞ is the concentration of a supersaturated solution far away from the crystal surface and D_∞ is the diffusion coefficient at $C = C_\infty$.

In view of (1), the problem is mathematically formulated as

$$\Delta C + A\nabla((C - C_\infty)\nabla C) = 0,$$
$$C(r \longrightarrow \infty) = C_\infty, \quad C_S = C_0(1 + \Gamma K), \qquad (2)$$

where Γ is the capillary constant [3], C_S is the concentration at the surface, and K is the surface curvature.

Solving equation (2), we obtain the solution concentration at a distance r from the center of a ball:

$$C(r) = \frac{1}{A}\left(\sqrt{1 + (G_1^2 - 1)R/r} - 1\right) + C_\infty, \qquad (3)$$

where $G_1 = A(C_R - C_\infty) + 1$, $C_R = C_0(1 = 2\Gamma/R)$ is the concentration at the crystal (particle) surface, C_0 is the equilibrium concentration at the straight-line boundary, and R is the radius of a growing ball.

If $A \longrightarrow 0$, $C = C_\infty + (C_R - C_\infty)R/r$, which is consistent with results in [3]. Figure 1 shows the concentration field of a spherical crystal. At $A > (<) 0$, the near-surface concentration varies sharper (smoother) than at $A = 0$. Hence, we can suppose that the critical stability radius of the crystal for negative A's (usually, $A < 0$ [7–9]) must increase. Let us verify this supposition and evaluate the stability radius.

Near a weakly distorted sphere (perturbations as spherical harmonics $Y_{lm}(\theta, \varphi)$ are used [3]), the concentration is distributed as

$$C(r, \theta, \varphi) = \frac{1}{A}\left\{\sqrt{1 + \frac{(G_1^2 - 1)R}{r}} - 1\right\}$$
$$+ \frac{C_0\Gamma G_1(l + 2)(l - 1) + (G_1^2 - 1)R/(2A)}{\sqrt{1 + (G_1^2 - 1)R/r}}, \qquad (4)$$

1063-7842/00/4506-0794$20.00 © 2000 MAIK "Nauka/Interperiodica"

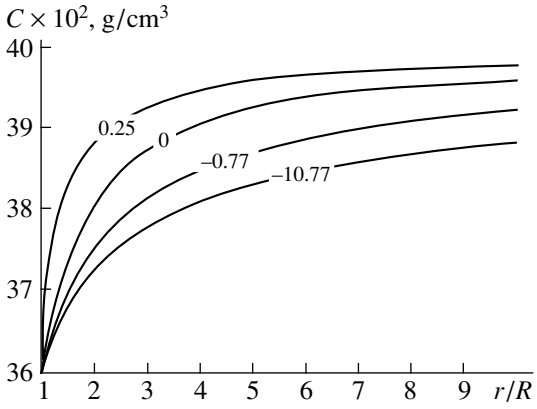

Fig. 1. Concentration of a solution C near a growing ball-like crystal vs. relative distance r/R from the center of the ball for various A's. $C_0 = 0.36$ g/cm^3, $C_\infty = 0.40$ g/cm^3, $\Gamma = 10^{-7}$ cm, and $R = 10^{-4}$ cm.

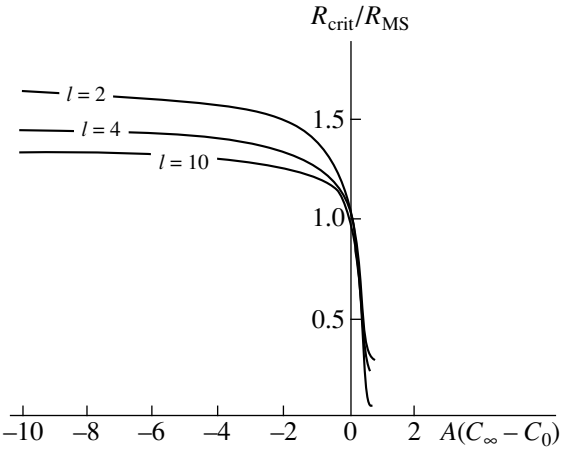

Fig. 2. R_{crit}/R_{MS} ratio (R_{MS} is the critical radius obtained in [3]) vs. dimensional parameter $A(C_\infty - C_0)$ for $l = 2$, 4, and 10.

$$\times \frac{R^{l-1}}{r^{l+1}}\delta Y_{lm} + C_\infty,$$

where l and δ are respectively the number and amplitude of a spherical harmonic ($\delta(t)/R \ll 1$).

Following [3], we assume that a plane tangent to the particle surface deviates from that tangent to the initial sphere infinitesimally; then, the growth rate of a particle is

$$V = \frac{dR}{dt} + \frac{d\delta}{dt}Y_{lm} = \frac{-D_\infty}{C_{sol} - C_R}\left(\frac{G_1^2 - 1}{2AR}\left(1 + \frac{l-1}{R}\delta Y_{lm} + \frac{2AC_0\Gamma(l+2)}{R^2 G_1}\delta Y_{lm}\right) + 2C_0\Gamma G_1 L(l-1)\frac{\delta Y_m}{R^3}\right), \quad (5)$$

where C_{sol} is the density of the solid phase and $L = (l + 1)(l + 2)/2$.

Using (5), we obtain the rate of increase of the spherical harmonic amplitude:

$$\frac{d\delta}{dt} = \frac{-D_\infty}{2AR^2(C_{sol} - C_R)}((G_1^2 - 1)(l-1) + 2AC_0\Gamma(G_1^2 l^2 - 1)(l+2)/(G_1 R))\delta Y_{lm}. \quad (6)$$

Equating (6) to zero yields the critical radius of stability. The resulting equation is nonlinear; however, only one root determined for $A < 2/3(C_\infty - C_0)^{-1}$is meaningful (since the critical radius of stability must exceed the size of a critical nucleus $R^* = 2C_0\Gamma/(C_\infty - C_0)$:

$$R_{crit} = R_{MS}K,$$

$$K = \frac{1 - G_2(3(l-1) + l^2(l+2)) + \sqrt{(1 - G_2 l^2(l+2))^2 + G_2(l+2)(l^2+3)/(1+L)}}{2 - 3G_2(1+L)(l-1)}, \quad (7)$$

where $G_2 = A(C_\infty - C_0)/(1 + L)(l - 1)$ and $R_{MS} = R^*(1 + L)$ is the critical radius found in [3].

Depending on whether the radius of a growing ball is larger or smaller than R_{crit}, the perturbing harmonic l increases or decreases. The variation of the critical radius with the dimensionless parameter $A(C_\infty - C_0)$ is depicted in Fig. 2. It is seen that taking into consideration the concentration dependence of the diffusion coefficient may increase the critical radius by a factor of more than 1.5 in relation to R_{MS}. Note that the R_{crit}/R_{MS} ratio depends on the number of a perturbing harmonic only slightly and rapidly attains its steady-state value.

If $A(C_\infty - C_0)$ is small, expression (7) can be rearranged to the more convenient form

$$R_{crit} = R\left\{1 - A(C_\infty - C_0)\frac{(l^2+3)(l+2)L}{4(l-1)(1+L)^2}\right\}. \quad (8)$$

Thus, we for the first time performed a stability analysis including the concentration dependence of the diffusion coefficient and found the analytical expression for the critical radius of stability for a growing ball. With allowance for the correction for this dependence, the critical radius of stability may substantially increase.

REFERENCES

1. J. S. Langer, Rev. Mod. Phys. **52** (1), 1 (1980).
2. J. S. Langer, Phys. Today **45** (10), 24 (1992).
3. W. W. Millins and R. F. Sekerka, J. Appl. Phys. **34**, 323 (1963).
4. S. R. Coriell and L. Parker, J. Appl. Phys. **36**, 632 (1965).
5. E. A. Brener and V. I. Melnikov, Adv. Phys. **40**, 53 (1991).
6. P. P. Debroy and R. F. Sekerka, Phys. Rev. E **51**, 4608 (1995).
7. L. Sorell and A. S. Myerson, AIChE J. **28**, 772 (1982).
8. Y. C. Chang and A. S. Myerson, AIChE J. **31**, 890 (1985).
9. A. F. Izmailov and A. S. Myerson, Phys. Rev. E **52** (1), 805 (1995).

Translated by V. A. Isaakyan

Technical Physics, Vol. 45, No. 6, 2000, pp. 797–800. Translated from Zhurnal Tekhnicheskoĭ Fiziki, Vol. 70, No. 6, 2000, pp. 128–131.

BRIEF COMMUNICATIONS

Investigation of the Plasma of a 308-nm XeCl Excimer Light Emitter Based on an Inert-Gas–CCl_4 Mixture

A. K. Shuaibov

Uzhgorod State University, Uzhgorod, 294000 Ukraine

Received June 4, 1999

Abstract—Results are presented from optical measurements of the plasma of a transverse volume discharge in He(Ar)/Xe/CCl_4(HCl) mixtures (at pressures of P = 10–100 kPa) that are used in excimer lamps emitting the XeCl 308-nm band. Emission spectra in different stages of the formation and degradation of the active medium, as well as temporal and resource characteristics of the emitter, are studied. The main products of decomposition of CCl_4 molecules that are detected by the plasma emission are C* atoms and C_2^* and CN* radicals. The operating resource of the XeCl emitter is found to be $(3–5) \times 10^4$ pulses and depends strongly on the pressure and composition of the active medium. The duration of the emission pulse at a wavelength of λ = 308 nm is 200–300 ns. © *2000 MAIK "Nauka/Interperiodica".*

INTRODUCTION

Powerful electric-discharge sources of spontaneous radiation in the spectral region $\Delta\lambda$ = 193–353 nm due to the *B–X* transitions of inert-gas monohalogenides are widely used in microelectronics, photochemistry, biology, and medicine [1]. This fact promotes their further improvement, as well as the development of a new method for diagnosing the processes occurring in the plasma of such sources. Based on a transverse volume discharge (TVD), a series of excimer lamps (ELs) have been designed. In active media of these lamps, HCl molecules are used as the carriers of chlorine atoms [2, 3]. Experimental studies of XeCl (*B–X*) laser emitters have shown that they are also highly efficient when such complex and low-aggressive carriers of chlorine atoms as CCl_4 [4] or BCl_3 [5] are used. Under certain conditions, the output characteristics of these emitters appear to be better than those of electric-discharge XeCl emitters based on He(Ne)/Xe/HCl mixtures. In [6], this fact was attributed to more efficient production of Cl^- ions in a BCl_3 plasma as compared to HCl-containing plasmas. The dissociative-attachment (with production of Cl^- ions) cross section of CCl_4 molecules, as well as BCl_3 molecules, is as high as 1.3×10^{-14} cm^2 at electron energies close to zero [7]. This property can be used in medium-pressure ELs. The destruction of CCl_4 molecules in TVD-based ELs at working-gas pressures of 10–100 kPa has not been studied.

In this paper, we present the results of investigations of the plasma of a TVD in He(Ar)/Xe/CCl_4(HCl) mixtures, which can be used in medium-pressure ELs. The nonsteady spectroscopy with nanosecond resolution is applied to study the destruction of CCl_4 molecules in a TVD plasma.

EXPERIMENTAL CONDITIONS

In experiments, we used a TVD-based excimer emitter with spark preionization. The volume of the active medium was $18 \times 2.2 \times (0.5–1.0)$ cm^3, the interelectrode distance being 2.2 cm. The capacitance of the main storage capacitor of the double-loop *LC* circuit of TVD ignition system was 30 nF, and that of the pulse sharper was 9.4 nF. The experimental conditions were analogous to those described in [8, 9], where the multimode regime of an EL operation was studied. The EL operated with the system of XeF 353-nm, XeCl 308-nm, KrF 249-nm, and KrCl 222-nm bands. At repetition rates of $f \le 5$ Hz, the experiments were carried out in a stationary working gas. At higher repetition rates ($5 \le f \le 40$ Hz), at which the resource characteristics of the excimer emitter were studied, the experiments were carried out with the use of a module for transverse electrical circulation of the working gas; the parameters of the module are described in [10].

SPECTRAL AND TEMPORAL CHARACTERISTICS OF EMISSION

In the initial stage of a repetitive TVD in the He/Xe/CCl_4 = 98/2.8/0.2-kPa mixture at voltages of U = 15–20 kV, the discharge was contracted and the main components of the emission spectrum were the XeCl (*B*, *C*, *D–X*) bands; HeI, XeI, and XeII lines; CI ($2p–3s$) 247.9-nm line; and CN (*B–X*) radical band. After $n \ge 5 \times 10^3$ TVD pulses, the spectrum contained only the XeI ($6s–7p$) 467.1-nm line and CN (*B–X*) band with the edge at λ = 388.3 nm and the intensity of the XeCl 308-nm band increased by a factor of about 50. This means that, during 5×10^3 pulses, the CCl_4 molecules transform into other compounds that allow a uniform TVD to exist. In order to use such a TVD in an EL

1063-7842/00/4506-0797$20.00

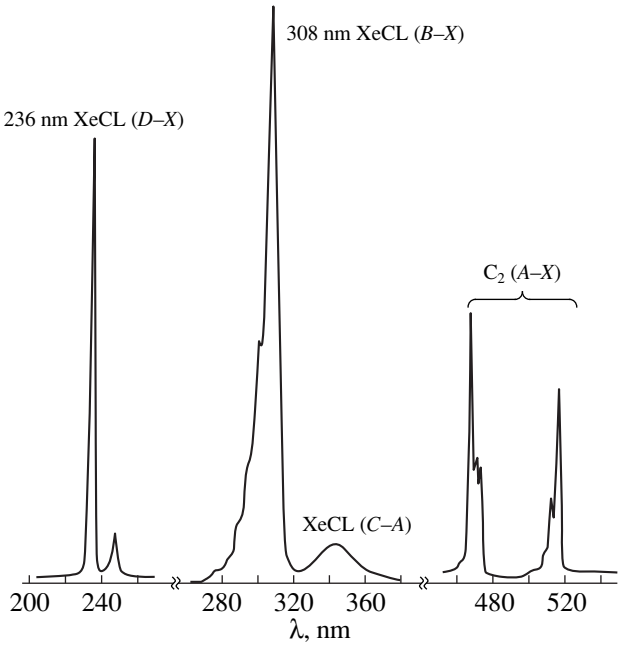

Fig. 1. Emission spectra of the plasma of a TVD in the $He/Xe/CCl_4$ = 28/4/0.12-kPa mixture at $1 \le n \le 5 \times 10^3$.

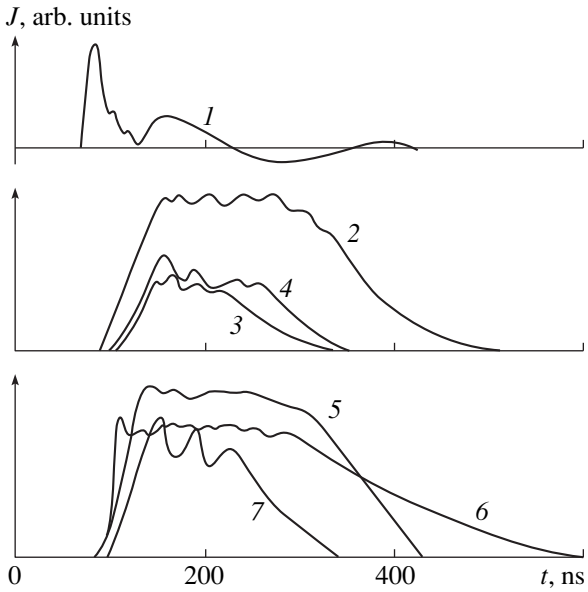

Fig. 2. Oscillograms of (*1*) the TVD current and (*2*–*7*) intensities of different components of plasma emission in the $Ar/Xe/CCl_4$ = 16/2/0.12-kPa mixture: (*2*) XeCl (*B*–*X*) 308 nm, (*3*) XeCl (*D*–*X*) 236 nm, (*4*) XeCl (*C*–*A*) 340 nm, (*5*) ArI (4*s*–5*p*) 430.0 nm, (*6*) XeI (6*s*–7*p*) 467.1 nm, and (*7*) CI (3*p*–3*s*) 247.9 nm.

at moderate voltages of $U \le 20$ kV, the working-gas pressure was decreased to 20–30 kPa. At the carbon-tetrachloride concentrations of $[CCl_4] \le 120$ Pa, the TVD was highly uniform from the very beginning. The emission spectrum of the TVD plasma is shown in Fig. 1. For fresh-prepared mixtures, in the visible part of the spectrum, the Swan bands with the edges at λ = 468.0 nm (for the C_2 (*A*–*X*) (6, 5) band) and λ = 516.5 nm (for the C_2 (*A*–*X*) (0, 0) band) were most pronounced. This is related to the nonequilibrium population of vibrational states of the C_2 molecule. Such a spectrum corresponding to *A*–*X* transitions of C_2 was also observed earlier in a transversal barrier discharge in Ar(Kr)/CO mixtures [11], as well as in steady-state and pulsed (with τ = 5–12 ms) longitudinal discharges in a He/CO mixture [12]. The resource of the Swan-band emission is $\le 5 \times 10^3$ pulses, and the presence of C_2^* emission indicates that the CCl_4 molecules transforms into other chlorine-containing molecules, which is accompanied by the deposition of solid carbon (soot) on the TVD electrodes. This deposition may contain such carbon compounds as C_{60} fullerene. After $n \ge 10^4$ pulses, in the visible part of the spectrum, there were only the most intense ArI, XeI, XeII, and ClI lines, which are characteristic of a XeCl plasma of emitters based on mixtures of inert gases with HCl molecules [13].

The oscillograms of the TVD current and the plasma emission are shown in Fig. 2. The maximum TVD current in the pulse attained 10–15 kA, and the duration of the first current peak was ≤50 ns. The emission due to the *D*–*X* transition of XeCl was delayed by 15–20 ns with respect to the emission at λ = 308 nm and was one order of magnitude less intense. The emission from the excited Xe* atoms in helium mixtures was characterized by a sharp leading edge, which coincided with the leading edge of the TVD current pulse. In Ar-containing mixtures, the XeI (6*s*–7*p*) 467.1-nm emission was delayed by 20 ns with respect to that from a TVD in a $He/Xe/CCl_4$ mixture. This is due to the energy transfer from Ar(m) and Ar_2(m) to Xe atoms [14]. The spectral lines of Ar^{+}* and Xe^{+}* ions were delayed and had flatter leading edges of the emission pulses. This is associated with a multistage mechanism for the population of the upper exited states of these ions with participation of Ar(m) and Xe(m) and their positive ions in the ground states [15]. The CI (2*p*–3*s*) 247.9-nm emission was observed in the afterglow of a TVD and was related to dissociation of CCl_4 molecules, production of C atoms, and further excitation of carbon by electron impact. The oscillator strength for this CI line is rather great (f_{ik} = 0.05 [16]), and the corresponding lower state is metastable. This fact can be used to develop sources of spontaneous and stimulated emission of UV radiation at the CI (2*p*–3*s*) 247.9-nm line similar to hybrid lasers based on Cu/HBr(HJ) mixtures [17]. Interest in such an UV source is related to the fact that its wavelength coincides with the amplification band of electric-discharge KrF amplifiers. In a $He/Xe/CCl_4$ mixture under atmospheric pressure, the duration of XeCl (*B*–*X*) emission decreased to 100–150 ns and that of

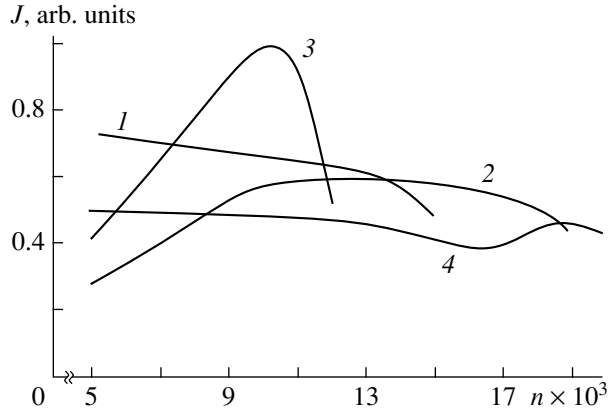

Fig. 3. Intensities of XeCl (*B–X*) 308-nm emission band from a TVD in different mixtures as functions of the discharge number: (*1*) He/Ar/Xe/CCl_4 = 23/8/0.12, (*2*) He/Xe/CCl_4 = 28/4/0.12, (*3*) He/Xe/CCl_4 = 98/2.8/0.2, and (*4*) Ar/Xe/CCl_4 = 16/2/0.12 kPa.

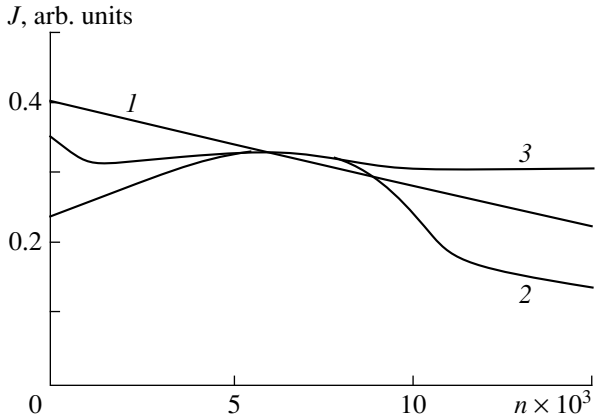

Fig. 4. Intensities of XeCl (*B–X*) 308-nm emission band from a TVD in different mixtures as functions of the discharge number: (*1*) Ar/Xe/HCl = 16/4/0.27, (*2*) Ar/Xe/CF_2Cl_2 = 20/0.27/0.04, and (*3*) He/Xe/HCl = 98/2.8/0.2 kPa.

Xe (6*s*–7*p*) emission reduced to 300 ns. The duration of CI (2*p*–3*s*) and CN (*B–X*) emission was ≤100 ns. The C_2 (*A–X*) emission, which appeared after the intensity of CI 247.9-nm emission had reached its maximum, had a duration of 400–500 ns. This is evidence of an impact mechanism for the population of C_2 (A, v) level in a TVD plasma. Based on the data from [12], we can conclude that, under the given conditions, the most probable mechanism for the production of C_2^* molecules is the reaction

$$C_2X + C \longrightarrow C_2^* + CX, \qquad (1)$$

where X represents Cl, F, or O.

In a medium with CF_2Cl_2 molecules, both C_2Cl and C_2F molecules can be involved in reaction (1). A small admixture of C_2O was always present in any fluorine-carbon-containing medium due to small additives of air, because the residual pressure in the discharge chamber was ≤5 Pa. The formation of C_2X complexes in the plasma proceeds through the interaction of CX radicals with metastable carbon atoms as it occurs when X is O [12].

RESOURCE CHARACTERISTICS

Figures 3 and 4 show the intensities of XeCl (*B–X*) emission in inert-gas mixtures with different chlorine carriers (CCl_4, CF_2Cl_2, or HCl) as functions of the number of discharge pulses. When helium was used as a buffer gas, the *n* dependence of the intensity of the 308-nm band was closest to that of the power of a XeCl laser based on a He/Xe/CCl_4 mixture [4]. In media enriched with CCl_4 molecules, the emission resource was relatively small. When argon was used as a buffer gas, the intensity of XeCl emission as a function of *n* reached its maximum somewhat faster (at $n = 3 \times 10^4$). The emission resource in such media is more than 3×10^4 pulses. For a TVD in an Ar/Xe/HCl mixture with the optimum content of HCl, the efficiency of the production of XeCl (*B*) molecules was less than in TVDs in mixtures of inert gases with CCl_4 molecules at nearly the same ratio between the Ar and Xe concentrations, though the resource of XeCl (*B–X*) emission exceeded 5×10^4 pulses. For all the HCl-based working media, the maximum intensity of XeCl (*B–X*) emission was attained in the initial stage of a repetitive discharge, after preparing a fresh mixture. For a TVD in a Ar/Xe/CF_2Cl_2 mixture, the intensity of emission as a function of *n* had a maximum at $5 \times 10^3 \le n \le 8 \times 10^3$; however, the efficiency of the production of working molecules was significant even at $n = 1$. The CCl_4 molecules do not participate directly in the production of XeCl* molecules in a TVD in He/Xe/CCl_4 mixtures. Measurements of IR absorption spectra of a similar plasma medium [4] showed that the coefficient of absorption of the main CCl_4 bands decreased sharply at $n \ge 6 \times 10^3$ and IR bands of HCl and CO molecules appeared in the spectrum. Therefore, for $n \ge 6 \times 10^3$, it is thought that the electric-discharge XeCl laser based on a He/Xe/CCl_4 mixture operates by a kinetic scheme with the production of HCl molecules in the reaction

$$CCl_4 + H_2O + h\nu \longrightarrow 2HCl + Cl_2 + CO. \qquad (2)$$

Since, in the experiments, we used commercially pure argon and high-purity helium, the fact that the intensity of XeCl (*B–X*) emission reached the plateau more rapidly in argon-containing mixtures can be due to a relatively large content of water vapor in these mixtures, which, in this case, was a positive effect. When CF_2Cl_2 molecules were used as halogen carriers, in addition to XeCl (*B–X*) emission, we observed XeF (*B–X*) emission. The ratio between the band intensities was XeCl 308 nm/XeF 353 nm = 9/1, which was equal to

the ratio between the concentrations Cl^- and F^- ions in the reaction of dissociative attachment of electrons to CF_2Cl_2 molecules [18, 19]. A CF_2Cl_2-containing plasma is characterized by both the direct production of XeF and XeCl molecules (i.e., the recombination of Cl^-, F^-, Xe^+, and Xe_2^+ ions in a buffer gas) and the production of excimer molecules via secondary processes including conversion of CCl_4 molecules in HCl.

CONCLUSIONS

Thus, the investigations of the active medium of a repetitive electric-discharge source of XeCl 308-nm emission have shown that, at moderate discharge voltages, Ar/Xe/CCl_4 mixtures at a pressure of 20 kPa have the greatest emission resource and efficiency: the duration of the XeCl (*B*–*X*) emission pulses is ≤300 ns, and the resource is $\geq 3 \times 10^4$ pulses. He(Ar)/Xe/HCl mixtures are characterized by a lower efficiency. CF_2Cl_2-based working media take an intermediate position between CCl_4 and HCl-based media with respect to the role the direct and secondary processes of the XeCl (*B*) production play in a TVD. In the emission spectra of the plasma of TVDs in fluorinecarbon-containing media, nonequilibrium visible emission in Swan bands of C_2 molecules is observed. In the UV region, the CI (2*p*–3*s*) 247.9-nm emission and CN (*B*–*X*) (0, 0) band emission with λ_{max} = 388.3 nm are the most pronounced.

ACKNOWLEDGMENTS

I am grateful to A. I. Dashchenko and I. V. Shevera for their assistance in the experiments.

REFERENCES

1. U. Kogelschatz and H. Esrom, Laser Optoelektron. **22** (4), 55 (1990).
2. B. A. Koval', V. S. Skakun, V. F. Tarasenko, *et al.*, Prib. Tekh. Éksp., No. 4, 224 (1992).
3. A. N. Panchenko, É. A. Sosnin, and V. F. Tarasenko, Zh. Tekh. Fiz. **67** (1), 78 (1997) [Tech. Phys. **42**, 68 (1997)].
4. A. Luches, V. Nassisi, and M. R. Perrone, Opt. Commun. **51**, 315 (1984).
5. V. E. Peet, A. B. Treschalov, and E. V. Slivinskij, Appl. Phys. B **52**, 234 (1991).
6. A. N. Malinin, L. L. Shimon, V. M. Dobash, and B. Ya. Khomyak, Kvantovaya Élektron. (Moscow) **22**, 1195 (1995).
7. S. C. Chu and P. D. Burrov, Chem. Phys. Lett. **172**, 17 (1990).
8. A. K. Shuaibov, L. L. Shimon, and I. V. Shevera, Prib. Tekh. Éksp., No. 3, 142 (1998).
9. A. K. Shuaibov, Zh. Tekh. Fiz. **68** (12), 64 (1998) [Tech. Phys. **43**, 1459 (1998)].
10. A. K. Shuaibov, Zh. Tekh. Fiz. **68** (5), 48 (1998) [Tech. Phys. **43**, 522 (1998)].
11. I. I. Galaktionov and G. N. Zvereva, Opt. Spektrosk. **73**, 111 (1992) [Opt. Spectrosc. **73**, 62 (1992)].
12. Yu. Z. Ionikh, I. N. Kostyukevich, and N. V. Chernysheva, Opt. Spektrosk. **76**, 406 (1994) [Opt. Spectrosc. **76**, 361 (1994)].
13. A. K. Shuaibov and A. I. Minya, Zh. Prikl. Spektrosk. **64**, 523 (1997).
14. C. H. Chen and J. P. Judish, J. Phys. B **11**, 2189 (1978).
15. J. Coutts and M. R. Osborne, J. Mod. Opt. **34**, 1513 (1987).
16. A. A. Radtsig and B. M. Smirnov, *Reference Data on Atoms, Molecules, and Ions* (Énergoatomizdat, Moscow, 1986; Springer-Verlag, Berlin, 1985).
17. K. I. Zemskov, A. A. Isaev, and G. G. Petrash, Kvantovaya Élektron. (Moscow) **24**, 596 (1997).
18. E. Illenberger, H. U. Sheunemann, and H. Baumgartel, Chem. Phys. **37**, 21 (1979).
19. V. M. Peicev, M. V. Kurepa, and I. M. Cadez, Chem. Phys. Lett. **63**, 301 (1979).

Translated by V. A. Voitenko

Technical Physics, Vol. 45, No. 6, 2000, pp. 801–802. Translated from Zhurnal Tekhnicheskoĭ Fiziki, Vol. 70, No. 6, 2000, pp. 132–133.

BRIEF COMMUNICATIONS

Excitation of Iron Atoms in a Plasma of Excimer Emitters under Transverse-Discharge Pumping

A. K. Shuaibov, L. L. Shimon, A. I. Dashchenko, and Yu. Yu. Neĭmet

Uzhgorod State University, Podgornaya ul. 46, Uzhgorod, 294000 Ukraine

Received June 15, 1999

Abstract—The optical characteristics of a transverse-discharge plasma initiated in He/Xe(Kr)/HCl(CF_2Cl_2) mixtures were studied. The mixtures contained a small amount of iron vapor due to metal cathode erosion. The iron atoms were shown to be excited by the spontaneous emission of KrCl (λ = 22 nm) and XeCl (λ = 308 nm) molecules in a nanosecond transverse discharge. © *2000 MAIK "Nauka/Interperiodica".*

Electrodes exposed to high-power nanosecond transverse discharges are often sputtered [1]. In a pulse–periodic regime ($f \geq 5$ Hz), this may lead to the opacity of optical windows of electric-discharge excimer emitters (EDEEs). However, an iron plasma itself is of interest for generating stimulated emission in the UV range. In [2], where iron vapor was pumped by a KrF laser with λ = 249 nm, FeI emission lines were observed at λ = 299.95, 305.16, and 304.04 nm. Therefore, the possibility of applying high-power spontaneous emission from excimer molecules to excite iron atoms merits consideration.

In this work, we investigated the optical characteristics of an iron-containing EDEE plasma. The iron vapor was derived from the erosion of cathodes exposed to a pulsed transverse discharge. Two discharge-initiating systems were used: (1) a grid cathode and a continuous anode with UV preionization and (2) continuous metal electrodes with spark preionization. The continuous anode was made from stainless steel. Its radius of curvature and length were 1.7 and 17 cm, respectively. In system 1, the cathode was a planar grid (made from stainless steel) with 1 × 1-mm meshes. The interelectrode distance was 20 mm [3]. The discharge gap was preionized with a pulsed corona initiated between the needles and the grid 100–150 ns before the main discharge. In the system with spark preionization, the transverse discharge occupied the volume 18 × 2.2 × 0.7 cm (here, 2.2 cm is the interelectrode distance). Gap preionization was accomplished with two rows of spark discharges [4]. A capacitive $C - C_0$ circuit, where a 30-nF capacitor C charged a 9.4-nF capacitor C_0, and a thyratron switch were energized by a pulse voltage generator. The discharge and optical characteristics of the plasma were measured with a laser diagnostic complex [3, 4].

Figure 1 illustrates the general view of the emission spectrum that was obtained in the transverse-discharge plasma excited in the mixtures of the inert gases and HCl molecules for an emitter with corona preionization. All such spectra had FeI emission lines. Note that noticeable FeI emission was observed only under conditions optimal for the formation of excimer molecules. A small amount of HCl molecules in the working medium and a low pressure are the factors causing the emission due to transitions in FeI to decrease. The most intense lines from iron atoms are listed in the table (with regard for the spectral sensitivity of the recording system). The intensity of the FeI lines is fairly high (≤5% of that of the *RX* lines), which may be used to extend the spectral range of excimer lamps. Such emitters can be applied for analysis of an iron plasma with a time resolution of ≤100 ns. The iron vapor spectrum and the FeI band diagram indicate that lower energy levels of iron can be optically excited by *RX* UV emission. The energy of *B–X* emission quanta is 5.57 eV for KrCl and 4.96 eV for XeCl. Such values are sufficient for the occupation of only upper Fe* levels through

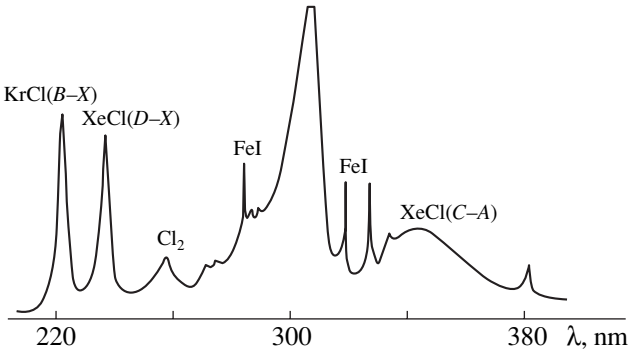

Fig. 1. General spectrum of the transverse-discharge plasma with corona preionization for the mixture He/Kr/Xe/HCl = 200/1.6/0.4/0.4 kPa.

1063-7842/00/4506-0801$20.00 © 2000 MAIK "Nauka/Interperiodica"

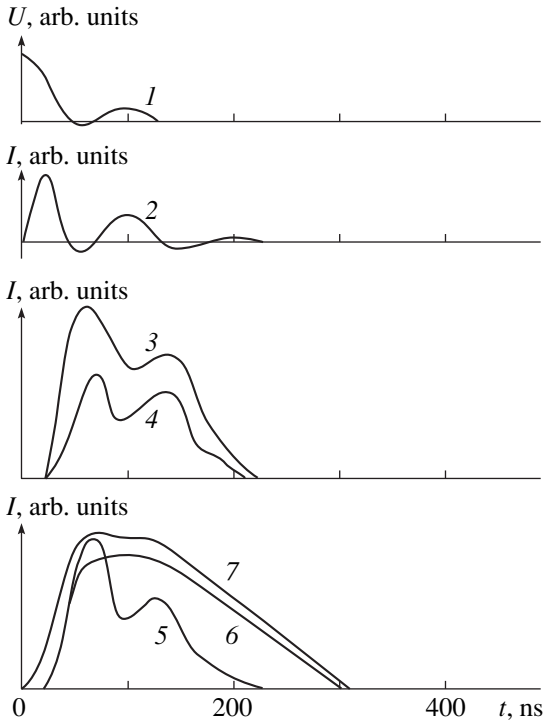

Fig. 2. Oscillograms of the (*1*) voltage, (*2*) current, and (*3*–*7*) emission of the transverse-discharge plasma with spark preionization for the mixture He/Kr/CF_2Cl_2 = 7/4/0.08 kPa; (*3*) 222 nm, KrCl; (*4*) 249 nm, KrF; (*5*) 258 nm, Cl_2; (*6*) 318.8 nm, FeI; and (*7*) 516.5 nm, C_2 (*A*–*X*).

lower levels of FeI, which are excited by discharge electrons. In our electrode system, iron vapor may arise from hot spots on the continuous cathode and grid, as well as from hot zones of the corona in the preionization system. In this case, iron vapor enters the discharge gap by means of electric wind, formed in the corona [5].

FeI emission was also observed in a He/Kr/CF_2Cl_2 plasma initiated in a typical electrode system with automated spark preionization (see table). To gain a better insight into iron emission, we took time variations of the emission intensities for *RX*, FeI, and products of CF_2Cl_2 decomposition (Fig. 2). As follows from the table, the energy of quanta of KrCl and KrF molecules produced in the given plasma is sufficient only for step occupation of Fe*. Oscillograms were recorded at U = 15 kV and f = 3 Hz. The maximum discharge current was less than 15 kA. The intensity of all the iron lines varied with time in a similar way. The emissions of *RX* molecules and Fe* atoms correlate in time, indicating a considerable contribution of optical pumping to the population of FeI higher excited levels. In the CF_2Cl_2-based media, the emission intensity ratio for KrCl, KrF, and Cl_2 molecules was found to be KrCl/KrF/Cl_2 = 9/1/1. This can be explained by almost the same ratio between the densities of negatively charged Cl^- and F^- ions, which are produced by dissociative attachment of electrons to CF_2Cl_2 [6, 7].

Thus, the emission spectra of an EDEE plasma involve iron lines. Iron results from electrode sputtering in the main and auxiliary discharges. Optical pumping (FeI excimer emission from lower energy levels) seems to be the most plausible mechanism for occupying higher excited levels of iron. *RX* high-power spontaneous emission can be used for generating nonequilibrium UV emission from Fe atoms.

Most intense iron lines in the EDEE plasma

λ, nm	*I*, arb. units	E_{low}, eV	E_{up}, eV	Transition
corona-preionization emitter				He/Xe/HCl mixture
270.8	1.00	–	–	–
283.8	0.25	0.99	5.35	a^5F_2–$y^5G^0_2$
317.8	0.10	2.40	6.30	$z^7D^0_5$–f^7D_4
326.5	0.11	0.09	3.89	a^5D_5–$z^3D^0_3$
332.9	0.20	3.26	6.99	b^3H_5–$u^3H^0_5$
344.7	0.24	2.20	5.79	a^5P_2–$y^3P^0_2$
spark-preionization emitter				He/Kr/CF_2Cl_2 mixture
292.9	1.00	2.20	6.41	a^5P_2–$y^5F^0_2$
294.1	0.52	0.09	4.30	a^5D_2–$y^5F^0_1$
304.8	0.59	0.09	4.16	a^5D_2–$y^5D^0_3$
318.9	0.52	2.48	6.37	$z^7D^0_1$–e^5G_2
323.1	0.27	2.45	6.29	$z^7D^0_3$–f^5D_2

REFERENCES

1. L. L. Babich, T. V. Loĭko, and V. A. Tsukerman, Usp. Fiz. Nauk **160** (7), 49 (1990) [Sov. Phys. Usp. **33**, 521 (1990)].
2. H. Yoshida and H. Ninomada, Opt. Commun. **107** (1–2), 71 (1994).
3. A. K. Shuaibov and A. Ĭ. Minya, Zh. Prikl. Spektrosk. **64**, 523 (1997).
4. A. K. Shuaibov, L. L. Shimon, A. I. Dashchenko, and A. I. Minya, Ukr. Fiz. Zh. **43** (1), 27 (1998).
5. I. P. Vereshchagin, *Corona Discharge in Electronic and Ionic Process Equipment* (Énergoatomizdat, Moscow, 1985).
6. V. M. Pejcev, M. V. Kurepa, and I. M. Cadez, Chem. Phys. Lett. **63**, 301 (1979).
7. D. L. McCorkle, A. A. Chiristodoulides, L. G. Chiristophorou, *et al.*, J. Chem. Phys. **72**, 4049 (1980).

Translated by V. A. Isaakyan

Technical Physics, Vol. 45, No. 6, 2000, pp. 803–805. Translated from Zhurnal Tekhnicheskoĭ Fiziki, Vol. 70, No. 6, 2000, pp. 134–136.

BRIEF COMMUNICATIONS

Dynamics of Local Magnetic Flux Vortexes in Superconductors

I. M. Golev, V. E. Miloshenko, and N. A. Andreeva

Voronezh State Technical University, Voronezh, Moskovskiĭ pr. 14, 394026 Russia

Received June 9, 1999

Abstract—The dynamics of local magnetic flux vortexes in high-temperature semiconductors is studied with a mechanical method. Physical conditions in a gradient magnetic field are analyzed. Obtained results are treated within a model of free and pinned vortexes. The magnitudes of elastic modula, pinning strength, dissipated energy, viscous friction of the vortexes, and pinning potential were calculated. The method allows the determination of local, rather than integrated, superconductor characteristics. This makes it possible to map pinning centers over the crystal structure. © *2000 MAIK "Nauka/Interperiodica".*

High-temperature superconductors (HTSCs) hold much promise in various domains of industry. Usually, a specimen is subjected to a uniform magnetic field, and the integrated critical parameters and their derivatives are evaluated [1–3]. However, for applications (cryogenic machine building or designing devices with HTSC components [4–6]), of great interest is the distribution of structure inhomogeneities (particularly, pinning centers) over the specimen volume. In this work, we experimentally studied the dynamics of vortexes of a local gradient magnetic flux in yttrium-based metal oxides.

A mechanical method where an HTSC plate is placed between magnet poles [7] was employed (Fig. 1). If an external field B exceeds the first critical field B_{c1}, a magnetic flux spot forms in the middle of the plate. The setup enables us to examine various specimen parts. The magnetic system is mobile, and the sensitivity can be improved by narrowing the spot. The length a of the spot depends on the specimen geometry, and its width b is defined by the thickness of the pole pieces and the field distribution between the poles. The field between the poles can be written as

$$B(z) = B_0 \exp(-\beta z^2). \quad (1)$$

In view of the B_{c1} value,

$$b = 2\sqrt{\ln\left(\frac{B_0}{B_{k1}}\right)^{\frac{1}{\beta}}}, \quad (2)$$

where B_0 is the maximum value of the magnetic field, β is the magnetic system constant (2.2×10^5 m^{-2}), and z is a linear displacement.

When the plate is displaced under the action of a force F, each of the vortexes moving in the nonuniform magnetic field together with the superconductor will experience a restoring force

$$f = p_{mz}\frac{\partial B}{\partial z} = -2p_{mz}B_0\beta z\exp(-\beta z^2), \quad (3)$$

where p_{mz} is the magnetic moment of a vortex.

If f is smaller than the pinning strength f_{pi} of the vortex, the vortex displacement is elastic (reversible). A further movement of the plate will cause f to grow. When this force becomes equal to f_{pi}, vortexes will begin to unpin from pinning centers and naturally become in a certain sense fixed relative to the magnetic system. The pinning strengths of the vortexes differ; therefore, the number of unpinned vortexes will increase as the plate is more and more displaced. The number of unpinned (fixed) vortexes N_f as a function of plate displacement is given by

$$N_f(z) = N\left[1 - \exp\left(-\frac{z}{k_1}\right)\right], \quad (4)$$

where k_1 is a factor that characterizes a spread of the

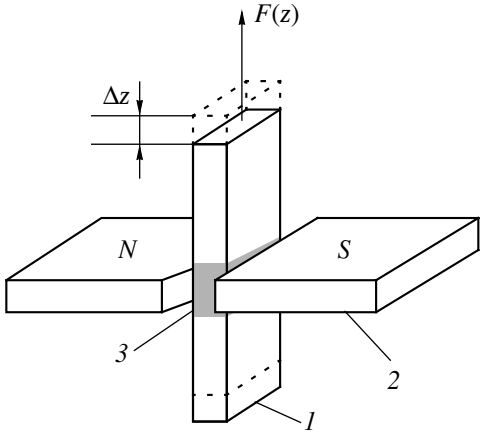

Fig. 1. Superconducting plate in a magnetic system: (*1*) superconducting plate; (*2*) magnet poles; and (*3*) magnetic flux spot.

1063-7842/00/4506-0803$20.00

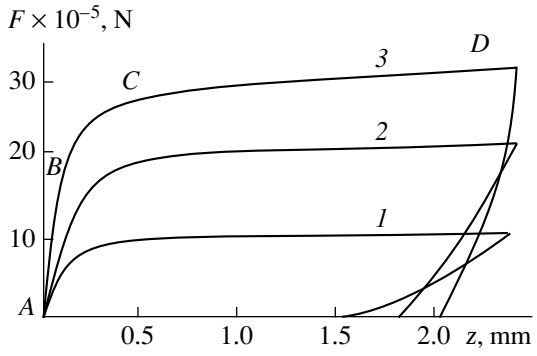

Fig. 2. Applied force F vs. superconductor displacement z (*1–3*, specimen nos.).

vortex pinning strengths, $N = \Phi/\Phi_0$ is the number of vortexes, and Φ is the magnetic flux per area under study:

$$\Phi = k_2 a B_0 \int_{-b/2}^{b/2} \exp(-\beta z^2) dz. \quad (5)$$

Here, k_2 is the attenuation coefficient of the external field B_0 in the superconductor. Its value was estimated at no less than 0.9 for $B > 0.01$T. We will assume that all the vortexes are pinned at the initial time instant and the net force needed to unpin all of them is $F = \sum_{i=1}^{N} f_{pi}$. With regard for (4), the displacement of a specimen and the displacing force are related as

$$F(z) = \sum_{i=1}^{N} f_{pi} N\left[1 - \exp\left(-\frac{z}{k_1}\right)\right]. \quad (6)$$

The motion of unpinned vortexes induces an additional force due to viscous friction between them inside the superconductor. The viscous friction coefficient η is then written as

$$\eta = \frac{\Delta F \Delta z}{VS}, \quad (7)$$

where ΔF is a change in the force when the specimen is displaced by Δz, V is the specimen velocity, $S = ad$ is the specimen cross section, and d is the specimen thickness. In our experiments, the force sensitivity was 10^{-7} N, and the displacements, on the order of 10^{-6} m.

Specimens used were YBaCuO metal oxides with different compositions and densities (see table, specimens *1–3*). They measured $4 \times 1.5 \times 20$ mm and were obtained by the two-stage ceramic process at 78 K. In fields ranging from 0.007 to 0.1 T, the magnetic flux spot width varied between 5.5×10^{-3} and 9×10^{-3} m. The specimens were displaced with a velocity of 3×10^{-5} m/s.

The force F is known to depend both on the vortex density and on the crystal structure of a ceramic material. Therefore, the experiments were carried out in various magnetic fields and also on specimens differing in porosity and grain size, all other things being equal.

For all of the metal oxides used in the experiments, the curves $F(z)$ taken under permanent magnetic fields are similar. They are shown in Fig. 2 for $B = 0.025$ T.

Initially, at small displacements, the force increases linearly, pointing to the elastic displacement of the vortexes (Fig. 2, portion *AB*). The measured elastic modula of the vortex structure are given in the table. At larger displacements, the curve is no longer linear (portion *BC*) and exhibits hysteresis, which is an indication of vortex unpinning from the pinning centers. Subsequently, when all vortexes are unpinned, the curves saturate (portion *CD*). The slope of the last portion is defined by the coefficient of viscous friction between moving vortexes, and the measured force F just characterizes the pinning strength. The viscous friction coefficients and the pinning strengths are also listed in the table. Naturally, the direct and return (as the displacement z decreases) runs of the curves $F(z)$ are different. The area of the hysteresis loop reflects the energy W dissipated during this quarterperiod because of the viscous motion of the vortexes. The values of W for the displacement $z(0 –2– 0)$ mm are presented in the table.

The pinning strength in superconductors depends on the energy U_0 needed to pin vortexes at pinning centers. The pinning energy can be estimated from the relaxation value. To this end, the specimen placed in the permanent magnetic field was displaced by a distance z under the action of force F. Once the force ceased to grow, the displacement continued to increase (Δz) with time because of the thermally activated creep of some of the vortexes. The pinning energy was calculated by the formula

$$U_0^* = -\left[\ln\left(1 - \exp\left(-\frac{\Delta z}{k_1}\right)\right) kT\right], \quad (8)$$

Table

Specimen no.	Density, g/cm^3	$p_H \times 10^{-5}$, Ω m	$F_{p\,\mathrm{mech}}$, N/m^3	$F_{p\,\mathrm{cur}}$, N/m^3	C, N/m^2	$W \times 10^{-7}$, J	η, kg/m s	U_0, meV
1	3.3	3.4	1900	9.8	68	7.2	20	16
2	4.2	1.5	3445	210	26×10^2	16.4	52	27
3	5.2	0.76	4282	1480	94×10^2	18.8	300	31

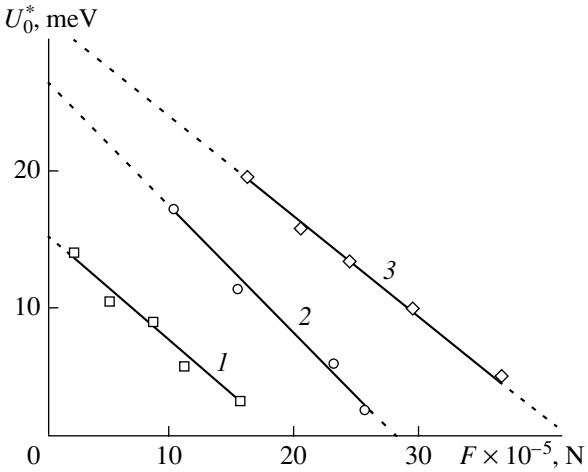

Fig. 3. U_0^* vs. applied force F (*1–3*, specimen nos.).

where $U_0^* = U_0 - f_i b$, b is the vortex displacement due to an applied force $f_i = F/N$, and k is the Boltzmann constant.

Dependences $U_0^*(F)$ for $B_0 = 0.025$ T are presented in Fig. 3. The energy of activation U_0^* drops with increasing force F applied at the initial time instant. By extrapolating the dependence $U_0^*(F)$ to $F = 0$, it is possible to find U_0 for the superconductors (see table). Knowing U_0, one can determine the vortex displacement b due to the force F applied at the initial time instant. The value of b was found to be independent of F: it equaled 86×10^{-10}, 42×10^{-10}, and 36×10^{-10} m for specimens *1–3*, respectively. With an increase in the YBaCuO density, the elastic modulus, pinning strength and energy, and dissipated energy grow, whereas the viscous friction coefficient is inversely proportional to the resistivity of the superconductor in the normal state. Our results are consistent with vortex behavior in a permanent magnetic field [8].

In the same experimental environment (in particular, for the same vortex velocity), we also measured the critical current by a resistive method. The pinning strength derived from the critical current, $F_{p\text{cur}}$, turned out to be smaller than $F_{p\text{mech}}$ (see table). The reason is that the critical current, from which $F_{p\text{cur}}$ is deduced, is measured from the motion of weakly pinned vortexes. Conversely, in our case, the ultimate pinning strength of the semiconductor was measured.

To conclude, the mechanical method for studying the dynamics of a localized magnetic flux in superconductors is suggested. It allows the evaluation of the ultimate pinning strength and energy, elastic modulus of vortexes, and viscous friction coefficient. With this method, one can also map effective pinning centers.

REFERENCES

1. V. E. Miloshenko and I. M. Shushlebin, Sverkhprovodimost': Fiz., Khim., Tekh. **5** (2), 229 (1992).
2. E. H. Brant, Prog. Phys. **58**, 1465 (1995).
3. R. Vijayraghavan and L. C. Gupta, Int. J. Mod. Phys. B **9**, 663 (1995).
4. V. E. Miloshenko and V. M. Karmazin, Tekh. Élektrodinamika, No. 6, 10 (1982).
5. Yu. F. Antonov and E. Ya. Kozovskiĭ, Élektrotekhnika, No. 11, 29 (1982).
6. Yu. A. Baurov, S. P. Merkurova, and Yu. F. Antonov, Sverkhprovodimost': Fiz., Khim., Tekh., Nos. 8–9, 1453 (1994).
7. I. M. Golev, N. A. Andreeva, and V. E. Miloshenko, Prib. Tekh. Éksp., No. 5, 161 (1998).
8. V. M. Pan, Zh. Vses. Khim. O–va **34**, 509 (1989).

Translated by V. A. Isaakyan

Technical Physics, Vol. 45, No. 6, 2000, pp. 806–808. Translated from Zhurnal Tekhnicheskoĭ Fiziki, Vol. 70, No. 6, 2000, pp. 137–139.

BRIEF COMMUNICATIONS

A Superconducting Vibrator with a Trapped Magnetic Field

S. G. Bodrov and A. A. Semenov

Ioffe Physicotechnical Institute, Russian Academy of Sciences, St. Petersburg, 194021 Russia

Received June 28, 1999

Abstract—A design of a superconducting vibrator of bending oscillations is proposed. The magnetic-field dependence of the vibrator natural frequency is calculated. It is shown that, for the suggested construction, the natural frequency is tens of times more sensitive to the magnetic field than for all the resonators used before. It is proposed to use such a resonator to study the magnetic field penetrating into superconductors. *© 2000 MAIK "Nauka/Interperiodica".*

INTRODUCTION

The magnetic properties of type-II superconductors have not been adequately studied up to the present day. In particular, it is associated with a limitation of the investigation methods. The use of the technique of oscillating superconducting rods and plates, placed in the magnetic field, opened up new effective possibilities of studying various processes in superconductors [1–10]. When a superconductor oscillates in a magnetic field, currents are induced in its surface layer. An interaction between these currents and the field results in the rise of magneto-elastic forces changing the natural oscillation frequency of a superconducting specimen. Oscillations of the vortex lattice together with the specimen induce bulk currents; the interaction between them and the magnetic field results in the appearance of a force and, consequently, in a change in the natural oscillation frequency. When the vortex lattice is fixed stiffly at the pinning centers, the square of the specimen's natural frequency varies in direct proportion with the square of the magnetic field intensity. A departure from this proportionality is a source of information on, for example, the pinning. Use of a superconducting screen located parallel to the plate surface or rod axis increases the accuracy and extends the capabilities of this technique, in particular, permitting the determining of the penetration depth of a magnetic field disturbance into a superconductor. For the first time, the use of a screen was considered in [6, 10] for the limiting cases of an infinitely wide plate and a round rod. In [6], it has been shown that the square of the bending oscillation frequency of the infinitely wide plate increases in inverse proportion to the distance between it and a screen, i.e., increases indefinitely. Consideration of the similar problem for a round rod has shown that, in this case, increasing the natural oscillation frequency tends to a definite limit. The problem of elastic oscillations of a finitely wide plate above the screen was considered in [10]. It has been shown that, in this case, as well as in the case of an infinitely wide plate, a magneto-elastic force increases indefinitely when the plate approaches the screen.

In all the cited papers, the magnetic field was parallel to the vibrator length. In this case, during vibrator oscillations, the magnetic lines of force are distorted and the magnetic field induction has different magnitudes at different areas of the vibrator surface, making it difficult to consider the magnetic field penetration into a superconductor.

In this paper, we consider a superconducting vibrator without these limitations.

SETTING AND SOLVING THE PROBLEM.

The suggested vibrator is a superconducting pipe of rectangular cross-section and length L, for which the opposite walls have an equal thickness. The inner pipe sizes are (width) l and (height) $2a$ (Fig. 1a). The side walls B and B' are fixed and sufficiently thick to fulfil the condition for the A and A' wall ends to be stationary. Antiphase bending oscillations are excited in the A and A' opposite walls whose thickness is h.

Under the condition that the pipe length is much more than the linear size of the hole, a vibrator may be regarded to be infinitely wide. The vibrator is placed in a homogeneous magnetic field with induction B_0 parallel to the walls (perpendicular to the plane of Fig. 1). Taking into account that oscillations of the AA' walls occur in opposite phases due to the law of reflection on a superconducting surface, the problem is reduced to analyzing oscillations of the A wall of thickness h of the rectangular cavity of width l and height a made in superconducting half-space (Fig. 1b) placed in a homogeneous magnetic field parallel to the cavity walls.

At oscillations of the vibrator, the magnetic field outside of the cavity changes neither its direction nor magnitude. The magnetic field trapped in the cavity remains homogeneous and parallel to the cavity walls, and its magnitude varies with time due to variations resulting from the cavity cross-sectional area oscillations.

1063-7842/00/4506-0806$20.00

For convenience, let us consider the vibrator presented in Fig. 1b. Since the magnetic field is trapped in the vibrator cavity, the flux keeps constant during oscillations, i.e.,

$$S_0 B_0 = S(t)B(t), \quad \text{where}$$

$$S_0 = al; \quad S = al + \int_0^l \xi(z)dz e^{i\omega t},$$

where $\xi(z)$ is the oscillation amplitude and ω is the radian frequency.

In the approximation of small oscillations,

$$B(t) = B_0 \frac{S_0}{S} = B_0\left(1 - \frac{1}{al}\int_0^l \xi(z)dz \exp(i\omega t)\right). \quad (1)$$

The force acting on a unit area of the oscillating plate from the magnetic field is equal to the difference of the magnetic pressures on its plane,

$$F_m = -\frac{B_0^2}{\mu_0 al}\int_0^l \xi(z)dz \exp(i\omega t). \quad (2)$$

Here, μ_0 is the magnetic constant. The equation of elastic harmonic oscillations of the plate taking into account F_m can be written as [11]

$$h\rho\omega^2\xi(z) = \frac{h^3 E}{12(1-\mu^2)}\Delta^2\xi(z) - \frac{B_0^2}{\mu_0 al}\int_0^l \xi(z)dz. \quad (3)$$

Here, E is the Young modulus, μ is the Poisson coefficient, and ρ is the density. The general solution of equation (3) can be written as

$$\xi(z) = A\cos kz + B\sin kz + C\cosh kz + D\sinh kz + \frac{1}{k^4 l^5} M\int_0^l \xi(z)dz. \quad (4)$$

Here,

$$M = \frac{12(1-\mu^2)l^4 B_0^2}{h^3 a\mu_0 E}; \quad k^4 = \rho\omega^2\frac{12(1-\mu^2)}{h^2 E};$$

A, B, C, and D are constants of integration. They can be determined from the following boundary conditions:

$$\xi(z)|_{z=0,1} = 0, \quad \left.\frac{d\xi(z)}{dz}\right|_{z=0,1} = 0. \quad (5)$$

Boundary conditions (5) give four algebraic equations connecting the integration constants and

$$\int_0^l \xi(z)dz.$$

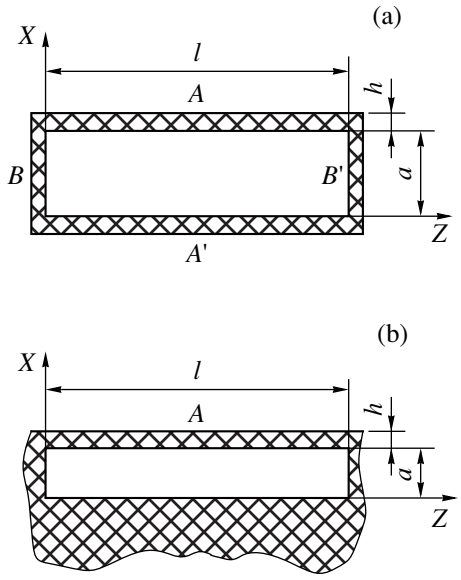

Fig. 1. Schematic view of the vibrator.

Upon integrating (4) over z, we obtain the fifth equation. Thus, we have the system of five equations in five unknown,

$$A + C + \frac{1}{k^4 l^5} M\int_0^l \xi(z)dz = 0,$$

$$A\cos kl + B\sin kl + C\cosh kl + D\sinh kl + \frac{1}{k^4 l^5} M\int_0^l \xi(z)dz = 0,$$

$$B + D = 0, \quad (6)$$

$$-A\sin kl + B\cos kl + C\sinh kl + D\cosh kl = 0,$$

$$A\sin kl + B(1-\cos kl) = C\sinh kl + D(\cosh kl - 1) + \xi\left(\frac{1}{k^4 l^4}M - 1\right)\int_0^l \xi(z)dz = 0.$$

Only when the determinant composed of the coefficients at A, B, C, D, and $\int_0^l \xi(z)\,dz$ is equal to zero, system (6) has a nontrivial solution. This results in the dispersion equation

$$(1 - \cos kl\cosh kl)k^5 = M[kl(1 - \cos kl\cosh kl) - 2\sin kl - 2\sinh kl + 2\sinh kl\cosh kl + 2\cos kl\sinh kl]. \quad (7)$$

From equation (7), taking account of (4), the following relation between the natural oscillation frequency

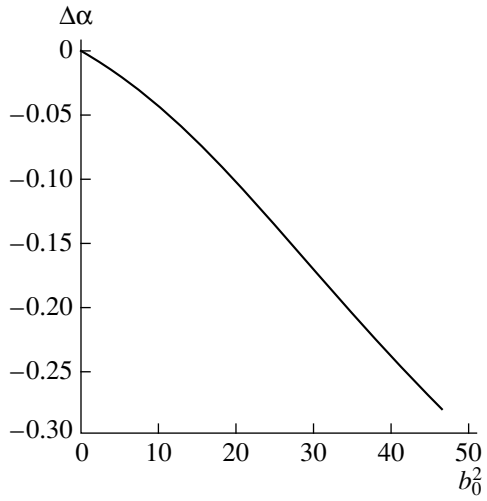

Fig. 2.

and the magnetic field is obtained:

$$\frac{\omega^2 - \omega_0^2}{\omega_0^2} = \alpha \frac{B_0^2}{\rho h a \omega_0^2 \mu_0}. \quad (8)$$

The coefficient α remains constant with a high degree of accuracy and is equal to $\alpha = 0.690$, when the right side of equation (8) varies in a wide range. For high values of the magnetic field induction, when $\omega \gg \omega_0$, the magnitude of α decreases. The dependence of $\Delta\alpha = \alpha - 0.690$ on

$$b_0^2 = \frac{B_0^2}{\rho h a \omega_0^2 \mu_0}$$

is shown in Fig. 2.

As an example, let us consider a niobium resonator with the parameters: $\rho = 8.6 \times 10^3$ kg, $E = 1.6 \times 10^{11}$ N/m^2, $\mu = 0.39$, $l = 4$ cm, $h = 0.5$ mm, $a = 0.5$ mm, and $B = 0.4$ T. When the field is absent, the natural oscillation frequency of such a resonator is $\omega(0) = 1.25 \times 10^4$ Hz. In the field with induction of 0.4 T, the oscillation frequency is $\omega(0.4) = 1.4 \times 10^4$ Hz. Thus, at the magnetic field with an induction of 0.4 T, the oscillating frequency varies by 12%. At a magnetic field of the same magnitude parallel to the resonator length, the frequency varies by 0.126% [10], i.e., by a factor 100 times smaller than for our situation.

In the calculations presented above, it has been taken into consideration that the penetration depth of the magnetic field disturbance, appearing in oscillations, into the superconducting material is equal to zero. For an actual situation, the magnetic field disturbance penetrates into the superconducting material to a finite depth, thus increasing the effective size of the gap *a*. Therefore, the measured oscillation frequency of the superconducting resonator in the magnetic field is always smaller than the calculated one. The comparison between the measured and calculated frequencies permits determining the penetration depth. Using flat parallel plates of a superconducting material, inserted into the vibrator cavity, a gap of 5 μm and less may be obtained. Under the condition that the gap is measured to an accuracy of 0.1%, absolute measurements of the penetration depth to an accuracy better than 50 Å can be performed. Considering that the natural frequency of mechanical vibrations can be measured to an accuracy of 10^{-4}% and that, at such a small gap, the frequency is almost fully determined by the magnetic forces even in the field of several tenths of a tesla, variations in the penetration depth of several hundredths of an angstrom may be registered.

In conclusion, it should be emphasized once again that the proposed construction has essential advantages over the resonators used at present. Firstly, oscillations of such a resonator do not lead to the distortion of the magnetic lines of force (excepting the edge effects which are negligible at a sufficiently wide resonator) and, secondly, the oscillation frequency of such a resonator is more sensitive to the magnetic field. The limitation is that, to vary the field in the resonator cavity, it is necessary to convert at least a part of the resonator to the normal state and then to cool it to the initial temperature again.

REFERENCES

1. S. G. Bodrov, B. P. Peregud, and A. A. Semenov, Zh. Tekh. Fiz. **54**, 2201 (1984) [Sov. Phys. Tech. Phys. **29**, 1290 (1984)].
2. B. N. Brandt, P. Esquinazi, and H.-L. Neckel, Temp. Phys. **63** (3/4), 187 (1986).
3. B. N. Brandt, P. Esquinazi, and H.-L. Neckel, Temp. Phys. **64** (1/2), 1 (1987).
4. S. G. Bodrov, B. P. Peregud, and A. A. Semenov, Sverkhprovodimost: Fiz., Khim., Tekh. **2** (4), 97 (1989).
5. S. G. Bodrov and A. A. Semenov, Zh. Tekh. Fiz. **59** (12), 14 (1989) [Sov. Phys. Tech. Phys. **34**, 1377 (1989)].
6. S. G. Bodrov and A. A. Semenov, Sverkhprovodimost: Fiz., Khim., Tekh. **4** (19), 1668 (1991).
7. S. G. Bodrov, A. D. Danilov, and A. A. Semenov, Sverkhprovodimost: Fiz., Khim., Tekh. **4** (19), 1678 (1991).
8. S. G. Bodrov, A. D. Danilov, A. I. Rusakov, and A. A. Semenov, Zh. Tekh. Fiz. **63** (4), 67 (1993) [Tech. Phys. **38**, 300 (1993)].
9. S. G. Bodrov, A. I. Rusakov, and A. A. Semenov, Zh. Tekh. Fiz. **63** (4), 80 (1993) [Tech. Phys. **38**, 356 (1993)].
10. A. I. Rusakov and A. A. Semenov, Sverkhprovodimost: Fiz., Khim., Tekh. **7**, 1179 (1994).
11. L. D. Landau and E. M. Lifshitz, *Theory of Elasticity* (Nauka, Moscow, 1965; Pergamon Press, Oxford, 1986, 3rd ed.).

Translated by M. Astrov

Technical Physics, Vol. 45, No. 6, 2000, pp. 809–811. Translated from Zhurnal Tekhnicheskoĭ Fiziki, Vol. 70, No. 6, 2000, pp. 140–142.

BRIEF COMMUNICATIONS

Radial Focusing of Ion Beams in a Mass Analyzer with an Electrostatic Lens and a Sector-Shaped Inclined-Wall Magnetic Prism

A. S. Kuzema, S. N. Mordik, and S. A. Kuzema

Institute of Applied Physics, National Academy of Sciences of Ukraine, Sumy, 244030 Ukraine

Received June 28, 1999

Abstract—The ionic and optical properties of an inclined-wall magnetic mass analyzer with electrostatic direction focusing of ions in a nonuniform (r^{-1}) magnetic field were studied. A condition for ion focusing in the radial plane was derived, and the basic parameters of the mass analyzer were determined. © *2000 MAIK "Nauka/Interperiodica".*

Prismatic mass analyzers with an r^{-1} magnetic field offer a number of advantages over those based on uniform two-dimensional magnetic fields. Among these advantages are greater dispersion, flexible geometry of the instrument, and no need for mechanical adjustment.

Mass analyzers with an r^{-1} magnetic field use either magnetic direction focusing of ions or electrostatic focusing. The latter are easier to fabricate and use, because there is no need for intricately shaped pole pieces of a magnet and precision arrangement of ionic–optical elements in this case.

The first to come into being were mass analyzers with magnetic direction focusing [1, 2]. Therefore, their properties are well-understood [3–5]. Sector-shaped magnetic mass analyzers with electrostatic direction focusing are comparatively recent [6] and still under investigation. By now, single-stage and multistage mass-analyzers, achromatic-focusing mass separators, and analyzers with direction and velocity focusing have been investigated in a linear approximation. The studies were made under the assumption that the central trajectory of ions entering and leaving the prism is normal to its boundaries [6, 7].

The ionic and optical properties of the systems with an inclined-boundary prism are of specific interest for instrument makers. In this case, the angles of entry and departure of an ion beam are additional independent parameters of a mass analyzer. Varying them, one can optimize the properties of the instrument and extend its capabilities.

The aim of this paper is to find (in a first approximation) the focusing properties (in the radial plane) and to determine the basic characteristics of a mass analyzer that involves an electrostatic lens and a magnetic prism producing an r^{-1} nonuniform magnetic field when the central ion trajectory cuts the magnetic-field boundaries at different-from-right angles.

The ionic–optical system of the mass analyzer is depicted in the figure. The system consists of ion source *1*, electrostatic lens *2*, magnetic prism *3* (an ion beam enters the prism at an angle ε' and leaves it at an angle ε''), and ion collector *4*.

In such a system, ion trajectories are described by linear differential equations; therefore, the system may be thought of as a device that transforms the initial parameters of a trajectory into the final ones, and this transformation can be represented in terms of matrix algebra [8–10]. We will consider the electrostatic lens as being thin, because its field extends to a distance much less than the focal distance. The leakage magnetic fields will be taken into account by replacing the actual magnetic field with an ideal one that is equivalent of the former in rotation angle; hence, within the accuracy of the given study, corrections for leakage field can be neglected.

In our system, an ion trajectory can be divided into the following regions: free transit from the ion source to the lens, the path over the lens area, free transit from the lens to the input boundary of the prism, the path at the entrance into the prism, the path in the magnetic field of the prism, the path at the exit from the prism, and free transit from the output prism boundary to the ion collector. Then, the three-dimensional matrix transformation that relates the initial and final parameters of the trajectory can be written as

$$\begin{vmatrix} y_7 \\ y_7' \\ \mu_7 \end{vmatrix} = M_7M_6M_5M_4M_3M_2M_1 \begin{vmatrix} y_0 \\ y_0' \\ \mu_0 \end{vmatrix} = M \begin{vmatrix} y_0 \\ y_0' \\ \mu_0 \end{vmatrix}, \quad (1)$$

where y_0, y_0', and μ_0 (all referred to the initial conditions of ion movement at the exit from the ion source) are the initial displacement in terms of the radius of the central trajectory, as well as the direction and relative

1063-7842/00/4506-0809$20.00

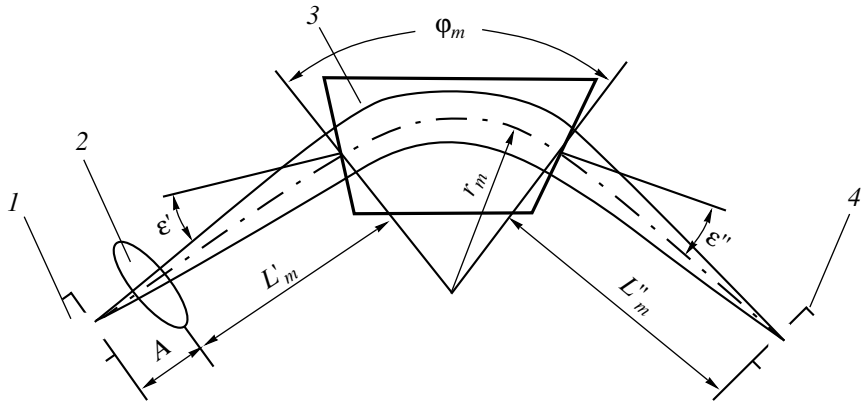

The ionic–optical system of the mass analyzer: (*1*) ion source, (*2*) electrostatic lens, (*3*) magnetic prism, and (*4*) ion collector.

change of the momentum, respectively; M_i is the transfer matrix for the corresponding ion path; and y_7, y'_7, and μ_7 are the parameters of the trajectory at the collector slit.

The transfer matrices for the ion paths at the input and output boundaries of the magnetic prism are defined [10] by

$$M_4 = \begin{vmatrix} 1 & 0 & 0 \\ \tan\varepsilon' & 1 & 0 \\ 1 & 0 & \end{vmatrix}, \quad M_6 = \begin{vmatrix} 1 & 0 & 0 \\ \tan\varepsilon'' & 1 & 0 \\ 1 & 0 & \end{vmatrix}. \qquad (2)$$

The other matrices appeared in (1) are presented in [6] and here are left out.

Sequentially multiplying the matrices for the corresponding ion paths, we will obtain the full first-order transfer matrix in the radial plane:

$$M = \begin{vmatrix} a_{11} & a_{12} & a_{13} \\ a_{21} & a_{22} & a_{23} \\ a_{31} & a_{32} & a_{33} \end{vmatrix}, \qquad (3)$$

where the top-line matrix elements, defining the ion-beam spread in the plane of the collector slit, are

$$a_{11} = \left(1 - \frac{l'_m}{f_{xy}}\right)[1 + \varphi_m\tan\varepsilon' + l''_m\tan\varepsilon''$$

$$+ l''_m\tan\varepsilon'(1 + \varphi_m\tan\varepsilon)] - \frac{\varphi_m}{f_{xy}} - \frac{l''_m}{f_{xy}}(1 + \varphi_m\tan\varepsilon''),$$

$$a_{12} = \left[a\left(1 - \frac{l'_m}{f_{xy}}\right) + l''_m\right][1 + \varphi_m\tan\varepsilon' + l''_m\tan\varepsilon''$$

$$+ l''_m\tan\varepsilon'(1 + \varphi_m\tan\varepsilon'')] + \left(1 - \frac{a}{f_{xy}}\right)$$

$$\times[\varphi_m + l''_m(1 + \varphi_m\tan\varepsilon'')],$$

$$a_{13} = \frac{\varphi_m^2}{2} + l''_m\left(\varphi_m + \frac{\varphi_m^2}{2}\tan\varepsilon''\right), \quad f_{xy} = \frac{F_{xy}}{r_m},$$

$$a = \frac{A}{r_m}, \quad l'_m = \frac{L'_m}{r_m}, \quad l''_m = \frac{L''_m}{r_m}.$$

Here, f_{xy} is the radial focal distance of the lens in terms of the radius of the central trajectory and l'_m, l''_m, and a are the geometric parameters of the mass analyzer (see figure). According to (1) and (2), the deflection of an ion (subjected to arbitrary initial conditions) from the central trajectory at the collimator slit can be written as

$$y_7 = a_{11}y_0 + a_{12}y'_0 + a_{13}\mu_0. \qquad (4)$$

Putting $a_{12} = 0$ in (4), we will obtain the condition for direction focusing of ions:

$$\left[a\left(1 - \frac{l'_m}{f_{xy}}\right) + l'_m\right][1 + \varphi_m\tan\varepsilon' + l''_m\tan\varepsilon''$$

$$+ l''_m\tan\varepsilon'(1 + \varphi_m\tan\varepsilon'')] + \left(1 - \frac{a}{f_{xy}}\right) \qquad (5)$$

$$\times[\varphi_m + l''_m(1 + \varphi_m\tan\varepsilon'')] = 0.$$

Equation (5) relates the lens power to the geometrical parameters of mass analyzer.

The dispersion of the mass analyzer is

$$D_m = \frac{1}{2}a_{13}r_m.$$

Taking into account that $l''_m = L''_m/r_m$, we have

$$D_m = r_m\frac{\varphi_m^2}{4} + \frac{L''_m}{2}\left(\varphi_m + \frac{\varphi_m^2}{2}\tan\varepsilon''\right). \qquad (6)$$

The dispersion is independent of the angle of entry of an ion beam into the magnetic field of the prism.

The dispersion of a mass analyzer with the inclined boundaries exceeds that of a prismatic mass analyzer with the right-angled boundaries by a value of

$$\Delta D_m = \frac{L_m''\varphi_m^2}{4}\tan\varepsilon''.$$

This makes it possible to improve the resolving power of a mass analyzer without increasing the overall dimensions of its ionic–optical system.

A mass analyzer with $l_m' = 0$, $\varepsilon' = 0$, and $a = f_{xy}$ (the lens shapes a parallel ion beam at the entrance into the prism) seems to be of practical interest. In this case, the condition for direction focusing of ions and the dispersion of the mass analyzer are given by

$$\tan\varepsilon'' = -\frac{r_m}{L_m}, \quad (7)$$

and

$$D_m = \frac{L_m''\varphi_m}{2}. \quad (8)$$

The magnifying power of this mass analyzer depends on the coefficient a_{11}. To estimate its value from the condition for direction focusing, one should first find the focal distance of the lens and then calculate the magnifying power.

Since r_m and L_m'', the angle of ion departure from the magnetic field of the prism should be negative to ensure direction focusing; that is, the inclination of the output boundary to the central trajectory must be such that the central trajectory and its center of curvature lie on the opposite sides of the normal to the field boundary.

Our results show that the electrostatic focusing of ions in the direction to a sector-shaped inclined-boundary magnetic prism makes the mass analyzer geometry flexible, increases the dispersion, and suppresses the effects of leakage fields and ion-beam space charge on the instrument parameters.

REFERENCES

1. N. A. Shekhovtsev, *Magnetic Mass Spectrometers* (Atomizdat, Moscow, 1971).
2. N. A. Shekhovtsev, V. F. Shkurdoda, A. S. Kuzema, and A. S. Koloskov, At. Énerg. **22**, 506 (1964).
3. A. F. Malov, V. A. Suzdalev, and E. P. Fedoseev, Zh. Tekh. Fiz. **35**, 914 (1965) [Sov. Phys.–Tech. Phys. **10**, 705 (1965)].
4. E. P. Fedoseev, Zh. Tekh. Fiz. **38**, 1320 (1968) [Sov. Phys.–Tech. Phys. **13**, 1081 (1968)].
5. E. P. Fedoseev, Zh. Tekh. Fiz. **38**, 1330 (1968) [Sov. Phys.–Tech. Phys. **13**, 1088 (1968)].
6. S. A. Kuzema and V. T. Shablya, Ukr. Fiz. Zh. **42** (1), 124 (1997).
7. A. S. Kuzema, N. S. Zinchenko, and O. R. Savin, Zh. Tekh. Fiz. **47**, 2368 (1977) [Sov. Phys.–Tech. Phys. **22**, 1371 (1977)].
8. A. S. Kuzema, O. R. Savin, and I. Ya. Chertkov, *Analyzers for Magnetic Mass Spectrometers* (Naukova Dumka, Kiev, 1987).
9. S. Penner, Rev. Sci. Instrum. **32**, 150 (1961).
10. V. M. Kel'man, I. V. Rodnikova, and L. M. Sekunova, *Static Mass Spectrometers* (Nauka, Almaty, 1985).

Translated by B.A. Malyukov